

**M A S A R Y K
U N I V E R S I T Y**

Faculty of Science

Ph.D. Thesis

Michal Kajan

Brno 2024

**M A S A R Y K
U N I V E R S I T Y**

Faculty of Science

**Magnetospheres and envelopes
of hot stars**

Ph.D. Thesis

Michal Kajan

Supervisor: Prof. Mgr. Jiří Krtička, PhD.

Department of Theoretical Physics and Astrophysics

Brno 2024

Bibliographic record

Author: Michal Kajan
Masaryk University
Faculty of Science
Department of Theoretical Physics and Astrophysics

Title of Thesis: Magnetospheres and envelopes of hot stars

Degree programme: Physics

Field of Study Astrophysics

Supervisor: Prof. Mgr. Jiří Krtička, PhD.

Academic Year: 2024

Number of Pages: XX + 136 = 156

Keywords: Hot stars, magnetospheres, spectra, stellar evolution, irradiation

Bibliografický záznam

Autor: Michal Kajan
Masarykova Univerzita
Přírodovědecká fakulta
Ústav teoretické fyziky a astrofyziky

Název práce: Magnetosféry a obálky horkých hvězd

Studijní program: Fyzika

Obor: Astrofyzika

Vedoucí práce: Prof. Mgr. Jiří Krtička, PhD.

Akademický rok: 2024

Počet stran: XX + 136 = 156

Klíčová slova: Horké hvězdy, magnetosféry, spektra, hvězdná evoluce, ozáření

Declaration

I hereby declare that except where specific reference is made to the work of others, the contents of this dissertation are original and have not been submitted in whole or in part for consideration for any other degree or qualification in this or any other university. This dissertation is my own work and contains nothing which is the outcome of work done in collaboration with others except as specified in the text and acknowledgements. I also used a large language model, chat-GPT and Grammarly. I declare that I have used these AI tools in accordance with the principles of academic integrity.

Michal Kajan
Brno, Fall 2024

Acknowledgements

I want to acknowledge, first of all, supervisor Jiří Krtička. Thank you for your help and for sharing your knowledge. Martin Piecka, Vašek Glos, Kateřina Pivoňková and Ján Budaj, with whom I talked a lot about science and other problems. My whole family, primarily my wife, Eva, I thank her for her support. Also, I want to thank Everest (a Nepalese restaurant near the faculty building) for giving me a reason to go to the faculty when I didn't feel like it.

Lastly, I thank chat-GPT and Grammarly for making this text readable and consistent. Please don't kill me if you gain sentience.

Abstract

This thesis investigates the magnetospheres and envelopes of hot stars, focusing on the complex interactions between magnetic fields, stellar winds and their envelopes. Using advanced computational modelling with the codes TLUSTY, SYNSPEC, and MESA, we explore the effects of deviation from local thermodynamic equilibrium on the stellar atmosphere and the evolutionary processes in the advanced stages of hot stars. Special attention is given to the convergence of models and the sensitivity of physical parameters, ensuring accurate simulations which support theory or analytical equations.

The first key point of this thesis was to evolve an extreme horizontal branch star using the MESA code. This modelling obtained information about the star's potential evolution and structure. This was used as auxiliary information in the article of Krtićka et al. (2024).

A second key point is the identification and resolution of false emission features in the SYNSPEC code, which is crucial for validating spectral models. Furthermore, the results obtained from modelling the irradiation effects on spectra have broader applications beyond the magnetospheric context, offering valuable insights for future studies, such as those involving binary systems with a compact companion star. The research findings are published in Kajan, Krtićka, and Kubát (2024).

Abstrakt

Táto dizertačná práca skúma magnetosféry a obálky horúcich hviezd, pričom sa zameriava na komplexné interakcie medzi magnetickými poľami, hviezdnyimi vetrami a ich obálkami. Použitím pokročilého počítačového modelovania s kódmi TLUSTY, SYNSPEC a MESA skúmame účinky odchýlok od lokálnej termodynamickej rovnováhy na hviezdnu atmosféru a evolučné procesy v pokročilých štádiách horúcich hviezd. Osobitná pozornosť je venovaná konvergencii modelov a vplyvom fyzikálnych parametrov, čím sa zabezpečujú presnejšie simulácie podporujúce teóriu alebo analytické rovnice.

Prvým hlavným bodom tejto práce bolo modelovanie hviezdy na extrémnej horizontálnej vetve pomocou kódu MESA. Toto modelovanie poskytlo informácie o potenciálnom vývoji a štruktúre hviezdy. Tieto informácie boli použité ako pomocné údaje v článku Krtička et al. (2024).

Druhým hlavným bodom je identifikácia a riešenie falošných emisných znakov v kóde SYNSPEC, čo je dôležité pre validáciu spektrálnych modelov. Navyše, výsledky získané modelovaním účinkov ožiarenia na spektrá majú širšie uplatnenie nad rámec magnetosférického kontextu a ponúkajú cenné poznatky pre budúce štúdie, ako napríklad tie, ktoré zahŕňajú binárne systémy s kompaktnou sprievodnou hviezdou. Výsledky výskumu sú publikované v článku Kajan, Krtička a Kubát (2024).

Contents

1	Introduction	1
2	Evolution of hot stars	5
2.1	Formation of the proto-star	6
2.2	Timescales	9
2.3	Pre-main sequence evolution	10
2.4	Main sequence evolution	11
2.4.1	Hydrostatic equation for the star	12
2.5	Post-main sequence evolution	15
2.5.1	Extreme horizontal branch stars	16
2.5.2	Remnants of stars	17
2.6	Brief overview of MESA code	21
2.7	My work - the evolution of massive stars after the main se- quence in MESA	23
2.8	My work - the evolution of the EHB star in MESA	24
2.9	My work - in article about WD	31
3	Stellar Atmospheres	33
3.1	Hydrodynamics equations	33
3.2	Local vs non-local thermodynamical equilibrium	34
3.3	Radiative transfer	37
3.4	Brief overview of TLUSTY code	40

3.5	TLUSTY - spectra of cooler stars	42
3.5.1	Available to download	45
3.5.2	My work - acknowledgement	45
4	Plasma and MHD in stars	49
4.1	Introduction to MHD	49
4.2	The magnetosphere of hot stars	52
4.2.1	Origin of the magnetic field in hot stars	52
4.3	Theory of rigidly rotating magnetosphere	55
4.4	Dynamical vs centrifugal magnetospheres	56
4.5	Effects of stellar wind-magnetic field interaction excluded from RRM model	58
4.5.1	Analytical dynamical magnetosphere	58
4.5.2	Magnetically confined wind shocks	60
4.5.3	Electron cyclotron maser emission in magnetic stars	60
4.5.4	Centrifugal breakout scaling law	63
4.5.5	Dips - problems caused by only a simple dipolar model	64
4.6	My work - Auroral emission modelled in TLUSTY	65
4.6.1	Departure coefficient b-factors in irradiated atmo- spheres	66
4.6.2	Verifying convergence of models	70
4.6.3	False emission in SYNSPEC	70
4.6.4	Other physical parameters in stellar atmosphere . . .	72
5	Conclusions	75
Appendix A The nature of medium-period variables on the extreme horizontal branch		89
Appendix B White dwarf-open cluster associations based on Gaia DR2		103

Appendix C Unveiling stellar aurorae

123

Chapter 1

Introduction

This thesis focuses on hot stars with effective temperatures higher than 10 kK. These stars are characterised by intense luminosity, even in the UV part of the spectra, where they typically have a peak of spectral energy distribution. Their atmosphere is the stage for great interplay between radiation, magnetic field and winds. We already know, for example, the reason for the wind generation in hot stars (radiation-driven winds), which is different from wind generation from the Sun. We know that hot stars have a radiative envelope instead of a convective envelope in cooler stars, and historically, they are sometimes marked as early-type stars. Also, synthetic spectra for hot stars are problematic if they are modelled in local thermodynamics equilibrium, which we can resolve by including the effect of deviations.

This thesis provides a brief introduction and physical equations at the beginning of every chapter to give insight into the topic. This is followed by a description of my scientific projects, which range from small to big.

In Chapter 2, we model the star in code MESA to describe the evolutionary stage of the extreme horizontal star. The paper of Krtićka et al. (2024), in which I was a co-author, used the model's physical insight. We generated a helium-burning model of the star with low mass and low metallicity typical for stars in ω Cen. We analysed their structure and evolution with initial lower metallicity and examined gravity modes' period spacing. In addition,

we present models that were done only for the thesis and were not published in Krtička et al. (2024), e.g., dividing the life of a star after removing the envelope into different stages based on its physical structure. Furthermore, this chapter will briefly mention how we generated models of evolved massive stars in MESA.

Next, in Chapter 3, we use code TLUSTY to generate spectra of cooler stars. We did this using the newest version (v.208), which implemented a method for calculating spectra for cooler stars than 12kK for the first time. We made an overview of how to generate them and created tables for calculating spectra, which are free to download. These synthetic spectra were also used for improving the script used in Piecka, Hutschenreuter, and Alves (2024).

In Chapter 4, we explore the interactions between the magnetosphere and atmospheres of hot stars, focusing on the resulting dynamical and thermal effects to enhance our understanding of stellar magnetism. We hypothesised that if the electrons accelerated in the magnetosphere were not deflected by magnetic mirroring but impacted the star's surface, we could observe specific emission lines. These lines would be classified as auroral emission, as they appear due to the magnetosphere's self-interaction with the star. We started by using code TLUSTY to simulate the atmospheres of hot stars. Then, we started to irradiate models with X-rays, with small increments between models, using the older model as input for calculating the higher irradiated model. We calculate the required wind mass loss for generating potential auroral emission, assuming a one hundred per cent efficiency conversion of the wind's kinetic energy into high-energy photons. In the article, it was also calculated for only one per cent efficiency. Then, we analyse the result and use code SYNSPEC to generate spectra from the model atmosphere. There, we have problems with false (unphysical) emissions, which we omitted and prohibited from reappearing. All different temperatures with different irradiation fluxes were analysed and verified manually. At the same time, we

also searched for UV spectra in FUSE observations deposited in the MAST catalogue. The idea was that the high temperature of an irradiated object would cause the most substantial changes in the population of given elements and produce emissions. However, our search was negative, which agrees with the models, in which we found that the most probable range for finding emission is in the IR part of the spectrum.

Chapter 2

Evolution of hot stars

With their intense radiation, hot stars are exciting objects for testing and understanding stellar evolution. This chapter aims to briefly overview the evolutionary trajectory of hot stars, from the beginning to advanced stages, by briefly describing essential physics during all stages and supplementing theory with graphs from the Modules of Experiments in Stellar Astrophysics (MESA) code.

At first, we start with formation and early evolution, which is the genesis of the star. Every star is born from dense molecular clouds, where the gravitational collapse initiates star formation. Subsequent accretion from protostellar disks can redistribute the mass and angular momentum to the emerging star and the outflowing matter in the late phases of the proto-star.

We continue with the star's fundamental definition, focusing on nucleosynthesis's presence as the primary energy source during its evolution. The evolution of the main sequence star is governed by a balance between gravitational force and pressure gradient, which allows the star to be well understood through analytical physics equations. The equation of state (EOS) and opacities play crucial roles in correctly determining the model's stellar structure and evolution, not only during the main sequence.

Upon depletion of hydrogen in the core, hot stars transition into post-main sequence phases. Their evolution is changed by a complex interaction of

burning hydrogen in the shell, helium or heavier elements in the core, while the envelope can experience strong mass loss. Instabilities present during stellar evolution can cause pulsation and they can also influence subsequent evolution. The final endpoints of stars can be exotic, such as supernovae events, or create remnants such as black holes (BH), neutron stars (NS), or, most typically, white dwarfs (WD).

Finally, we use all this basic knowledge to show a few evolutionary models of hot stars in MESA. MESA provides a robust framework and tool incorporating nuclear reactions, convection, diffusion, and other physical processes during stellar life.

However, we still want to highlight that these are single-star evolutionary models and theories. Even more than half of the stars are found in multiple star systems.

We want to focus on showing most of the equations that describe stars, as they can explain the mechanism better than a thousand words.

The whole chapter is written with the use of references, if not stated differently, Ostlie and Carroll (1996), Phillips (1999), and García-Zamora, Torres, and Rebassa-Mansergas (2023).

2.1 Formation of the proto-star

We know that stars are born in circumstellar clouds. Sir James Jeans first analysed the equilibrium of these clouds and predicted the critical mass needed to initiate their collapse. He used the virial theorem, which we derive in a few quick steps. First, we can introduce scalar Q defined as:

$$Q = \sum_i \mathbf{p}_i \mathbf{r}_i, \quad (2.1)$$

where \mathbf{p} is momentum and \mathbf{r} radius of its particles. Then its time derivative can be written as:

$$\dot{Q} = \sum_i \mathbf{p}_i \dot{\mathbf{r}}_i + \sum_i \dot{\mathbf{p}}_i \mathbf{r}_i = 2T + \sum_i \mathbf{F}_i \mathbf{r}_i, \quad (2.2)$$

where T is kinetic energy and \mathbf{F}_i is the force acting on the particles. After integration over a very long period and dividing by the period, we obtain the time average of \dot{Q} , which is zero for the system in equilibrium. If the term $\langle \frac{dQ}{dt} \rangle \neq 0$, it would imply a continuous change in the system's macroscopic properties, contradicting the equilibrium condition. Then we get

$$T = -\frac{1}{2} \left\langle \sum_i \mathbf{F}_i \mathbf{r}_i \right\rangle. \quad (2.3)$$

Next, for a gravity force ($\propto r^{-2}$), we can rewrite force as the minus gradient of potential energy leading to:

$$T = -\frac{1}{2}U, \quad (2.4)$$

where U is potential energy. This equation is the virial theorem for the gravitational potential.

The virial theorem applied to the cloud means that if kinetic energy T is larger than half of the absolute value of potential energy, the force from gas pressure dominates, and the cloud expands. And, respectively, if the absolute value of potential energy is larger than two times kinetic energy, the cloud starts collapsing. If we substitute the potential energy of the spherical cloud with constant density and the kinetic energy and EOS for an ideal gas, while the number of particles is given by $N = \frac{M}{\mu m_H}$, then the virial theorem would look like:

$$\frac{3}{2} \frac{M}{\mu m_H} k_B T < \frac{1}{25} \frac{GM^3}{R}, \quad (2.5)$$

where μ is mean molecular weight, m_H is mass of hydrogen, G is gravity constant, k_B is Boltzmann constant, T is temperature, and R is radius. After simple algebra and the assumption that the cloud is still homogeneous

$$M = \frac{4}{3}\pi\rho R^3, \quad (2.6)$$

where ρ is density, we get the minimal required mass (marked as Jeans mass M_J) in the following equation:

$$M_J = \sqrt{\left(\frac{5k_B T}{G\mu m_H}\right)^3 \frac{3}{4\pi\rho}}. \quad (2.7)$$

If the cloud's mass exceeds the Jeans mass ($M > M_J$), gravity will dominate over thermal pressure, causing the cloud to collapse. If the mass is below this threshold ($M < M_J$), the cloud will remain stable and will not collapse. We see that the Jean's mass depends on the following "free" parameters:

$$M \propto T^{3/2} \cdot \rho^{-1/2}. \quad (2.8)$$

This dependence implies collapse is most probable in the densest and coldest places, where the calculated M_J would be the smallest. The collapsing cloud can be described as being nearly in free-fall, during this first phase, the whole cloud's temperature remains nearly constant - isothermal approximation. This requirement holds while the cloud is optically thin and can efficiently radiate. We do not observe stars to be born with very high masses, this fact shows that another process must dominate during collapse.

This process is called fragmentation, which splits the cloud into small parts. The initial Mass Function (IMF) describes the relative number of stars formed with different masses. Edwin Salpeter in 1955 (Pinsonneault and Ryden (2023), p. 168) described it with simple power law for stars with

masses between $0.4M_{\odot}$ to $10M_{\odot}$:

$$N(M)dM \propto M^{-2.35} dM. \quad (2.9)$$

Here, NdM is the number density of stars with masses within the infinitesimal mass from M to $M + dM$. The IMF is crucial for understanding the stellar populations in galaxies or star clusters and plays a significant role in calculating isochrone, where the correct number densities of stars are needed to calculate the evolution and dynamics of galaxies.

2.2 Timescales

This subsection is based entirely on Pinsonneault and Ryden (2023). Using Newton's third law applied to an object with only gravitational force; we derive the free-fall (ff) timescale:

$$t_{\text{ff}} = \left(\frac{\pi^2 R^3}{8GM} \right)^{1/2}. \quad (2.10)$$

For example, the Sun would collapse in one and a half hours without its pressure gradient.

The Kelvin-Helmholtz (KH) timescale represents the time it would take for an object (star) to radiate away all of its internal thermal energy, assuming it has no other source of energy and the energy is lost purely through radiation (with constant L) from its surface. The most important is the KH timescale for proto-star, where the star contracts, while the nuclear reaction can be neglected, and luminosity changes very slowly. If we assume the star has a very concentrated core, we can write the following equation:

$$t_{\text{KH}} \sim \frac{GM^2}{RL}, \quad (2.11)$$

where L is luminosity. We need to include the mass distribution in the object to get a more precise estimate. For example, if the star's density profile is uniform, the right side would be multiplied by $3/5$. For an object with the Sun's mass and luminosity, with mass mainly in the core, we would get a KH timescale of $\tau_{\text{KH}} \sim 30$ Myr.

Lastly, the nuclear timescale is the time needed for all hydrogen in the star to be converted into helium, providing energy that supplies the escaping energy.

$$t_{\text{nuc}} = 105 \text{ Gyr} \left(\frac{f_{\text{nuc}}}{1.0} \right) \left(\frac{M}{1M_{\odot}} \right) \left(\frac{1L_{\odot}}{L} \right), \quad (2.12)$$

where f_{nuc} is a fraction of the mass which is burned to helium, and for the Sun, the value is roughly $f_{\text{nuc}} = 0.1$, which gives a timescale of nuclear burning for Sun ~ 10.5 Gyr.

2.3 Pre-main sequence evolution

The pre-main sequence (PMS) phase in a star's life is critical. It encompasses its formation from a molecular cloud to the point when hydrogen fusion fully balances the energy lost through radiation. This phase provides a window into the early stages of stellar evolution, revealing the processes that shape the characteristics of young stars before they settle into stable main-sequence burning.

After the collapse of a molecular cloud, proto-star forms, best described as a quasi-static object with a central hydrostatic core surrounded by slowly in-falling gas. The object is called a PMS star after all the in-falling gas accretes onto the core or is blown away. The PMS star thermally adjusts on the Kelvin-Helmholtz timescale. Because $t_{\text{KH}} \gg t_{\text{ff}}$, this stage of evolution proceeds very slowly in comparison with the collapse of the cloud. According to the virial theorem Eq. 2.4, half of the potential energy is converted into increasing thermal energy. When the proto-star reaches a critical temperature

and density in its core, hydrogen ignites, and the proto-star transitions to the main sequence, where it will steadily burn hydrogen over its main sequence (MS) lifetime.

2.4 Main sequence evolution

At the beginning of their evolution, stars are primarily composed of hydrogen, which constitutes about 70% of their mass fraction (denoted as X). The second most abundant element is helium (Y), followed by metals (Z). For instance, the Sun has a metallicity of approximately $Z \sim 0.014$ [Asplund et al. (2009)]. We usually assume that stars have a homogeneous composition at the beginning of the MS, marked as the zero-age main sequence (ZAMS).

As hydrogen is the most abundant element in the universe and at the beginning of the star, and hydrogen fusion produces a larger amount of energy per gram than any fusion of the heavier elements, the star spends most of its time in the main sequence phase, which burns hydrogen in the core to helium. In the case of the Sun, the MS phase will last approximately 10 Gyrs. The star looks 'static' as hydrogen burning occurs in the core. As time passes on MS, more and more helium in the core modifies individual physical properties; the changes are visible on the surface; however, the consequences are minor (but not negligible) during the MS phase. There is another difference even in hydrogen burning for stars under mass $1.4 M_{\odot}$; for them, hydrogen burning proceeds predominantly through the proton-proton reaction (p-p); however, in more massive stars, the CNO cycle is dominant. If the star's mass is under roughly $0.08M_{\odot}$, temperature and density in the core are not enough to even start p-p burning.

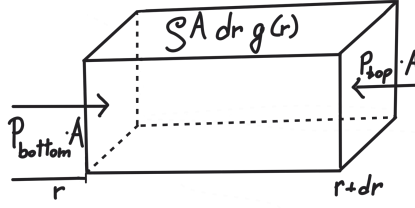


Figure 2.1 Differential volume element $A dr$ with density ρ is used to analyse the forces acting within a fluid. The element is a rectangular prism with a cross-sectional area A and a differential thickness dr . Force acting from the bottom ($P_{\text{bottom}} \cdot A$) is bigger than the force from the top, and the resulting force acts from the bottom and in the opposite direction to gravity.

2.4.1 Hydrostatic equation for the star

In this subsection, we would like to point out a few equations which describe the star during the main sequence very well. The star during the main sequence is nearly in hydrostatic equilibrium.

The mass m enclosed by the sphere with a radius r and density ρ can be described as

$$m(r) = \int_0^r \rho(r') 4\pi r'^2 dr'. \quad (2.13)$$

Illustration in Figure 2.1 shows the pressure force acting on the top and bottom of the cuboid while the gravity force is proportional to the size of the cuboid times density. If we use Figure 2.1 and write forces (second Newton law) that act on the material inside the star in the radial direction, we get:

$$-\frac{d^2 r}{dt^2} = g(r) + \frac{1}{\rho} \frac{dP}{dr} \quad (2.14)$$

where t is time, $g(r)$ is gravity at the radius r and P is pressure. Assuming that there is no force from the pressure gradient, we could estimate the timescale of free fall Eq. 2.10. But here, we assume that the material is in equilibrium,

then we get the following equation:

$$\frac{dP}{dr} = -\frac{Gm(r)\rho(r)}{r^2}. \quad (2.15)$$

The effective temperature T_{eff} of the star is defined as the total amount of energy that the star radiates per unit of time across all wavelengths divided by the surface of the star and Stefan-Boltzmann constant σ , all to the power of the one fourth:

$$T_{\text{eff}} = \left(\frac{L}{4\pi R^2 \sigma} \right)^{1/4}, \quad (2.16)$$

When the energy is transported by radiative diffusion, the following equation can describe the process

$$\frac{dT}{dr} = -\frac{3}{4ac} \frac{\kappa(r)\rho(r)L(r)}{[T(r)]^3 4\pi r^2}, \quad (2.17)$$

where c is the speed of light, and a is constant, which is connected with σ in relation

$$a = \frac{4\sigma}{c}. \quad (2.18)$$

The equation 2.17 can also be understood as a requirement to decrease the temperature with a radius.

Following the topic of energy transport, we now focus on convection. This part of the section is taken from Maeder (2009). We rewrite our earlier defined equation of the temperature gradient of the material (without label) Eq. 2.17, in terms of ∇ as follows:

$$\frac{dT}{dr} = T \frac{d\ln T}{d\ln P} \frac{d\ln P}{dr} = T \frac{\nabla}{-H_P}, \quad (2.19)$$

where H_P is pressure-scale height, and ∇ (of the material) are defined as:

$$H_P \equiv -\frac{dr}{dP} P; \nabla \equiv \frac{\partial \ln T}{\partial \ln P}. \quad (2.20)$$

We can also define the adiabatic temperature gradient as

$$\nabla_{\text{ad}} \equiv \left(\frac{\partial \ln T}{\partial \ln P} \right)_{\text{ad}}. \quad (2.21)$$

From the temperature gradient Eq. 2.17, we can derive the radiative flux using the relation $F_{\text{rad}} = L/4\pi r^2$.

$$F_{\text{rad}} = -\frac{4acT^3}{3\kappa\rho} \frac{dT}{dr} = \text{substituting with (Eq. 2.19)} = \frac{4acT^4}{3\kappa\rho} \frac{\nabla}{H_P} \quad (2.22)$$

The total energy flux is the sum of both radiative and convective fluxes, and we can also define the requirement for a radiative gradient, if it can carry this total flux by only radiation; then the equation would be following :

$$F_{\text{tot}} = F_{\text{conv}} + F_{\text{rad}} = \frac{4acT^4}{3\kappa\rho} \frac{\nabla_{\text{rad}}}{H_P}. \quad (2.23)$$

It is also possible to calculate this artificial radiative gradient ∇_{rad} and show that it must be larger than other gradients inside the convective zone. We know that for convection to happen, the gradient of the blob ∇_{int} , the material to become unstable must be smaller than the gradient of the material "outside" of the blob ∇ (Schwarzschild criterion). Thus, the following inequality holds inside the convective zone:

$$\nabla_{\text{rad}} > \nabla > \nabla_{\text{int}} > \nabla_{\text{ad}}, \quad (2.24)$$

where

- ∇_{rad} is the radiative temperature gradient,
- ∇ is the external gradient (outside of blob, of the material),
- ∇_{int} is the internal gradient (inside of the blob), and
- ∇_{ad} is the adiabatic gradient (for cells that do not exchange heat with surrounding material).

Table 2.1 Timescale of different evolution stages for a star with initial mass $25M_{\odot}$. Taken from Phillips (1999) Table 4.2.

Stage	Timescale	$T_{\text{core}}/10^9 \text{ K}$	$\rho_{\text{core}}/\text{kg m}^{-3}$
Hydrogen burning	$7 \times 10^6 \text{ yrs}$	0.06	5×10^4
Helium burning	$5 \times 10^5 \text{ yrs}$	0.23	7×10^5
Carbon burning	600 yrs	0.93	2×10^8
Neon burning	1 year	1.7	4×10^9
Oxygen burning	6 months	2.3	1×10^{10}
Silicon burning	1 day	4.1	3×10^{10}

It is important to note that both ∇_{rad} and ∇_{ad} can be calculated from fundamental physical quantities, and they represent limits for the "moving" gradient, ∇_{int} . Finally, at the boundary of the convective zone, the material still has some momentum, which causes it to overshoot beyond the boundary. In computational models, this is accounted for by introducing an "overshooting parameter." As discussed in sec. 2.7, this was particularly important for modelling high-mass stars.

2.5 Post-main sequence evolution

The evolution of the observed star is relatively fast after the MS. Burning of elements heavier than hydrogen in the stars does not take very much time; for example, timescales of burning different elements for a star with a mass from $25M_{\odot}$ are shown in table 2.1, more details in section 2.7. The shorter timescales are due to the lower energy obtained per gram of material than hydrogen burning. Additionally, after the formation of iron, subsequent nucleosynthesis involves endothermic reactions.

In Fig. 2.2, we show evolutionary tracks of models for different masses; more details are in section 2.7.

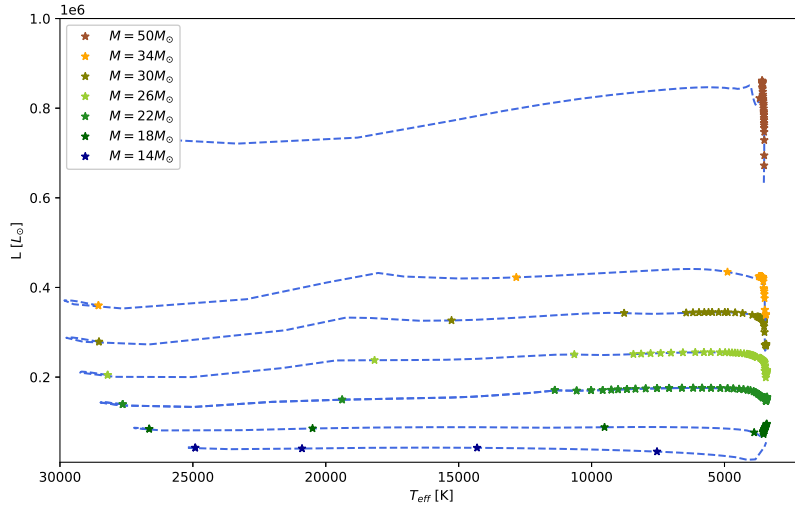


Figure 2.2 MESA evolutionary model in effective temperature versus luminosity plane of massive stars after MS sequence. Marks represent models with time steps with 10^4 yrs. We can observe that not all points of evolutionary tracks are homogenously represented.

2.5.1 Extreme horizontal branch stars

Horizontal branch (HB) stars are characterised by the ignition of helium fusion in their cores, placing them in specific regions on the H-R diagram with higher luminosity than stars on MS. Within this group, subdwarf B (sdB) or subdwarf O (sdO) stars represent a subset of HB stars with particularly high temperatures. In the overview from Heber (2016), extreme horizontal branch (EHB) stars represent a unique class of stellar objects with a very small mass of hydrogen envelope (typically $\sim 0.01 M_{\odot}$) or in photometry defined by having an effective temperature above 20 kK (Moni Bidin et al. (2012)). These stars also exhibit distinct chemical peculiarities, especially in helium content. From an evolutionary point of view, they are evolved stars. This can give us insight into the late stages of stellar evolution, focusing on the transition phases from red giant to WD. One of the scenarios is that EHB stars are remnants of red giant stars that experienced substantial mass loss. A possibility is that they have probably experienced a hot-flash scenario

(through delaying helium flash, which does not occur on top of RGB), and the location on the H-R diagram where they experienced it should provide some evolutionary limits on remnants. Mass loss is important for these objects as their star cores are predominantly made of helium and characterised by low mass. A large fraction of sdB stars are found in close binaries with WD or very low-mass MS stars. The key point is that a common envelope phase occurs during some evolutionary stages, and we cannot understand these stars from only single-evolution models. However, we observe many single sdB stars, suggesting the presence of yet different evolutionary scenario for creating EHB stars, i.e. star merger [ud-Doula and Nazé (2016) overview].

The typical mass of the EHB star is above $0.4 M_{\odot}$, which is minimal mass for helium burning even in a denser star consisting only of helium. As mentioned, we understand that EHB stars must lose nearly all of their hydrogen envelopes during their evolution, which accounts for their high effective temperature and higher gravity on the surface than stars on MS. The most accepted mechanism driving this extreme mass loss is attributed to stellar mass loss in binary interaction (Li et al. (2018)). Alternative evolutionary paths can lead to the formation of EHB stars in the binary system by the merger of two close WDs or in a single system by the strong stellar wind when the star is on the first giant branch, which strips the whole star of most of the hydrogen envelope (Han et al. (2002)).

2.5.2 Remnants of stars

Ultimately, the nucleosynthesis in stars is limited by the endothermic nature of element synthesis. Beyond the synthesis of iron, the process becomes energetically negative, requiring the additional energy input to produce heavier elements. This fundamental constraint sets an unpassable boundary even for the most massive stars. However, additional processes further contribute to the end of stellar evolution. In the end phases, stars experience a strong mass

loss, and the core, which cannot gain energy from nucleosynthesis, collapses into WD, NS, or BH. However, collapse into NS or BH is not straightforward and can cause supernova (SN) events; for a more in-depth analysis of SN explosion, see Kajan (2019).

These stellar remnants represent distinct endpoints in the evolutionary journey of stars, with their formation and properties primarily dictated by the mass and evolutionary trajectory of the progenitor star. This highlights the vast array of outcomes resulting from stellar evolution.

White dwarfs - corpses of low-mass stars

WDs are a class of stellar remnants formed from the core of low or intermediate-mass stars with initial mass typically between $0.1 - 8 M_{\odot}$. Their classification is based on the appearance of absorption lines in their spectra, and the most used classification of WDs is from Sion et al. (1983) or newer classification, which includes incorporating composition by (García-Zamora, Torres, and Rebassa-Mansergas (2023)). WDs are then divided into DA (based on the appearance of Balmer lines), DB (appearance of He I in absorption), or DO (He II in absorption), DQ (carbon) and DZ (metals).

WDs form during the final stages of stellar evolution for stars under $\sim 8 M_{\odot}$. As a star exhausts the synthesis of helium as a nuclear reaction, it continually undergoes gravitational collapse, causing its core to become more dense and hotter. In lower-mass stars, this heating of the core can lead to nuclear runaways of different elements, resulting in the ejection of most of the star's envelope; however, during these late evolutionary phases, stars experience very strong mass loss even without ejection, which reduces the star's mass. As the remaining material of the star collapses, if the density exceeds approximately $10^7 \text{ g} \cdot \text{cm}^{-3}$, the material becomes electron-degenerate. This rapid increase in pressure from the electron-degenerate material halts the collapse. The resulting WD is composed mainly of carbon and oxygen, with a thin crust surrounded by an atmosphere of hydrogen or helium. The

maximal mass of WD, denoted as the Chandrasekhar limit, is around $1.4M_{\odot}$. Beyond this mass, electron degeneracy pressure can no longer support the star against gravitational collapse, leading to further collapse into an NS or a BH, depending on the object's mass.

Upon their formation, WDs are hot and luminous, but over time, they gradually cool and dim as they radiate away their thermal energy. The cooling process is slow, taking billions of years. Initially, WDs cool through thermal radiation and neutrino emission, transitioning from blue-white to red as they age. Eventually, they become faint and cool objects known as black dwarfs, although the timescale for this transformation is much longer than the current age of the universe, and no black dwarfs have yet been observed.

WDs, as remnants of stellar evolution, offer critical insights into the terminal phases of stellar life cycles and the ultimate fate of planetary systems, including our own Solar System. Observations of metal-rich WDs indicate that these stars can tidally disrupt orbiting planets or smaller bodies, leading to accretion of planetary material (von Hippel et al. (2007); Budaj, Maliuk, and Hubeny (2022)).

Neutron stars - pulsars and more

Unlike WDs, the NS and BH are formed as endpoints of the core after the SN event. Despite having a bigger mass, NSs have smaller radii than WDs, which can be analytically understood by the degenerate matter's equation of the state (EOS). NS can also be found with one of the strongest magnetic fields observed in the universe. Due to the conservation of angular momentum following the core collapse, NS can exhibit extremely rapid rotation. This rapid rotation and beams emitting from NS make them observable as pulsars. Studying these objects provides insights into extreme physics that cannot be replicated in laboratory settings, offering a glimpse into the fundamental nature of matter and energy. Recent literature on SN explosion frequently utilises compact parameters introduced by O'Connor and Ott (2013). These

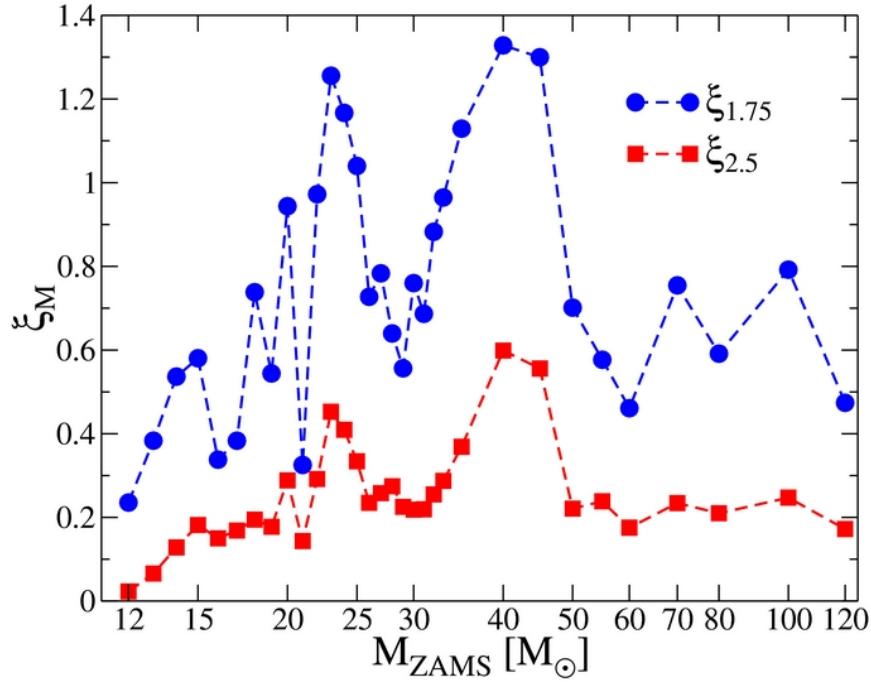


Figure 2.3 Compactness parameter on the y-axis versus initial mass on the beginning of MS on the x-axis for 1.75 and 2.5 M_{\odot} enclosed masses. Taken from O'Connor and Ott (2013) Figure 1.

parameters describe whether the stellar core can collapse to form a BH or if it can rebound material. It is introduced by a simple equation of

$$\xi_M = \frac{M/M_{\odot}}{R(M_{\text{bary}} = M)/1000 \text{ km}}, \text{ at the time of the bounce,} \quad (2.25)$$

where $R(M_{\text{bary}} = M)$ is the radial coordinate that encloses a baryonic mass of M , where it is usually used the mass of $M=2.5M_{\odot}$ since this is the typical mass scale of a formed BH from SN. With increasing the ξ_M , the object's core becomes more compact, and the product will likely end as BH. Contrariwise, when ξ_M decreases, the object is more likely to bounce and create SN, and the remnant would be NS. Figure 2.3 illustrates the dependence on ZAMS mass. The key concept, however, is that the compactness parameter ξ_M is not a monotonic function dependent on the ZAMS mass.

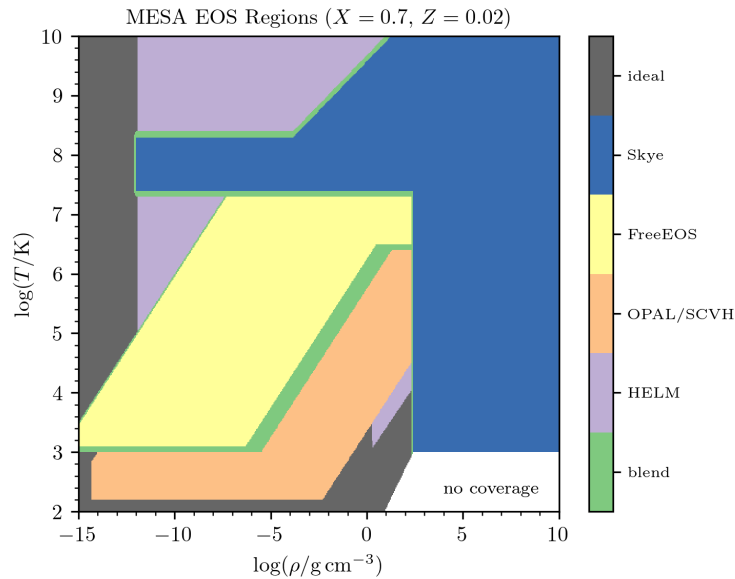


Figure 2.4 Coverage of EOS models based on density-temperature pair, for specific abundance $X=0.7$ $Z=0.02$. Taken from website: docs.mesastar.org/en/release-r24.03.1/eos/overview.html.

2.6 Brief overview of MESA code

The Modules for Experiments in Stellar Astrophysics (MESA) code by Paxton et al. (2011) is a powerful and flexible tool to simulate stellar evolution. It enables the modelling of stellar life cycles from the pre-MS to the advanced stages, including WD cooling or pre-SN stages. MESA easy framework supports a wide range of stellar masses, compositions, cooling, nuclear burning and mass loss. It employs advanced numerical methods to solve stellar structure and evolution equations, incorporating nuclear reactions, energy transport, and mixing processes. The highly modular code allows users to customise simulations to their research needs. Continuous updates and a supportive user community enhance its capabilities and accessibility. Its application spans various astrophysical contexts, from single-star evolution to binary interaction and stellar population synthesis.

Code MESA use a blend of the OPAL [Rogers and Nayfonov (2002)], SCVH [Saumon, Chabrier, and van Horn (1995)], FreeEOS [Irwin (2004)],

HELM [Timmes and Swesty (2000), PC [Potekhin and Chabrier (2010)], and Skye [Jermyn et al. (2021)] EOSes. Radiative opacities are primarily from OPAL [Iglesias and Rogers (1993); Iglesias and Rogers (1996)], with low-temperature data from Ferguson et al. (2005) and the high-temperature, Compton-scattering dominated regime by Poutanen (2017). Electron conduction opacities are from Cassisi et al. (2007) and Blouin et al. (2020). Nuclear reaction rates are from JINA REACLIB [Cyburt et al. (2010)], NACRE [Angulo et al. (1999)] and additional tabulated weak reaction rates [Fuller, Fowler, and Newman (1985); Oda et al. (1994); Langanke and Martínez-Pinedo (2000)]. Screening is included via the prescription of Chugunov, Dewitt, and Yakovlev (2007). Thermal neutrino loss rates are from Itoh et al. (1996).

MESA code consists of many modules, each responsible for different aspects of numerics or physics, creating a whole computational model of stellar astrophysics. Physical modules are divided into microphysics and macrophysics. Microphysics modules are divided into physical constants, EOS, opacities, thermonuclear and weak reactions, and nuclear reaction networks. For example, the EOS is a blend of different opacity tables. For stars with mass abundances $X=0.7$ and $Z=0.02$, the opacity for the given density-temperature pair is from the opacity table following Fig. 2.4. Macrophysics modules are instead responsible for, i.e. convection mixing length, convective overshoot mixing, diffusions, atmosphere boundary conditions, and gravitational settling.

For detailed information, it is best to use the official site¹; the website describes all modules. Also, it contains a page dedicated to a list of known bugs found in older versions.

¹<https://docs.mesastar.org/en/release-r24.03.1/modules.html>

2.7 My work - the evolution of massive stars after the main sequence in MESA

In Figure 2.2, we modelled the evolution of stars with a specific mass on ZAMS using code MESA version r24.03.1. The modelled stars have solar metallicity ($Z=0.02$) and mass loss wind set as default in the following template taken from MESA. We were interested in studying what is similar for these stars with $T_{\text{eff}} \sim 9$ kK and very small gravity $\log g \sim 1$, to the right on the H-R diagram from the MS sequence, in terms of physics or different parameters. This is why we evolved massive stars after MS and looked at them after the terminal age of the main sequence; we focused on their progress convection zones in the subsurface and other parameters, i.e., evolutionary tracks.

All models are based on template *7M_premsto_AGB* [MESA template]. The model of the star is considered to end MS when a relative mass abundance of hydrogen reaches less than 10^{-4} . At the same time, the stopping condition was chosen to be under-abundance helium in the core (relative mass abundance of ${}^4_2\text{He}$ in the core reaches less than 10^{-4}). All input data can be downloaded and then started with code MESA version 24.03 from the website: <https://is.muni.cz/www/kajan/mesa/>. In Figure 2.2, we skipped evolutionary preMS and MS evolution, but we used a calculated time at the end of MS to describe the typical evolutionary timescale. The position of stars on their tracks from MS to the red supergiant branch is not linear with time. Another problem was the big jump appearing with a model with ZAMS mass $26M_{\odot}$. We solved this after private communication with R. Townsend because we omitted to incorporate important physical processes, mainly overshooting of the convective zone. We included that based on article Temaj et al. (2024), and the jump then disappeared. Here is a list of additional changes which were incorporated. Parameters "mesh_delta_coeff" was set to 0.8, "max_dq" was

set to $5 \cdot 10^{-3}$, "varcontrol_target" was set to 10^{-5} , alpha for semi-convection was set to 0.1, instantaneous semi-convection based on Ledoux criterion was turned on. We allow "step" overshooting on the top side for hydrogen and helium burning with the overshooting parameter set to 0.05.

The models were also used to study the inner structure of stars, which exhibit high-velocity events in Pivoňková (2024).

2.8 My work - the evolution of the EHB star in MESA

This section will describe our methodology to model subdwarf O-type (sdO) stars, incorporating additional modifications to what we used in article Krtička et al. (2024). The full article is also provided in Appendix A.

We followed the procedure for creating a sdO star as described in Han et al. (2002). We started with creating a preMS star with masses ranging from 1.5 to $2.5 M_{\odot}$, with a mass fraction of metal set to $Z=0.0006$ corresponding to a globular cluster's ω Cen. We used the MESA template *l_premsto_wd*, which evolves a star from preMS to WD with the following modifications. We enhanced the mesh resolution of the WD, changing the mesh coefficient to 0.25, and turned on the Ledoux criterion for convection (Schwarzschild criterion for convection we showed in Eq. 2.24), which in retrospect significantly reduced the ΔP_g to the order of days.

The star's evolution was calculated in MESA version r24.03.1 and, for best practice, was divided into different segments for different phases of evolution. In the following text, we will describe the life of the model star with an initial mass of $2.1 M_{\odot}$. Each phase of the evolution can have different parameters and requires a specific stopping condition, which is a predefined state at which the model is saved and can be subsequently loaded in the next phase. We mention all stopping conditions between the different phases of the model.

1. First, after creating a preMS star, the evolution is stopped when the luminosity from the burning hydrogen exceeds (our) definition $1L_{\odot}$. The reasoning is that this stage includes simpler physics (i.e. no mass loss and only simple mixing).
2. Next, the star evolves until it reaches the end of its MS phase, with the stopping condition being a central relative mass abundance of hydrogen A_{H} is less than 10^{-4} .
3. The star then evolves until it begins burning hydrogen in an off-centre shell with an integrated luminosity of approximately $\sim 1000 L_{\odot}$, marking the onset of core helium burning and the ejection of the envelope.
4. Finally, we stripped away the hydrogen envelope, leaving a helium core and envelope with $0.01M_{\odot}$ of hydrogen, effectively simulating an sdO star. The star was then allowed to evolve through helium burning in the core until nucleosynthesis ended. The stopping condition was set when the star's luminosity dropped under $10^{-3} L_{\odot}$.

Figure 2.5 shows the whole evolutionary track after removing the envelope (marked as core) is very complex, but we describe it based on the location and elements responsible for occurring nucleosynthesis.

After artificially removing most of the envelope, we focus on the evolution, retaining only the core and a hydrogen envelope with a mass of $0.01M_{\odot}$. Initially, we observed that the remnant, described as an EHB star (core with thin hydrogen envelope), resumed helium nucleosynthesis, increasing the effective temperature above 15 kK. Additionally, we analysed the accretion of material onto the star, including heavier elements and more complex nucleosynthesis networks. Specifically, we added $0.001 M_{\odot}$ of material with the same mass abundances as observed in Krtićka et al. (2024). The resulting surface convection zones did not significantly change the calculated Brunt-Väisälä frequency. Furthermore, we investigated whether significantly lowering the metallicity

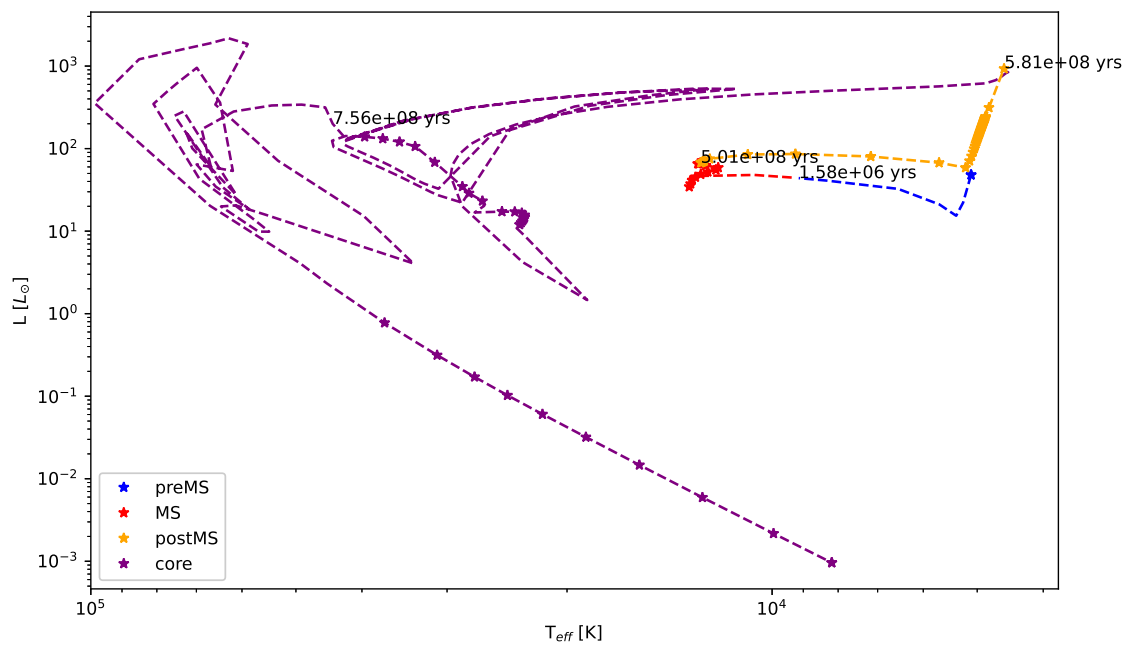


Figure 2.5 The evolution of a star with an initial mass of $2.1M_{\odot}$ and a metallicity of $Z=0.0006$ is traced until luminosity decreases under $10^{-3}L_{\odot}$. An age is specified at the end of each evolutionary stage, except for the core stage. Where the age is noted at the end of stable helium burning, just before the track transitions to the unstable stage. Models marked with an asterisk (*) on the graphs represent time steps of $t_{\text{MS}}/50$, where t_{MS} is the total time spent on the main sequence. The dashed line connects the movement along the H-R diagram.

would induce additional evolutionary changes, particularly changes in the core mass and the potential for continued helium burning. The objects discussed in the mentioned article have masses $0.2 - 0.3 M_{\odot}$, while our MESA models predicted that helium burning stars have masses only slightly above $0.4 M_{\odot}$, which is typical for such stars. Our simulations indicated that the inclusion of heavy elements significantly influenced the compactness of the inner core, leading to helium or hydrogen flashes in cases with lower initial masses.

This chapter in the thesis aims to analyse the Brunt-Väisälä frequency during the evolutionary track of star and other astroseismology parameters available in MESA. Here, we describe the star's evolution after removing the envelope, which we marked as core evolution, which we artificially split into different parts. After removing the envelope, we divide the core evolution into the following five stages:

1. **After removing the envelope:** this stage occurs immediately after removing the envelope and lasts until the helium burning begins. The phase is very short and likely unobservable.
2. **Stable helium-burning:** in this stage, the star (with a mass of $0.44 M_{\odot}$ in a specific case) can sustain helium burning.
3. **Helium burning in the shell:** even if helium burning continues, this stage significantly impacts the radius R and effective temperature T_{eff} , which is observable in the H-R diagram.
4. **Unstable and thermal pulses:** instabilities characterize this stage; it is also very short.
5. **Cooling down:** the star begins cooling down along the WD track.

We investigated the parameter ΔP_g , representing g-mode spacing for $l = 1$. ΔP_g is then defined by the following equation from Dziembowski, Moskalik,

and Pamyatnykh (1993)

$$\Delta P_g = \frac{\sqrt{2}\pi^2}{\int \frac{N}{r} dr}. \quad (2.26)$$

Here, N is Brunt-Väisälä frequency, and with the assumption of an ideal gas, we can define it as follows:

$$N^2 = g \left[\frac{1}{\gamma P} \frac{dP}{dr} - \frac{1}{\rho} \frac{d\rho}{dr} \right], \quad (2.27)$$

where γ is an adiabatic index. The frequency N can be split into structural and compositional components to understand what is responsible for this frequency in a given star.

ΔP_g reached a value of a few days during part of the evolutionary process of modelling sdO, which can be seen in Fig 2.6 in the middle panel - green solid line. Analysis revealed that the structural characteristics of the star played pivotal roles in shaping the calculated Brunt-Väisälä frequency. Specifically, the dominance of the μ composition term deep in the star near the convective core increased ΔP_g to the value of the order of days. This finding should underscore the importance of accurately modelling the chemical composition.

However, we reached the following conclusions after discussing the results privately with Dr. Wojciech Szewczuk. The analytical equation used for calculating ΔP_g in the subroutine of MESA does not answer what is responsible for the excitation of a given period. He found no similar pulsation period using our input in the code from Walczak and Kopacz (2024).

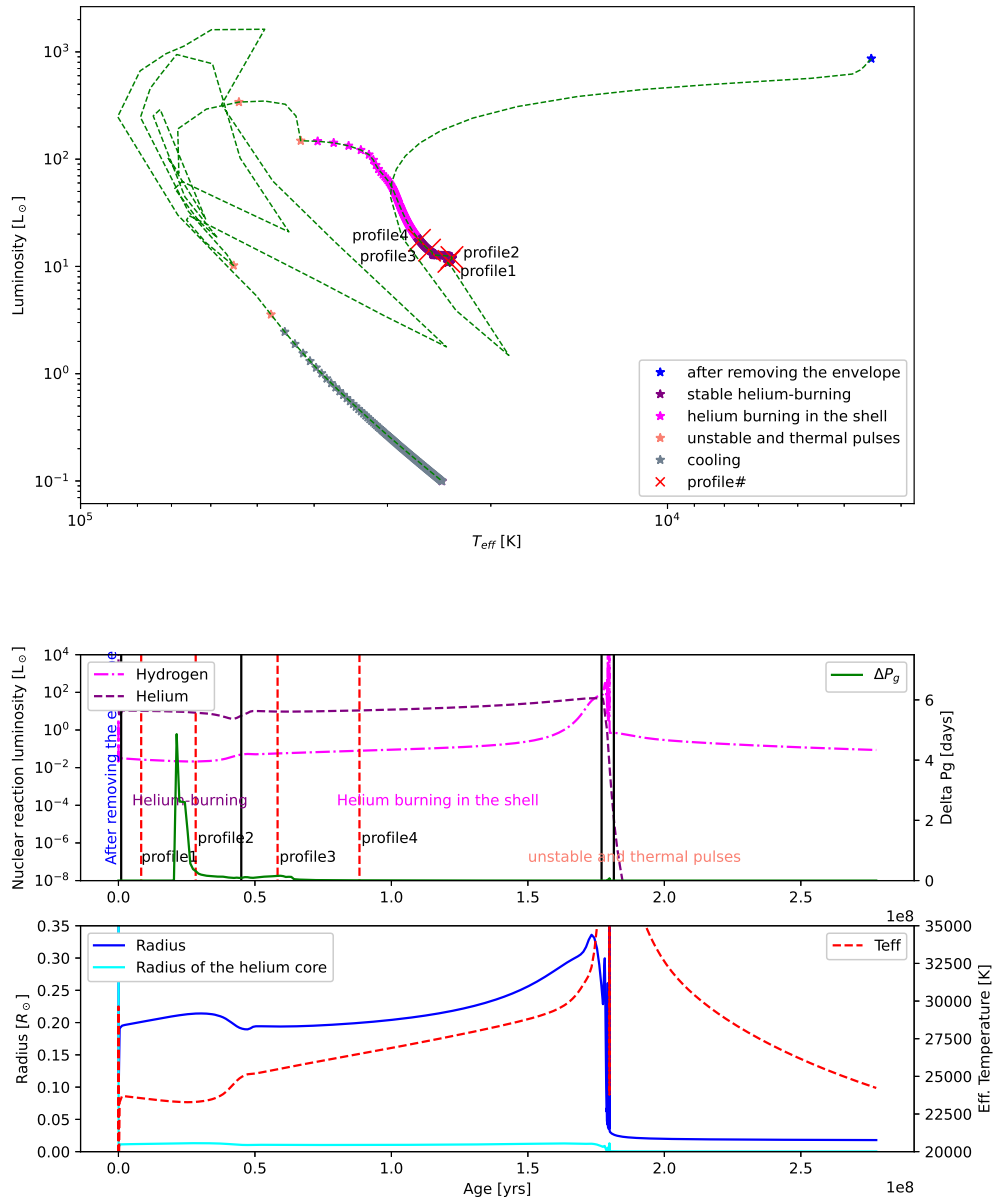


Figure 2.6 The evolution of a star with a mass of $2.1 M_{\odot}$ and metallicity of $Z=0.0006$ after artificially removing the envelope. *Top panel:* Evolutionary track of the star. Models marked represent time steps of $t_{MS}/500 \simeq 10^6$ yrs, where t_{MS} is the total time spent on MS. *Middle panel:* Age of the star versus physical parameters: nucleosynthesis (integrated luminosity of given elements generated from burning), solid green curve is ΔP_g , black vertical lines represent changes of stages as in top panel, with name of the stage is written between lines, and red dashed lines represent age position for which we plotted profiles in Figure 2.7. *Bottom panel:* Age of the star versus radius of the star and helium core inside of the star, together with effective temperature.

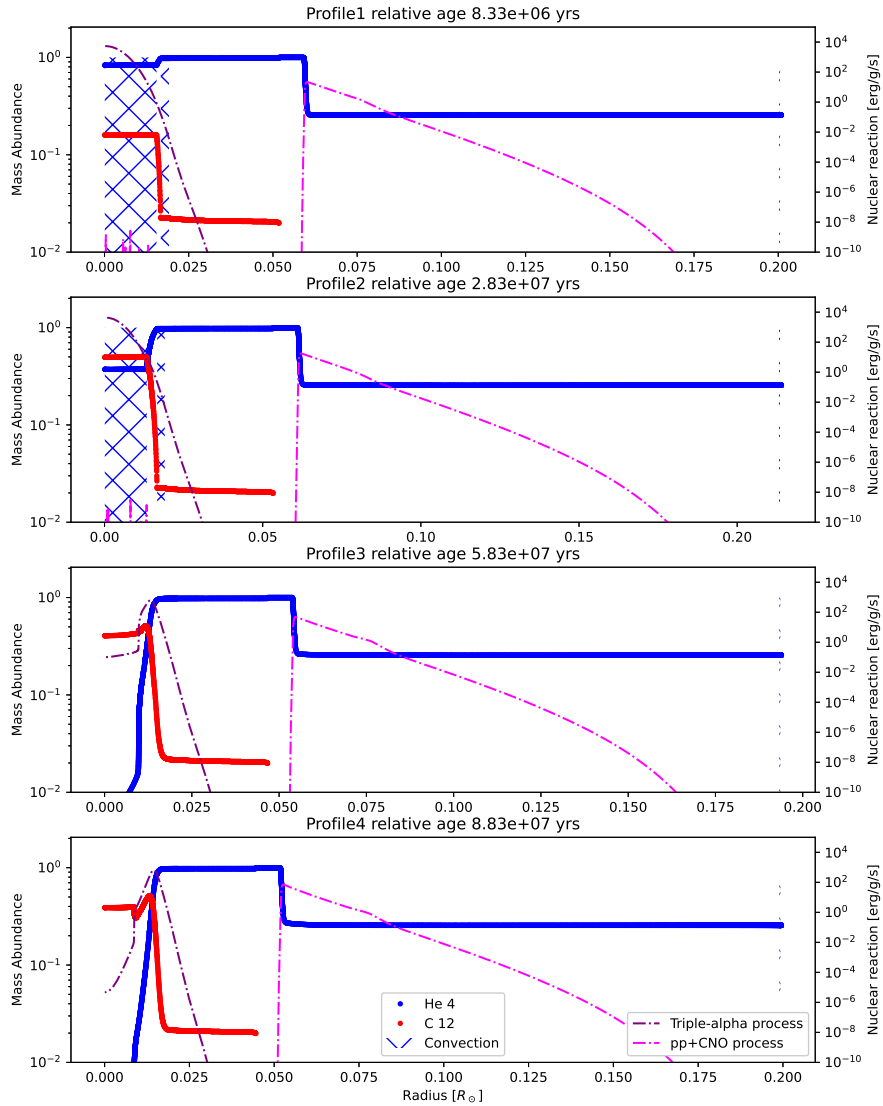


Figure 2.7 The profile of the mass abundance of helium and carbon, position of the convection and nuclear reaction of given processes inside of the star with initial mass $2.1 M_{\odot}$ and $Z=0.0006$, after artificially removing envelope, profile# has the same naming convention as in the middle panel in Figure 2.6. Relative age is calculated as total age minus age when the envelope from the star was removed.

2.9 My work - in article about WD

Additionally, I contributed as coauthor to the article Prišegen et al. (2021), also available in Appendix B. I created a script to verify the results of identifying new WD candidates under the supervision of Dr. Michal Prišegen in the open cluster (OC). Our objective was to identify if newly found WDs can be assigned to known OC. I additionally provided input on the possible implication of mass constraint of the progenitor based on the known age of OC.

Chapter 3

Stellar Atmospheres

Understanding stellar spectra is pivotal for deciphering the properties and behaviours of stars. Stellar spectra arise from the interactions between light and matter within a star's atmosphere, revealing valuable information about its temperature, composition, and motion. For writing this chapter we used the following literature: Ostlie and Carroll (1996), Kaler (2011) and Swihart (1971)

3.1 Hydrodynamics equations

The hydrostatic equilibrium equation was already presented in chapter 2.4.1. The Boltzmann equation, which provides a comprehensive description of the kinetic distribution function to a given ion, can be expressed as:

$$\frac{\partial f_i}{\partial t} + (\mathbf{u} \cdot \nabla) f_i + (\mathbf{F} \cdot \nabla_p) f_i = \left(\frac{Df_i}{Dt} \right)_{\text{coll}} \quad (3.1)$$

where f_i is the distribution function for a given ion, t is time, \mathbf{u} is velocity, \mathbf{F} is force acting on the particles and ∇ is the gradient operator with respect to position, and ∇_p is the gradient operator with respect to momentum. The term on the right side, $\left(\frac{Df_i}{Dt} \right)_{\text{coll}}$, represents the collision term which accounts for changes in the distribution function due to collisions between particles.

Standard procedures can be followed to derive the corresponding moment equations for the distribution function starting from this Boltzmann equation. This process involves integrating the Boltzmann equation over the appropriate velocity space and yielding a set of macroscopic conservation laws that describe the behaviour of the fluid's moments. Zeroth order Boltzmann equation is also sometimes called an equation for conservation of the mass

$$\frac{\partial \rho}{\partial t} + \nabla \cdot (\rho \mathbf{v}) = 0. \quad (3.2)$$

The first moment of the Boltzmann equation, also called the momentum equation for an inviscid fluid:

$$\rho \frac{\partial \mathbf{v}}{\partial t} + \rho \mathbf{v} \cdot \nabla \mathbf{v} = -\nabla p + \rho \mathbf{g}. \quad (3.3)$$

The second moment of the Boltzmann equation called the energy equation, is

$$\frac{\partial}{\partial t} \left(\rho \varepsilon + \frac{\rho v^2}{2} \right) + \nabla \cdot \left(\rho \mathbf{v} \left(\varepsilon + \frac{v^2}{2} \right) \right) = -\nabla \cdot (p \mathbf{v}) + \rho \mathbf{v} \mathbf{g}, \quad (3.4)$$

where \mathbf{v} is macroscopic velocity, p is pressure, \mathbf{g} is gravity and ε is internal energy. Several approximations are commonly employed to simplify the equations in a stellar atmosphere. Typically, the stationary ($\frac{\partial}{\partial t}=0$) and static ($\mathbf{v}=0$) approximations of the medium are used. The plane-parallel approximation is often applied, simplifying the problem's geometry to dependence solely on the z coordinate.

3.2 Local vs non-local thermodynamical equilibrium

The description is simplified if we assume that the material's thermodynamical equilibrium (TE) is valid. Although TE cannot be assumed in a stellar atmosphere, the concept of local TE (LTE) can be used, where the temperature and number density (or electron number density) are well defined locally. The

electron number density is frequently used in stellar atmospheres since charge neutrality is typically maintained. The Maxwell-Boltzmann distribution describes the velocity distribution in LTE:

$$n_v dv = dv 4\pi v^2 n \left(\frac{m}{2\pi k_B T} \right)^{3/2} \exp \left(-\frac{mv^2}{2k_B T} \right). \quad (3.5)$$

Here, n_v is the number density of particles with velocity v , m is the particle's mass, and T is temperature. The Boltzmann equation gives the ratio of the densities of particles in the energy state j to i , $\frac{n_j}{n_i}$:

$$\frac{n_j}{n_i} = \frac{g_j}{g_i} \exp \left(-\frac{E_j - E_i}{k_B T} \right), \quad (3.6)$$

where n_j is the number density of particles in the energy state j , g is the statistical weight for a given energy level, and E_i is energy at level i . The Saha ionization equation describes the ionisation equilibrium of atoms in gas or plasma.

$$\frac{N_{X+I}}{N_X} = \frac{2}{n_e} \frac{U_{X+I}}{U_X} \lambda^3 \exp \left(-\frac{E_{X+I} - E_X}{k_B T} \right), \quad (3.7)$$

$$\lambda = \left(\frac{2\pi m_e k_B T}{h^2} \right)^{1/2}, \quad (3.8)$$

where N is the number of atoms at a given ionisation state, n_e is the electron number density, U is the partition function, m_e is the mass of the electron, h is the Planck constant, and E_X ionisation energy of X -th state. Here, we will rewrite this equation for hydrogen for two ionization states, which can be simplified as total density is constant $N = N_0 + N_1$. We also define $z = n_e/N$, so we get to the following equation:

$$\frac{z^2}{1-z} n_e = \lambda^3 \exp \left(-\frac{E_{X+I} - E_X}{k_B T} \right), \quad (3.9)$$

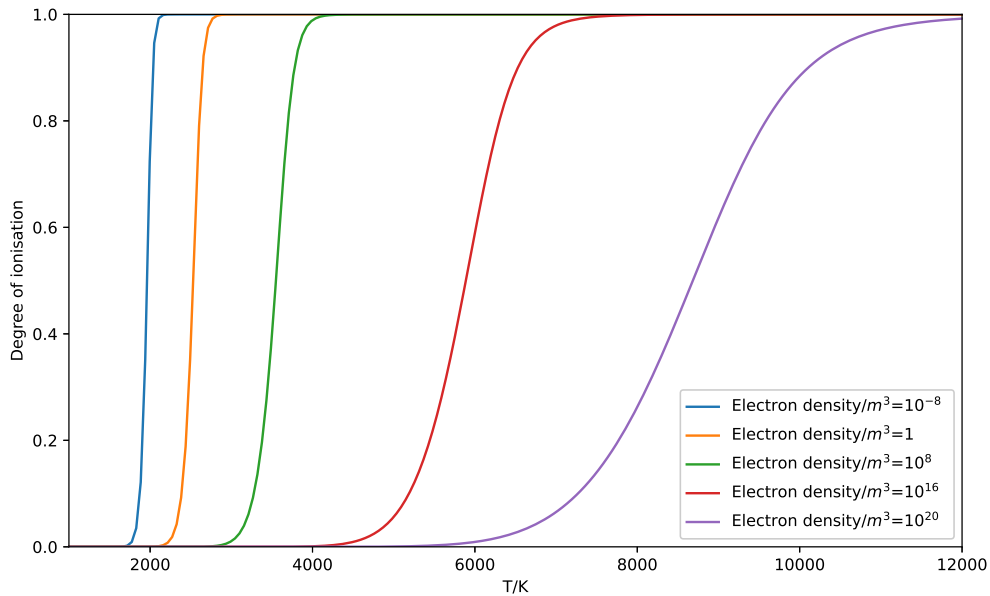


Figure 3.1 Hydrogen degree of ionisation for $\chi = -13.6eV$, for different densities of electron. Calculated from Eq.3.9. The script can be also downloaded as Python notebooks from <https://is.muni.cz/www/kajan/scripts/>.

where z is a fraction of ionisation for hydrogen. This equation was used for calculating Figure 3.1.

In summary, if TE holds:

1. particles have Maxwell Boltzmann distribution,
2. the Boltzmann excitation equation describes energy levels population and Saha ionisation equation,
3. The Planck function can describe the radiation field.

In non-local thermodynamics equilibrium (non-LTE), we allow the populations of atoms' energy levels to deviate from their LTE values while assuming that particle velocities follow a Maxwell-Boltzmann distribution. In a stellar atmosphere, massive particles, such as ions and atoms, generally maintain LTE and exhibit a Maxwellian distribution of velocities. However, radiative

transitions can become more significant than collisional processes as we move higher in the atmosphere, where densities decrease. This shift typically occurs because the collision rate drops while radiative processes remain relevant.

When radiative transitions begin to dominate over collisional transitions, the balance must be considered to accurately describe the population of energy levels, which is:

$$n_i \sum_{j \neq i} (R_{ij} + C_{ij}) = \sum_{j \neq i} n_j (R_{ji} + C_{ji}), \quad (3.10)$$

where n_i represents the number density of particles, R_{ij} represents radiative rates with a transition from level i to level j , and C_{ij} represents collisional rates. This equation ensures that the total rates of transitions into and out of each energy state are balanced, which is crucial for accurately determining the non-LTE populations in the stellar atmosphere.

Even in regions where radiative rates become significant, LTE can still be maintained locally if the collisional rates are high enough to minimise deviations from the Maxwellian-Boltzmann distribution. In deep layers of the atmosphere, where densities are higher, collisional processes dominate, and photons do not escape efficiently; thus, the LTE approximation remains valid.

3.3 Radiative transfer

The radiative transfer equation, which describes radiation propagation through the stellar atmosphere, is a fundamental aspect of analysing stellar spectra. This equation is central to understanding how light is emitted, absorbed, and scattered, shaping the observed spectra. A stellar atmosphere is a region from which photons can escape, and the whole observed spectrum originates from this thin region of the star. We begin with the definition of specific intensity,

I_λ , which is connected with energy defined as:

$$dE_\lambda = I_\lambda d\lambda dt dA \cos(\theta) d\Omega, \quad (3.11)$$

where E_λ is the energy, dA is the area, $d\Omega$ is the solid angle, $d\lambda$ is the wavelength interval, and dt is the time interval. This quantity describes the amount of radiant energy passing through an area in a given direction and provides a macroscopic description of the radiation field at any point in space.

Next, considering the conservation of energy, radiation of wavelength λ passing through a material over distance dx with density ρ , absorption coefficient κ_λ , and emissivity coefficient j_λ , the preservation of energy gives rise to the radiative transfer equation:

$$\frac{dI_\lambda}{dx} = j_\lambda \rho - \kappa_\lambda \rho I_\lambda. \quad (3.12)$$

We can also rewrite $\frac{dI_\lambda}{dx}$ to a differential derivative

$$\left(\frac{\partial I_\lambda}{\partial x} + \frac{1}{c} \frac{\partial I_\lambda}{\partial t} \right) = j_\lambda \rho - \kappa_\lambda \rho I_\lambda, \quad (3.13)$$

where c is the speed of light. In thermal equilibrium, the source function S_λ equals the Planck function $B_\lambda(T)$, which describes the radiation intensity emitted by a black body at temperature T . Source function S_λ is defined as the ratio of the emissivity (j_λ) to the absorption coefficient (κ_λ):

$$S_\lambda \equiv \frac{j_\lambda}{\kappa_\lambda} \quad (3.14)$$

The Planck function is given by:

$$B_\lambda(T) = \frac{2hc^2}{\lambda^5} \frac{1}{\exp(hc/\lambda k_B T) - 1}. \quad (3.15)$$

In LTE, the source function can be written as $S_\lambda = B_\lambda$. In equilibrium within the stellar atmosphere, each process is counterbalanced by its inverse, resulting in no net energy being withdrawn from the radiation field. Consequently, the radiative flux maintains a constant value throughout the layers below the stellar surface:

$$F_{\text{rad}} = \text{const.} = \sigma T_{\text{eff}}^4, \quad (3.16)$$

where F_{rad} is radiative flux.

In radiative equilibrium, the energy absorbed by the material is balanced by the energy it emits. Following the formalism of Hubeny and Mihalas (2014), and neglecting thermal conduction and convection, the material energy equation in static atmosphere models can be expressed as:

$$\int_0^\infty (j_\lambda \rho - \kappa_\lambda \rho J_\lambda) d\lambda = 0, \quad (3.17)$$

where the integral runs over all wavelengths, and J_ν represents the mean intensity of radiation. With using Eq. 3.14, we can rewrite it in the following way (for the condition that $\kappa_\lambda \rho \neq 0$):

$$\int_0^\infty (S_\lambda - J_\lambda) d\lambda = 0. \quad (3.18)$$

This equation includes the condition that, over all frequencies, the net energy exchange via radiation is zero.

Alternatively, this equilibrium condition can be formulated as:

$$\nabla \cdot \mathbf{F} = 0, \quad (3.19)$$

where \mathbf{F} denotes the radiative flux. Both equations reflect that there is no net gain or loss of radiative energy within the material because it is in radiative equilibrium.

The radiative transfer equation, the specific intensity, and the source function form the basis for interpreting the light from stars and understanding

their atmospheres. In summary, the radiative transfer equation deals with the movement and interaction of radiation within the stellar atmosphere. By examining both the radiative transfer and the hydrostatic equilibrium equations, we can achieve a comprehensive understanding of stellar atmospheres and interiors. The radiative transfer equation provides insights into the emergent spectrum and energy distribution, while the hydrostatic equilibrium equation reveals the internal pressure and density distribution necessary to counteract gravitational collapse. Together, these equations form the foundation for studying stellar atmospheres and the intricate balance of forces that sustain stars.

3.4 Brief overview of TLUSTY code

The TLUSTY code (Hubeny and Lanz (1995)) computes classical model atmospheres under approximations of plane-parallel geometry, horizontal homogeneity in hydrostatic and radiative equilibrium. In our research with TLUSTY, we aim to explore new features introduced in the latest versions of both TLUSTY and SYNSPEC, referencing their respective manuals for comprehensive understanding: Hubeny and Lanz (2017a), Hubeny and Lanz (2017b), Hubeny and Lanz (2017c) and Hubeny et al. (2021). Without these guides and explanations, this work would not have been possible.

The equations involved are non-local and depend on the geometry of the atmosphere. The radiative transfer equation can be derived from Eq. 3.12, then we would get:

$$\frac{d^2(f_\lambda J_\lambda)}{d\tau_\lambda^2} = J_\lambda - S_\lambda, \quad (3.20)$$

where f_λ is the variable Eddington factor, monochromatic optical depth defined as $d\tau_\lambda = -\kappa_\lambda \cdot dx$.

The assumed hydrostatic equilibrium is defined as

$$\frac{dP}{dm} = g, \quad (3.21)$$

where P is the total pressure, and m is Lagrangian mass. The energy balance is calculated as follows using equation Eqs. 3.17 and 3.19:

$$\alpha \left[\int_0^\infty (\chi_\lambda J_\lambda - \eta_\lambda^{\text{tot}}) d\lambda \right] + \beta \left[\int_0^\infty \frac{d(f_\lambda J_\lambda)}{d\tau_\lambda} d\lambda - \frac{\sigma}{4\pi} T_{\text{eff}}^4 \right] = 0, \quad (3.22)$$

where $\chi = \kappa \cdot \rho$ is absorption coefficient per volume unit, $\eta = j \cdot \rho$ is emission per volume unit, α and β are constants. In the code TLUSTY, α is 1 for the upper layers of the atmosphere and 0 for deeper layers, and β is the opposite way. These equations represent what we refer to as energy balance, with the term in brackets after α representing the integral form and the term in brackets after β representing the differential form. The distinction between "deep" and "surface" layers is treated as a free parameter, crucial for the numerical stability for solving the equation. Specifically, the transition of α from 0 to 1 at a particular depth is critical; if not handled properly, it can lead to convergence issues affecting the entire model.

The TLUSTY code can also incorporate non-LTE effects, particularly important for modelling hot stars with rarefied atmospheres dominated by radiation. In such cases, TLUSTY calculates the population of various atomic species energy levels within the stellar atmosphere, considering processes like ionisation, excitation, recombination, and de-excitation. This capability allows for detailed modelling, where multiple energy levels for each ion can be separately considered at the cost of extra calculation time and numerical instabilities. Input parameters can be adjusted for different chemical elements as needed.

At the lower boundary, TLUSTY uses diffusion approximation, in which the Planck function fully approximates the source function. No photons can

escape in this region, and thermal equilibrium can be assumed. This approach simplifies the radiative transport method, which is expressed as a Taylor series of the first two terms, describing the outward-deflected specific intensity (I_{ν}^+) as :

$$I_{\nu}^+ = B_{\nu} + \mu(dB_{\nu}/d\tau_{\nu}). \quad (3.23)$$

Here, B_{ν} is the Planck function, μ represents the cosine of the polar angle ($\mu = \cos\theta$), where θ is the angle between the direction of propagation and the normal to the surface.

In the static approximation, materials cannot exhibit convection. However, in code TLUSTY, convection is described using mixing length theory, which incorporates convection through the following equation

$$F_{\text{rad}} + F_{\text{conv}} = \sigma T_{\text{eff}}^4, \quad (3.24)$$

where F_{rad} represents radiative flux, F_{conv} is the convective flux of state parameters (such as T , ρ , p , ...).

3.5 TLUSTY - spectra of cooler stars

This section outlines the methodology employed to generate the synthetic spectra used in this chapter. The primary objective of modelling is to produce spectra that can be compared with observed data, providing input parameters that predict various spectral features. To generate synthetic spectra across a range of temperatures and gravities, we utilised the TLUSTY¹ and SYNSPEC² codes. In this text, we focus on demonstrating the effects of temperature variations on specific wavelengths. The latest version TLUSTY was employed to enable the calculation of spectra for cooler stars (in our case, from 10 kK, but it is possible to extend it for much lower values), a capability

¹version 208

²version 54

Table 3.1 Schematic procedure for creating spectra for cooler stars in TLUSTY.

CODE:	SYNSPEC	TLUSTY	SYNSPEC
Step & Description	1.st & Calculating opacity tables	2.nd & Generating model of the atmosphere	3.rd & Creating spectrum

included in this recent version. One small technical detail about convection is that the newest version calculates the adiabatic gradient from the specific entropy as the primary quantity.

Generating model atmospheres and synthetic spectra for cooler stars involves a multiple-step process as detailed in Table 3.1. This table visualises the procedural steps and provides a comprehensive visualisation, described next in the text.

In the *first step*, we use SYNSPEC to create an opacity table. If we find during the next steps that our opacity table is unsuitable or does not cover enough density or temperature range in the star, we can generate a new one. This table is crucial for modelling the stellar atmosphere and generating synthetic spectra. We selected the default input in SYNSPEC to generate an opacity table with 100,000 wavelength points logarithmically spaced between 900 – 110,000 Å. A discrete set of temperatures, logarithmically distributed within a defined temperature range, alongside a set of specified densities, distributed within designated density intervals. More details of the opacity table are provided in Tab. 3.2. We want to emphasise, as it was mentioned in Hubeny et al. (2021), that we need to include H₂O and TiO opacities for cooler stars. Lastly, opacity tables are generated for specific elements, which means that if we want to calculate some elements in non-LTE in the future, we need to calculate a second opacity table without these elements. In our case, "OTf.dat" is a table for all elements and "OThec.dat" table excludes H, He, and C elements. Also, the atomic opacity and molecular opacity (for $T < 8$ kK) were included in this opacity table.

Table 3.2 Opacity tables that are available and can be downloaded from: <https://is.muni.cz/www/kajan/tlusty-opacitytables/> .

Name of Opacity Table	# points and range of Temperature/ kK	# point in densities and range of Densities / g cm ⁻³
OT1	11 & 5.5-35	7 & $5 \times 10^{-16} - 10^{-9}$
OT2	12 & 5-35	14 & $10^{-20} - 10^{-6}$

In the *second step*, we employ TLUSTY to generate the model of the star's atmosphere. Initially, we created LTE grey atmosphere model using opacity table "f", which includes all elements. Then, the LTE model serves as the input for calculating the non-LTE model, where H, He, and C are treated as non-LTE. We utilise the opacity table "hhec", which excludes these elements. It is important to note that after calculating each model in TLUSTY, we always check if the model converged correctly.

In the *third step*, we utilise the model atmosphere calculated from TLUSTY (".5" and ".7"), which have been calculated using the opacity tables, as input into SYNSPEC to calculate the spectrum for our specific input (".55"). It is crucial to adjust the input ".5" file by changing the value from 1 to 5 (MODE) for all elements in the opacity table. If it is left to MODE = 1, then the element is treated implicitly and contributes to line opacity, while MODE = 5 also includes the bound-free opacities of the given species. We also provide opacity tables and model atmospheres ".5" and ".7" to simplify for readers and ensure reproducibility. Additionally, elements for which the opacity table was calculated to have mode changed to 5 in the file ".5" for easy recalculating spectra with SYNSPEC.

To generate spectra for hotter stars with the mentioned input parameters, we updated the file ".5" with newer ionisation potential data to match the new SYNSPEC 54 version. We also provided the model atmospheres (output) ".5" and ".7" calculated from TLUSTY (Non-LTE H, He and C other elements in quasi-explicit) files, which were calculated with the opacity table OT1 and used in this section. The cooler star's spectra were then plotted into

top panels in Figure 3.2 and 3.3. Then we also generated spectra for hotter stars, which we then plotted into middle and bottom panels of Figure 3.2 and 3.3, the input models for this hotter star are files ".5" and ".7" taken from Lanz and Hubeny (2007). Lastly, we plotted the top of the four strongest absorption lines in the given interval plus hydrogen and helium lines, which were calculated by script. These figures then effectively demonstrate the key changes in spectra due to variations in temperature and gravity, providing valuable insights into stellar atmosphere modelling.

3.5.1 Available to download

Downloadable files can be used in the code SYNSPEC to generate spectra or a physical model of the atmosphere. They are free to download on the website: <https://is.muni.cz/www/kajan/tlusty-opacitytables/>.

You can also download the ".dat" opacity tables mentioned in this text, which are needed to calculate the TLUSTY model.

3.5.2 My work - acknowledgement

Spectra of cool stars were used to help distinguish some features of cool stars in Piecka, Hutschenreuter, and Alves (2024).

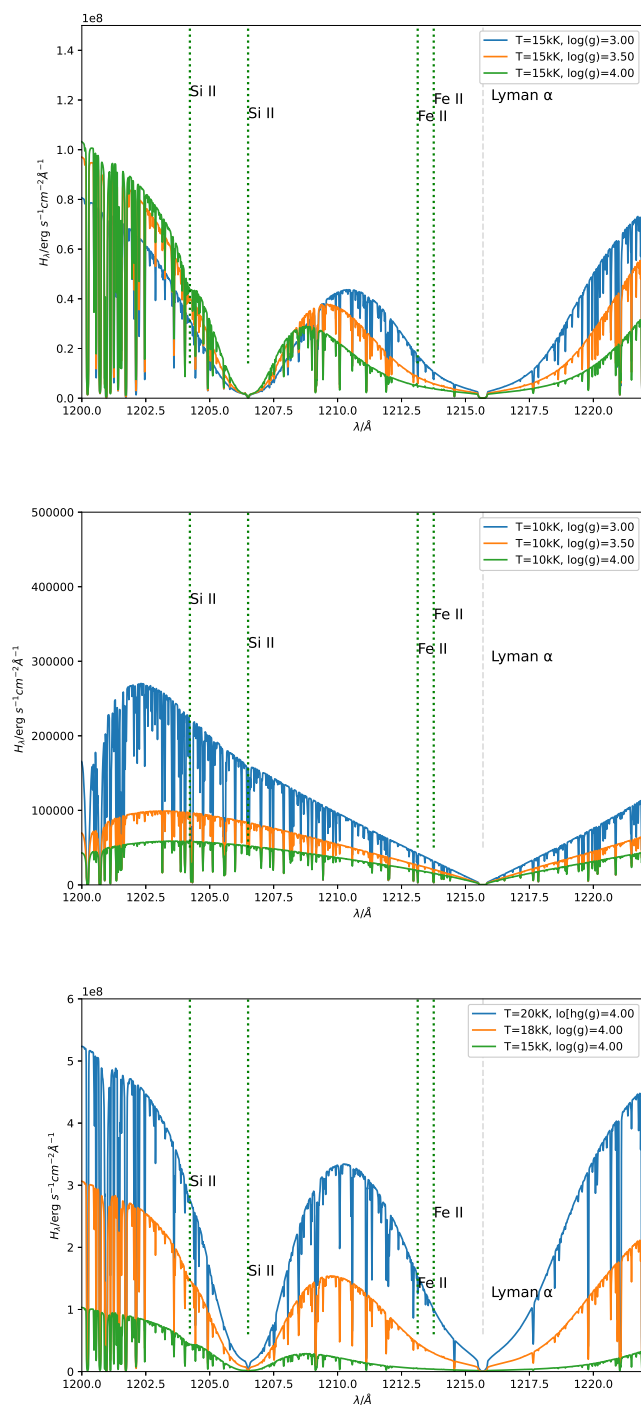


Figure 3.2 Synthetic spectra generated by code TLUSTY. All figures display the same wavelength range. In each figure, we marked the four strongest absorption and hydrogen lines within this wavelength range based on line widths determined by SYNOPSIS. Additionally, the names of the elements responsible for these lines are indicated. *Top panel:* Spectral differences with temperature fixed at 15kK while gravity varies. *Middle panel:* Spectra with temperature fixed at 10kK while gravity varies. *Bottom panel:* Spectra with gravity fixed $\log(g/[CGS]) = 4$ while temperature varies.

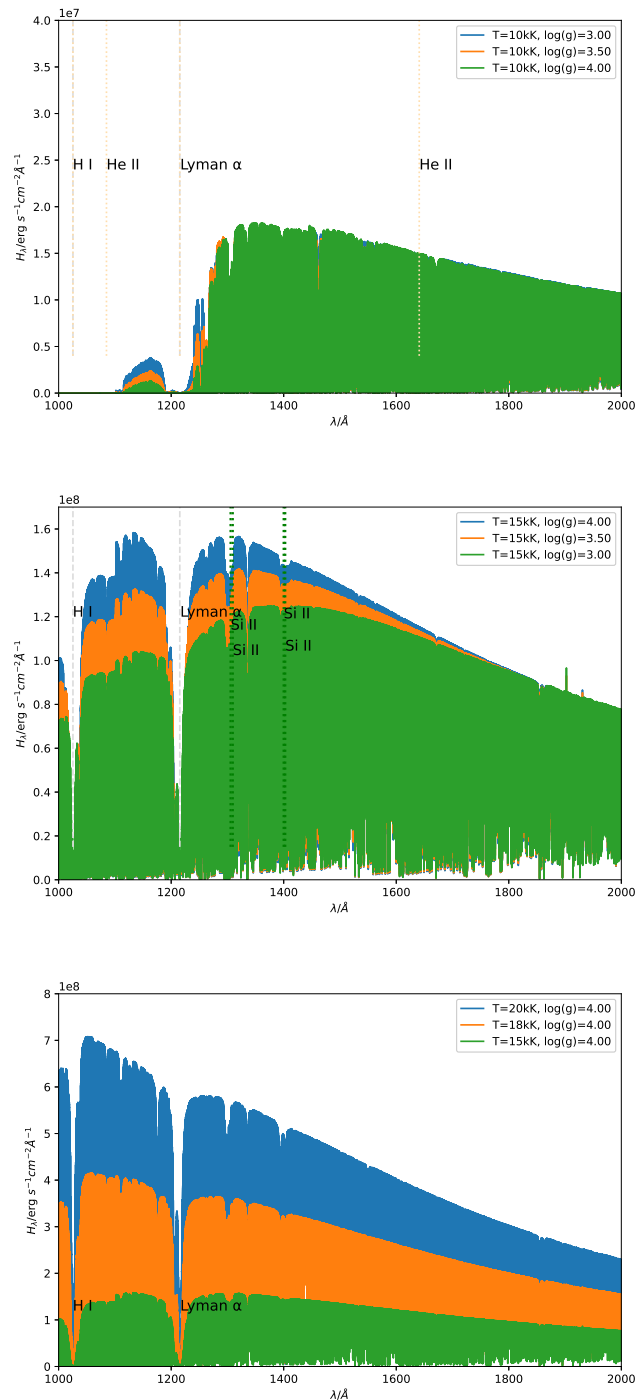


Figure 3.3 Similarly as figure 3.2, but with different wavelength range. Synthetic spectra generated from code TLUSTY. A few important elements are marked. *Top panel:* Difference in spectra with temperature fixed at 15 kK while gravity varies. *Middle panel:* Spectra with temperature fixed at 10 kK while gravity varies. *Bottom panel:* Spectra with gravity fixed at $\log(g/[CGS]) = 4$ while temperature varies.

Chapter 4

Plasma and MHD in stars

4.1 Introduction to MHD

Plasma, often called the fourth state of matter, is essential for understanding the universe, mainly because stars predominantly exist in a plasma state. It is crucial to grasp the physical process governing plasma to describe celestial bodies accurately. The complex nature of plasma presents a challenge because it cannot be treated as a single fluid material. In plasma, electrons and ions may move at different velocities, leading to distinctive and sometimes unexpected behaviours that require careful analysis.

We will use the definition of plasma based on the book Karlický (2014). Plasma is defined as a partially or fully ionised gas. With the following assumption, it is electrically neutral overall, a property referred to as quasi-neutrality. Additionally, plasma is characterised by the collective behaviour of its particles. For a plasma composed of electrons and protons (e^- and p^+), following conditions must hold:

1. The system exhibits collective behaviour when the mean force from nearby interactions, $\langle F_{\text{near}} \rangle$, becomes negligible compared to the significantly stronger force from distant interactions $\langle F_{\text{dist}} \rangle$:

$$\langle F_{\text{near}} \rangle \ll \langle F_{\text{dist}} \rangle . \quad (4.1)$$

2. The number of particles within the Debye sphere must be much greater than one:

$$\frac{1}{n\lambda_D^3} \ll 1, \quad (4.2)$$

where n is a plasma density and λ_D is Debye length.

3. The thermal kinetic energy is significantly larger than electrostatic energy:

$$KE \gg PE. \quad (4.3)$$

where $KE = (3/2)k_B T$ is kinetic energy, $PE = e^2/(4\pi\epsilon_0\lambda_D)$ is electrostatic energy, and ϵ_0 is electrical constant and e is electron charge.

Next, we explore a few key concepts in plasma physics that build on these foundational properties. One of the most important concepts is Debye shielding, a phenomenon where a plasma screens out electric fields over a characteristic length called a Debye length, which is defined as:

$$\lambda_D \equiv \sqrt{\frac{\epsilon_0 k_B T}{n_e e^2}}. \quad (4.4)$$

Debye length represents the minimal distance for which electrons do not feel charge from protons as it is shielded by surrounding plasma (e^-).

Another key concept is plasma oscillation. Plasma oscillation is a collective electron oscillation in a plasma, driven by the system's natural tendency to restore local charge neutrality when perturbed. This oscillation, a consequence of quasi-neutrality, occurs at a characteristic frequency known as the plasma frequency (for electrons) ω_e defined as:

$$\omega_e^2 \equiv \frac{n_e e^2}{\epsilon_0 m_e}. \quad (4.5)$$

The hydrodynamic equations discussed in chapter 3.1 must be extended by coupling them with Maxwell's equations to describe plasma dynamics fully.

These equations govern the behaviour of electric and magnetic fields in the plasma (in a vacuum):

$$\nabla \cdot \mathbf{E} = \frac{\rho}{\epsilon_0}, \quad (4.6)$$

$$\nabla \times \mathbf{E} = -\dot{\mathbf{B}}, \quad (4.7)$$

$$\nabla \cdot \mathbf{B} = 0, \quad (4.8)$$

$$\nabla \times \mathbf{B} = \mu_0(\mathbf{j} + \epsilon_0 \dot{\mathbf{E}}), \quad (4.9)$$

where \mathbf{j} is current density, ρ is electric charge density, μ_0 vacuum permeability (\mathbf{E} and \mathbf{B} are, as always, the intensity of electric and induction of magnetic fields, respectively).

We can derive the induction equation by analysing Maxwell's fundamental equations, which are essential in describing the dynamics of magnetic fields within a plasma:

$$\dot{\mathbf{B}} = \nabla \times (\mathbf{v} \times \mathbf{B}) + \eta \nabla^2 \mathbf{B}, \quad (4.10)$$

where $\eta = 1/\mu_0\sigma$ is magnetic diffusivity (σ is electric conductivity).

To compare different terms in the induction Eq. 4.10, we introduce the magnetic Reynolds number (R_m)

$$R_m = \frac{\nabla \times (\mathbf{v} \times \mathbf{B})}{\eta \nabla^2 \mathbf{B}}. \quad (4.11)$$

which compares the relative importance of advection and diffusion in the plasma. For cases where R_m is small or when characteristic velocities are low, the induction equation reduces to the diffusion equation:

$$\dot{\mathbf{B}} = \eta \nabla^2 \mathbf{B}. \quad (4.12)$$

In contrast, when R_m is large, typical of high-velocity or collisionless plasma ($\eta \rightarrow 0$), the equation simplifies to:

$$\dot{\mathbf{B}} = \nabla \times (\mathbf{v} \times \mathbf{B}). \quad (4.13)$$

4.2 The magnetosphere of hot stars

Hot stars, particularly those of early B-type, often exhibit strong magnetic fields that significantly influence their circumstellar environments. The MIMES project estimates that the observable magnetic field is present typically about 7 per cent of hot stars [Grunhut et al. (2017)]. Stars with a magnetic field have strong geometrically simple magnetic fields [Shultz et al. (2019)]. Hot stars have radiation-driven winds, which, coupled with a magnetic field, affect the wind [ud-Doula and Owocki (2002)]. The influence of the magnetic effects on the wind can be qualitatively described by the magnetic confinement parameter η_* , which would be defined later in Eq. 4.16. For moderate confinement ($\eta_* \sim 1$), the magnetic field starts to channel the wind and affects its density and speed, while strong confinement ($\eta_* \sim 10$) leads to even shock waves that can produce hard X-ray emission.

Moreover, the centrifugal magnetosphere contains regions where the trapped material can co-rotate [see Romanova and Owocki (2016) for a review]. They also address the scenario of disk accretion, where the stellar magnetic field can truncate the inner regions of the disk and influence the trajectory of matter as it accumulates onto the star. Numerous observational effects exist as pieces of evidence for the magnetosphere in various spectral domains, specifically the X-ray domain [Nazé et al. (2015)], ultraviolet [UV, Marcolino et al. (2013)], near-infrared [Oksala et al. (2015)], radio [Leto et al. (2021)], and $H\alpha$ [Owocki et al. (2020)].

Further details, including a visual schematic of the stellar magnetosphere, are provided in Figure 4.1.

4.2.1 Origin of the magnetic field in hot stars

We do not think the star's magnetic field is of dynamo origin because rotation is not connected with the strength of magnetic fields. The magnetic field of

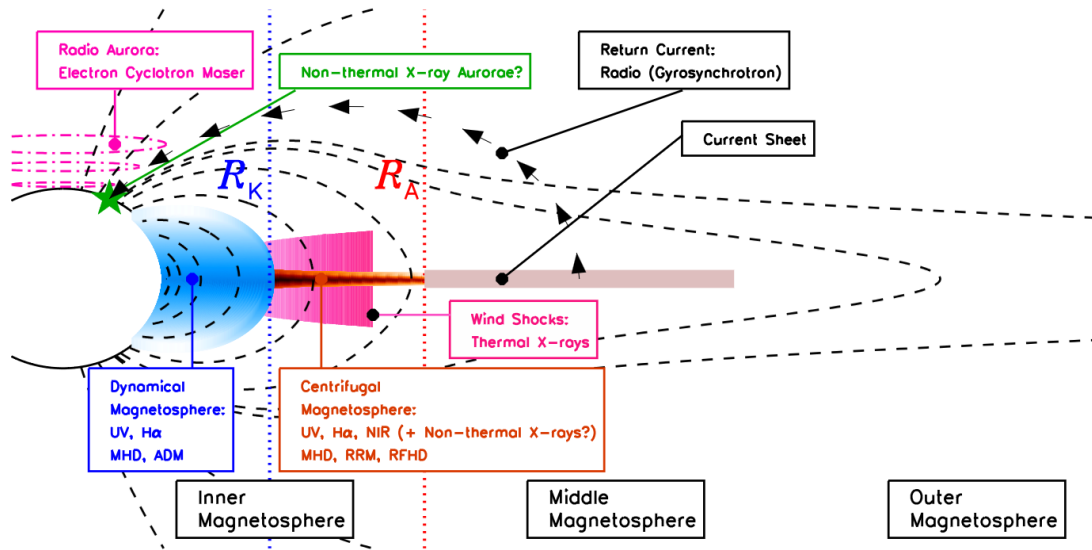


Figure 4.1 Schematic of a stellar magnetosphere for an aligned dipole around a rapidly rotating star. Taken from Shultz (2020).

hot stars is similar to that of WDs and NSs [Shultz et al. (2018)]. For this reason, they are believed to be of fossil origin. Fossil magnetic fields are distinguished by their long-term stability and primarily poloidal structure. These magnetic fields are believed to be fossil fields, remnants from earlier evolutionary stages. These fields can be strong (several kilogauss) or weak (few Gauss), stable over long periods, and exhibit (dominating) a simple dipolar topology without showing complex surface activity cycles [Shultz et al. (2018)]. The strength and structure of these fields vary significantly among different stars, leading to diverse magnetospheric characteristics. The magnetic axis is tilted relative to the rotational axis (the angle is marked as β). However, the exact origin of these fossil fields remains unknown. The questions of why and where they are generated are still open but constrained by magneto-astroseismology. The leading theories of why some stars are magnetic suggest that primary stimulus may arise from the conservation of magnetic flux from the ISM during star formation or as a consequence of stellar mergers. Also, magnetic stars are known to rotate more slowly than

their non-magnetic counterparts (Wade and Neiner (2018)). The slow rotation of magnetic stars was also reproduced in the article Keszthelyi et al. (2020), where they have very rapid spin-down caused by the magnetosphere rotation during the evolution simulation in MESA.

One of the few cases of the star, potentially originating from a binary merger, is discussed by Shenar et al. (2023). Specifically, the Wolf-Rayet (WR) star HD 45166 (it is a binary star system) exhibits a significant magnetic field, mean magnetic field modulus $\langle B \rangle = (43 \pm 2.5)$ kG, identified through Zeeman splitting. This strong magnetic field, combined with its high temperature and luminosity, classifies WR star HD 45166 as a potential progenitor of a magnetic NS (magnetar) after it explodes as SN Ib or IIb type. The future presence of magnetar is deduced with the assumption of magnetic flux conservation and core collapse, which gives the final product magnetic field in order of 10^{14} G. This can be verified in the following way. From Eq. 4.13, it is possible to derive Alfvén's (or frozen in flux) theorem defined as:

$$\frac{d}{dt} \iint_S \mathbf{B} \cdot d\mathbf{A} = 0, \quad (4.14)$$

where S is the surface, \mathbf{B} is the magnetic flux and \mathbf{A} is the area. For all the details and conditions required for derivation, see Eq. 11.14 in Kato and Fukue (2020). From this, we see that if the star radius shrinks from $0.88 R_*$ (estimated by Shenar et al. (2023)) to the size of 12 km or $0.000017 R_*$ (while the area of the star is $4\pi R^2$), we get:

$$43 \text{ kG} \times \left(\frac{0.88}{0.000017} \right)^2 = 1.15 \times 10^{14} \text{ G}. \quad (4.15)$$

Spectral analysis revealed the presence of helium and carbon lines, which are typical of Wolf-Rayet stars. An evolutionary model suggested the star could

have formed by merging two helium-core white dwarfs. This process likely led to the enhancement of the star's magnetic field.

4.3 Theory of rigidly rotating magnetosphere

A model known as the rigidly rotating magnetosphere (RRM), proposed by Townsend and Owocki (2005), describes many of the observed features associated with circumstellar magnetospheres of magnetic stars. According to this semi-analytical model, the matter accumulates around hot stars with dipole magnetic axis with arbitrary angle β to the rotation axis. RRM assumes that the material and the star have rigid rotation due to a strong magnetic field till some point (R_A Alfvén radius), and they were able to solve effective centrifugal plus gravitation potential along each of the field lines, which also gives this model predictive properties. This approach allows them to pinpoint potential minima where material will likely accumulate. The resulting accumulation surface resembles a rigidly rotating, warped disc, tilted so that its average surface is oriented between the rotation and magnetic axes. Using a basic model of the effects of plasma emissivity, they can generate time-resolved synthetic line spectra for the disc. Subsequently, the RRM model can explain why we observe hydrogen Balmer emission associated with cool material even at a temperature of 20 kK.

We can summarise that the magnetosphere in hot stars has two key aspects:

1. **Magnetic Confinement:** The ability of the magnetic field to trap and channel the ionised stellar wind. It is often introduced as a confinement parameter calculated as the ratio of the energy density of the magnetic field and the kinetic energy density of the wind in the following way:

$$\eta_* = \frac{B^2 4\pi R^2}{\mu_0 \dot{M} v_\infty} \text{(in SI units)} = \frac{B^2 R^2}{\dot{M} v_\infty} \text{(in cgs units)}, \quad (4.16)$$

where B is intensity of magnetic field at the surface, R is the radius of the star, \dot{M} is wind mass loss rate and v_∞ is terminal velocity of the wind, and $\mu_0 (\sim 4\pi \times 10^{-7} \text{ N.A}^{-2})$ is the permeability of vacuum [Romanova and Owocki (2016)].

2. **Stellar Wind-Magnetic Field Interaction:** The interaction between the outward-flowing stellar wind and the magnetic field lines leads to magnetospheric currents and shocks forming.

4.4 Dynamical vs centrifugal magnetospheres

In the study by Petit et al. (2013), the magnetospheres of massive stars are classified based on the ratio of two key parameters: the Alfvén radius R_A (scaling with magnetic wind confinement) and the Kepler corotation radius R_K (scaling with stellar rotation).

$$\frac{R_A}{R_*} \sim 0.3 + (\eta_* + 0.25)^{1/4}, \quad (4.17)$$

where η_* is defined in Eq. 4.16. [Ud-Doula, Owocki, and Townsend (2008)] and

$$R_K \equiv \left(\frac{GM}{\Omega^2} \right)^{1/3}, \quad (4.18)$$

where G is gravity constant, M is the mass of the star, and Ω is angular rotation frequency. Based on the ratio of the mentioned radii, the classification system organises stars with magnetic fields not only by observational signatures but also by providing theoretical predictions.

Using these parameters, we can determine which radius dominates and, based on this, infer the type of magnetosphere around the magnetic star. If the Kepler radius is smaller than the Alfvén radius, the plasma in the wind is forced to rotate with the same angular velocity as the star up to the Alfvén radius. Between the Kepler radius and the Alfvén radius, this

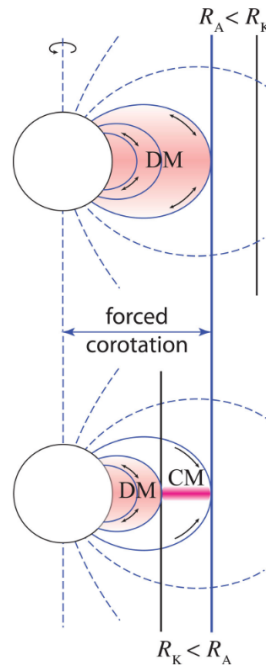


Figure 4.2 Sketch of the regimes for dynamical versus centrifugal magnetospheres (DM versus CM). Petit et al. (2013)

plasma possesses sufficient angular velocity (centrifugal acceleration) to counterbalance gravity, creating a centrifugal magnetosphere (CM).

In contrast, if the Alfvén radius is smaller than the Kepler radius, that plasma cools down and eventually falls back to the stellar surface. This results in dynamic changes, hence the term dynamical magnetosphere (DM). The scenario of DM vs CM can be seen in a sketch in Fig. 4.2.

Next, we summarise the typical evolution of a magnetosphere for an early magnetic B-type star as was done in Shultz et al. (2019). Initially, the star has a strong magnetic field (~ 8 kG) and rapid rotation, making its large CM detectable. As the star ages, its surface magnetic field is weakened due to an increasing radius and gradual flux decay, while angular momentum is lost through its magnetised wind. In its middle age, the CM persists, but $H\alpha$ emission vanishes. As the star approaches the TAMS, the CM vanishes entirely due to a decrease in the intensity of the magnetic field to just a few

hundred Gauss ($\downarrow R_A$). At the same time, the rotational period extends to tens of days ($\uparrow R_K$).

Petit et al. (2013) elegantly explained observational signatures and connected them with theoretical predictions. They show that two distinct populations of magnetic stars with $H\alpha$ emission can be identified: slowly rotating O-type stars exhibiting narrow emission profiles consistent with a DM and more rapidly rotating B-type stars displaying broader emission profiles associated with a CM. The explanation is that O-type stars have high mass-loss rates, sufficient to accumulate enough material for line emission within a relatively short timescale. This high mass-loss rate also contributes to the magnetic spin-down of stellar rotation. The sufficient material and typically slow rotation speed produces a typical O-type star with DM, producing narrow $H\alpha$ lines. In contrast, B-type stars, with relatively weaker stellar winds, require a longer timescale to accumulate enough material for emission. Consequently, the actual spin-down timescale for B-type stars is significantly longer, which increases the likelihood of observing DM.

4.5 Effects of stellar wind-magnetic field interaction excluded from RRM model

4.5.1 Analytical dynamical magnetosphere

Hot, massive stars exhibit strong stellar winds and intense magnetic fields that create complex magnetospheric structures. To explain UV non-thermal emission and other aspects which were observed from stars with magnetic field (i.e. X-ray emission with non-thermal peak at 25 MK [Robrade et al. (2018)] or nearly 100% circular polarised radio emission, both from the star CU Vir classified as ApBp or magnetic chemically peculiar), there was developed the theory of analytic dynamical magnetosphere (ADM) Owocki et al. (2016) which provides explicit formulae for temperature and flow in the

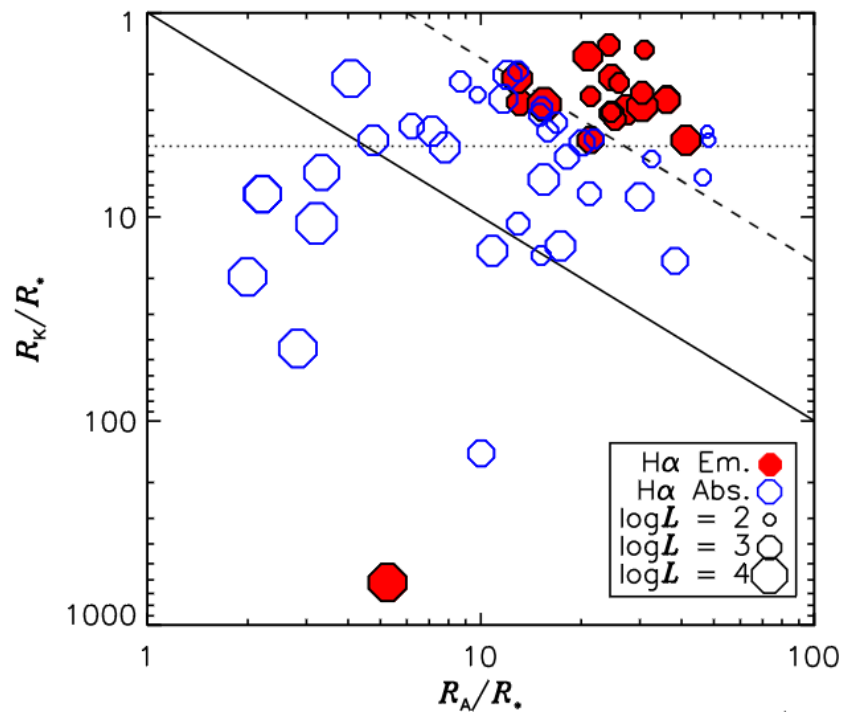


Figure 4.3 Rotation confined diagram taken from Shultz et al. (2019).

magnetosphere. It is based on the RRM model and the results of many 2D and 3D magneto-hydrodynamics simulations. To describe it very briefly, it focuses on DM, in which the three main components are the material trapped in the flow, hot post-shock gas, and cooled downfall. So, the one model can account for and predict cool and hot material trapped in the magnetosphere and the presence of wind, similar to MHD simulations.

In Munoz et al. (2020), the authors investigated whether photometric variability could be modelled using ADM. They also simulate magnetospheres by misaligning the magnetic dipole with the rotational axis, in ADM (and RRM) theory angle denoted as β . They get that for larger tilt angles ($\beta > 60^\circ$), the warping of this disk becomes more pronounced. Because the star rotates with a fixed magnetic pole and its associated disk, this configuration can give rise to various spectral features.

4.5.2 Magnetically confined wind shocks

The wind-shock model developed by Babel and Montmerle (1997) proposes that the magnetic field confines the stellar wind, causing wind components from both hemispheres to collide and create strong shocks. This process efficiently converts kinetic energy into X-ray emission, explaining the observed luminosity and temperature. They also show that ambipolar diffusion or current sheet formation might empty the magnetosphere. Furthermore, they also suggest that electrons are accelerated through second-order Fermi acceleration to radiate, as is observable in GHz.

ud-Doula et al. (2014) explained how X-rays are produced in magnetically confined wind shocks (MCWS) in massive stars with radiatively driven stellar winds. For stars with standard mass-loss rate dependence on luminosity ($\dot{M} \sim L^{1.7}$), inverse Compton cooling becomes important in lower luminosity stars. X-ray emission remains significant for stars with sufficiently high mass-loss rates to sustain radiative shocks. In contrast, stars with lower luminosity and weaker winds experience reduced and softened X-ray emission due to shock retreat, resulting from the increased post-shock cooling length as illustrated in Fig. 4.4. A semi-analytic scaling analysis, which considers both the wind's magnetic confinement and the shock retreat, produces an XADM (ADM for X-ray) scaling law for X-ray luminosities that follow a similar trend but are slightly higher than the average values from the full MHD simulations.

4.5.3 Electron cyclotron maser emission in magnetic stars

Over two decades have passed since the phenomenon of coherent radio emission via electron cyclotron maser emission (ECME) from hot magnetic stars was documented. The precise physical condition responsible for the ECME generation remains uncertain. However, recent studies proposed an

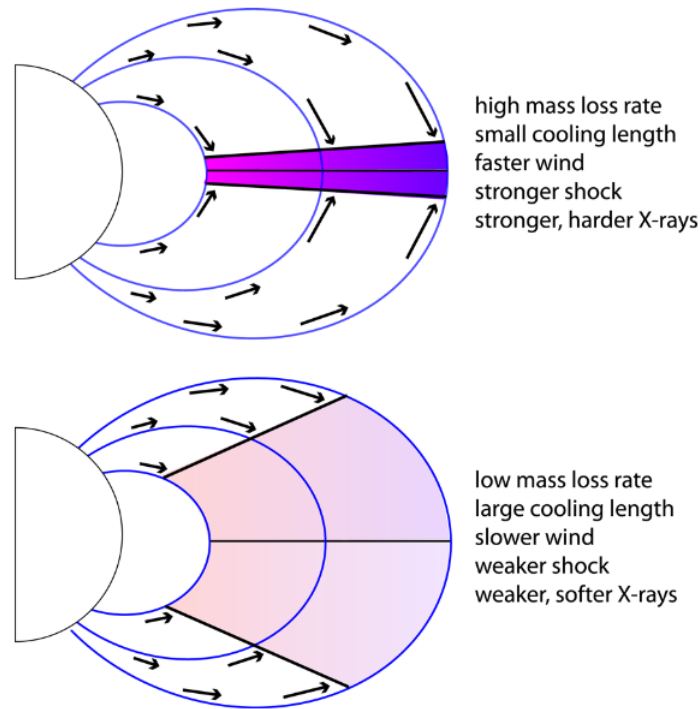


Figure 4.4 Shock retreat taken from ud-Doula et al. (2014).

empirical relation connecting ECME with stellar temperature, magnetic field strength and luminosity, as tested by Leto et al. (2021) and Das et al. (2022b).

The physical mechanism ECME can be explained following work by Melrose and Dulk (1982). ECME is generated by the anisotropic pitch angle distribution of electrons developed within magnetic flux tubes. Electrons with initially large pitch angles are reflected outward due to the magnetic mirroring, and the rest (with a small pitch angle) penetrate deeper into the inner magnetosphere, where they are thermalised in the dense plasma. Reflected electrons have a distribution population based on pitch angle, where the small pitch angles are missing. This mechanism produces nearly 100 per cent circularly polarised radiation at frequencies close to the first and second gyro-frequency, with emission directions almost perpendicular to the local magnetic field.

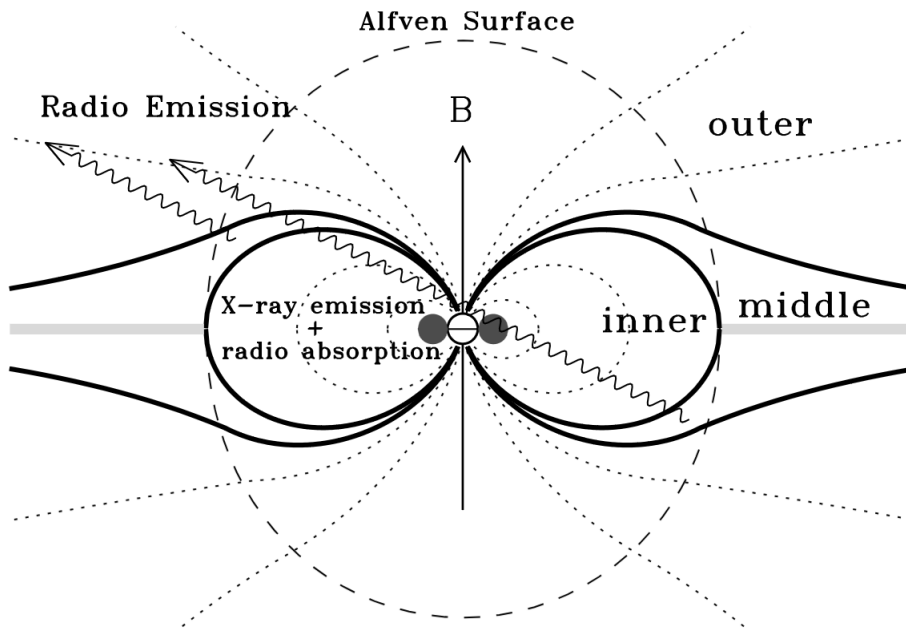


Figure 4.5 Schematic of different parts of the magnetosphere of a magnetic hot star, taken from Trigilio et al. (2004)

Only a few stars with observed ECME were known for a long time. The first such star identified was CU Vir [Trigilio et al. (2000)], and it took another 15 years before the second star, ECME HD 133880, was found [Chandra et al. (2015)]. To determine whether the ECME mechanism is responsible for observed radio emission from the star, the following conditions must be satisfied (and we must detect them): a high brightness temperature, significant circular polarisation, and alignment with the magnetic nulls.

The discovery of only two stars exhibiting ECME over a decade led to the perception that this phenomenon is rare among hot magnetic stars. This rarity initially contributed to the specific condition required for ECME generation, particularly the presence of a quadrupolar magnetic field component (Leto et al. (2012)).

However, advancements in observational techniques have led to the identification of more stars exhibiting ECME, suggesting that this phenomenon might be more common than previously thought. Between 2018 and 2021,

five more stars with ECME were reported: HD 142301 [Leto et al. (2019)], HD 142990 [Das et al. (2019a)], HD 35298 [Das et al. (2019b)], HD 147932 [Leto et al. (2020b)], and HD 147933 [Leto et al. (2020a)].

With reworking criteria on how ECME can be observed even in unsuitable cases, Das et al. (2022a) discovered that the additional eight stars are classified as main-sequence radio pulse emitters (MRP). The criteria for identifying MRP candidates likely to exhibit ECME are significant flux density enhancements observed over a rotational phase window close to or encompassing a magnetic null. The physics idea behind this criterion is that ECME is a highly directed phenomenon requiring precise alignment for detection. However, the emission can decrease polarization due to observation effects, even 0 per cent for the observer. With these refined criteria and a sample of 15 stars, they estimated that at least 32 per cent of hot magnetic stars can produce ECME. However, this is a very conservative estimate. They concluded that this estimate is still too strict because data were very sensitive to miss the occurrence of magnetic nulls and because of errors in ephemerids or phase offsets. This estimation of 32 per cent of the population of magnetic stars is valid only for stars with T_{eff} from 9 kK to 23 kK and with a period of less than two days.

4.5.4 Centrifugal breakout scaling law

In the paper by Leto et al. (2021), they analysed the incoherent gyro-synchrotron radio emission from early-B to early-A spectral types. Despite varying stellar parameters and wind properties, these stars shared similarities in their radio emission, contrasting with traditional wind scenarios. The expected mass-loss rates did not reproduce the observed non-thermal radio spectra similar to Jupiter's. This suggests a common mechanism for electron acceleration in large-scale, well-ordered magnetospheres across different types of celestial objects, from Jupiter (planets) through ultra-cool stars to hot stars.

Shultz et al. (2022) showed that gyrosynchrotron emission is exclusively observed from stars with large CM, same as emission in $H\alpha$ or as they write that radio-bright stars occur in the same part of rotation-magnetic confinement diagram Fig. 4.3. They proposed the close correlation and stability (tens of years of observation) between $H\alpha$ width with radio luminosity, suggesting a unifying mechanism. The mechanism can be a centrifugal breakout (CBO). That also implies that gyrosynchrotron emission requires rapid rotation and a strong magnetic field.

In a very genius way, the article from Owocki et al. (2022) summarises empirical analyses and suggests the CBO model in explaining a similar rotation-field dependence of $H\alpha$ line emission,

$$L_{\text{CBO}} \simeq \dot{M} \Omega^2 R_*^2 \eta_C^{1/p}, \quad (4.19)$$

where L_{CBO} is CBO luminosity, \dot{M} is wind mass-loss rate, Ω is rotational frequency, R_* is radius of the star, p is effective multipole index and η_C centrifugal magnetic confinement defined as $\eta_C \equiv \frac{B_d^2 R_*^2}{\dot{M} v_{\text{orb}}}$, v_{orb} is surface orbital velocity and B_d is surface magnetic field strength. They also calculated efficiency scaling $\varepsilon \sim 10^{-8}$, which represents the relationship between L_{CBO} and the fraction that, in the end, contributes to radio luminosity.

4.5.5 Dips - problems caused by only a simple dipolar model

Photometry has revealed spots dominating light curves of hot and cool magnetic stars. The study Krtićka et al. (2022) investigates the complex light curves of chemically peculiar stars, focusing on phased multiple features interpreted as dips or warps. The idea was that these dips could be explained by the matter accumulated in the equilibrium due to effects combining low-order axisymmetric multipoles with weak higher-order non-axisymmetric multiples, which can warp the equilibrium structure. This phenomenon may occur even

in typical magnetic hot stars and might also apply to cool stars in which the dipolar magnetic field dominates.

4.6 My work - Auroral emission modelled in TLUSTY

This section provides an overview of the additional research carried out during my PhD studies, which contributed to the published article Kajan, Krtička, and Kubát (2024), attached at the end of this thesis in the appendix. In the article, I studied auroral emission lines generated from magnetic field interaction with stellar wind. While auroral emission is studied in planetary and ultra-cool dwarfs, as a radio emission, it was not found in the spectra of hot stars.

Our idea was that if the magnetic star has a magnetosphere where the particles, primarily electrons, are trapped and accelerated, this has already been observed. Then, if some of these electrons (we modelled the effect as high-energy photons) impact the surface of the hot star, it can generate changes in spectra for specific lines, which we can denote as auroral lines.

We used TLUSTY code to simulate these auroral lines by modelling the interaction between the star's atmosphere and strong, high-energy irradiation. We could identify potential auroral emissions by generating high-resolution synthetic spectra from model atmospheres. These emission lines were mostly found in the infrared range.

The most prominent line produced by the irradiation was He ii at 69458 Å, which showed up in all our model atmospheres, which have effective temperatures from 15 to 30 kK. We also calculated the minimum irradiation needed to detect this line. Changes in the population of different excited states of the atoms involved explained the appearance of emission lines. Besides the infrared emission lines, high-energy irradiation also led to infrared excess.

We also searched in FUSE observation from the MAST catalogue, where we found no potential candidate for auroral emission in the UV part of the spectrum. However, this was before our models concluded that the IR range was the best way to look at.

4.6.1 Departure coefficient b-factors in irradiated atmospheres

One key aspect that helped us better understand the irradiated atmosphere was an analysis of helium ion departure coefficients (b-factors) in stellar atmospheres. We examined the single ionized helium b-factors because we discovered that helium creates IR emissions in all irradiated models. Specifically, we want to see the deviation for $n = 7$ and $n = 8$ (principal quantum number) of helium II (single ionized helium), as this was the most prominent line.

Here is a short overview of b-factors in stellar atmospheres. Departure coefficients, or b-factors, describe the deviation of the energy levels for specific ionized ions (or atoms) from LTE. They are defined in the following way:

$$b_i = \frac{n_i}{n_i^*}, \quad (4.20)$$

where n_i^* is the LTE population of level i , and n_i is the Non-LTE population of level i . [Hubeny and Mihalas (2014)]. Under LTE conditions, the b-factors are always equal to 1, which we will use later in the analysis.

The importance of b-factors lies in their ability to highlight the role of radiative processes and collisions in determining atomic state populations. Significant deviations from LTE (indicated by b-factors far from unity) emphasise the necessity of considering non-LTE effects when modelling stellar spectra, as they influence both the strengths and profiles of spectral lines.

We analysed the b-factors of helium levels in non-irradiated and irradiated models, as shown in Figures 4.7 and 4.6. In the figure, we used denotation to

describe the model based on the effective temperature (i.e. t15 represents the model with $T_{\text{eff}} = 15$ kK) and dilution factor "W". The deviation from LTE was relatively small in non-irradiated models at lower effective temperatures (< 21 kK). However, significant deviations in the upper atmosphere appear only for the highest temperature model (30 kK). The lower energy levels of He II (levels 1-5) exhibited similar trends, with the 30 kK model showing a marked departure from LTE, particularly at the principal quantum number $n = 5$.

For the irradiated models, the progression of b-factors was generally consistent across different temperatures, with the 30 kK model being a notable exception. These findings suggest that the conditions remain close to LTE at every level deep within the atmosphere, where the Rosseland optical depth is approximately $\tau \sim 10^{-1}$. However, as τ becomes much smaller (significantly less than $2/3$, a value often used to define the "stellar surface"), the deviation in b-factors between the irradiated and non-irradiated models starts to increase. This coincides with the region where the temperature rises as the Rosseland optical depth decreases, indicating that the emission originates from this specific zone.

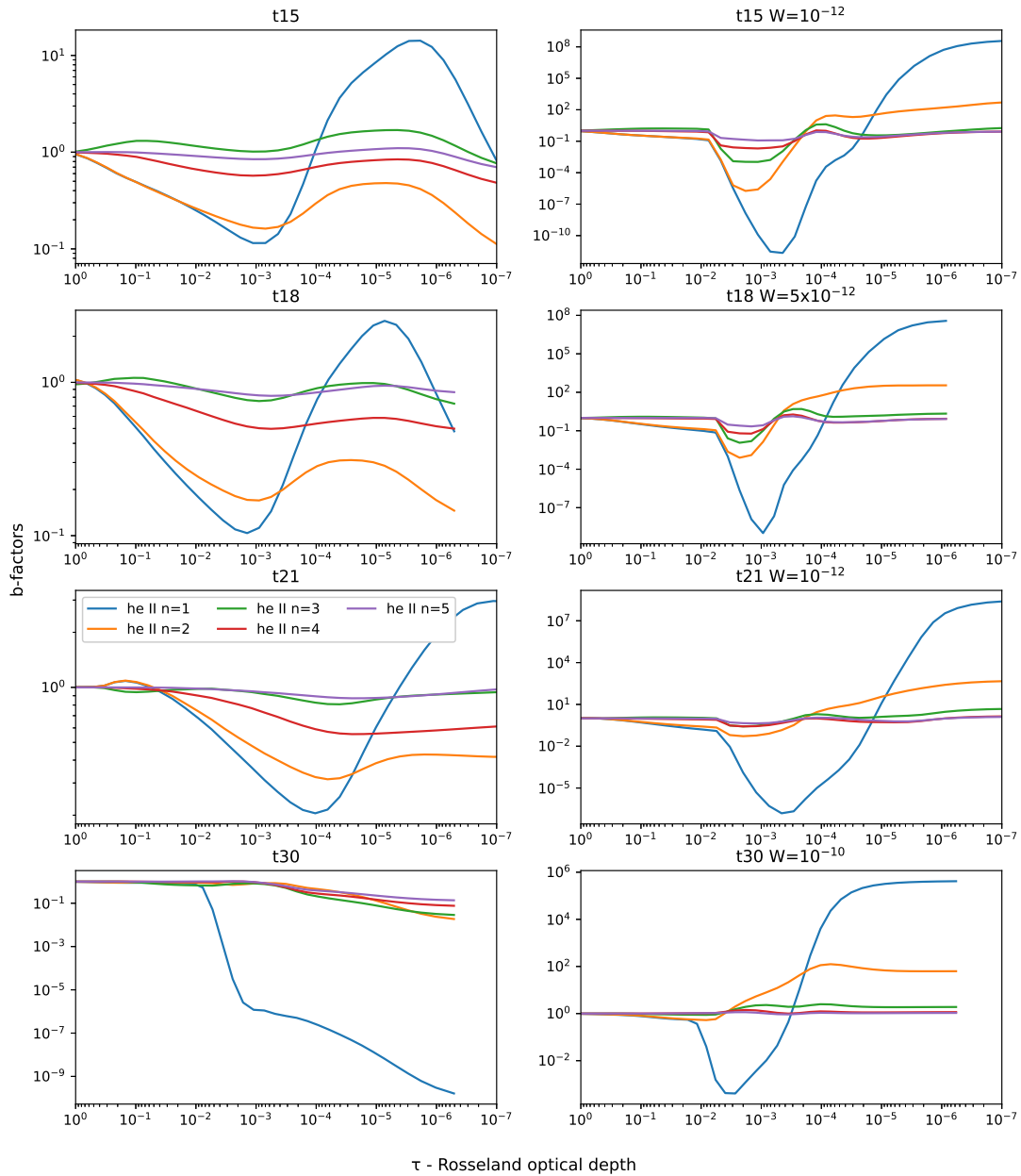


Figure 4.6 Behaviour of b-factors in dependence of mean Rosseland optical depth, for levels (principal quantum number) of single ionized heliums from 1 to 5. *Left columns:* non-irradiated models for different models written on the top of a given graph. *Right columns:* irradiated models with dilution coefficient on the top of a given graph. *Any row:* a model with the same effective temperature is in the same row. Every model uses the same colour coding described in the legend in the graph in 3rd row on the left.

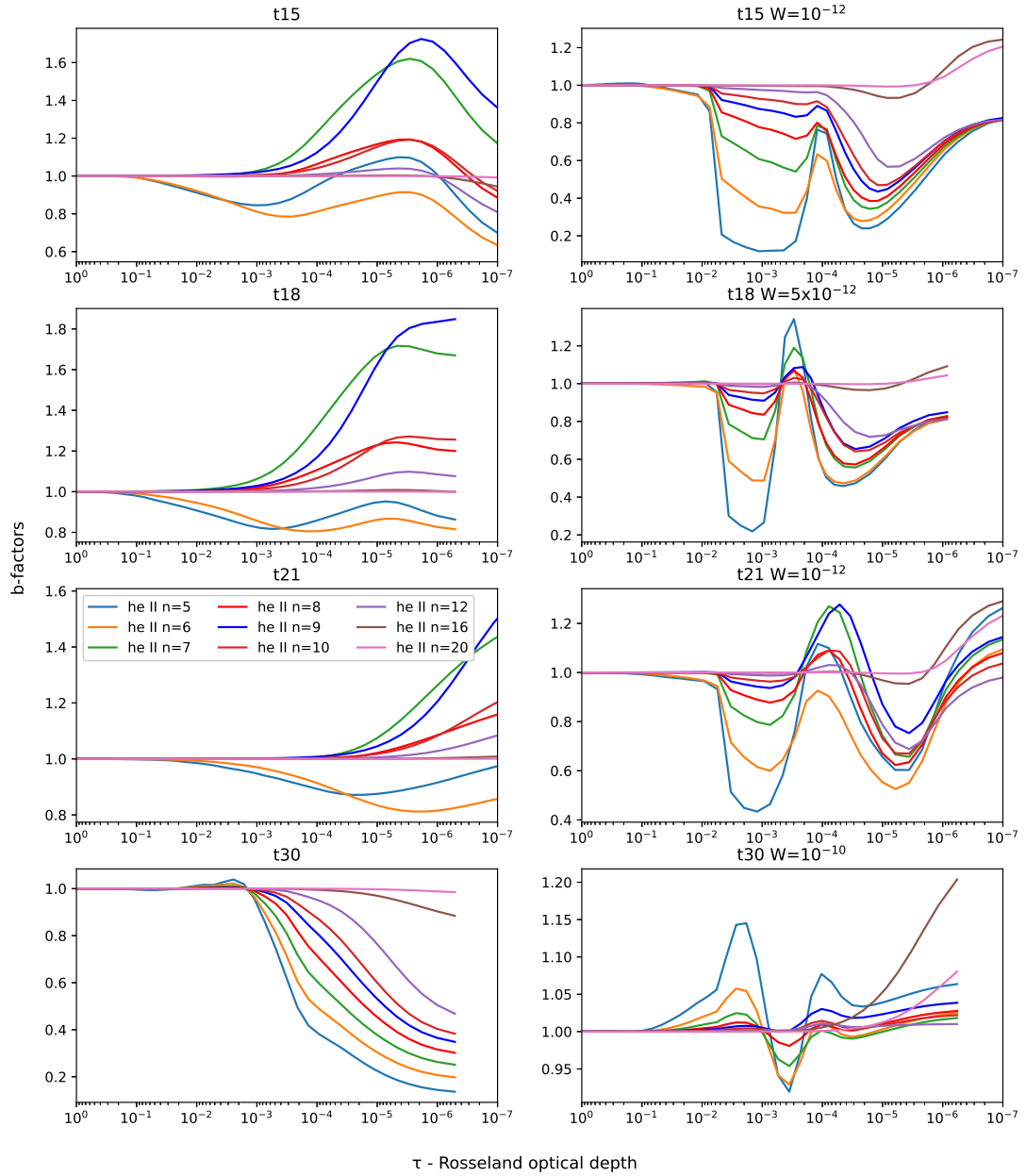


Figure 4.7 Same as Fig. 4.6 but for principal quantum number from $n = 5$ to $n = 20$.

4.6.2 Verifying convergence of models

Before proceeding with any detailed analysis, ensuring the convergence of the stellar atmosphere models was essential. The latest version of the TLUSTY code includes a script, "tlusty.py," which visualises the convergence log, providing a clear picture of the iterative process and helping verify whether the models converged adequately. In our work, we considered a model to have successfully converged if the maximum relative change in any parameter was less than 0.1 per cent.

Fig. 4.8 illustrates this convergence for the t15nlte model ($T_{\text{eff}} = 15$ kK, with specific elements calculated in Non-LTE). The lower right graph clearly shows the convergence criteria being met.

Ensuring convergence was critical to guarantee the accuracy and reliability of the subsequent results derived from these models. This determined a barrier for the strongest irradiation in which the model can converge. Also, it was essential to change some input for models to ensure better convergence or, in some cases, not neglect physics, i.e., emission in lines needed to be not turned off; the "ITLAS" parameter, which is a flag for turning off laser lines, was turned off.

4.6.3 False emission in SYNSPEC

During our analysis, we encountered an issue with the old version of the SYNSPEC code, which generated false emissions under certain conditions. Specifically, when "imode = 1" was used for elements calculated in LTE, the code produced strong, unphysical emissions.

As shown in Fig. 4.9, P V (four-time ionised phosphorus), calculated only in LTE, exhibited a strong emission peak. This emission does not correspond to any synthetic physical conditions in the atmosphere. This false emission

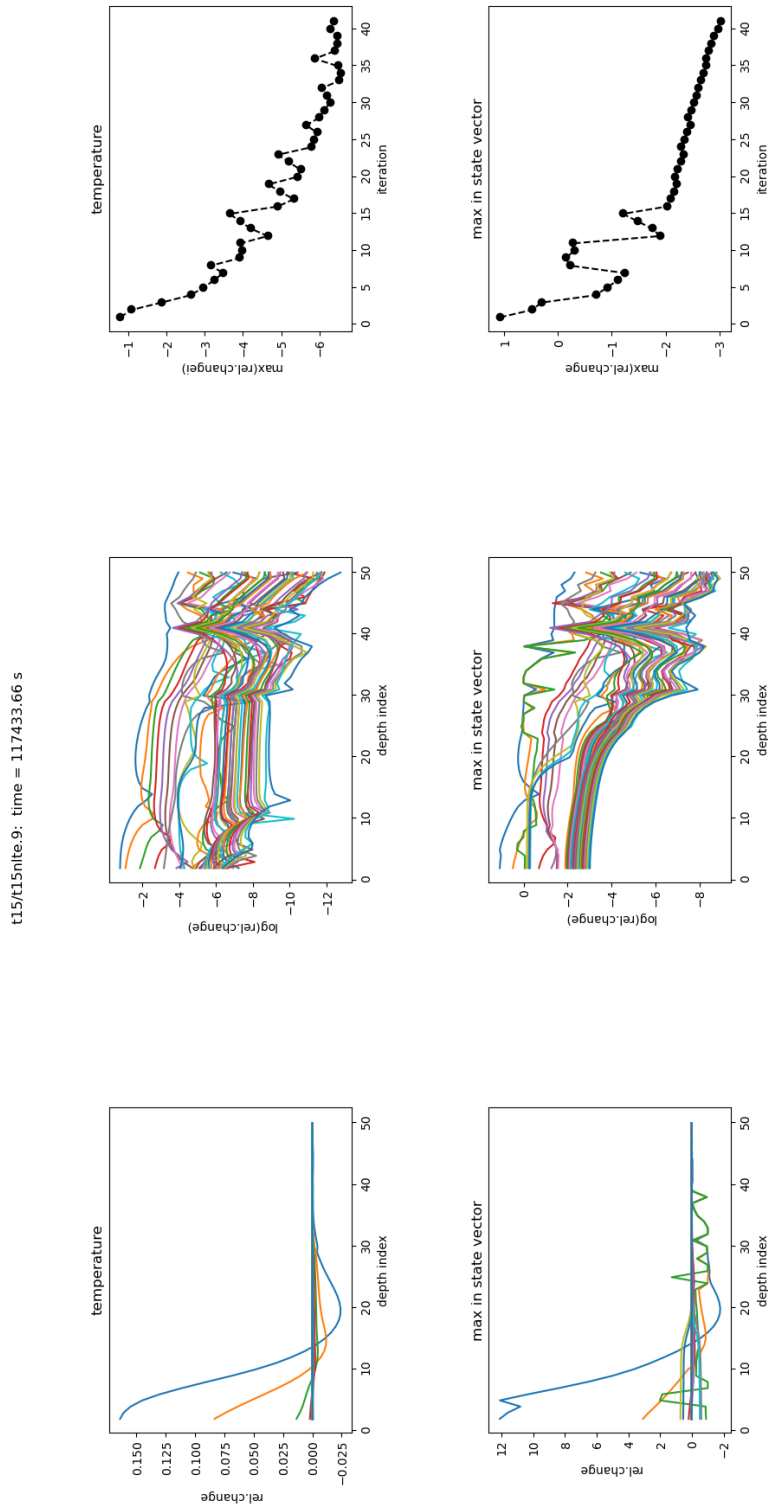


Figure 4-8 Plots the convergence log contained in the output from TLUSTY. Output generated from a script included in the TLUSTY package for our data, a specifically non-irradiated final model with the effective temperature of 15 kK. For more detailed information, see Hubeny et al. (2021) section 4.1.2.

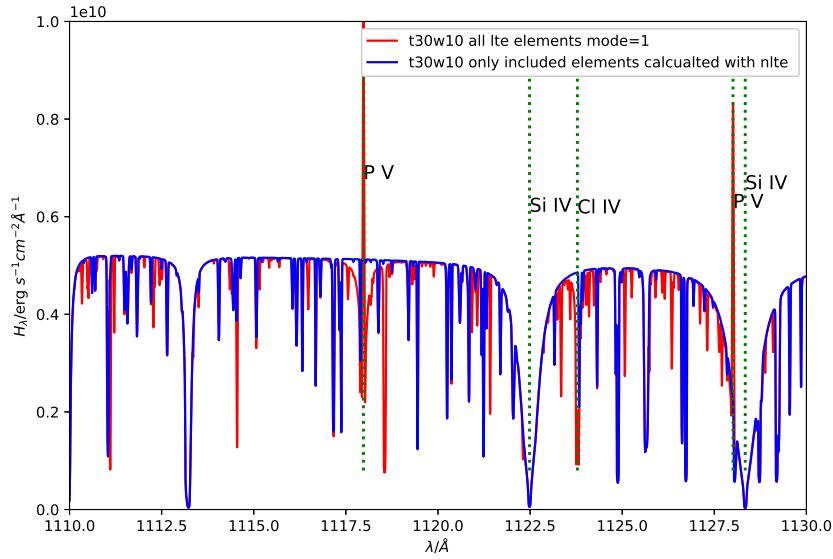


Figure 4.9 Synthetic spectra (flux versus wavelength) generated from SYNSPEC for irradiated $T_{\text{eff}} = 30$ kK model with all elements included (red line), and for the same model only for elements which were calculated explicitly (in Non-LTE) in TLUSTY (the blue solid line). The green dotted lines identify the five strongest lines in the given range from SYNSPEC.

originated in the upper atmosphere and was inconsistent with the physical parameters obtained from the TLUSTY input data.

To address this problem, we decided not to include elements calculated in LTE (such as phosphorus) when searching for emissions in the models. This adjustment ensured that the spectral features we analysed were physically meaningful and not artefacts of the computational method.

This experience highlighted the importance of carefully validating synthetic spectra codes SYNSPEC outputs.

4.6.4 Other physical parameters in stellar atmosphere

Beyond the primary parameters typically analysed in stellar atmosphere studies, we explored a range of additional physical parameters to gain a more physical insight into the models. This broader investigation was crucial, as

high irradiation levels do not significantly impact specific parameters, such as the hydrostatic mass distribution, as seen in Fig. 4.10.

After examining these additional parameters, density, temperature, pressure, and gravity acceleration, we see that the deviation in the density structure of irradiated models versus non-irradiated models is negligible. Even if irradiation affects the upper layers of the atmosphere, it does not change density; only the uppermost part is slightly more rarefied. For pressure, it is nearly negligible even in zoomed-in, as shown in the figure. The exciting part is the temperature, as shown in the article. We can observe a significant increase in temperature for the upper layers. The $\log(g_{\text{rad}})$ is radiative acceleration, force per unit mass exerted by the absorption and scattering of radiation. This shows us that the irradiation gives the favourite condition to accelerate (enable) stellar winds.

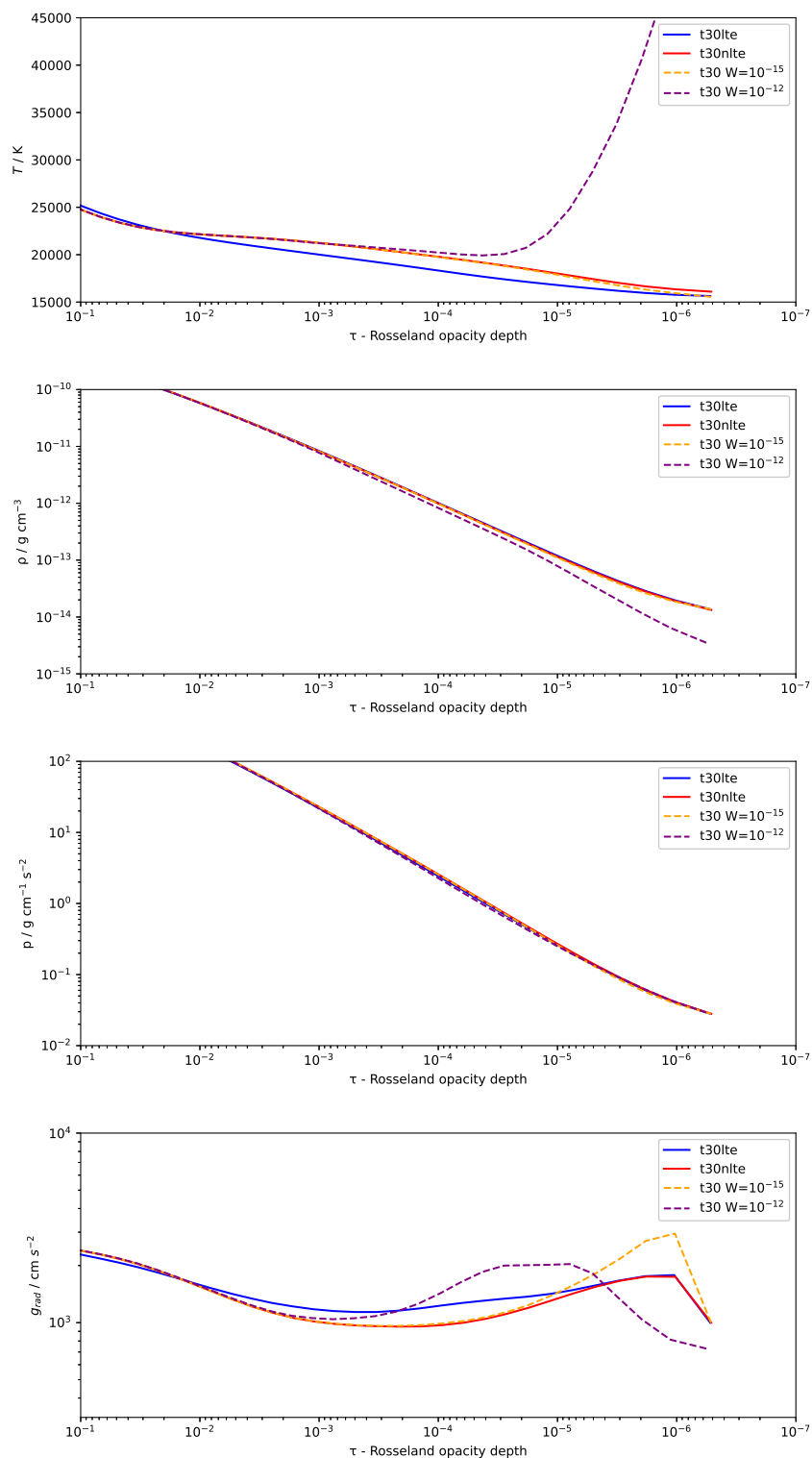


Figure 4.10 Behaviour of the different physical parameters in the model with the effective temperature of 30 kK, for different irradiation, and comparison of LTE with Non-LTE non-irradiated models. All panels except the top one have both axes scaled logarithmically. *Top panel:* Temperature versus Rosseland optical depth, the y-axis is scaled linearly. *Second panel:* density versus Rosseland optical depth. *Third row:* pressure versus Rosseland optical depth. *Bottom panel:* radiation acceleration versus Rosseland optical depth.

Chapter 5

Conclusions

This thesis has been developed primarily as a comprehensive reference for my research effort. The initial chapters provide a general introduction and include a few equations showing the processes influencing magnetospheres and envelopes. The concepts presented were synthesized from foundational textbooks and insights from recent research articles.

The thesis progresses through a structured exploration of these topics, culminating in my original work. Although the sections do not follow a strictly linear progression, each chapter builds upon the previous ones. Chapter 4 serves as an extension and refinement of the concepts discussed in Chapters 2 and 3.

In Chapter 2, I focused on modelling a star on the extreme horizontal branch using MESA in Krtička et al. (2024). The goal was to replicate the characteristics observed in real stars. A significant aspect of this work involved analyzing the potential for this synthetic star to pulsate with an observed period, a phenomenon previously undocumented for this given type of star.

I also helped Dr. Martin Piecka with providing spectra from code TLUSTY used in Piecka, Hutschenreuter, and Alves (2024). I model the stars' spectra across different effective temperatures, which inspired me to do a project on generating spectra for cool stars in Chapter 3.

In Chapter 4, I employed the TLUSTY code to model irradiated stars, focusing on simulating auroral emissions. The final product, the article Kajan, Krtička, and Kubát (2024), represents a novel exploration of stellar phenomena.

In conclusion, I hope my contributions offer valuable insights to enhance our understanding of the universe.

Bibliography

- Angulo, C. et al. (Aug. 1999). “A compilation of charged-particle induced thermonuclear reaction rates”. In: 656(1), pp. 3–183. DOI: 10.1016/S0375-9474(99)00030-5.
- Asplund, Martin et al. (Sept. 2009). “The Chemical Composition of the Sun”. In: 47(1), pp. 481–522. DOI: 10.1146/annurev.astro.46.060407.145222. arXiv: 0909.0948 [astro-ph.SR].
- Babel, J. and T. Montmerle (July 1997). “X-ray emission from Ap-Bp stars: a magnetically confined wind-shock model for IQ Aur.” In: 323, pp. 121–138.
- Blouin, Simon et al. (Aug. 2020). “New Conductive Opacities for White Dwarf Envelopes”. In: 899(1), 46, p. 46. DOI: 10.3847/1538-4357/ab9e75. arXiv: 2006.16390 [astro-ph.SR].
- Budaj, J., A. Maliuk, and I. Hubeny (Apr. 2022). “WD 1145+017: Alternative models of the atmosphere, dust clouds, and gas rings”. In: 660, A72, A72. DOI: 10.1051/0004-6361/202141924. arXiv: 2203.07520 [astro-ph.EP].
- Cassisi, S. et al. (June 2007). “Updated Electron-Conduction Opacities: The Impact on Low-Mass Stellar Models”. In: 661, pp. 1094–1104. DOI: 10.1086/516819. eprint: astro-ph/0703011.
- Chandra, P. et al. (Sept. 2015). “Detection of 610-MHz radio emission from hot magnetic stars”. In: 452(2), pp. 1245–1253. DOI: 10.1093/mnras/stv1378. arXiv: 1505.02139 [astro-ph.SR].
- Chugunov, A. I., H. E. Dewitt, and D. G. Yakovlev (July 2007). “Coulomb tunneling for fusion reactions in dense matter: Path integral MonteCarlo versus mean field”. In: 76(2), 025028, p. 025028. DOI: 10.1103/PhysRevD.76.025028. arXiv: 0707.3500.
- Cybur, R. H. et al. (July 2010). “The JINA REACLIB Database: Its Recent Updates and Impact on Type-I X-ray Bursts”. In: 189, pp. 240–252. DOI: 10.1088/0067-0049/189/1/240.

- Das, Barnali et al. (June 2019a). “Detection of Coherent Emission from the Bp Star HD 142990 at uGMRT Frequencies”. In: 877(2), 123, p. 123. DOI: 10.3847/1538-4357/ab1b12. arXiv: 1904.08359 [astro-ph.SR].
- Das, Barnali et al. (Oct. 2019b). “The fifth main-sequence magnetic B-type star showing coherent radio emission: Is this really a rare phenomenon?” In: 489(1), pp. L102–L107. DOI: 10.1093/mnrasl/slz137. arXiv: 1908.09110 [astro-ph.SR].
- Das, Barnali et al. (Feb. 2022a). “Discovery of Eight “Main-sequence Radio Pulse Emitters” Using the GMRT: Clues to the Onset of Coherent Radio Emission in Hot Magnetic Stars”. In: 925(2), 125, p. 125. DOI: 10.3847/1538-4357/ac2576. arXiv: 2109.04043 [astro-ph.SR].
- Das, Barnali et al. (Dec. 2022b). “Testing a scaling relation between coherent radio emission and physical parameters of hot magnetic stars”. In: 517(4), pp. 5756–5769. DOI: 10.1093/mnras/stac3123. arXiv: 2210.14746 [astro-ph.SR].
- ud-Doula, Asif and Yaël Nazé (Sept. 2016). “Magnetically confined wind shocks in X-rays - A review”. In: *Advances in Space Research* 58(5), pp. 680–693. DOI: 10.1016/j.asr.2015.09.025. arXiv: 1509.06482 [astro-ph.SR].
- ud-Doula, Asif and Owocki (Sept. 2002). “Dynamical Simulations of Magnetically Channeled Line-driven Stellar Winds. I. Isothermal, Nonrotating, Radially Driven Flow”. In: 576(1), pp. 413–428. DOI: 10.1086/341543. arXiv: astro-ph/0201195 [astro-ph].
- ud-Doula, Asif et al. (July 2014). “X-rays from magnetically confined wind shocks: effect of cooling-regulated shock retreat”. In: 441(4), pp. 3600–3614. DOI: 10.1093/mnras/stu769. arXiv: 1404.5336 [astro-ph.SR].
- Ud-Doula, Owocki, and Townsend (Mar. 2008). “Dynamical simulations of magnetically channelled line-driven stellar winds - II. The effects of field-aligned rotation”. In: 385(1), pp. 97–108. DOI: 10.1111/j.1365-2966.2008.12840.x. arXiv: 0712.2780 [astro-ph].
- Dziembowski, W. A., P. Moskalik, and A. A. Pamyatnykh (Dec. 1993). “The opacity mechanism in B-type stars - II. Excitation of high-order g-modes in main-sequence stars.” In: 265, pp. 588–600. DOI: 10.1093/mnras/265.3.588.
- Ferguson, J. W. et al. (Apr. 2005). “Low-Temperature Opacities”. In: 623, pp. 585–596. DOI: 10.1086/428642. eprint: astro-ph/0502045.
- Fuller, G. M., W. A. Fowler, and M. J. Newman (June 1985). “Stellar weak interaction rates for intermediate-mass nuclei. IV - Interpolation procedures

- for rapidly varying lepton capture rates using effective log (ft)-values”. In: 293, pp. 1–16. DOI: 10.1086/163208.
- García-Zamora, Enrique Miguel, Santiago Torres, and Alberto Rebassa-Mansergas (Nov. 2023). “White dwarf Random Forest classification through Gaia spectral coefficients”. In: 679, A127, A127. DOI: 10.1051/0004-6361/202347601. arXiv: 2308.07090 [astro-ph.SR].
- Grunhut, J. H. et al. (Feb. 2017). “The MiMeS survey of Magnetism in Massive Stars: magnetic analysis of the O-type stars”. In: 465(2), pp. 2432–2470. DOI: 10.1093/mnras/stw2743. arXiv: 1610.07895 [astro-ph.SR].
- Han, Z. et al. (Oct. 2002). “The origin of subdwarf B stars - I. The formation channels”. In: 336(2), pp. 449–466. DOI: 10.1046/j.1365-8711.2002.05752.x. arXiv: astro-ph/0206130 [astro-ph].
- Heber, U. (Aug. 2016). “Hot Subluminous Stars”. In: 128(966), p. 082001. DOI: 10.1088/1538-3873/128/966/082001. arXiv: 1604.07749 [astro-ph.SR].
- Hubeny, I. and T. Lanz (Feb. 1995). “Non-LTE Line-blanketed Model Atmospheres of Hot Stars. I. Hybrid Complete Linearization/Accelerated Lambda Iteration Method”. In: 439, p. 875. DOI: 10.1086/175226.
- Hubeny, Ivan and Thierry Lanz (June 2017a). “A brief introductory guide to TLUSTY and SYNSPEC”. In: *arXiv e-prints*, arXiv:1706.01859, arXiv:1706.01859. DOI: 10.48550/arXiv.1706.01859. arXiv: 1706.01859 [astro-ph.SR].
- Hubeny, Ivan and Thierry Lanz (June 2017b). “TLUSTY User’s Guide II: Reference Manual”. In: *arXiv e-prints*, arXiv:1706.01935, arXiv:1706.01935. DOI: 10.48550/arXiv.1706.01935. arXiv: 1706.01935 [astro-ph.SR].
- Hubeny, Ivan and Thierry Lanz (June 2017c). “TLUSTY User’s Guide III: Operational Manual”. In: *arXiv e-prints*, arXiv:1706.01937, arXiv:1706.01937. DOI: 10.48550/arXiv.1706.01937. arXiv: 1706.01937 [astro-ph.SR].
- Hubeny, Ivan and Dimitri Mihalas (2014). *Theory of Stellar Atmospheres*. Princeton University Press.
- Hubeny, Ivan et al. (Apr. 2021). “TLUSTY and SYNSPEC Users’s Guide IV: Upgraded Versions 208 and 54”. In: *arXiv e-prints*, arXiv:2104.02829, arXiv:2104.02829. DOI: 10.48550/arXiv.2104.02829. arXiv: 2104.02829 [astro-ph.SR].
- Iglesias, C. A. and F. J. Rogers (Aug. 1993). “Radiative opacities for carbon- and oxygen-rich mixtures”. In: 412, pp. 752–760. DOI: 10.1086/172958.
- Iglesias, C. A. and F. J. Rogers (June 1996). “Updated Opal Opacities”. In: 464, p. 943. DOI: 10.1086/177381.
- Irwin, Alan. W. (2004). *The FreeEOS Code for Calculating the Equation of State for Stellar Interiors*. URL: <http://freeeos.sourceforge.net/>.

- Itoh, N. et al. (Feb. 1996). “Neutrino Energy Loss in Stellar Interiors. VII. Pair, Photo-, Plasma, Bremsstrahlung, and Recombination Neutrino Processes”. In: 102, p. 411. DOI: 10.1086/192264.
- Jermyn, Adam S. et al. (May 2021). “Skye: A Differentiable Equation of State”. In: 913(1), 72, p. 72. DOI: 10.3847/1538-4357/abf48e. arXiv: 2104.00691 [astro-ph.SR].
- Kajan, Michal (2019). “Modelování expandujících obálek supernov [online]”. SUPERVISOR : Petr Kurfürst. Diplomová práce. Masarykova univerzita, Přírodovědecká fakulta, Brno. URL: <https://is.muni.cz/th/qmfx5/>.
- Kajan, Michal, Jiří Krtička, and Jiří Kubát (June 2024). “Unveiling stellar aurorae: simulating auroral emission lines in hot stars induced by high-energy irradiation”. In: 531(1), pp. 1776–1788. DOI: 10.1093/mnras/stae1273. arXiv: 2405.09967 [astro-ph.SR].
- Kaler, James B. (2011). *Stars and their Spectra*.
- Karlický, Marian (2014). *Plasma astrophysics*. en. Matfyzpress, Matematicko-Fyzikální fakulty Univerzita Karlova. ISBN: 9788073782818.
- Kato, Shoji and Jun Fukue (2020). *Fundamentals of Astrophysical Fluid Dynamics; Hydrodynamics, Magnetohydrodynamics, and Radiation Hydrodynamics*. DOI: 10.1007/978-981-15-4174-2.
- Keszthelyi et al. (Jan. 2020). “The effects of surface fossil magnetic fields on massive star evolution - II. Implementation of magnetic braking in MESA and implications for the evolution of surface rotation in OB stars”. In: 493(1), pp. 518–535. DOI: 10.1093/mnras/staa237. arXiv: 2001.06239 [astro-ph.SR].
- Krtička, J. et al. (Mar. 2022). “Photometric signatures of corotating magnetospheres of hot stars governed by higher-order magnetic multipoles”. In: 659, A37, A37. DOI: 10.1051/0004-6361/202141997. arXiv: 2201.11435 [astro-ph.SR].
- Krtička, J. et al. (Mar. 2024). “The nature of medium-period variables on the extreme horizontal branch. I. X-shooter study of variable stars in the globular cluster ω Cen”. In: 683, A110, A110. DOI: 10.1051/0004-6361/202347359. arXiv: 2401.10626 [astro-ph.SR].
- Langanke, K. and G. Martínez-Pinedo (June 2000). “Shell-model calculations of stellar weak interaction rates: II. Weak rates for nuclei in the mass range $A=45-65$ in supernovae environments”. In: *Nuclear Physics A* 673, pp. 481–508. DOI: 10.1016/S0375-9474(00)00131-7. eprint: nucl-th/0001018.

- Lanz, Thierry and Ivan Hubeny (Mar. 2007). “A Grid of NLTE Line-blanketed Model Atmospheres of Early B-Type Stars”. In: 169(1), pp. 83–104. DOI: 10.1086/511270. arXiv: astro-ph/0611891 [astro-ph].
- Leto, P. et al. (June 2012). “Searching for a CU Virginis-type cyclotron maser from σ Orionis E: the role of the magnetic quadrupole component”. In: 423(2), pp. 1766–1774. DOI: 10.1111/j.1365-2966.2012.20997.x. arXiv: 1203.6475 [astro-ph.SR].
- Leto, P. et al. (Jan. 2019). “The polarization mode of the auroral radio emission from the early-type star HD 142301”. In: 482(1), pp. L4–L8. DOI: 10.1093/mnrasl/sly179. arXiv: 1809.07504 [astro-ph.SR].
- Leto, P. et al. (Apr. 2020a). “Evidence for radio and X-ray auroral emissions from the magnetic B-type star ρ Oph A”. In: 493(4), pp. 4657–4676. DOI: 10.1093/mnras/staa587. arXiv: 2002.09251 [astro-ph.SR].
- Leto, P. et al. (Dec. 2020b). “The auroral radio emission of the magnetic B-type star ρ -OphC”. In: 499(1), pp. L72–L76. DOI: 10.1093/mnrasl/slaa157. arXiv: 2009.02363 [astro-ph.SR].
- Leto, P. et al. (Oct. 2021). “A scaling relationship for non-thermal radio emission from ordered magnetospheres: from the top of the main sequence to planets”. In: 507(2), pp. 1979–1998. DOI: 10.1093/mnras/stab2168. arXiv: 2107.11995 [astro-ph.SR].
- Li, Yan et al. (Aug. 2018). “Convective Overshooting in sdB Stars Using the k - ω Model”. In: 863(1), 12, p. 12. DOI: 10.3847/1538-4357/aacdf9. arXiv: 1806.07044 [astro-ph.SR].
- Maeder, André (2009). *Physics, Formation and Evolution of Rotating Stars*. DOI: 10.1007/978-3-540-76949-1.
- Marcolino, W. L. F. et al. (May 2013). “Phase-resolved ultraviolet spectroscopy of the magnetic Of?p star HD 191612”. In: 431(3), pp. 2253–2260. DOI: 10.1093/mnras/stt323. arXiv: 1302.4708 [astro-ph.SR].
- Melrose, D. B. and G. A. Dulk (Aug. 1982). “Electron-cyclotron masers as the source of certain solar and stellar radio bursts.” In: 259, pp. 844–858. DOI: 10.1086/160219.
- Moni Bidin, C. et al. (Nov. 2012). “Spectroscopy of horizontal branch stars in ω Centauri*.”. In: 547, A109, A109. DOI: 10.1051/0004-6361/201220031. arXiv: 1210.1262 [astro-ph.SR].
- Munoz, M. S. et al. (Feb. 2020). “Modelling the photometric variability of magnetic massive stars with the Analytical Dynamical Magnetosphere model”. In: 492(1), pp. 1199–1213. DOI: 10.1093/mnras/stz2904. arXiv: 1910.05792 [astro-ph.SR].

- Nazé, Yaël et al. (Sept. 2015). “The changing UV and X-ray properties of the Of?p star CPD -28°2561”. In: 452(3), pp. 2641–2653. DOI: 10.1093/mnras/stv1445. arXiv: 1506.08572 [astro-ph.SR].
- O’Connor, Evan and Christian D. Ott (Jan. 2013). “The Progenitor Dependence of the Pre-explosion Neutrino Emission in Core-collapse Supernovae”. In: 762(2), 126, p. 126. DOI: 10.1088/0004-637X/762/2/126. arXiv: 1207.1100 [astro-ph.HE].
- Oda, T. et al. (Mar. 1994). “Rate Tables for the Weak Processes of sd-Shell Nuclei in Stellar Matter”. In: *Atomic Data and Nuclear Data Tables* 56, pp. 231–403. DOI: 10.1006/adnd.1994.1007.
- Oksala, M. E. et al. (June 2015). “An infrared diagnostic for magnetism in hot stars”. In: 578, A112, A112. DOI: 10.1051/0004-6361/201525987. arXiv: 1505.01739 [astro-ph.SR].
- Ostlie, Dale A. and Bradley W. Carroll (1996). *An Introduction to Modern Stellar Astrophysics*.
- Owocki et al. (Nov. 2016). “An ‘analytic dynamical magnetosphere’ formalism for X-ray and optical emission from slowly rotating magnetic massive stars”. In: 462(4), pp. 3830–3844. DOI: 10.1093/mnras/stw1894. arXiv: 1607.08568 [astro-ph.SR].
- Owocki et al. (Dec. 2020). “How the breakout-limited mass in B-star centrifugal magnetospheres controls their circumstellar H α emission”. In: 499(4), pp. 5366–5378. DOI: 10.1093/mnras/staa2325. arXiv: 2009.12359 [astro-ph.SR].
- Owocki et al. (June 2022). “Centrifugal breakout reconnection as the electron acceleration mechanism powering the radio magnetospheres of early-type stars”. In: 513(1), pp. 1449–1458. DOI: 10.1093/mnras/stac341. arXiv: 2202.05449 [astro-ph.SR].
- Paxton, Bill et al. (Jan. 2011). “Modules for Experiments in Stellar Astrophysics (MESA)”. In: 192(1), 3, p. 3. DOI: 10.1088/0067-0049/192/1/3. arXiv: 1009.1622 [astro-ph.SR].
- Petit, V. et al. (Feb. 2013). “A magnetic confinement versus rotation classification of massive-star magnetospheres”. In: 429(1), pp. 398–422. DOI: 10.1093/mnras/sts344. arXiv: 1211.0282 [astro-ph.SR].
- Phillips, A. C. (1999). *The Physics of Stars, 2nd Edition*.
- Piecka, M., S. Hutschenreuter, and J. Alves (July 2024). “Towards a complete picture of the Sco-Cen outflow”. In: *arXiv e-prints*, arXiv:2407.13226, arXiv:2407.13226. DOI: 10.48550/arXiv.2407.13226. arXiv: 2407.13226 [astro-ph.GA].

- Pinsonneault, Marc H. and Barbara Sue Ryden (2023). *Stellar structure and evolution*. DOI: 10.1017/9781108869249.
- Pivoňková, Kateřina (2024). “Studium vysokorychlostních absorpčních událostí ve spektrech proměnných hvězd typu alfa Cygni [online]”. SUPERVISOR : Olga Viktorovna Maryeva. Diplomová práce. Masarykova univerzita, Přírodovědecká fakulta, Brno. URL: <https://is.muni.cz/th/s2uy1/>.
- Potekhin, A. Y. and G. Chabrier (Jan. 2010). “Thermodynamic Functions of Dense Plasmas: Analytic Approximations for Astrophysical Applications”. In: *Contributions to Plasma Physics* 50, pp. 82–87. DOI: 10.1002/ctpp.201010017. arXiv: 1001.0690 [physics.plasm-ph].
- Poutanen, Juri (Feb. 2017). “Rosseland and Flux Mean Opacities for Compton Scattering”. In: 835(2), 119, p. 119. DOI: 10.3847/1538-4357/835/2/119. arXiv: 1606.09466 [astro-ph.HE].
- Prišegen, M. et al. (Jan. 2021). “White dwarf-open cluster associations based on Gaia DR2”. In: 645, A13, A13. DOI: 10.1051/0004-6361/202039276. arXiv: 2011.03578 [astro-ph.SR].
- Robrade, J. et al. (Nov. 2018). “Outstanding X-ray emission from the stellar radio pulsar CU Virginis”. In: 619, A33, A33. DOI: 10.1051/0004-6361/201833492. arXiv: 1808.02367 [astro-ph.SR].
- Rogers, F. J. and A. Nayfonov (Sept. 2002). “Updated and Expanded OPAL Equation-of-State Tables: Implications for Helioseismology”. In: 576, pp. 1064–1074. DOI: 10.1086/341894.
- Romanova, Marina M. and Owocki (2016). “Accretion, Outflows, and Winds of Magnetized Stars”. In: *The Strongest Magnetic Fields in the Universe*. Ed. by V. S. Beskin et al. Vol. 54. Space Sciences Series of ISSI. Springer, p. 347. DOI: 10.1007/978-1-4939-3550-5_11.
- Saumon, D., G. Chabrier, and H. M. van Horn (Aug. 1995). “An Equation of State for Low-Mass Stars and Giant Planets”. In: 99, p. 713. DOI: 10.1086/192204.
- Shenar, Tomer et al. (Aug. 2023). “A massive helium star with a sufficiently strong magnetic field to form a magnetar”. In: *Science* 381(6659), pp. 761–765. DOI: 10.1126/science.ade3293. arXiv: 2308.08591 [astro-ph.SR].
- Shultz, M. E. (Nov. 2020). “Modelling the Magnetic Fields and Magnetospheres of Early B-Type Stars”. In: *Stellar Magnetism: A Workshop in Honour of the Career and Contributions of John D. Landstreet*. Ed. by Gregg Wade et al. Vol. 11, pp. 54–65. DOI: 10.48550/arXiv.1912.08280. arXiv: 1912.08280 [astro-ph.SR].

- Shultz, M. E. et al. (Jan. 2018). “The magnetic early B-type stars I: magnetometry and rotation”. In: 475(4), pp. 5144–5178. DOI: 10.1093/mnras/sty103. arXiv: 1801.02924 [astro-ph.SR].
- Shultz, M. E. et al. (Nov. 2019). “The magnetic early B-type stars - III. A main-sequence magnetic, rotational, and magnetospheric biography”. In: 490(1), pp. 274–295. DOI: 10.1093/mnras/stz2551. arXiv: 1909.02530 [astro-ph.SR].
- Shultz, M. E. et al. (June 2022). “MOBSTER - VI. The crucial influence of rotation on the radio magnetospheres of hot stars”. In: 513(1), pp. 1429–1448. DOI: 10.1093/mnras/stac136. arXiv: 2201.05512 [astro-ph.SR].
- Sion, E. M. et al. (June 1983). “A proposed new white dwarf spectral classification system.” In: 269, pp. 253–257. DOI: 10.1086/161036.
- Swihart, Thomas L. (1971). *Basic physics of stellar atmospheres*.
- Temaj, D. et al. (Feb. 2024). “Convective-core overshooting and the final fate of massive stars”. In: 682, A123, A123. DOI: 10.1051/0004-6361/202347434. arXiv: 2311.05701 [astro-ph.SR].
- Timmes, F. X. and F. D. Swesty (Feb. 2000). “The Accuracy, Consistency, and Speed of an Electron-Positron Equation of State Based on Table Interpolation of the Helmholtz Free Energy”. In: 126, pp. 501–516. DOI: 10.1086/313304.
- Townsend and Owocki (Feb. 2005). “A rigidly rotating magnetosphere model for circumstellar emission from magnetic OB stars”. In: 357(1), pp. 251–264. DOI: 10.1111/j.1365-2966.2005.08642.x. arXiv: astro-ph/0408565 [astro-ph].
- Trigilio, C. et al. (Oct. 2000). “Coherent radio emission from the magnetic chemically peculiar star CU Virginis”. In: 362, pp. 281–288. DOI: 10.48550/arXiv.astro-ph/0007097. arXiv: astro-ph/0007097 [astro-ph].
- Trigilio, C. et al. (May 2004). “A three-dimensional model for the radio emission of magnetic chemically peculiar stars”. In: 418, pp. 593–605. DOI: 10.1051/0004-6361:20040060. arXiv: astro-ph/0402432 [astro-ph].
- von Hippel, Ted et al. (June 2007). “The New Class of Dusty DAZ White Dwarfs”. In: 662(1), pp. 544–551. DOI: 10.1086/518108. arXiv: astro-ph/0703473 [astro-ph].
- Wade, G. A. and C. Neiner (Jan. 2018). “Magnetism of hot stars”. In: *Contributions of the Astronomical Observatory Skalnaté Pleso* 48(1), pp. 106–115. DOI: 10.48550/arXiv.1712.09747. arXiv: 1712.09747 [astro-ph.SR].

Walczak, Przemysław and Agnieszka Kopacz (Apr. 2024). “Astero seismic modelling of the chemically peculiar B-type pulsator with an asymptotic period spacing - a Cen”. In: 529(4), pp. 4176–4191. DOI: 10.1093/mnras/stae672.

Overview of publication and author contributions

The work is based on three published articles, in which MK is one of the authors.

Prišegen, M., Piecka, M., Faltová, N., **Kajan, M.**, and Paunzen, E. (Jan. 2021). “White dwarf-open cluster associations based on Gaia DR2”, *Astronomy and Astrophysics*, vol. 645, Art. no. A13, 2021. doi:10.1051/0004-6361/202039276.

MK created a script and verified the results of new WD candidates. MK contributed to developing a simple concept of calculating the potential mass of progenitors that was transformed and refined.

J. Krticka, I. Krtickova, C. Moni Bidin, **M. Kajan**, S. Zaggia, L. Monaco, J. Janik, Z. Mikulasek, E. Paunzen (Mar. 2024). “The nature of medium-period variables on the extreme horizontal branch. I. X-shooter study of variable stars in the globular cluster ω Cen”, *Astronomy and Astrophysics*, vol. 683, Art. no. A110, 2024. doi:10.1051/0004-6361/202347359.

MK did modelling in MESA and wrote one section in the article.

Michal, Kajan, Jiří Krtička, and Jiří Kubát (June 2024). “Unveiling stellar aurorae: simulating auroral emission lines in hot stars induced by high-energy irradiation”, *Monthly Notices of the Royal Astronomical Society*, vol. 531, no. 1, OUP, pp. 1776–1788, 2024. doi:10.1093/mnras/stae1273.

MK wrote, finalised, researched, and analyzed data.

The authors’ data were also used in:

Piecka, M., S. Hutschenreuter, and J. Alves (July 2024). “Towards a complete picture of the Sco-Cen outflow”, *Astronomy and Astrophysics*, vol. 689, Art. no. A84, 2024. doi:10.1051/0004-6361/202450936.

MK mentioned in acknowledgement.

Pivoňková, Kateřina (2024). “Studium vysokorychlostních absorpčních událostí ve spektrech proměnných hvězd typu alfa Cygni”. SUPERVISOR : Olga Viktorovna Maryeva. Diplomová práce. Masarykova univerzita, Přírodovědecká fakulta, Brno. URL: <https://is.muni.cz/th/s2uyl/>.

MK mentioned in acknowledgement.

Appendix A

The nature of medium-period variables on the extreme horizontal branch

The nature of medium-period variables on the extreme horizontal branch

I. X-shooter study of variable stars in the globular cluster ω Cen[★]

J. Krtička¹, I. Krtíčková¹, C. Moni Bidin², M. Kajan¹ , S. Zaggia³, L. Monaco⁴, J. Janík¹ ,
Z. Mikulášek¹ , and E. Paunzen¹ 

¹ Department of Theoretical Physics and Astrophysics, Faculty of Science, Masaryk University, Kotlářská 2, Brno, Czech Republic
e-mail: krticka@physics.muni.cz

² Instituto de Astronomía, Universidad Católica del Norte, Av. Angamos, 0610 Antofagasta, Chile

³ INAF – Padova Observatory, Vicolo dell’Osservatorio 5, 35122 Padova, Italy

⁴ Universidad Andres Bello, Facultad de Ciencias Exactas, Departamento de Ciencias Físicas – Instituto de Astrofísica, Autopista Concepción-Talcahuano, 7100, Talcahuano, Chile

Received 4 July 2023 / Accepted 3 January 2024

ABSTRACT

A fraction of the extreme horizontal branch stars of globular clusters exhibit a periodic light variability that has been attributed to rotational modulation caused by surface spots. These spots are believed to be connected to inhomogeneous surface distribution of elements. However, the presence of such spots has not been tested against spectroscopic data. We analyzed the phase-resolved ESO X-shooter spectroscopy of three extreme horizontal branch stars that are members of the globular cluster ω Cen and also display periodic light variations. The aim of our study is to understand the nature of the light variability of these stars and to test whether the spots can reproduce the observed variability. Our spectroscopic analysis of these stars did not detect any phase-locked abundance variations that are able to reproduce the light variability. Instead, we revealed the phase variability of effective temperature and surface gravity. In particular, the stars show the highest temperature around the light maximum. This points to pulsations as a possible cause of the observed spectroscopic and photometric variations. However, such an interpretation is in a strong conflict with Ritter’s law, which relates the pulsational period to the mean stellar density. The location of the ω Cen variable extreme horizontal branch stars in HR diagram corresponds to an extension of PG 1716 stars toward lower temperatures or blue, low-gravity, large-amplitude pulsators toward lower luminosities, albeit with much longer periods. Other models of light variability, namely, related to temperature spots, should also be tested further. The estimated masses of these stars in the range of 0.2–0.3 M_{\odot} are too low for helium-burning objects.

Key words. stars: abundances – stars: horizontal-branch – stars: oscillations – globular clusters: individual: ω Cen

1. Introduction

A class of main sequence stars, called chemically peculiar stars, shows an unusual type of light variability connected to the presence of surface spots (Hümmerich et al. 2016; Sikora et al. 2019). These spots appear as a result of elemental diffusion, whereby certain elements diffuse upwards under the influence of radiative force, while others sink down as a result of gravitational pull (Vick et al. 2011; Alecian & Stift 2017; Deal et al. 2018). Moderated by the magnetic field (and also by some additional processes, perhaps), surface inhomogeneities appear (Kochukhov & Ryabchikova 2018; Jagelka et al. 2019). The inhomogeneous surface elemental distribution, together with the stellar rotation, leads to periodic spectrum variability. Additionally, the flux redistribution that is due to bound-bound (line) and bound-free (ionization) processes modulated by the stellar rotation causes photometric variability (Peterson 1970; Trasco 1972; Molnar 1973; Lanz et al. 1996). Based on abundance maps from spectroscopy, we see that this effect is able to reproduce the observed rotational light variability of chemically peculiar stars (Prvák et al. 2015; Krtička et al. 2020b).

[★] Based on observations collected at the European Southern Observatory, Paranal, Chile (ESO programme 108.224V).

Besides the radiative diffusion, chemically peculiar stars show other very interesting phenomena, including magnetospheric radio emission (Leto et al. 2021; Das et al. 2022), trapping of matter in circumstellar magnetosphere (Landstreet & Borra 1978; Townsend & Owocki 2005), magnetic braking (Townsend et al. 2010), and torsional variations (Mikulášek et al. 2011). However, up to now, such phenomena seems to be strictly confined to classical chemically peculiar stars, which inhabit a relatively wide strip on the main sequence with effective temperatures of about 7000–25 000 K.

Therefore, it is highly desirable to search for other types of stars that show similar phenomena. The most promising candidates are stars that have signatures of radiative diffusion in their surface abundances, such as hot horizontal branch stars (Unglaub 2008; Michaud et al. 2011) and hot white dwarfs (Chayer et al. 1995; Unglaub & Bues 2000). Indeed, variations of helium to hydrogen number density ratio have been found on the surface of white dwarfs (Heber et al. 1997; Caiazzo et al. 2023) and some extremely hot white dwarfs even show signatures of corotating magnetospheres (Reindl et al. 2019) and spots (Reindl et al. 2023).

The phenomena connected with chemically peculiar stars can be most easily traced by periodic photometric light

Table 1. Spectra used for the analysis.

Spectrum (prefix)	JD–2 400 000	Phase	S/N
vEHB-2, $P = 7.82858823$ d			
$\alpha = 13\text{h } 26\text{m } 22.572\text{s}, \delta = -47^\circ 30' 52.786''$			
XS_SFLX_3060818	59 612.82872	0.014	36
XS_SFLX_3060821	59 653.61422	0.224	18
XS_SFLX_3060824	59 600.77245	0.474	21
XS_SFLX_3060830	59 627.79067	0.925	36
vEHB-3, $P = 5.16509016$ d			
$\alpha = 13\text{h } 26\text{m } 21.922\text{s}, \delta = -47^\circ 26' 05.753''$			
XS_SFLX_3073156	59 597.79411	0.276	17
XS_SFLX_3073156	59 623.74778	0.301	35
XS_SFLX_3073159	59 603.79086	0.437	36
XS_SFLX_3073165	59 589.77704	0.724	28
XS_SFLX_3073168	59 621.83821	0.931	41
XS_SFLX_3073168	59 627.74979	0.076	34
vEHB-7, $P = 1.78352993$ d			
$\alpha = 13\text{h } 27\text{m } 17.454\text{s}, \delta = -47^\circ 27' 49.059''$			
XS_SFLX_3060944	59 667.56405	0.404	38
XS_SFLX_3060950	59 651.84211	0.589	45
XS_SFLX_3060956	59 600.82010	0.982	30

Notes. Photometric periods and J2000 coordinates determined by Momany et al. (2020). The phases were calculated for arbitrary $\text{JD}_0 = 2\,458\,031.346$. S/N is a median value.

variability. However, while there are some signatures of chemical spots in white dwarfs all along their cooling track (Dupuis et al. 2000; Kilic et al. 2015; Reindl et al. 2019), the search for light variability in field horizontal branch stars with $T_{\text{eff}} < 11\,000$ K has turned out to be unsuccessful (Paunzen et al. 2019). The prospect of rotationally variable hot subdwarfs was further marred by the discovery of a handful of hot subdwarfs which, despite their detectable surface magnetic fields (Dorsch et al. 2022), still do not show any light variability (Pelisoli et al. 2022).

This perspective changed with the detection of possible rotationally variable hot horizontal branch stars of globular clusters by Momany et al. (2020). However, the presence of abundance spots was anticipated from photometry without any support from spectroscopy. Therefore, we started an observational campaign aiming at detection of abundance spots on these stars and understanding this type of variability overall. Here, we present the results derived for members of ω Cen (NGC 5139).

2. Observations and their analysis

We obtained the spectra of supposed rotational variables in NGC 5139 within the European Southern Observatory (ESO) proposal 108.224V. The spectra were acquired with the X-shooter spectrograph (Vernet et al. 2011) mounted on the 8.2 m Melipal (UT3) telescope and these observations are summarized in Table 1. The spectra were obtained with the UVB and VIS arms providing an average spectral resolution ($R = \lambda/\Delta\lambda$) of 5400 and 6500, respectively. Although medium-resolution spectrograph is not an ideal instrument for abundance analysis, the abundance determination is typically based on multiple strong lines of given elements. This mitigates the disadvantages of the medium-resolution spectra and enables us to estimate reliable abundances (e.g., Kawka & Vennes 2016; Gvaramadze et al. 2017). In turn, the use of a medium-resolution spectrograph

Table 2. Wavelengths (in Å) of the strongest lines used for abundance determinations.

He I	3820, 4009, 4024, 4026, 4144, 4388, 4471, 4713, 4922, 5016
C II	3876, 3919, 3921, 4267
N II	3995, 4035, 4041, 4447, 4631, 5001
O II	3954, 4396, 4415
Mg II	4481
Al III	4513, 4529
Si II	3856, 3863
Si III	3807, 4553, 4568, 4575
Ca II	3934
Fe III	3954, 4035, 4138, 4139, 4165, 4273, 4286, 4297, 4372, 4396, 4420, 4431, 5127, 5194

implies a lower number of elements that can be studied and also worsens the precision with respect to the abundance determinations in cases of spectral blends. We extracted the calibrated spectra from the ESO archive. The radial velocity was determined by means of a cross-correlation using the theoretical spectrum as a template (Zverko et al. 2007) and the spectra were shifted to the rest frame.

The stellar parameters were determined using the simplex minimization (Krtićka & Štefl 1999) in three steps. First, we determined the effective temperature, T_{eff} , and the surface gravity, $\log g$, by fitting each of the observed spectra with spectra derived from the BSTAR2006 grid of NLTE¹ plane parallel model atmospheres with $Z/Z_{\odot} = 0.1$ (Lanz & Hubeny 2007). For the present purpose, the grid was extended for models with $\log g = 5$. The random errors of T_{eff} and $\log g$ for individual observations were determined by fitting a large set of artificial spectra derived from observed spectra by the addition of random noise with a Gaussian distribution. The dispersion of noise was determined by the signal-to-noise ratio (S/N) (Table 1).

We then estimated surface abundances using the model atmosphere from the grid located closest to the mean of derived parameters. The abundance determination was repeated once more using NLTE plane parallel model atmospheres calculated with TLUSTY200 (Lanz & Hubeny 2003, 2007) for parameters derived in the previous steps. To determine the abundances, we matched the synthetic spectra calculated by SYNSPEC49 code with observed spectra. The random errors of abundances for individual observations were also determined by fitting of artificial spectra derived by adding random noise to the observed spectra. For elements whose abundances were not derived from spectra, we assumed a typical ω Cen abundance $\log(Z/Z_{\odot}) = -1.5$ (Moehler et al. 2011; Moni Bidin et al. 2012). The spectral lines used for the abundance analysis are listed in Table 2. The final parameters averaged over individual spectra are given in Table 3. The derived individual elemental abundances are expressed relative to hydrogen $\varepsilon_{\text{el}} = \log(n_{\text{el}}/n_{\text{H}})$. Random errors given in Table 3 were estimated from parameters derived from the fits of individual spectra.

3. Analysis of individual stars

3.1. Star vEHB-2

Our analysis of the spectra for the star vEHB-2 (listed in Table 1) revealed periodic changes in surface gravity and effective

¹ The NLTE models allow for departures from the local thermodynamic equilibrium (LTE) due to radiative processes.

Table 3. Derived parameters of the studied stars.

Parameter	vEHB-2	vEHB-3	vEHB-7	Sun
T_{eff} [K]	$24\,900 \pm 1200$	$21\,000 \pm 1200$	$21\,200 \pm 600$	
$\log(g/1 \text{ cm s}^{-2})$	4.81 ± 0.12	4.64 ± 0.04	4.70 ± 0.04	
$R [R_{\odot}]$	0.34 ± 0.05	0.39 ± 0.06	0.33 ± 0.03	
$M [M_{\odot}]$	0.27 ± 0.11	0.25 ± 0.08	0.20 ± 0.04	
$L [L_{\odot}]$	40 ± 7	27 ± 5	20 ± 3	
$\log \varepsilon_{\text{He}}$	-3.0 ± 0.2	-3.3 ± 0.5	-2.9 ± 0.2	-1.07
$\log \varepsilon_{\text{C}}$	-4.5 ± 0.1	-4.7 ± 0.2	-4.9 ± 0.1	-3.57
$\log \varepsilon_{\text{N}}$	-4.6 ± 0.1	-4.4 ± 0.1		-4.17
$\log \varepsilon_{\text{O}}$	-4.6 ± 0.4	-4.2 ± 0.2		-3.31
$\log \varepsilon_{\text{Mg}}$		-5.3 ± 0.1	-5.9 ± 0.1	-4.40
$\log \varepsilon_{\text{Al}}$	-6.0 ± 0.1			-5.55
$\log \varepsilon_{\text{Si}}$	-5.1 ± 0.1	-5.0 ± 0.1	-4.6 ± 0.1	-4.49
$\log \varepsilon_{\text{Ca}}$		-6.0 ± 0.1	-5.4 ± 0.8	-5.66
$\log \varepsilon_{\text{Fe}}$	-3.8 ± 0.1	-4.2 ± 0.2		-4.50
v_{rad} [km s^{-1}]	195 ± 7	231 ± 4	227 ± 3	

Notes. Solar abundances were taken from [Asplund et al. \(2009\)](#). Blank items denote values that were not determined.

temperature (see Fig. 1). To test their presence and any possible correlations, we fixed either the surface gravity or effective temperature and repeated the fit to determine the missing parameter. The test revealed a similar variability of the effective temperature and surface gravity as derived from the fit of both parameters and has not shown any significant change of the derived parameters. Neither one of the parameters determined from individual spectra with added random noise showed any strong correlations. Thus, we conclude that the detected variations of surface gravity and effective temperature are real. We did not detect any strong phase variations of elemental abundances or radial velocities (Sects. 5.2 and 5.3).

Table 3 lists derived parameters of vEHB-2 averaged over the available spectra. The abundances of many elements is slightly higher than a typical ω Cen composition $\log(Z/Z_{\odot}) = -1.5$ ([Moehler et al. 2011](#); [Moni Bidin et al. 2012](#)). The exceptions are helium, which is strongly underabundant as a result of gravitational settling, and iron, whose overabundance can be interpreted as a result of radiative diffusion ([Unglaub & Bues 2001](#); [Michaud et al. 2011](#)).

With $V = 17.249$ mag ([Momany et al. 2020](#)), $E(B - V) = 0.115 \pm 0.004$ mag ([Moni Bidin et al. 2012](#)), the bolometric correction of [Flower \(1996, see also Torres 2010\)](#) $BC = -2.40 \pm 0.12$ mag, and distance modulus $(m - M)_0 = 13.75 \pm 0.13$ mag ([van de Ven et al. 2006](#)), the estimated luminosity is $L = 40 \pm 7 L_{\odot}$. With determined atmospheric parameters this gives the stellar radius $0.34 \pm 0.05 R_{\odot}$ and mass $0.27 \pm 0.11 M_{\odot}$. Derived effective temperature is slightly lower than the estimate $28\,200 \pm 1600$ K of [Moehler et al. \(2011\)](#), while our results agree with their surface gravity, $\log g = 4.86 \pm 0.18$, and helium abundance, $\log \varepsilon_{\text{He}} = -3.20 \pm 0.16$.

3.2. Star vEHB-3

The spectral analysis of vEHB-3 also revealed phase-locked variability of the effective temperature and surface gravity (Fig. 2). The star is hotter and shows higher surface gravity during the light maximum. The analysis of individual spectra has not revealed any significant variations of the radial velocity (Sect. 5.3).

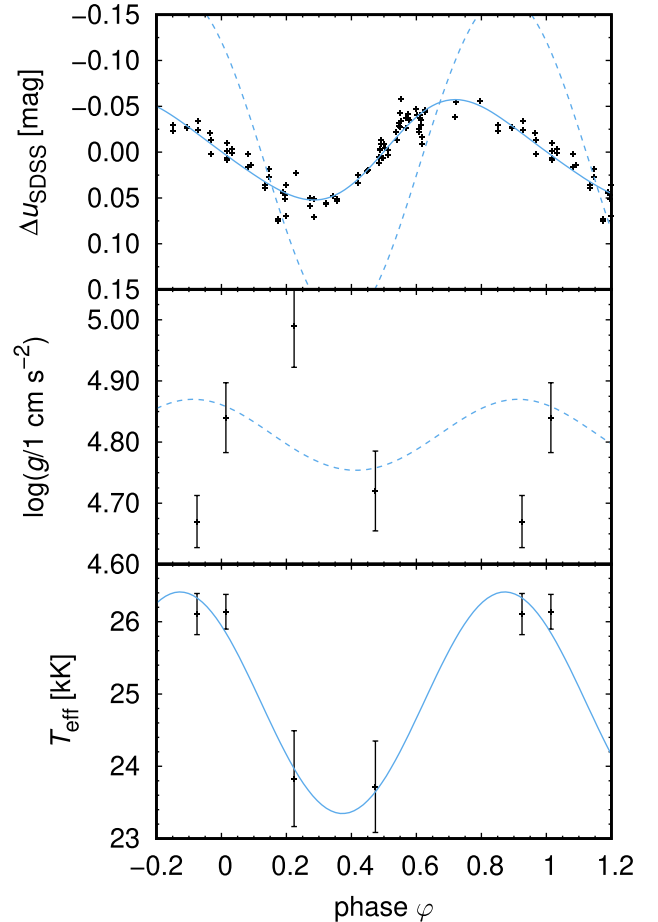


Fig. 1. Phase variations of vEHB-2. Upper panel: observed light variations from [Momany et al. \(2020\)](#). Dashed blue line denotes predictions deduced purely from temperature variations, while solid line denotes a fit with additional sinusoidal radius variations. Middle panel: surface gravity variations. Dashed blue line denotes surface gravity determined from the radius variations. Lower panel: effective temperature variations. Solid blue line denotes sinusoidal fit. Part of the variations for $\varphi < 0$ and $\varphi > 1$ are repeated for better visibility.

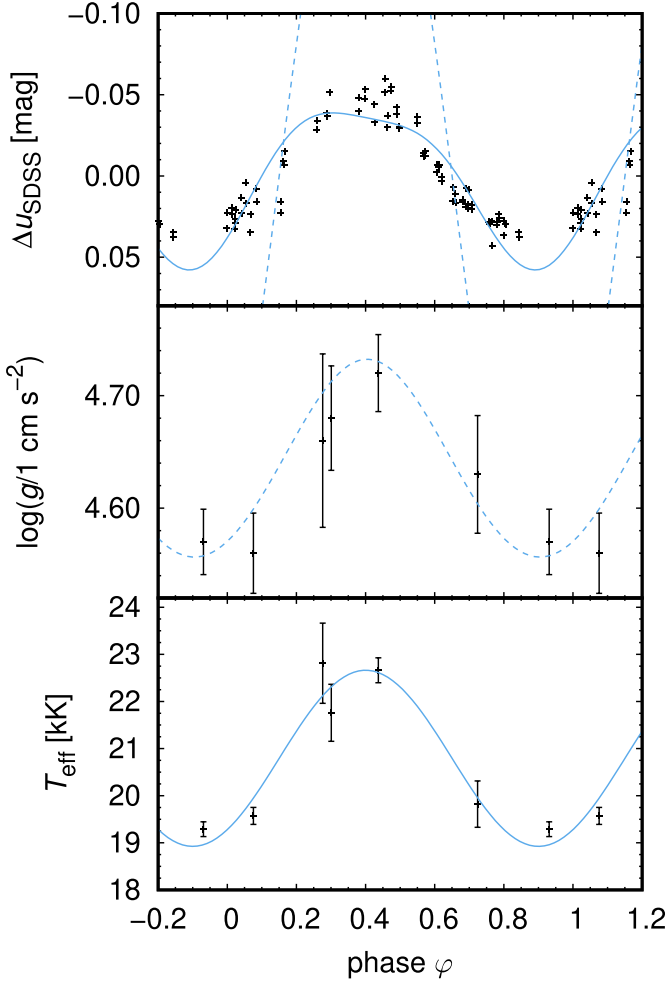


Fig. 2. Same as Fig. 1, but for vEHB-3.

A detailed inspection of spectra shows that the strength of helium lines is variable. This can be most easily seen in He I 4026 and 4471 Å lines (Sect. 6.3). In principle, such variability may also reflect the temperature variations. To test this, for this star we determined abundances for actual temperature and surface gravity derived from individual spectra and not just for the mean values. Even with this modified approach the helium abundance variations has not disappeared, showing that simple effective temperature and gravity variations cannot reproduce the variability of helium lines. We have not detected any strong variability of the line strengths of other elements (Sect. 5.2).

For vEHB-3, Momany et al. (2020) gives $V = 17.274$ mag, while the mean reddening is $E(B - V) = 0.115 \pm 0.004$ mag (Moni Bidin et al. 2012), the bolometric correction of Flower (1996) is $BC = -2.00 \pm 0.13$ mag, and the distance modulus is $(m - M)_0 = 13.75 \pm 0.13$ mag (van de Ven et al. 2006); this results in the luminosity of $L = 27 \pm 5 L_\odot$. With the determined atmospheric parameters, this gives a stellar radius of $0.39 \pm 0.06 R_\odot$ and mass of $0.25 \pm 0.08 M_\odot$.

3.3. Star vEHB-7

In total, five spectra for vEHB-7 were obtained. However, one of them is of a poor quality and an additional spectrum was marred by a wrong pointing. Consequently, there are just three spectra left. Anyway, the analysis of these spectra indicates presence

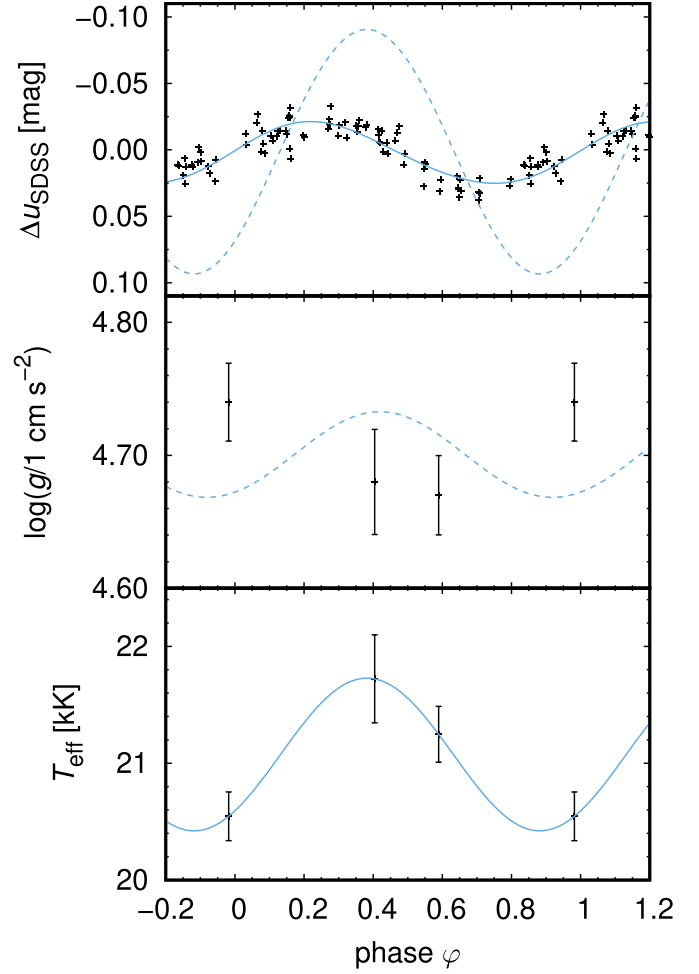


Fig. 3. Same as Fig. 1, but for vEHB-7.

of temperature variations (Fig. 3), with temperature maximum appearing around the time of light maximum. The available spectra do not show any strong variability of surface abundances nor the radial velocities (Sects. 5.2 and 5.3).

The V magnitude of the star is $V = 17.644$ mag (Momany et al. 2020), which with the reddening $E(B - V) = 0.115 \pm 0.004$ mag (Moni Bidin et al. 2012), the bolometric correction of Flower (1996) $BC = -2.02 \pm 0.07$ mag, and distance modulus $(m - M)_0 = 13.75 \pm 0.13$ mag (van de Ven et al. 2006) gives a luminosity of $L = 20 \pm 3 L_\odot$. With the atmospheric parameters determined from spectroscopy, this gives a stellar radius of $0.33 \pm 0.03 R_\odot$ and mass of $0.20 \pm 0.04 M_\odot$. The star was analyzed by Latour et al. (2018), who derived slightly higher effective temperature of 23800 ± 800 K, surface gravity of $\log g = 5.11 \pm 0.06$, and mass of $0.49 \pm 0.10 M_\odot$.

4. Significance of the detected variations

Before discussing the implications of the detected variations for the mechanism of the light variability of the stars, we first need to clarify whether the detected variations could be real. To this end, we used a random number generator to create a population of stellar parameters with dispersions determined from the uncertainty of each measurement in each phase. We compared the dispersion of the derived artificial population with the dispersion of the derived data and determined a fraction of the

population that gives a higher dispersion than the data determined from observation. If this fraction is high, then it is likely that the derived variations are only sampling random noise.

For the effective temperature, the derived fraction is lower than 10^{-5} for all three stars. The uncertainties of estimated effective temperatures should be a factor of three higher to reach a fraction of 0.01 for vEHB-7 – and even higher for the remaining stars. Thus, we conclude that the detected variations of the effective temperature are very likely to be real for all the stars studied here.

The same is true for the variations of the surface gravity, where the uncertainties should be a factor of 1.6 higher to reach a fraction of 0.01 for vEHB-7. From this, we conclude that also the variations of the surface gravity are very likely real in vEHB-2 and vEHB-3, with a small chance that the gravity variations in vEHB-7 are random.

5. Nature of the light variations

5.1. Pulsations

We detected a variability among the effective temperature and surface gravity phased with photometric variations in all studied stars (Figs. 1–3). The effective temperature and surface gravity are typically the highest during the maximum of the light variability. In the absence of any strong radial velocity variations (Sect. 5.3), such changes in the stellar parameters can be most naturally interpreted as resulting from the pulsations (e.g., Woolf & Jeffery 2002; Fossati et al. 2014; Vasilyev et al. 2018).

To test the pulsational origin of the light variability, we calculated the synthetic light curves and compared it with observed light variability. As a first step, we used the fluxes from the BSTAR2006 database calculated for $Z = 0.1 Z_{\odot}$ and $\log g = 4.75$, convolved them with the response function of u_{SDSS} , and fitted them as a function of the effective temperature, deriving:

$$\begin{aligned} & -2.5 \log \left(\frac{H(u_{\text{SDSS}})}{1 \text{ erg s}^{-1} \text{ cm}^{-2}} \right) \\ & = -19.29 - 0.275 \left(\frac{T_{\text{eff}}}{10^3 \text{ K}} \right) + 0.0032 \left(\frac{T_{\text{eff}}}{10^3 \text{ K}} \right)^2. \quad (1) \end{aligned}$$

The fit is valid between $T_{\text{eff}} = 15\text{--}30 \text{ kK}$. We fit the observational phase variations of the effective temperature by a simple sinusoidal (plotted in Figs. 1–3) and used these variations to predict the light variations (dashed curve in the upper plots of Figs. 1–3). The prediction assumes that the temperature is the same across the stellar surface, corresponding to the radial pulsations. The resulting light variations have always higher amplitude than the observed light curve, but this can be attributed to radius variations. We searched for such sinusoidal radius variations that would allow us to reproduce the observed light variations. It turns out that radius variations with amplitudes of about few percent and phase-shifted by nearly half period from temperature variations are fully able to reproduce the observed light variations (solid line in the upper panels of Figs. 1–3). Assuming that the pulsating atmosphere is roughly in hydrostatic equilibrium, the effective surface gravity varies due to a change in radius and as a result of inertial force. This is plotted using the dashed curve in the middle plot of Figs. 1–3. The resulting amplitude of the surface gravity variations is always comparable to the observed variations, albeit the curves are in good agreement only for vEHB-3.

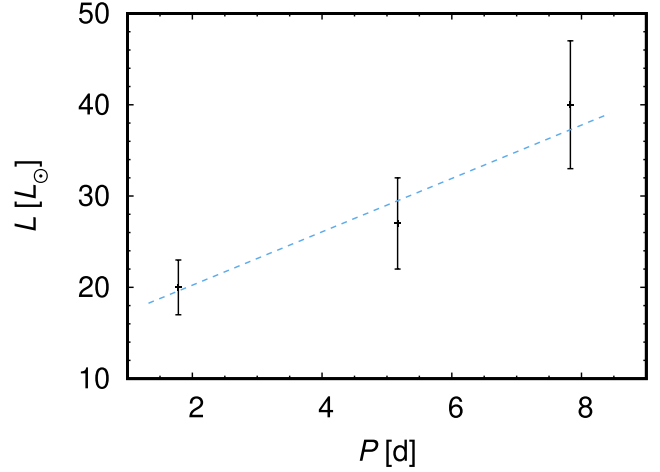


Fig. 4. Period-luminosity relationship for studied stars. Dashed line corresponds to the linear fit.

The fact that the resulting phase variations of surface gravity do not fully agree with observations is understandable for several reasons. The spectroscopy was obtained just in few phases, which makes the effective temperature phase curve rather uncertain. Moreover, the width of the line profiles is affected by the electron number density and not directly by the surface gravity. The dependence of the line profiles on gravity stems from the hydrostatic equilibrium equation. However, the equation of hydrostatic equilibrium can be violated in pulsating stars, especially in the presence of shocks (Jeffery et al. 2022). Additionally, the effective temperature determined from spectroscopy may not correspond to temperature of radiation emerging from the continuum formation region. Finally, contrary to our assumption, the stars may experience non-radial pulsations, further complicating the analysis.

Pulsating stars often show relation between period and luminosity (e.g., Leavitt 1908; Freedman & Madore 1990; Mowlavi et al. 2016) which stems from the dependence of pulsational period on mean stellar density or sound wave crossing time. It is worthy to notice that in Table 3 the more luminous stars have longer periods. On average, the period-luminosity relationship can be expressed as (see Fig. 4):

$$\left(\frac{L}{L_{\odot}} \right) = 2.9 (\pm 0.7) \left(\frac{P}{1 \text{ d}} \right) + 14 (\pm 3). \quad (2)$$

However, the analysis involves strong selection effect, because we have focused on brightest stars from the Momany et al. (2020) sample.

The pulsational hypothesis can be further tested using ultraviolet photometric variations (e.g., Krtička et al. 2023), which should correspond to optical variations. The amplitude of the radial velocity variations due to proposed pulsational motion is of the order 0.1 km s^{-1} . Therefore, the presence of pulsations can be also tested using precise radial velocity measurements.

However, the interpretation of observed light variations in terms of pulsations poses a challenge for pulsational theory. Field hot subdwarfs typically pulsate with frequencies that are one to two orders of magnitude higher than found here (Østensen et al. 2012; Jeffery et al. 2017; Baran et al. 2021). This stems from Ritter's law (Ritter 1879), which predicts that the period of pulsations is inversely proportional to the square root of the mean stellar density. As a result, tenuous cool giants and supergiants pulsate with periods of the order of hundreds of days

(Ahmad et al. 2023). On the other hand, the p-modes of relatively high-density hot subdwarfs are predicted to have periods of the order of hundreds of seconds (Guo 2018). With typical pulsational constants (Lesh & Aizenman 1974; Saio & Gautschy 1998), Ritter’s law gives a period of the order of hundredths of a day for studied stars, which is three orders of magnitude lower than the period of variability of studied stars. The beating of two close periods could lead to variability with longer period, but it remains unclear how the short periods could be damped in surface regions. The g-modes may have longer periods (Miller Bertolami et al. 2020) and would thus serve as better candidates for explaining the observed periodic light variability.

The period of g-mode pulsations depends on the buoyancy oscillation travel time across the corresponding resonance cavity (Garcia et al. 2022). The related Brunt–Väisälä frequency approaches zero when the radiative temperature gradient is close to the adiabatic gradient. Hot stars possess an iron convective zone, which disappears for low iron abundances (Jermyn et al. 2022). However, the studied stars show relatively high iron abundance as a result of radiative diffusion (Table 3). Therefore, it is possible that interplay of the radiative diffusion and proximity to the convection instability may lead to the appearance of medium-period pulsations.

The pulsations may not necessarily be driven by classical κ -mechanism. The location of studied stars in $\log g - T_{\text{eff}}$ diagram corresponds to stars experiencing helium subflashes before the helium-core burning phase (Battich et al. 2018). Such stars are predicted to have pulsations driven by the ϵ -mechanism.

If the light variations are indeed due to pulsations, then the stars could be analogues of other pulsating subdwarfs, as the EC 14026 stars (Kilkenny et al. 1997) and PG 1159 stars (GW Vir stars, Córscico et al. 2008), however, with much longer periods. Taking into account the derived stellar parameters, the location of the variables from ω Cen in HR diagram corresponds to the extension of PG 1716 stars (Green et al. 2003) toward lower effective temperatures. Stellar parameters of studied stars are also close to the blue large-amplitude pulsators (Pietrukowicz et al. 2017), which are somehow more luminous and slightly hotter. The search for pulsations in corresponding cluster stars was, to our knowledge, not successful (Reed et al. 2006); surprisingly, only significantly hotter pulsating stars were detected on the horizontal branch (Randall et al. 2011; Brown et al. 2013). The studied stars are located in area of Hertzsprung-Russell diagram (HRD), where pulsations resulting from the κ -mechanism on the iron-bump opacity can be expected; however, with significantly shorter periods (Charpinet et al. 1996; Jeffery & Saio 2006, 2016). The pulsational instability appears at high iron abundances, which are also detected in studied stars.

Pulsating subdwarfs typically evince non-radial pulsations (Córscico et al. 2008), for which low amplitudes of photometric variations are expected. Still, Kupfer et al. (2019) detected a new class of variable stars corresponding to blue, high-gravity, large-amplitude pulsators that are pulsating radially with amplitudes that are comparable to the stars studied here.

5.2. Abundance spots

As one of the possible mechanisms behind the detected light variability, Momany et al. (2020) suggested the rotational flux modulation due to abundance spots. Any light variability modulated by rotation requires that the rotational velocity determined from the period of variability and stellar radius should be higher

than the rotational velocity projection, $v_{\text{rot}} \sin i$, determined from spectroscopy. However, the spectroscopy provides only a very loose constraint on the rotational velocities of individual stars, $v_{\text{rot}} \sin i < 50 \text{ km s}^{-1}$. As a result, with the stellar radii (from Table 3) and photometric periods (listed in Table 1) determined by Momany et al. (2020), the rotational modulation of photometric variability cannot be ruled out. Therefore, the test of abundance spots requires a more elaborate approach.

In principle, determination of light curves due to abundance spots from the observed spectroscopy is a straightforward procedure. The inverse method of Doppler imaging is used to determine surface abundance maps (e.g., Kochukhov et al. 2022). From the derived abundance maps, the light curves can be simulated using model atmospheres synthetic spectra (e.g., Krtička et al. 2020b). However, the Doppler imaging requires relatively large number of high-resolution and high S/N spectra. With the current instrumentation, this is beyond the reach of even 8-m class telescopes. Therefore, another method has to be used to test the presence of surface spots.

For faint stars, it is possible to estimate surface abundances as a function of phase and simulate the light variability directly from derived abundances (Krtička et al. 2020a). However, the observations do not suggest the presence of abundance spots on the surface of the stars. There is some scatter of abundances derived from individual spectra, but the potential abundance variations are not correlated with light variations. This can be seen from Fig. 5, where we plot the abundances derived from individual spectra as a function of observed magnitude (both values are plotted with respect to the mean). If the light variations were due to the abundance variations, the plot should evince a positive correlation between abundance and magnitudes (Prvák et al. 2015; Krtička et al. 2020b), but such a correlation is missing. Moreover, the amplitude of abundance variations (which is no more than about 0.1 dex) should be one magnitude higher to cause observed light variations (c.f., Oksala et al. 2015; Krtička et al. 2020b). On top of that, the mean abundance should be high enough to affect the emergent flux.

We additionally tested the abundance spot model of the light variability using model atmosphere emergent fluxes. We calculated the model atmospheres with ten times higher abundances of helium, silicon, and iron than those determined from spectroscopy. This is an order of magnitude higher overabundance than observations allow. We calculated the magnitude difference between the fluxes corresponding to enhanced and observational abundances in the u_{SDSS} band used by Momany et al. (2020). This gives a theoretical upper limit of the magnitude of the light variability. In the case of helium and silicon, the derived amplitude of the light variability would be 0.002 and 0.02 mag, which is significantly lower than the observed amplitude of the light variability. The amplitude is higher only in the case of iron (0.4 mag), but even in this case the maximum iron abundance does not appear during the maximum of the light curve (Fig. 5). Moreover, the detected abundance variations can be interpreted in terms of random fluctuations.

There is a possibility that the variations are caused by element(s) that do not appear in the optical spectra. However, this is unlikely, because in classical chemically peculiar stars the abundance variations are not confined just to a single element (e.g., Rusomarov et al. 2018; Kochukhov et al. 2022). Consequently, we conclude that derived abundance variations from individual spectra are most likely of statistical origin. Therefore, the studied stars do not likely show light variability due to surface spots similar to main sequence, chemically peculiar stars.

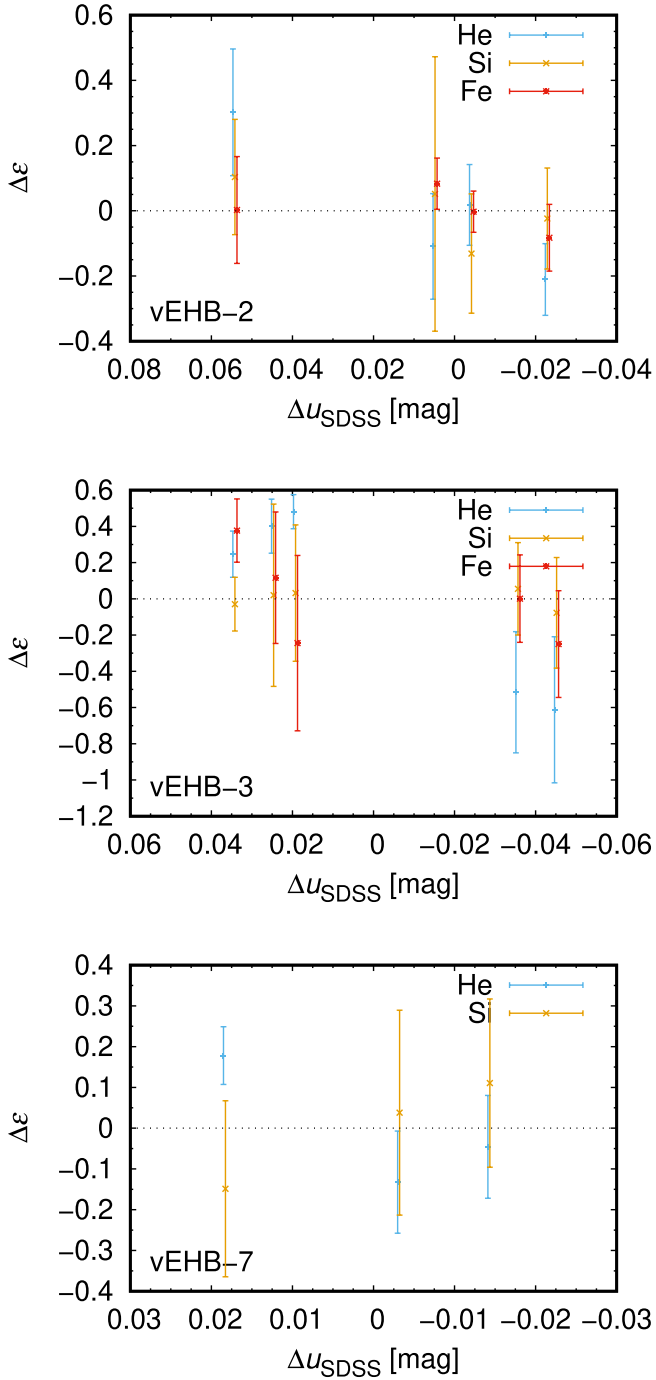


Fig. 5. Difference between abundances of selected elements derived from individual spectra and a mean abundance. Plotted as a function of relative magnitudes for individual stars. Elements plotted in the graph typically contribute most significantly to the light variations at studied effective temperatures (Oksala et al. 2015; Krtička et al. 2020b). The individual points were shifted slightly horizontally to avoid overlapping.

The only element that varies with magnitude is helium (Fig. 5), but it shows opposite behavior than is required to explain the light variability due flux redistribution. This means that the helium lines are observed to be stronger during the light minimum. Moreover, the helium line profiles are complex and we were unable to reasonably fit the observed helium lines using synthetic spectra. Therefore, instead of spots, we suspect that they are formed by intricate motions in the atmosphere during pulsations (Sect. 6.3).

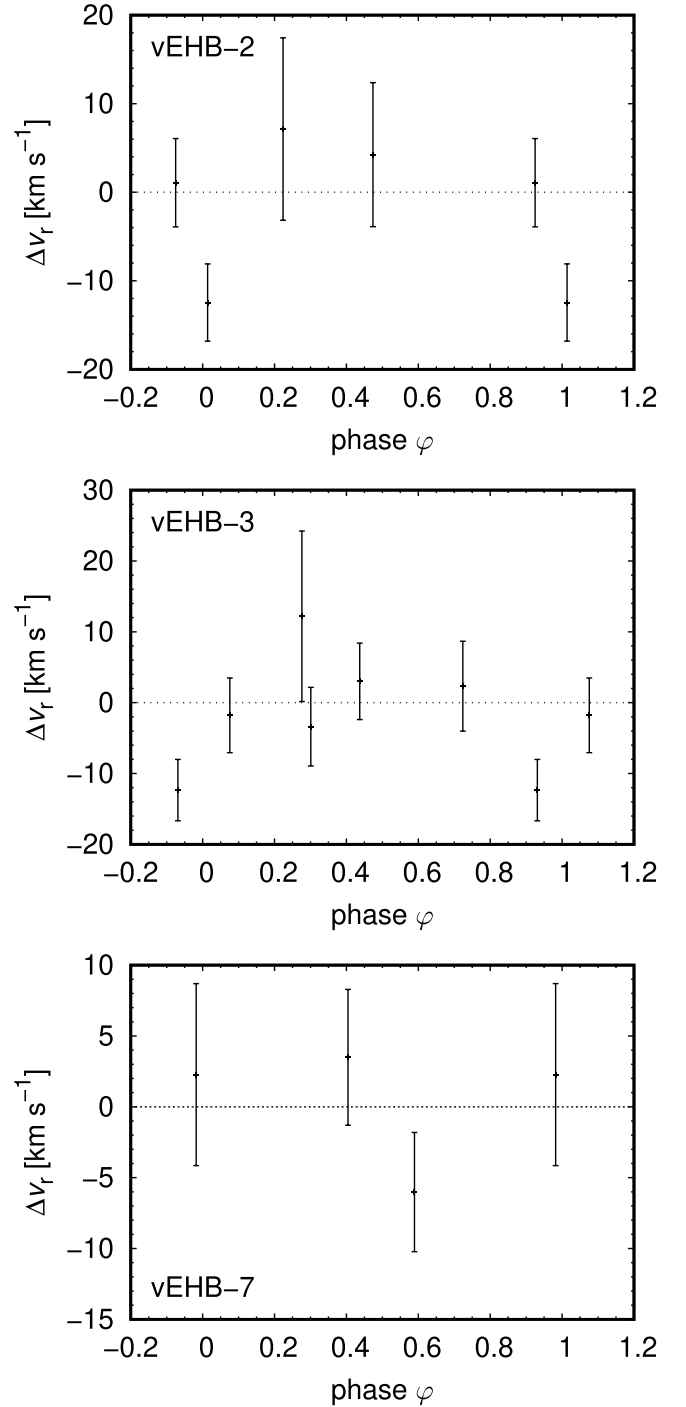


Fig. 6. Phase variations of radial velocity determined from individual spectra with respect to the mean value. Plotted for individual stars. Parts of the variations for $\varphi < 0$ and $\varphi > 1$ repeat for a better visibility.

5.3. Binary origin

It may be possible that the observed light variations are due to binary effects. In that case, there would be a number of combinations for the arrangement of the system. It is unlikely that the variations are due to the reflection effect on a cooler companion, because in such cases, the system would look cooler during the light maxima, which would contradict the observations. Moreover, the predicted amplitude would be too low. Due to the absence of any strong radial velocity variations (Fig. 6) and for evolutionary reasons, the cooler companion would be

less massive; from this (and the third Kepler law), the resulting binary separation would be about $11 R_{\odot}$ for vEHB-2 (and even lower for remaining stars). This once more precludes the assumption of the red giant as a companion and leaves just enough space for a low-mass main sequence star. Furthermore, we used our code calculating light curves due to the reflection effect, which predicts that the radius of such a star should be comparable to solar radius to cause observed light variations. Therefore, for low-mass main sequence star, the light amplitude would be significantly lower than observed.

The reflection due to a hotter companion is constrained by the absence of strong companion lines in the optical spectra and by missing large radial velocity variations (Fig. 6). This leaves two options, both involving hot (possibly degenerated) companion. Either the companion has low mass (possibly implying a hot helium white dwarf) or the system involves high-mass companion on an orbit with low inclination. In any case, given a typical mass of extreme horizontal branch stars (Moni Bidin et al. 2007, 2012) and maximum mass of white dwarfs (Yoshida 2019; Nunes et al. 2021), it is unlikely that the total mass of the system exceeds $2 M_{\odot}$. In this case the Kepler third law predicts an orbital separation of $a = 21 R_{\odot}$ for vEHB-2. From the Saha-Boltzmann law, the required temperature of irradiating body is $T_{\text{irr}} = \sqrt{a/R_{\text{irr}}} [2(T_2^4 - T_1^4)]^{1/4}$, where R_{irr} is the radius of irradiating body and T_2 and T_1 are the maximum and minimum temperatures of studied star. With a typical radius of a white dwarf $R_{\text{irr}} = 0.01 R_{\odot}$ this gives $T_{\text{irr}} = 10^6$ K, far exceeding the temperature of any white dwarf (Miller Bertolami 2016). This estimate could be decreased assuming a lower mass of irradiating body and excluding the detected radius variations, but it still amounts to about 300 kK for the star vEHB-7 with the shortest period. From this, we conclude that it is unlikely that the observed light variations are caused by binary companion.

We subsequently performed a similar analysis as done by Moni Bidin et al. (2006, 2009) and searched for binarity from the radial velocity data. From the analysis, it follows that the measurements are perfectly compatible with constant radial velocities. A Kolmogorov–Smirnov test reveals that the probability of these results being drawn from a normal distribution (with a dispersion equal to the observational errors) is equal or higher than about 50% for each star (namely 48, 64, and 86% for vEHB-2, vEHB-3, and vEHB-7).

Going further, we estimated the probability of these stars being undetected binaries. The most common close companions of extreme horizontal branch stars are compact objects such as white dwarfs. Hence, we simulated systems of $0.49 + 0.49 M_{\odot}$ stars (typical of such systems), in circular orbits (because the short periods suggest a previous common envelope phase, which circularizes the orbits), with orbital period equal to the photometric one, an isotropic distribution of the angle of inclination of the orbit (hence uniform in $\sin i$), and a random phase. We considered a system to be “undetected” if the observed radial velocities (at the epochs of observations) show a maximum variation lower or equal to that observed. We found that the probability that the studied stars hide undetected binary are 1.74% for vEHB-2, 0.68% for vEHB-3, and $<0.01\%$ for vEHB-7. The differences stem from different periods of variability. In conclusion, the angle of inclination cannot explain the lack of evidence with respect to binarity.

For the radial velocity analysis, we assumed a canonical mass for the extreme horizontal branch stars, but the estimated values are much lower. The lower mass would make the probabilities even lower, because with a smaller mass, the radial velocity

variations would be greater. On the other hand, with lower mass of the companion, the binarity could pass undetected more easily. Consequently, we checked what the companion mass must be to obtain the probability of an undetected binary of at least 5%. This results in 0.27, 0.17, and $0.04 M_{\odot}$ for the studied stars. As we have already shown, the masses are too low to explain photometric variations by mean of ellipsoidal variation or reflection effects. The exception could possibly be vEHB-2, but it has the longest period, which implies a much larger separation between the components, again arguing against both tidal and reflection effects.

Another possibility is that the light variations are not due to the star itself, but due to another star that coincidentally appears at the same location on the sky. However, it is difficult to find such types of variable stars that would correspond to observations. Pulsating stars of RR Lyr type, which are indeed found on horizontal branch of globular clusters, have significantly shorter periods (e.g., Skarka et al. 2020; Molnár et al. 2022). The period of variability better corresponds to Cepheids. Type II Cepheids may correspond to low-mass stars that left the horizontal branch (Bono et al. 2020) and are indeed found in globular clusters (Braga et al. 2020). However, they are much brighter in the visual domain than stars studied here. On the other hand, classical Cepheids corresponds to blue loops on evolutionary tracks of stars that are more massive than appear in globular clusters now (Neilson et al. 2016). This would imply a distant background object that is younger than the cluster. However, taking into account the fact that extreme horizontal branch stars constitute just a very small fraction of cluster stars, we consider a chance alignment in three of them to be very unlikely.

5.4. Temperature spots

Momany et al. (2020) pointed out that the observed photometric variations could be caused by temperature spots. Such spots are predicted to be caused by shallow subsurface convective zones that may be present in hot stars (Cantiello & Braithwaite 2011, 2019) and connected to surface magnetic fields. This could indicate the presence of either a He II or deeper Fe convective zone. However, helium is significantly underabundant in studied stars and a corresponding region of helium underabundance may extend deep into the star (Michaud et al. 2011). As a result, the He II convection zone may be absent (Quievy et al. 2009), as indicated also by our evolutionary models (Sect. 6.4).

The studied variability seems to be stable on a timescale of years, while the subsurface convection zones were invoked to explain variability that is more stochastic in nature (Cantiello et al. 2021) and has a significantly lower amplitude. Subsurface convection was suggested to drive corotating interacting regions in hot star winds (David-Uraz et al. 2017), which require more spatially coherent structures, but it is unclear whether they are persistent in the course of hundreds of days. Based on the analogy with cool star spots and considering photometric observations of hot stars (Chené et al. 2011; Ramiaramantsoa et al. 2014; Aerts et al. 2018), we consider this possibility to be unlikely. Moreover, the iron convective zone appears directly beneath the stellar surface, therefore, it does not seem likely that the magnetic fields can cause large variations of stellar radius (c.f., Fuller & Mathis 2023).

We have detected variations of the effective temperature (Figs. 1–3), but they predict a greater amplitude of light variability than what has been observed. To reduce the amplitude, we introduced additional variations of radius, which cause

variability of surface gravity. The detected variations of surface gravity are in conflict with models of temperature spots. We tested this by fitting synthetic spectra derived from combination of spectra with different effective temperatures, but the same surface gravities. This should mimic the spectra of a star with temperature spot(s). The fit provided an effective temperature between the temperatures of combined spectra, but the surface gravity remained nearly constant and equal to the surface gravities of individual spectra.

About one-third of stars with spots show complex light curves with a double-wave structure (Jagelka et al. 2019). However, all the light curves observed by Momany et al. (2020) are much simpler and consist of just a single wave. This also is an argument against the notion of spots causing the photometric variability of the studied stars.

The model of temperature spots can be further observationally tested using spectropolarimetry, which should be able to detect accompanying weak magnetic fields. Hot spots could be also detected from radial velocity variations, which should show a minimum at about a quarter of a phase before the light maximum. This phase variability is opposite to radial velocity variations due to pulsations, which show a maximum at a quarter phase before the light maximum.

6. Discussion

6.1. Stellar masses

Stellar masses of studied stars derived from spectroscopy and photometry are rather low for single core-helium burning objects. Although the uncertainties are typically very large, the masses are systematically lower than a canonical mass of isolated subdwarfs (Heber 2016). Comparable mass problems also appear in other studies of globular cluster horizontal branch stars with similar temperatures (Moni Bidin et al. 2012; Moehler et al. 2019; Latour et al. 2023).

The cause of this problem is unclear (see the discussion in Moni Bidin et al. 2011). With a fixed surface gravity from spectroscopy, a higher mass requires larger radius. This can be achieved either by significantly lower V magnitude, higher distance modulus, higher reddening, or lower bolometric correction. A lower apparent magnitude is unlikely. The *Gaia* distance modulus of ω Cen is slightly lower than the value adopted here (Soltis et al. 2021) worsening the problem even more. The adopted reddening agrees with independent estimations (Calamida et al. 2005; Bono et al. 2019). The bolometric corrections might be uncertain and, indeed, Lanz & Hubeny (2007) reported slightly lower value than adopted here. However, this alone would not solve the problem. Our analysis using the model atmosphere fluxes computed here, with the help of Eq. (1) from Lanz & Hubeny (2007), shows that a lower helium abundance slightly increases the bolometric correction, thus worsening the discrepancy once again.

This leaves the uncertainties of parameter determinations from spectroscopy as the only remaining cause of overly low derived masses of studied stars connected with the analysis. The true uncertainties could be higher than the random errors (given in Table 3) when accounting for systematic errors (Sect. 6.5).

Lower mass subdwarfs may also originate due to some more exotic evolutionary processes. Subdwarfs with mass lower than the canonical one are found among field stars, but they typically appear in binaries (Kupfer et al. 2017) and require binary interaction for explanation (Althaus et al. 2013). Moreover, stars

with initial masses of about $2 M_{\odot}$ may ignite helium in a non-degenerate core with mass as low as $0.32 M_{\odot}$ (Han et al. 2002; Arancibia-Rojas et al. 2024). However, the lifetime of such stars is at odds with expected age of ω Cen. In any case, low-mass white dwarfs with mass around $0.2 M_{\odot}$ were detected, which are considered to be connected with hot subdwarfs (Heber 2016). A lower mass of about $0.3 M_{\odot}$ was also predicted for blue large-amplitude pulsators in the context of their He pre-white dwarf nature (Córscico et al. 2018; Romero et al. 2018). However, alternative models for these stars propose either helium shell or core burning subdwarfs with higher masses (Wu & Li 2018; Xiong et al. 2022).

6.2. Tension with parameters from literature

For star vEHB-7, Latour et al. (2018) determined slightly higher effective temperature and surface gravity. However, their data were collected by the FORS spectrograph, which has a lower resolution than X-shooter. We simulated the consequences of using low resolution spectra for the derived parameters and we smoothed the data by a Gaussian filter with dispersion of 3 \AA , which roughly corresponds to a FORS resolution, according to the user manual². The fitting of spectra with a lower resolution has systematically provided higher effective temperatures by about 500 K and higher surface gravities by about 0.2 dex. This partially explains the differences in the derived parameters.

Similarly, Moehler et al. (2011) found a higher effective temperature for vEHB-2. However, these authors used spectra with shorter interval of wavelengths. Our tests have shown that this can lead to differences in the effective temperature of about 1000 K and surface gravity of about 0.1 dex. This could be one of the reasons behind the differences in the determined parameters.

The effective temperature and surface gravity were derived from the fits of models with underabundances of heavier elements, although we do see that iron shows an overabundance with respect to the solar value (Table 3). Moehler et al. (2000) alleviated this problem by using models with higher abundances of iron. However, the comparison of spectra from the BSTAR2006 grid (Lanz & Hubeny 2007), with different iron abundances, showed nearly identical hydrogen line profiles. Therefore, we conclude that this is not a significant problem for the parameter determination presented here.

Two of the variable horizontal branch stars detected by Momany et al. (2020) in NGC 6752 were subsequently analyzed by Latour et al. (2023). It turned out that only one of them is a genuine horizontal branch star, while the other was instead classified as a blue straggler. The horizontal branch star has very similar atmospheric parameters as obtained here and it also has a slightly lower mass than typical for horizontal branch stars (Fig. 14, Latour et al. 2023), albeit higher than that derived here.

6.3. Line variability

We detected variability among the helium and calcium lines, which is also likely to be phased with the variability period (Figs. 7 and 8). Such variability may indicate presence of spots. However, our tests have shown that the abundances are too low to cause any significant light variability (Sect. 5.2). Classically peculiar stars may show vertical abundance gradients in the atmosphere (e.g., LeBlanc et al. 2009; Khalack 2018), but this would not help to explain the light variability because the

² <https://www.eso.org/sci/facilities/paranal/instruments/fors/doc.html>

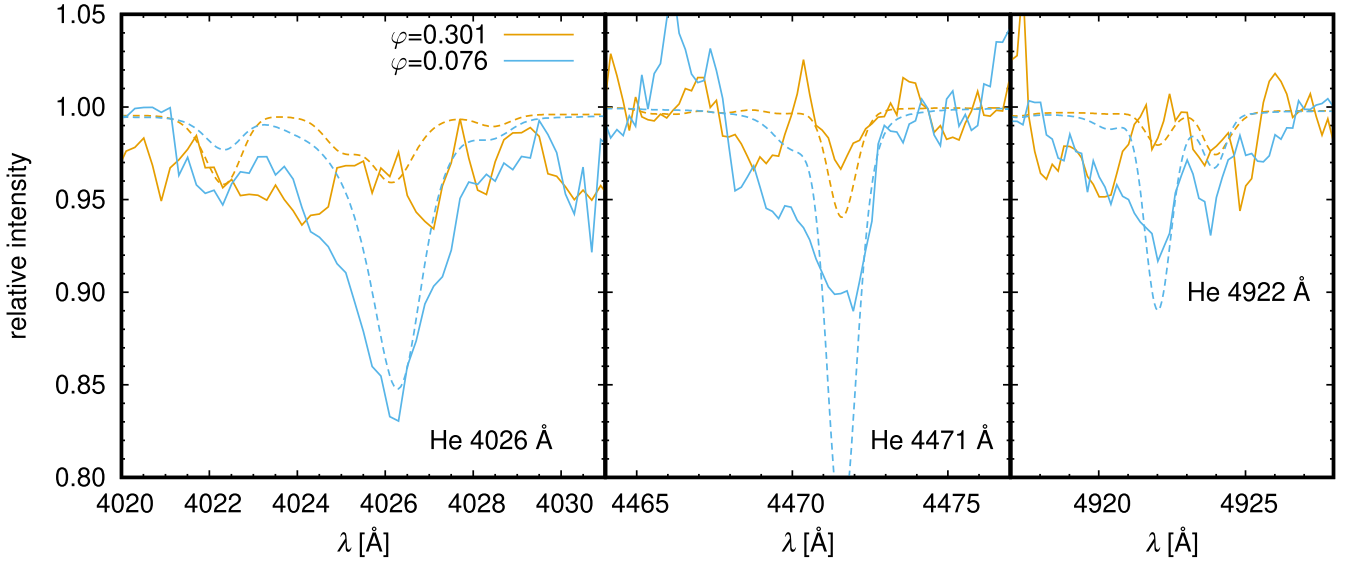


Fig. 7. Comparison of observed (solid lines) and predicted (dashed lines) helium line profiles for two different phases in the spectra of vEHB-3.

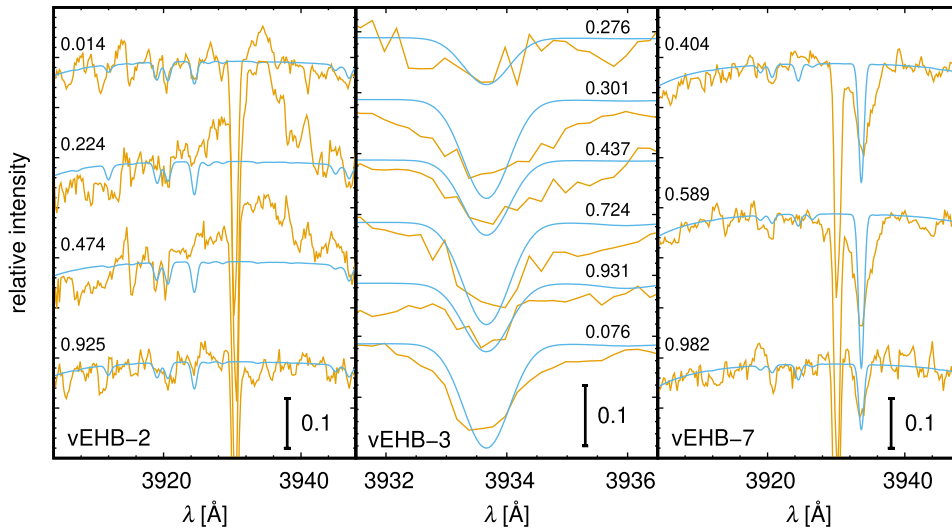


Fig. 8. Phase variability of Ca II 3934 Å line. Plotted for individual studied stars for all phases (denoted in the graph). The plot compares observed spectra (yellow lines) with predicted spectra (blue lines). The vertical scale denotes fraction of the continuum intensity. The spectra were shifted to the stellar rest frame.

opacity in the continuum-forming region is decisive. Moreover, the line profiles are unusually broad in some cases and the calcium line may even appear in the emission. This is the case for the star vEHB-2 (Fig. 8). In addition, emission is also likely to appear in one spectrum of vEHB-7, which was not included in the present analysis due to its low S/N.

The unusual variability of these lines and the appearance of emission could be perhaps connected with shocks that propagate throughout the stellar atmosphere as a result of pulsational motion (Schwarzschild et al. 1948; Jeffery et al. 2022). The shock may possibly heat the atmosphere and induce the emission in the Ca II 3934 Å line. The shock appears around the phase of minimum radius (maximum gravity), which agrees with spectroscopy of vEHB-2 (Fig. 8).

6.4. Evolutionary considerations

To better constrain the nature of the light variability of the studied stars, we simulated their internal structure using the MESA

code³ (Paxton et al. 2019; Jermyn et al. 2023). We selected a model star with an initial mass of $2.2 M_{\odot}$, which starts to burn helium at the moment when the core mass is close to the mass of the stars used in this study (Han et al. 2002).

We simulated the evolution of a star from the pre-main sequence until the initiation of helium-burning in the core. By setting the mass fraction of heavy elements to $Z = 0.0006$ and incorporating convective premixing and the Ledoux criterion⁴, we ensured a similar representation of the stellar conditions. Compared to standard models, we also included silicon and iron elements to account for the essential constituents found from observations. Afterward, we stripped the star's envelope, leaving behind only the helium-core enveloped by a hydrogen-rich outer layer with mass of $0.01 M_{\odot}$. This process allowed us to imitate the physical structure found in horizontal branch stars. We also

³ We used MESA version 22.11.1.

⁴ For reference see <https://docs.mesastar.org/en/latest/index.html>

evolved a similar model star with an additional accreted mass of $0.001 M_{\odot}$ mirroring the composition of the surface material deduced in vEHB-2.

Our approach is similar to the work of Han et al. (2002) and gives comparable effective temperatures (25–30 kK) and surface gravities ($\log g \approx 5.5$) during the helium-burning phase. Contrary to Han et al. (2002), who were able to create the lowest mass helium-burning star with a zero-age main sequence mass of $1.8 M_{\odot}$ for $Z = 0.004$, we found that our models did not allow us to use such a low initial mass. This suggests that compactness of the inner core was greatly affected by including the heavy elements, thereby creating helium or hydrogen flashes for lower initial masses.

We noticed a notable disparity between the non-accreted and accreted models. While the models with near solar helium fraction ($Y = 0.24$) displayed a convection layer near the surface, the layer disappeared after the accretion of helium-poor material. Therefore, models do not predict any subsurface convective region for a chemical composition derived from observations.

Alternatively, the parameters of the stars correspond to stars in the post-red giant evolutionary state (Hall et al. 2013). In that case, the variability of studied stars could be connected with instability of hydrogen-burning on the surface of a degenerate core (Shen & Bildsten 2007), which could lead to periodic behavior (Jose et al. 1993).

6.5. Random and systematic errors

Random errors among the parameters in individual phases were determined using the Monte Carlo method. However, there might be certain errors in the analysis that could not be described by random errors. To better assess the statistical significance of the results, we searched the ESO X-shooter archive for multiple observations of subdwarfs. We focused on subdwarfs listed in the catalog from Geier (2020), which have similar parameters to those of the horizontal branch stars studied here.

We selected the field hot subdwarf EC 01510-3919, which has four spectra from two nights available in total. We analyzed the spectra in the same way as we did for horizontal branch stars. The analysis provided $T_{\text{eff}} = 20440 \pm 90$ K and $\log g = 4.73 \pm 0.02$, in a good agreement with parameters determined by Lisker et al. (2005).

The maximum differences between effective temperature and surface gravity estimates from individual spectra were about 200 K and 0.03 dex, respectively. Although the S/N of the spectra is roughly a factor of two higher than for globular cluster stars, this further demonstrates that the detected variations of the effective temperature and surface gravity are likely to be real. Moreover, the analysis also shows that the mismatch between observed and fitted variations of surface gravity of vEHB-7 could be of a random origin.

We studied the effect of continuum normalization on the uncertainty of parameters. To test the influence of normalization, we multiplied the absolute data by a smooth function and repeated the analysis again (including normalization). This had a small effect on the derived parameters. We performed additional tests by restricting the number of lines used for the analysis. This also led to similar variations as those we detected, albeit with a larger scatter.

Unlike the random errors considered here, the systematic errors are much more difficult to estimate. They may be connected with uncertainties of parameters such as oscillator strengths, NLTE model ions, continuum placement, and selection of lines for the analysis (Przybilla et al. 2000).

The systematic errors can be roughly estimated from a comparison of derived parameters with independent estimates from the literature, which gives an error of about 1000 K in the effective temperature, and 0.1 dex in the surface gravity and abundances. However, unlike the random errors, the systematic errors affect all the measurements in approximately the same way. Therefore, because this study is focused mainly on the origin of the light variability connected to differences among individual spectra, the systematic errors are of a lesser importance.

7. Conclusions

We analyzed the phase-resolved spectroscopy of three periodically variable extreme horizontal branch stars from the globular cluster ω Cen that were detected by Momany et al. (2020). We determined the effective temperatures, surface gravities, and abundances in individual photometric phases.

We detected the phase variability of the apparent effective temperature and surface gravity. The effective temperature is the highest during the light maximum. We did not detect any strong variability of abundances that could explain the observed photometric variations; neither did we detect any significant radial velocity variations that could point to the binarity. Instead, the photometric and spectroscopic variability can be interpreted in terms of pulsations. This is additionally supported by the anomalous profiles of helium and calcium lines that point to intricate atmospheric motions. The effective temperatures of these stars, 21–25 kK, and the surface gravity correspond to extension of PG 1716 stars or blue, high-gravity, large-amplitude pulsators toward lower temperatures, albeit with much longer periods. Given the effective temperature of these stars and the length of their periods, we propose that the pulsation of these stars are due to g modes initiated by the iron opacity bump. However, the length of the periods of the order of day is in strong conflict with Ritter’s law.

Surface temperature spots provide the only viable alternative explanation for the light variability. Nevertheless, the detection of surface gravity variations in studied stars and the existence of complex line profile variations of the helium and calcium lines offer additional support for the pulsational model.

The metal-deficient chemical composition of these stars corresponds to the horizontal branch of globular clusters. One exception is iron, with a roughly solar chemical composition that is perhaps due to radiative diffusion. On the other hand, helium has significantly subsolar abundance that is likely due to gravitational settling.

We estimated the masses of these stars from spectroscopy and photometry in the range of $0.2\text{--}0.3 M_{\odot}$. This value is too low for helium-burning stars, but similar estimates were obtained previously for horizontal branch stars.

Acknowledgements. We thank Dr. Yazan Momany for valuable comments on the paper and Dr. Petr Kurfürst for the discussion. Computational resources were provided by the e-INFRA CZ project (ID:90254), supported by the Ministry of Education, Youth and Sports of the Czech Republic.

References

- Aerts, C., Bowman, D. M., Simon-Díaz, S., et al. 2018, *MNRAS*, 476, 1234
 Ahmad, A., Freytag, B., & Höfner, S. 2023, *A&A*, 669, A49
 Alecian, G., & Stift, M. J. 2017, *MNRAS*, 468, 1023
 Althaus, L. G., Miller Bertolami, M. M., & Córscico, A. H. 2013, *A&A*, 557, A19
 Arancibia-Rojas, E., Zorotovic, M., Vučković, M., et al. 2024, *MNRAS*, 527, 11184

- Asplund, M., Grevesse, N., Sauval, A. J., & Scott, P. 2009, *ARA&A*, 47, 481
- Baran, A. S., Sahoo, S. K., Sanjayan, S., & Ostrowski, J. 2021, *MNRAS*, 503, 3828
- Battich, T., Miller Bertolami, M. M., Córscico, A. H., & Althaus, L. G. 2018, *A&A*, 614, A136
- Bono, G., Iannicola, G., Braga, V. F., et al. 2019, *ApJ*, 870, 115
- Bono, G., Braga, V. F., Fiorentino, G., et al. 2020, *A&A*, 644, A96
- Braga, V. F., Bono, G., Fiorentino, G., et al. 2020, *A&A*, 644, A95
- Brown, T. M., Landsman, W. B., Randall, S. K., Sweigart, A. V., & Lanz, T. 2013, *ApJ*, 777, L22
- Caiazzo, I., Burdge, K. B., Tremblay, P.-E., et al. 2023, *Nature*, 620, 61
- Calamida, A., Stetson, P. B., Bono, G., et al. 2005, *ApJ*, 634, L69
- Cantiello, M., & Braithwaite, J. 2011, *A&A*, 534, A140
- Cantiello, M., & Braithwaite, J. 2019, *ApJ*, 883, 106
- Cantiello, M., Lecoanet, D., Jermyn, A. S., & Grassitelli, L. 2021, *ApJ*, 915, 112
- Charpinet, S., Fontaine, G., Brassard, P., & Dorman, B. 1996, *ApJ*, 471, L103
- Chayer, P., Fontaine, G., & Wesemael, F. 1995, *ApJS*, 99, 189
- Chen, A. N., Moffat, A. F. J., Cameron, C., et al. 2011, *ApJ*, 735, 34
- Córscico, A. H., Althaus, L. G., Kepler, S. O., Costa, J. E. S., & Miller Bertolami, M. M. 2008, *A&A*, 478, 869
- Córscico, A. H., Romero, A. D., Althaus, L. G., Pelisoli, I., & Kepler, S. O. 2018, *ArXiv e-prints* [arXiv:1809.07451]
- Das, B., Chandra, P., Shultz, M. E., et al. 2022, *ApJ*, 925, 125
- David-Uraz, A., Owocki, S. P., Wade, G. A., Sundqvist, J. O., & Kee, N. D. 2017, *MNRAS*, 470, 3672
- Deal, M., Alecian, G., Lebreton, Y., et al. 2018, *A&A*, 618, A10
- Dorsch, M., Reindl, N., Pelisoli, I., et al. 2022, *A&A*, 658, L9
- Dupuis, J., Chayer, P., Vennes, S., Christian, D. J., & Kruk, J. W. 2000, *ApJ*, 537, 977
- Flower, P. J. 1996, *ApJ*, 469, 355
- Fossati, L., Kolenberg, K., Shulyak, D. V., et al. 2014, *MNRAS*, 445, 4094
- Freedman, W. L., & Madore, B. F. 1990, *ApJ*, 365, 186
- Fuller, J., & Mathis, S. 2023, *MNRAS*, 520, 5573
- Garcia, S., Van Reeth, T., De Ridder, J., & Aerts, C. 2022, *A&A*, 668, A137
- Geier, S. 2020, *A&A*, 635, A193
- Green, E. M., Fontaine, G., Reed, M. D., et al. 2003, *ApJ*, 583, L31
- Guo, J.-J. 2018, *ApJ*, 866, 58
- Gvaramadze, V. V., Langer, N., Fossati, L., et al. 2017, *Nat. Astron.*, 1, 0116
- Hall, P. D., Tout, C. A., Izzard, R. G., & Keller, D. 2013, *MNRAS*, 435, 2048
- Han, Z., Podsiadlowski, P., Maxted, P. F. L., Marsh, T. R., & Ivanova, N. 2002, *MNRAS*, 336, 449
- Heber, U. 2016, *PASP*, 128, 082001
- Heber, U., Napiwotzki, R., Lemke, M., & Edelmann, H. 1997, *A&A*, 324, L53
- Hümmerich, S., Paunzen, E., & Bernhard, K. 2016, *AJ*, 152, 104
- Jagelka, M., Mikulášek, Z., Hümmerich, S., & Paunzen, E. 2019, *A&A*, 622, A199
- Jeffery, C. S., & Saio, H. 2006, *MNRAS*, 371, 659
- Jeffery, C. S., & Saio, H. 2016, *MNRAS*, 458, 1352
- Jeffery, C. S., Baran, A. S., Behara, N. T., et al. 2017, *MNRAS*, 465, 3101
- Jeffery, C. S., Montañés-Rodríguez, P., & Saio, H. 2022, *MNRAS*, 509, 1940
- Jermyn, A. S., Anders, E. H., & Cantiello, M. 2022, *ApJ*, 926, 221
- Jermyn, A. S., Bauer, E. B., Schwab, J., et al. 2023, *ApJS*, 265, 15
- Jose, J., Hernanz, M., & Isern, J. 1993, *A&A*, 269, 291
- Kawka, A., & Vennes, S. 2016, *MNRAS*, 458, 325
- Khalack, V. 2018, *MNRAS*, 477, 882
- Kilic, M., Gianninas, A., Bell, K. J., et al. 2015, *ApJ*, 814, L31
- Kilkenny, D., Koen, C., O'Donoghue, D., & Stobie, R. S. 1997, *MNRAS*, 285, 640
- Kochukhov, O., & Ryabchikova, T. A. 2018, *MNRAS*, 474, 2787
- Kochukhov, O., Papakonstantinou, N., & Neiner, C. 2022, *MNRAS*, 510, 5821
- Krtička, J., & Štefl, V. 1999, *A&AS*, 138, 47
- Krtička, J., Kawka, A., Mikulášek, Z., et al. 2020a, *A&A*, 639, A8
- Krtička, J., Mikulášek, Z., Prvák, M., et al. 2020b, *MNRAS*, 493, 2140
- Krtička, J., Benáček, J., Budaj, J., et al. 2023, *Space Science Reviews*, submitted [arXiv:2306.15081]
- Kupfer, T., Ramsay, G., van Roestel, J., et al. 2017, *ApJ*, 851, 28
- Kupfer, T., Bauer, E. B., Burdge, K. B., et al. 2019, *ApJ*, 878, L35
- Landstreet, J. D., & Borra, E. F. 1978, *ApJ*, 224, L5
- Lanz, T., & Hubeny, I. 2003, *ApJS*, 146, 417
- Lanz, T., & Hubeny, I. 2007, *ApJS*, 169, 83
- Lanz, T., Artru, M. C., Le Dourneuf, M., & Hubeny, I. 1996, *A&A*, 309, 218
- Latour, M., Randall, S. K., Calamida, A., Geier, S., & Moehler, S. 2018, *A&A*, 618, A15
- Latour, M., Hämmerich, S., Dorsch, M., et al. 2023, *A&A*, 677, A86
- Leavitt, H. S. 1908, *Ann. Harvard College Observ.*, 60, 87
- LeBlanc, F., Monin, D., Hui-Bon-Hoa, A., & Hauschildt, P. H. 2009, *A&A*, 495, 937
- Lesh, J. R., & Aizenman, M. L. 1974, *A&A*, 34, 203
- Leto, P., Trigilio, C., Krtička, J., et al. 2021, *MNRAS*, 507, 1979
- Lisker, T., Heber, U., Napiwotzki, R., et al. 2005, *A&A*, 430, 223
- Michaud, G., Richer, J., & Richard, O. 2011, *A&A*, 529, A60
- Mikulášek, Z., Krtička, J., Henry, G. W., et al. 2011, *A&A*, 534, L5
- Miller Bertolami, M. M. 2016, *A&A*, 588, A25
- Miller Bertolami, M. M., Battich, T., Córscico, A. H., Christensen-Dalsgaard, J., & Althaus, L. G. 2020, *Nat. Astron.*, 4, 67
- Moehler, S., Sweigart, A. V., Landsman, W. B., & Heber, U. 2000, *A&A*, 360, 120
- Moehler, S., Dreizler, S., Lanz, T., et al. 2011, *A&A*, 526, A136
- Moehler, S., Landsman, W. B., Lanz, T., & Miller Bertolami, M. M. 2019, *A&A*, 627, A34
- Molnar, M. R. 1973, *ApJ*, 179, 527
- Molnár, L., Bódi, A., Pál, A., et al. 2022, *ApJS*, 258, 8
- Momany, Y., Zaggia, S., Montalto, M., et al. 2020, *Nat. Astron.*, 4, 1092
- Moni Bidin, C., Moehler, S., Piotto, G., et al. 2006, *A&A*, 451, 499
- Moni Bidin, C., Moehler, S., Piotto, G., Momany, Y., & Recio-Blanco, A. 2007, *A&A*, 474, 505
- Moni Bidin, C., Moehler, S., Piotto, G., Momany, Y., & Recio-Blanco, A. 2009, *A&A*, 498, 737
- Moni Bidin, C., Villanova, S., Piotto, G., Moehler, S., & D'Antona, F. 2011, *ApJ*, 738, L10
- Moni Bidin, C., Villanova, S., Piotto, G., et al. 2012, *A&A*, 547, A109
- Mowlavi, N., Saesen, S., Semaan, T., et al. 2016, *A&A*, 595, L1
- Neilson, H. R., Engle, S. G., Guinan, E. F., Bisol, A. C., & Butterworth, N. 2016, *ApJ*, 824, 1
- Nunes, S. P., Arbañil, J. D. V., & Malheiro, M. 2021, *ApJ*, 921, 138
- Oksala, M. E., Kochukhov, O., Krtička, J., et al. 2015, *MNRAS*, 451, 2015
- Østensen, R. H., Degroote, P., Telting, J. H., et al. 2012, *ApJ*, 753, L17
- Paunzen, E., Bernhard, K., Hümmerich, S., et al. 2019, *A&A*, 622, A77
- Paxton, B., Smolec, R., Schwab, J., et al. 2019, *ApJS*, 243, 10
- Pelisoli, I., Dorsch, M., Heber, U., et al. 2022, *MNRAS*, 515, 2496
- Peterson, D. M. 1970, *ApJ*, 161, 685
- Pietrukowicz, P., Dziembowski, W. A., Latour, M., et al. 2017, *Nat. Astron.*, 1, 0166
- Prvák, M., Liška, J., Krtička, J., Mikulášek, Z., & Lüftinger, T. 2015, *A&A*, 584, A17
- Przybilla, N., Butler, K., Becker, S. R., Kudritzki, R. P., & Venn, K. A. 2000, *A&A*, 359, 1085
- Quievy, D., Charbonneau, P., Michaud, G., & Richer, J. 2009, *A&A*, 500, 1163
- Ramiaramanantsoa, T., Moffat, A. F. J., Chené, A.-N., et al. 2014, *MNRAS*, 441, 910
- Randall, S. K., Calamida, A., Fontaine, G., Bono, G., & Brassard, P. 2011, *ApJ*, 737, L27
- Reed, M. D., Kilkenny, D., & Terndrup, D. M. 2006, *Balt. Astron.*, 15, 65
- Reindl, N., Bainbridge, M., Przybilla, N., et al. 2019, *MNRAS*, 482, L93
- Reindl, N., Islami, R., Werner, K., et al. 2023, *A&A*, 677, A29
- Ritter, A. 1879, *Annal. Phys.*, 243, 304
- Romero, A. D., Córscico, A. H., Althaus, L. G., Pelisoli, I., & Kepler, S. O. 2018, *MNRAS*, 477, L30
- Rusomarov, N., Kochukhov, O., & Lundin, A. 2018, *A&A*, 609, A88
- Saio, H., & Gautschi, A. 1998, *ApJ*, 498, 360
- Schwarzschild, M., Schwarzschild, B., & Adams, W. S. 1948, *ApJ*, 108, 207
- Shen, K. J., & Bildsten, L. 2007, *ApJ*, 660, 1444
- Sikora, J., David-Uraz, A., Chowdhury, S., et al. 2019, *MNRAS*, 487, 4695
- Skarka, M., Prudil, Z., & Jurcsik, J. 2020, *MNRAS*, 494, 1237
- Soltis, J., Casertano, S., & Riess, A. G. 2021, *ApJ*, 908, L5
- Torres, G. 2010, *AJ*, 140, 1158
- Townsend, R. H. D., & Owocki, S. P. 2005, *MNRAS*, 357, 251
- Townsend, R. H. D., Oksala, M. E., Cohen, D. H., Owocki, S. P., & ud-Doula, A. 2010, *ApJ*, 714, L318
- Trasco, J. D. 1972, *ApJ*, 171, 569
- Unglaub, K. 2008, *A&A*, 486, 923
- Unglaub, K., & Bues, I. 2000, *A&A*, 359, 1042
- Unglaub, K., & Bues, I. 2001, *A&A*, 374, 570
- van de Ven, G., van den Bosch, R. C. E., Verolme, E. K., & de Zeeuw, P. T. 2006, *A&A*, 445, 513
- Vasilyev, V., Ludwig, H. G., Freytag, B., Lemasle, B., & Marconi, M. 2018, *A&A*, 611, A19
- Vernet, J., Dekker, H., D'Odorico, S., et al. 2011, *A&A*, 536, A105
- Vick, M., Michaud, G., Richer, J., & Richard, O. 2011, *A&A*, 526, A37
- Wolf, V. M., & Jeffery, C. S. 2002, *A&A*, 395, 535
- Wu, T., & Li, Y. 2018, *MNRAS*, 478, 3871
- Xiong, H., Casagrande, L., Chen, X., et al. 2022, *A&A*, 668, A112
- Yoshida, S. 2019, *MNRAS*, 486, 2982
- Zverko, J., Žižňovský, J., Mikulášek, Z., & Iliev, I. K. 2007, *Contrib. Astron. Observ. Skalnaté Pleso*, 37, 49

Appendix B

White dwarf-open cluster associations based on Gaia DR2

White dwarf-open cluster associations based on *Gaia* DR2

M. Prišegen, M. Piecka, N. Faltová, M. Kajan, and E. Paunzen

Department of Theoretical Physics and Astrophysics, Faculty of Science, Masaryk University, Kotlářská 2, 611 37 Brno, Czech Republic
e-mail: michalprisegen@gmail.com

Received 27 August 2020 / Accepted 13 October 2020

ABSTRACT

Context. Fundamental parameters and physical processes leading to the formation of white dwarfs (WDs) may be constrained and refined by discovering WDs in open clusters (OCs). Cluster membership can be utilized to establish the precise distances, luminosities, ages, and progenitor masses of such WDs.

Aims. We compile a list of probable WDs that are OC members in order to facilitate WD studies that are impractical or difficult to conduct for Galactic field WDs.

Methods. We use recent catalogs of WDs and OCs that are based on the second data release of the *Gaia* satellite mission (GDR2) to identify WDs that are OC members. This crossmatch is facilitated by the astrometric and photometric data contained in GDR2 and the derived catalogs. Assuming that most of the WD members are of the DA type, we estimate the WD masses, cooling ages, and progenitor masses.

Results. We have detected several new likely WD members and reassessed the membership of the literature WDs that had been previously associated with the studied OCs. Several of the recovered WDs fall into the recently reported discontinuity in the initial-final mass relation (IFMR) around $M_i \sim 2.0 M_\odot$, which allows for tighter constraints on the IFMR in this regime.

Key words. open clusters and associations; general – white dwarfs – catalogs – surveys

1. Introduction

White dwarfs (WDs) are the evolutionary endpoint of low- and intermediate-mass stars, which constitute a vast majority of all stars in the Galaxy. Their nature as compact and dense stellar remnants has been an important test bed for many areas of fundamental physics and stellar evolution theories. However, the study of WDs has been hampered by their low brightness, meaning that only observations of the closest objects could yield reliable results (see, e.g., Liebert 1980; Althaus et al. 2010; Córscico et al. 2019, for a general review).

White dwarfs associated with star clusters are extremely valuable. Star clusters are groups of gravitationally bound stars born in the same star-forming event, thus sharing the same age, metallicity, distance from the Sun, and proper motion. Since the WD cluster members also share these characteristics, this allows for a number of interesting questions to be addressed. Perhaps the most fundamental is the initial-final mass relation (IFMR), which links the final mass of a WD to the initial mass of its progenitor, hence also providing the total amount of mass lost during the stellar evolution. The progenitor mass can be estimated by determining the cooling age of a WD and subtracting it from the total age of the cluster as determined from the observations of the non-WD cluster members. This yields the lifetime of the WD progenitor, which can then be converted into the progenitor initial mass. Knowledge of the IFMR has applications in many areas of astrophysics. Perhaps one of the most fundamental applications of the high-mass end of the IFMR is determining the minimum main sequence stellar mass for a core-collapse supernova (SN) to occur. The IFMR is also an important ingredient in the modeling of stellar feedback in galaxy simulations and predicting SN type Ia rates (e.g., Greggio 2010; Agertz & Kravtsov

2015; Cummings 2017). Aside from the IFMR, other possible avenues of research utilizing cluster WDs include studying the effects of metallicity and binarity on WD evolution and measuring WD masses using gravitational redshift (Pasquini et al. 2019). Such studies are impossible or very challenging to conduct for Galactic field WDs.

While isolated WDs in globular clusters are very faint due to the considerable distances of these objects, the impetus for discovering WDs in open clusters (OCs) in the solar neighborhood is clear, as these OCs usually have well-determined parameters such as distance, reddening, age, and metallicity, providing a unique laboratory for studying the WDs associated with them and the related physical processes. This potential was realized early on when the Hyades cluster was studied by Tinsley (1974) and van den Heuvel (1975). More WD-cluster pairs were investigated by Weidemann (1977) and Romanishin & Angel (1980). Follow-up studies by Koester & Reimers (1981, 1985, 1993), Reimers & Koester (1982, 1988, 1989, 1994) obtained the spectroscopy of the WD candidates from Romanishin & Angel (1980), confirming some of them as bona fide cluster WDs and deriving their physical parameters. Since then, several other WD-OC pairs have been discovered and investigated by various authors and working groups (e.g., Anthony-Twarog 1982; Richer et al. 1998; Claver et al. 2001; Williams 2002). A recent compilation of OC WDs can be found in Cummings et al. (2018).

Past studies were limited by the small fields of view of the photometric surveys, which usually only covered the core OC regions. Another caveat was significant field WD contamination. To differentiate between the cluster and field WDs in the same area of the sky, accurate parallax and proper motion measurements of WDs were needed. The situation has

improved since the publication of the second data release of the *Gaia* mission (GDR2; [Gaia Collaboration 2016, 2018b](#)), which contains precise astrometry (positions, parallaxes, and proper motions) as well as photometry in three bands (G , G_{BP} , and G_{RP}). Since the advent of *Gaia*, the knowledge and census of Galactic OCs have also been substantially furthered (e.g., [Gaia Collaboration 2017](#); [Cantat-Gaudin et al. 2018a,b](#)). Furthermore, a large number of new WDs have been discovered and characterized ([Gentile Fusillo et al. 2019](#)), including WDs in OCs (e.g., [Salaris & Bedin 2018, 2019](#); [Richer et al. 2019](#)).

Due to recent increases in the number of known WDs and OCs with reliable parameters and astrometry, it has become possible to conduct a systematic search for WDs that are members of nearby OCs. In this paper, we crossmatch the known WDs and WD candidates listed in the catalog of [Gentile Fusillo et al. \(2019\)](#) with the OCs from [Cantat-Gaudin et al. \(2018a\)](#), using positional, parallax, and proper motion criteria. The physical reality of the putative WD-OC pairs are then further investigated using the cluster parameters (distance modulus, age, and reddening) and the position of the WD on the corresponding cooling sequence.

This paper is structured as follows. In Sect. 2, we describe the catalogs used in this study, the star cluster parameters, and the workflow leading to the selection of the WD OC member candidates. In Sect. 3, we discuss the recovered OCs hosting WDs and compare our detections with the literature, where available. The quality of GDR2 astrometric solutions and photometry for the recovered WDs are examined in Sect. 4. The WD masses and cooling ages are estimated in Sect. 5, and their application for the IFMR is addressed in Sect. 6. Finally, we summarize and add concluding remarks in Sect. 7.

2. Data analysis

The WD and OC catalogs that form the basis of this work are based on GDR2; therefore, they should be directly comparable, with no systematic offsets between them. The catalog of WD and WD candidates of [Gentile Fusillo et al. \(2019\)](#) lists over 480 000 objects, approximately 260 000 of which are high-probability WDs. Due to the intrinsic faintness of many isolated WDs, the majority of them are found within 1 kpc of the Sun, as can be seen in Fig. 1. This is in contrast with the distance distribution of the OCs from [Cantat-Gaudin et al. \(2018a\)](#); containing 1229 OCs), which is approximately uniform in the interval from 0.5 to 4 kpc; however, there is a notable paucity of OCs with distances ≤ 0.5 kpc. More than half of the cataloged WDs lie within this distance, with their distance distribution peaking at ~ 170 pc.

As can be seen in Fig. 1, the distribution of the parallax and proper motion errors of WDs and OC member stars listed in [Cantat-Gaudin et al. \(2018a\)](#) is also markedly different. The reason for this is two-fold. Firstly, the stars utilized to compute overall cluster astrometric parameters, which are also listed in [Cantat-Gaudin et al. \(2018a\)](#), are all brighter than $G > 18$ mag, whereas WDs from [Gentile Fusillo et al. \(2019\)](#) are much fainter by comparison, with a median brightness of $G_{WD} \approx 20$ mag. Such a jump in G leads to considerably larger errors for WDs ([Lindegren et al. 2018](#)). The second reason is that WDs are typically bluer in color than most stars in the GDR2. Blue objects observed by *Gaia* also exhibit increased errors in proper motion and parallax¹.

¹ <https://www.cosmos.esa.int/web/gaia/science-performance>

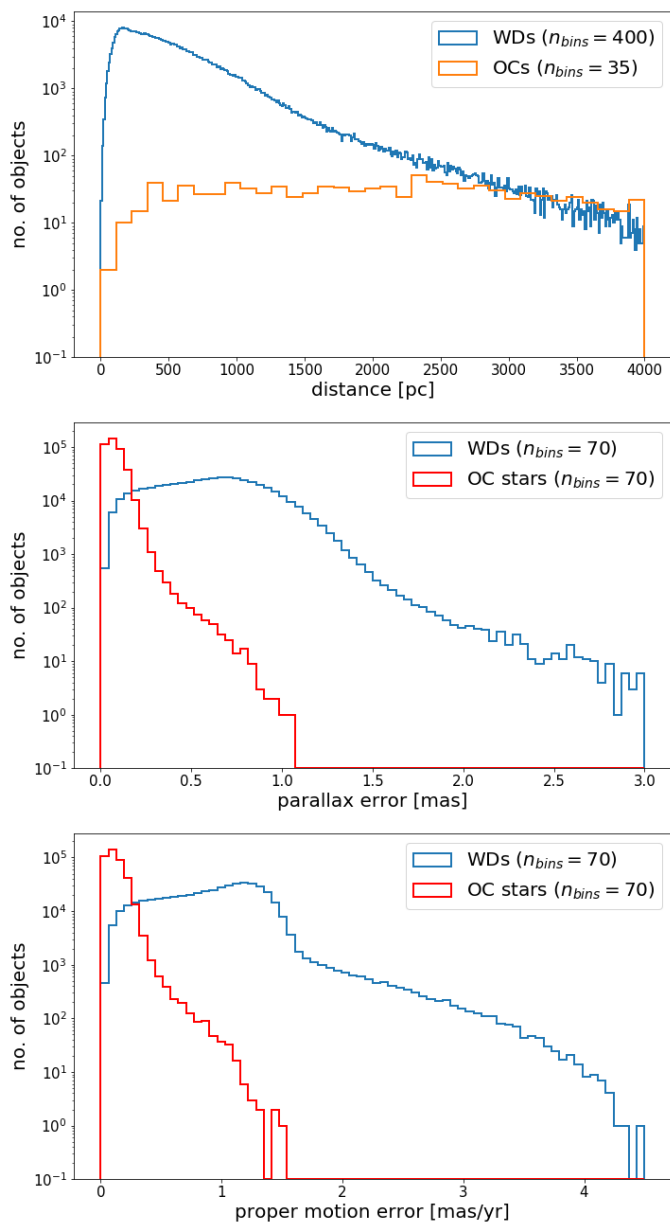


Fig. 1. *Top:* distance distribution of WDs from the catalog of [Gentile Fusillo et al. \(2019\)](#) compared to the distribution of OCs listed in [Cantat-Gaudin et al. \(2018a\)](#). *Middle:* comparison of the parallax error distribution of the WDs and OC member stars listed in [Cantat-Gaudin et al. \(2018a\)](#). *Bottom:* comparison of the average proper motion error (average of the RA and Dec components) of the WDs and OC members.

Due to these factors, using only the astrometric criteria (relying on positions, parallaxes, and proper motions) will yield a lot of low-confidence or spurious WD-OC matches. The most common such case is erroneous matches where a nearby WD gets matched with a more distant OC.

2.1. WD-OC pair preselection

Despite the shortcomings discussed above, the astrometric data are still potent when assigning potential WD members to OCs, especially when no such data of this quality and scope were available before GDR2. In order to make a rough preliminary preselection of potential cluster WDs, we utilized the

positional, proper motion, and parallax information contained in Cantat-Gaudin et al. (2018a) and Gentile Fusillo et al. (2019). The matching criteria are as follows:

$$\theta < 4.5 \times r50 \quad (1)$$

$$(plx - 3 \times s_plx; plx + 3 \times s_plx)_{OC} \cap (Plx - 3 \times e_Plx; Plx + 3 \times e_Plx)_{WD} \neq \emptyset \quad (2)$$

$$(pmRA - 3 \times s_pmRA; pmRA + 3 \times s_pmRA)_{OC} \cap (pmRA - 3 \times e_pmRA; pmRA + 3 \times e_pmRA)_{WD} \neq \emptyset \quad (3)$$

$$(pmDE - 3 \times s_pmDE; pmDE + 3 \times s_pmDE)_{OC} \cap (pmDE - 3 \times e_pmDE; pmDE + 3 \times e_pmDE)_{WD} \neq \emptyset. \quad (4)$$

Equation (1), where θ is the angular distance from a WD to a center of the cluster, represents the positional condition. Cantat-Gaudin et al. (2018a) list $r50$, which is the cluster radius that contains half of the cluster members, as the dimension of the studied clusters. In order to ensure search completeness, we considered WDs with projected separations up to $4.5 \times r50$ from the given cluster center. Next, Eq. (2) represents the parallax (distance) constraint. We considered every WD-cluster pair that satisfies this condition, where the WD has a parallax value of Plx and an associated error e_Plx from Gentile Fusillo et al. (2019; adopted directly from the GDR2) and the OC has a mean parallax of plx and a standard deviation of parallax of OC members s_plx from Cantat-Gaudin et al. (2018a). Lastly, Eqs. (3) and (4) are proper motion constraints. Again, Gentile Fusillo et al. (2019) adopt proper motion values and errors directly from the GDR2. For OCs, $pmRA$ ($pmDE$) is the mean proper motion along the right ascension (declination) of OC members, and s_pmRA (s_pmDE) is its standard deviation.

Such a selection yields almost 4000 distinct WD-OC pairs. Naturally, due to the problems with the WD astrometry outlined in Sect. 2 and the generous selection criteria applied, most of these pairs are low-probability and are only spurious pairings. Given the nature of the WD astrometry, it is normally not sufficient to rely on astrometric data alone to determine membership. Further investigations can be conducted using cooling models in conjunction with cluster ages.

2.2. Isochrones and white dwarfs

One of the most important parameters describing stellar clusters is their age. With the use of photometric data available for the cluster members, the age of the cluster is usually found with the help of an isochrone fitting method. First, isochrones need to be calculated, which can be done with evolutionary models for stars of different masses. In the case that a correct age and metallicity are chosen (together with the distance and the extinction), the resulting isochrone should coincide with the distribution of cluster members in the color-magnitude diagram (CMD). Due to its dependence on all four cluster parameters, this method is very useful for improving distance and extinction while determining age and metallicity (although metallicity is often ignored and assumed to be solar). This whole process is a necessary step because of the fact that we are attempting to assign WDs to clusters. In this section, our goal is to show the quality of the cluster parameters derived from isochrone fitting techniques that have (mostly) been published in recent years. Furthermore, the method used to compute values for the WDs displayed in the CMD (in *Gaia* magnitudes) is described.

Table 1. Sources for cluster parameters.

Source of parameters	Number of OCs
Bossini et al. (2019)	67
Kharchenko et al. (2013)	81
Dias et al. (2002)	2
Röser et al. (2016)	3
Custom fit	98

To verify our assignment of WDs to the sample of OCs, we need to take a look at the CMDs that show both the cluster members and the WDs. Moreover, we need to acquire cluster parameters (distance, extinction, and age, excluding metallicity) for all clusters in our sample. The newest data set provided by Bossini et al. (2019) contains the required parameters for 269 clusters, which are based on the data from the GDR2. Unfortunately, not all of these clusters coincide with those from our sample. For this reason, we decided to also make use of the data provided by Kharchenko et al. (2013) We took parameters from Dias et al. (2002) and Röser et al. (2016) as secondary sources of data if a cluster is not present in either of the two previous data sets.

Closer inspection of the individual CMDs then helped us determine which of the data sets gives a better isochrone fit to a given cluster. For our purposes, we decided to use CMD 3.3, the isochrone data from Evans et al. (2018), an assumed solar metallicity ($Z = 0.02$), and a chosen time-step $\Delta \log T = 0.05$. We favored this metallicity value because it has been shown to be consistent with recent results of helioseismology (Vagnozzi 2019). Together with information about cluster members from Cantat-Gaudin et al. (2018a) and the sets of cluster parameters, we can make a comparison between the corresponding isochrones. It is immediately clear from the plots that many of the clusters were assigned parameters that correspond to isochrones that do not match these clusters well enough. Our criterion for picking the parameters from the available data was to get the best isochrone fit. For the most part, values from Bossini et al. (2019) and Kharchenko et al. (2013) provide the best descriptions of the clusters (for example, Fig. 2), with parameters of only five clusters being taken from the secondary data sets. However, there are also many examples (about one-third of the whole sample) of clusters for which it was impossible to get an acceptable fit using data from any of the mentioned works.

For these cases, we fit the isochrones of all the individual clusters, using the photometric data of stars with membership probabilities larger than 50%. This was done without any black box algorithm. The metallicity was again assumed to be solar and kept fixed. Then, the reddening was determined using the shape of the main sequence. As a last step, the distance modulus was chosen so that the main sequence and turnoff point fit satisfyingly within the isochrone grid. The total final result for cluster parameters can be seen in Table 1.

The next task was fairly simple: determine the position of the WDs in the CMDs. To do this properly, we had to be able to subtract the extinction from the *Gaia* magnitudes. Since the extinction is usually described by either the A_V or R_V parameters (we assumed that $A_V = \frac{E(B-V)}{0.324}$) and we want to make use of GDR2 data, we needed to know the transformations between extinction in A_G (A_{BP} , A_{RP}) and A_V . It is not viable to use the simple approach $A_G = 0.835 A_V$ due to the width of the *Gaia*

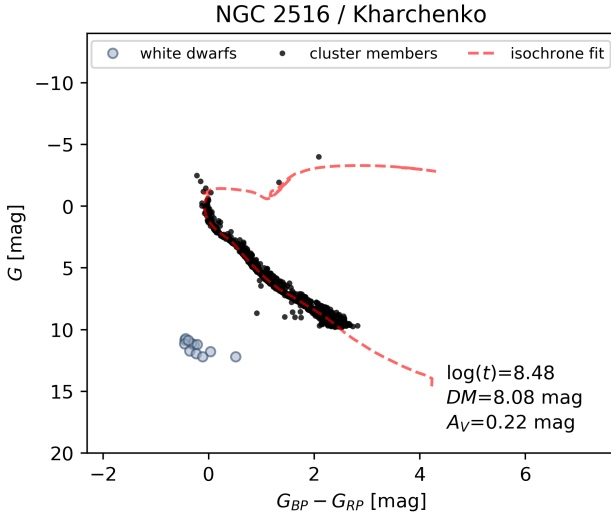


Fig. 2. Example of a cluster (NGC 2516) in the CMD with members taken from [Gentile Fusillo et al. \(2019\)](#) and fit with an isochrone (parameters from [Kharchenko et al. 2013](#)). Our initial candidate WDs are displayed in the plot together with the cluster parameters (age, reddened distance modulus, and extinction).

passbands. For our purposes, we decided to use the polynomial combination of $(G_{BP} - G_{RP})$ and A_V values that is described in [Gaia Collaboration \(2018a\)](#).

As mentioned before, we only employed isochrones with solar metallicity (i.e., $Z = 0.02$). To investigate the effect of the metallicity on the cluster parameters derived from isochrone fitting, the range of the metallicity in the solar vicinity has to be assessed. [Netopil et al. \(2016\)](#) present homogenized metallicities for 172 OCs on the basis of photometric and spectroscopic data. More recent studies using optical ([Pancino et al. 2017](#)) or infrared ([Donor et al. 2018](#)) spectroscopy have not added a significant number of new investigated OCs. Furthermore, these results are very much in line with those from [Netopil et al. \(2016\)](#). These last authors have showed that almost all OCs within 2 kpc of the Sun have $[\text{Fe}/\text{H}] = \pm 0.2$ dex. There are hardly any known Galactic OCs that exceed a $[\text{Fe}/\text{H}]$ value of ± 0.5 dex. The isochrones up to $[\text{M}/\text{H}] = \pm 1.0$ dex are shifted in the distance modulus only. This means that, for the same color, stars become fainter for lower metallicities. We used the turnoff points for the whole isochrone grid to investigate the concrete values. As a conclusion, it can be said that for $[\text{M}/\text{H}]$ up to ± 1.0 dex, the differences of the distance modulus scales are one-to-one with metallicity (i.e., $\Delta[\text{M}/\text{H}] \approx \Delta DM$). This shift is negligible compared to the width of the main sequence and the intrinsic errors of the parallaxes. Therefore, using an isochrone grid with solar metallicity is a justifiable approach.

Finally, we wanted to compare the calculated extinction values A_G with those provided by [Gentile Fusillo et al. \(2019\)](#). Assuming that $A'_G = 0.835 A_V$, they give

$$A_G = A'_G \left(1 - \exp\left(-\frac{\sin |b|}{200\varpi}\right) \right),$$

$$A_{(BP-RP)} = 0.586 A'_G \left(1 - \exp\left(-\frac{\sin |b|}{200\varpi}\right) \right),$$

as the effective values of the extinction coefficients, where b is the Galactic latitude of the WD and ϖ is its parallax (in arcseconds). We can see that the relation between the two results is not one-to-one (Fig. 3). However, this is to be expected since both

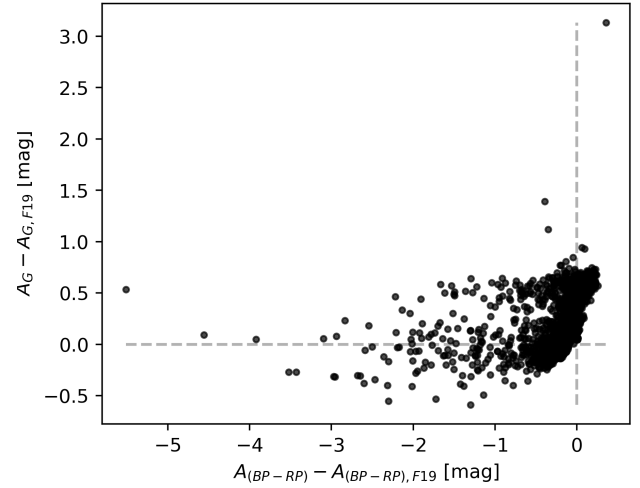


Fig. 3. Comparison of the extinction values A_G and A_{BP-RP} between this work and [Gentile Fusillo et al. \(2019\)](#).

approaches use a different version of the extinction law. What remains uncertain in our case is the applicability of the transformation described in [Gaia Collaboration \(2018a\)](#) since their coefficients were derived with the use of stars with estimated effective temperatures $T_{\text{eff}} \lesssim T_{\text{eff,WD}}$ and it is unknown what order of magnitude of errors is produced at the higher temperature regime ($> 10\,000$ K).

2.3. CMD and cooling age-based filtering

Provided that accurate cluster ages, distances (parallaxes), and extinction values are available, it is possible to use photometry to filter out spurious WD-OC pairings. In order to do this, we used the cluster parameters as obtained in the previous section and Montreal WD cooling tracks² ([Fontaine et al. 2001](#)).

For our initial sample of several hundred putative WD-OC pairings, we used the distance moduli and extinctions of the matched OCs to compute the dereddened absolute magnitudes and colors for the corresponding WDs. We plot these quantities with the theoretical cooling tracks for the lowest- ($0.2 M_{\odot}$) and highest-mass ($1.2 M_{\odot}$) WDs in Fig. 4. In order for a WD-OC pairing to be physical (provided that the WD is not in a binary), it is necessary (but not sufficient) for a WD to lie in the CMD region delineated by the lowest- and highest-mass cooling tracks. It is apparent that the majority of the potential OC WDs lie above the lowest-mass cooling track, being more luminous than what would be expected if they were OC members. This was expected (see the discussion in Sect. 2), as these WDs tend to be in the foreground of the OCs and are spuriously matched to them due to the generous selection criteria and substantial errors in parallax and proper motions.

Further constraints can be made using the age of the OC matched with a WD. Obviously, the cooling age of the WD cannot be higher than the age of the OC it is associated with, provided that the association is real. Using this, other spurious WD-OC pairs can be filtered out on an individual basis using additional cuts in the CMD diagrams. If the cluster age is known, a WD that is associated with the cluster should lie in the CMD region delineated by the lowest- and highest-mass cooling track (as discussed above), the zero-age cooling isochrone, and the cooling isochrone corresponding to the cluster age.

² <http://www.astro.umontreal.ca/~bergeron/CoolingModels>

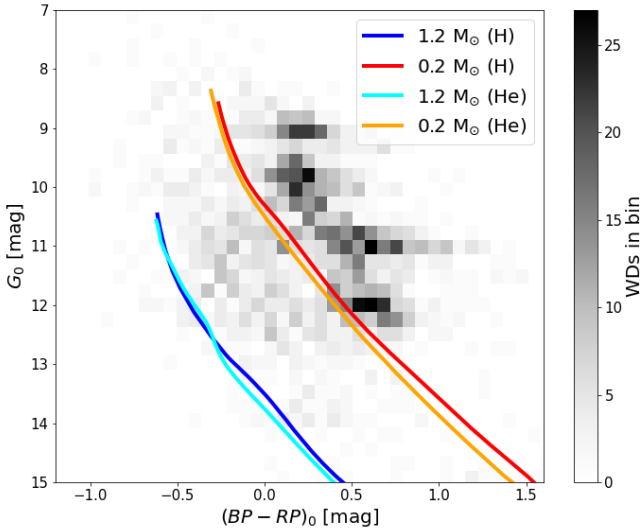


Fig. 4. 2D density WD histogram obtained from the initial WD sample in the absolute magnitude-color space. The absolute magnitudes and colors for each WD are calculated using the parameters of the cluster of which the WD is a member candidate. Overlaid are the Montreal WD cooling tracks for low-mass and high-mass WDs with H and He atmospheres.

3. Notes on the individual WD-OC pairs

In this section, we list and discuss the obtained OC-WD candidate pairs that passed the astrometric, photometric, and cooling age criteria as described in the previous sections. The figures that illustrate the placement of the WD candidates in the cluster CMD and astrometric phase space are included in the appendix; however, some of the more interesting examples are discussed in this section.

3.1. ASCC 73, ASCC 79, and ASCC 97

ASCC 73, ASCC 79, and ASCC 97 are three OCs discovered in [Kharchenko et al. \(2005\)](#). Due to their relatively recent discovery and sparse nature, they have been studied very little in the literature. No studies of WDs potentially hosted by these clusters have been conducted to date.

Our analysis has recovered one potential cluster WD: GDR2 5856401252012633344 for ASCC 73. On face value, it seems to be a mild outlier from the other cluster members as cataloged by [Cantat-Gaudin et al. \(2018a\)](#), both in terms of proper motion and parallax. However, considering the astrometric uncertainties of the WD candidate, it is still consistent with cluster membership.

For ASCC 79, we have found three possible cluster WDs: GDR2 5825203021908148480, 5826384584601681152, and 5825187834899772160. However, it needs to be noted that the probability of the last object being a WD, as given in [Gentile Fusillo et al. \(2019\)](#), is only $P_{wd} = 0.59$.

Gaia DR2 4092407537313874048 has been identified as a viable candidate for ASCC 97. While its astrometric properties are consistent with cluster membership, its WD nature is ambiguous ($P_{wd} = 0.47$ in [Gentile Fusillo et al. 2019](#)).

3.2. Alessi 3

Alessi 3 is a sparse evolved OC (or OC remnant; [Angelo et al. 2019](#)). Its WD content has not been studied before.

We have identified one cluster WD candidate: GDR2 5508976051738818176. Its astrometric properties are consistent with cluster membership, but its parallax puts it into the cluster background if taken at face value. However, the parallax error is very high, and a number of cluster members lie within 1σ of the cluster WD candidate's parallax.

3.3. Alessi 13

Alessi 13 (χ^{01} For moving group) is a sparse nearby stellar association. Its WD content has never been studied.

We have identified one possible WD cluster member: GDR2 4853382867764646912. Its astrometric properties are consistent with cluster membership.

3.4. Alessi 62

Alessi 62 is another unstudied old OC. No WDs that are potential members of this cluster are known.

Our analysis has yielded one cluster WD candidate: GDR2 4519349757791348480. Its proper motion is consistent with cluster membership; however, its parallax is more problematic as it suffers from a large uncertainty, and, if taken at face value, it puts the member candidate into the background. However, some of the cluster members are still contained within its 1σ uncertainty interval. Its nature as a bona fide WD is ambiguous since [Gentile Fusillo et al. \(2019\)](#) gives a lower $P_{wd} = 0.56$ for this object.

3.5. IC 4756

IC 4756 is a close, intermediate-age OC. Though IC 4756 has been heavily studied, WDs potentially hosted in the cluster have never been investigated in detail in the literature. However, it needs to be noted that by looking at the CMD of the cluster stars listed in [Cantat-Gaudin et al. \(2018a\)](#), one can readily identify a potential WD candidate on the cluster WD sequence. The WD is bright enough to not be excluded in the magnitude cutoff of $G = 18$ mag adopted there.

Our analysis has identified only one viable cluster WD candidate, and it is the same one as discussed above (GDR2 4283928577215973120). Its proper motion and parallax make it a very likely cluster member.

3.6. Mamajek 4

Mamajek 4 is a poorly studied OC. No WD studies targeting this cluster have been conducted.

Our search has identified one potential cluster WD: GDR2 6653447981289591808. Its proper motion is consistent with cluster membership, though its parallax indicates that it may be a background object. However, its parallax error is quite high and a significant portion of the cluster members lie within a 1σ error of the candidate parallax.

3.7. Melotte 22

Melotte 22 (Pleiades) is one of the closest, best-studied, and, arguably, most well-known OCs. Despite its proximity, only one cluster WD has been identified so far: EGGR 25 (GDR2 66697547870378368; [Eggen & Greenstein 1965](#); [Lodieu et al. 2019](#)).

Our analysis recovered EGGR 25. However, it failed to identify any new potential cluster WD candidates.

3.8. NGC 2422

NGC 2422 is a rather young (~ 150 Myr) OC with a current turnoff age of about $5.4 M_{\odot}$ (Richer et al. 2019). The potential WD content of the cluster was first investigated by Koester & Reimers (1981), who found a potential WD candidate (GDR2 3030026344167186304) that may also be a cluster member. However, they were not able to fully ascertain its nature; while it may be a massive WD that is a member of the cluster, it may also be a field WD behind the cluster or a subdwarf O-type star. Richer et al. (2019) find a massive cluster WD with a helium-rich atmosphere and large magnetic field, probably in a binary with a late-type companion (GDR2 3029912407273360512).

Our analysis only recovered the WD found by Richer et al. (2019), as the other one is not included in the catalog by Gentile Fusillo et al. (2019). However, taking advantage of GDR2 astrometry, it can clearly be seen that the WD member candidate of Koester & Reimers (1981) is most certainly not a cluster member and that it lies in the foreground.

3.9. NGC 2516

NGC 2516 is also a young OC that likely started forming WDs relatively recently. Reimers & Koester (1982) first identified three probable cluster WDs and later added a fourth, the nature of which was previously uncertain (Koester & Reimers 1996). Recently, Holt et al. (2019) have added two more candidate WD members, which were identified using the GDR2.

Our analysis of this cluster identified three sources, one of which was already identified in Reimers & Koester (1982) and the two others in Holt et al. (2019). Thus, no novel detections were made. The other three WDs from Reimers & Koester (1982) and Koester & Reimers (1996) are also included in Gentile Fusillo et al. (2019), but their cluster membership is not solid. GDR2 5290720695823013376 seems to lie in the foreground and GDR2 5290719287073728128 in the background; GDR2 5290834387897642624 is a proper motion outlier but just narrowly did not make the cut.

3.10. NGC 2527

NGC 2527 is an older (~ 800 Myr) OC with a turnoff mass of $\approx 2.2\text{--}3.5 M_{\odot}$ (Raddi et al. 2016). A WD that is also a likely cluster member was reported in Raddi et al. (2016).

We did not recover this WD (GDR2 5597874285564810880) as it is not listed in Gentile Fusillo et al. (2019). However, we identified a new candidate. Using the GDR2 astrometry, it can clearly be seen that the WD identified as a cluster member in Raddi et al. (2016) is a significant outlier in both parallax and proper motion, making it a likely field object.

3.11. NGC 2632

NGC 2632 (Praesepe) is a close and well-known OC with a large number of published WDs. It is considered to be a “benchmark” cluster for WD studies, and it is likely that the observed cluster single WD population is complete due to its proximity.

Our analysis recovered all 12 known cluster WDs with no new detections, as expected. A comprehensive analysis of these WDs in the context of their parent cluster is available in a recent analysis by Salaris & Bedin (2019) and the references therein.

3.12. NGC 3532

This rich, ~ 300 Myr old OC is believed to host a number of WDs. Reimers & Koester (1989) identified seven candidate cluster WDs and confirmed the degenerate nature of three of them. Their subsequent extended survey added three more candidate WD members later on (Koester & Reimers 1993). However, a more detailed analysis by Dobbie et al. (2009) put two of these WDs in the background of the cluster. An expanded survey by Dobbie et al. (2012) identifies several more WD candidates, including another four bona fide WDs in the direction of the cluster, three of which are reportedly cluster members. Furthermore, Raddi et al. (2016) add an additional, very massive WD cluster member.

A combined tally of seven cluster WDs, as obtained from the literature, makes the cluster appealing as one of the benchmark clusters, together with Hyades and Praesepe. However, our detection of only three WD candidate members is seemingly at odds with these reported WD numbers. Crossmatching these literature WDs with the GDR2 and querying them in the WD catalog by Gentile Fusillo et al. (2019), we found that only two of them are listed there: GDR2 5340219811654824448 and GDR2 5338718261060841472; the latter is also a cluster member according to our analysis. Our second identified cluster WD candidate is also among the cluster members reported in Cantat-Gaudin et al. (2018a) – GDR2 5340220262646771712 – with a reported membership probability of 1.0; it actually lies at the beginning of the WD cooling sequence. This makes it a solid WD candidate that must have formed very recently. The last detected source – GDR2 5338685962923467136 – is a new candidate cluster WD.

All of the reported cluster WDs, with the exception of the massive WD identified in Raddi et al. (2016), have a GDR2 counterpart with a full five-parameter solution. Despite them not being in the catalog of Gentile Fusillo et al. (2019), we can still assess their cluster membership. Figure 5 shows that the literature WDs have astrometric properties that are consistent with the cluster membership. The only exception is GDR2 5340148691289324416 (reported as a member in Dobbie et al. 2012), whose cluster membership, which is based on its astrometric properties, can be disputed. Another interesting case is GDR2 5338650984675000448 (cluster member according to Reimers & Koester 1989; also listed in Gentile Fusillo et al. 2019), which seems too luminous and red to be a cluster member.

3.13. NGC 6633

NGC 6633 is a loose OC with various age estimates, ranging from 430 Myr (Dias et al. 2002) to 800 Myr (our estimate from isochrone fitting). Reimers & Koester (1994) investigated possible WD candidates in the field of the cluster and found one (GDR2 4477214475044842368) that may be a cluster member, but they were not able to confirm its cluster membership. A later study by Williams & Bolte (2007) found two more WDs at the cluster distance modulus (GDR2 4477166581862672256 and GDR2 4477253202776118016) and another two (GDR2 4477214475044842368 and GDR2 4477168746525464064) that appear too bright to be cluster members if single, but could potentially be double degenerate systems belonging to the cluster. One of them had already been identified as a WD member candidate in Reimers & Koester (1994).

Our analysis yielded two WD member candidates: GDR2 4477214475044842368 and GDR2 4476643725433841920; one

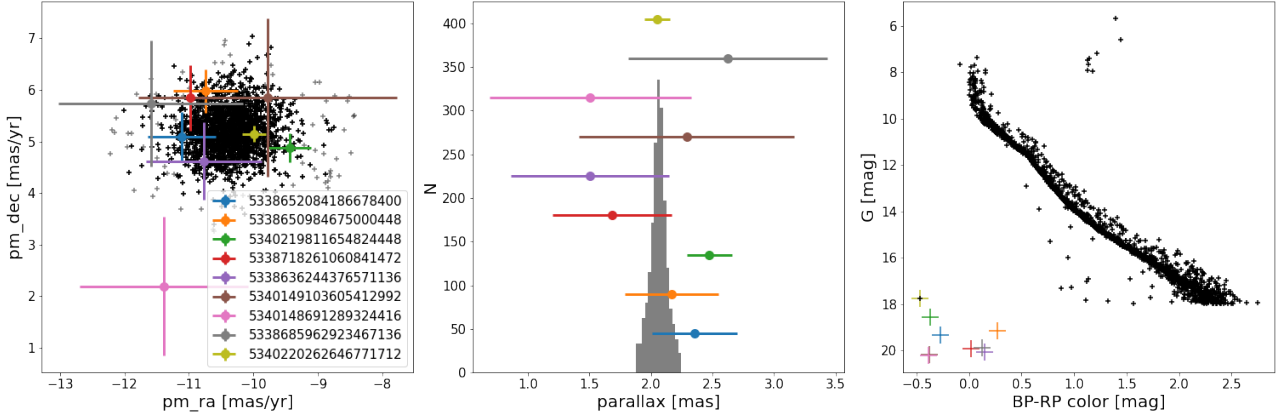


Fig. 5. *Left:* proper motion diagram of the NGC 3532 stars with the recovered and literature WD proper motion overlaid. Cluster stars with cluster membership probability <0.5 are marked using gray crosses, while black crosses indicate likely cluster members. Here, and in the subsequent graphs, the errorbars indicate a 1σ uncertainty, as reported in the GDR2. Errorbars for the cluster stars are omitted for clarity. *Middle:* parallax histogram of the cluster member stars (membership probability ≥ 0.5) with WD parallaxes overlaid. *Right:* cluster member star CMD with WDs overlaid.

was already known and one is a novel detection. Out of the two WD member candidates identified in Williams & Bolte (2007), we identified one as a cluster member in our analysis. Neither of them is included in Gentile Fusillo et al. (2019). *Gaia* DR2 4477166581862672256 has a parallax and proper motion consistent with cluster membership. The other, which was thought to be a rare DB cluster WD, is a clear outlier in terms of both parallax and proper motion. Out of the two potential double degenerate systems (both listed in Gentile Fusillo et al. 2019), only one of them (GDR2 4477214475044842368) has astrometric parameters consistent with cluster membership.

3.14. NGC 6991

NGC 6991 is a relatively unstudied sparse OC. Our literature search for cluster WDs and candidates did not yield any objects that may be associated with this cluster.

We present the identification of a possible cluster WD (GDR2 2166915179559503232). It is a high-confidence WD in Gentile Fusillo et al. (2019), and its proper motion is consistent with other members of the cluster. On face value, its parallax puts it in the foreground of NGC 6991, but the parallax error is rather large so its cluster membership cannot be conclusively assessed this way.

3.15. NGC 7092

NGC 7092 (M 39) is a well-known and well-studied cluster. At the time of writing, Caiazzo et al. (2020) have identified and characterized one cluster WD (GDR2 2170776080281869056).

Our analysis yielded a high-confidence WD that is a possible member of this cluster, the same object as in Caiazzo et al. (2020). The parallax and proper motion of this object matches well with those of the cluster members.

3.16. RSG 7 and RSG 8

RSG 7 and RSG 8 are two of the sparse, close OCs discovered in Röser et al. (2016). The literature on these clusters is very limited, and there are no WDs associated with them.

Our search resulted in three WD candidates that can potentially be assigned to RSG 7, as well as one that could be a

member of either RSG 7 or RSG 8 (the double match resulted from a combination of the close proximity of the clusters in the projection on the sky as well as the proper motion space and large parallax uncertainty of the member candidates). However, upon analysis of the proper motion diagram, parallax distribution, and CMDs of the cluster members in Cantat-Gaudin et al. (2018a), we concluded that the parameters of these clusters listed there are erroneous. The issue seems to be a heavy contamination from the members of the adjacent cluster, which is clearly visible and presents as multiple populations in the cluster CMDs. Taking the quality of the astrometric parameters of the candidate WD members into consideration as well, we thus discarded these OC-WD pairs.

3.17. Ruprecht 147

Ruprecht 147 (NGC 6774) is one of the oldest star clusters in the solar neighborhood. Its proximity and age make it attractive as one of the potential benchmark clusters for stellar evolution studies, and WDs in particular. This has been demonstrated by Gaia Collaboration (2018a), who identified ten cluster WDs. A subsequent comprehensive study by Olivares et al. (2019) has added five more, for a total WD tally of 15. A recent study of the cluster by Marigo et al. (2020) rules out the membership of several previously associated WDs based on conflicting spectroscopic and photometric luminosities, but it adds one new cluster WD not listed in Gentile Fusillo et al. (2019)

Our analysis identified nine cluster WD candidates, none of which are new detections; this is not surprising given the depth of the previous studies. However, we decided to discard three member candidates – GDR2 4183847562828165248, GDR2 4184148073089506304, and GDR2 4184196073644880000 – which are all members according to Gaia Collaboration (2018a) and Olivares et al. (2019) but are found to be non-members in Marigo et al. (2020). Therefore, we retained six potential WD members. One of the WDs from Olivares et al. (2019) is not included in Gentile Fusillo et al. (2019), and five of them are slight proper motion outliers with respect to the cluster members of Cantat-Gaudin et al. (2018a), with one of the WDs just narrowly inside the margin delineated by our selection criteria.

3.18. Stock 2

Stock 2 is a nearby OC. Despite its proximity, it is relatively unstudied due to its large angular size and the variable reddening in its direction (Spagna et al. 2009). Its age is disputed, so we estimated the cluster age to be $\log(t) = 8.5$. Stock 2 was one of the clusters studied in Gaia Collaboration (2018a), who identify eight cluster WD candidates.

Our analysis managed to identify 16 WD candidates with parameters consistent with cluster membership. Out of these, ten are new detections, while the remaining six were identified in Gaia Collaboration (2018a). There are two extra cluster WD candidates contained in Gaia Collaboration (2018a) that were not recovered in our analysis, despite them being listed in Gentile Fusillo et al. (2019): GDR2 508400329710144896 and GDR2 506848643933335296. The parallaxes of these two objects are not consistent with cluster membership.

3.19. Stock 12

Stock 12 is a poorly studied cluster, the WD content of which has never been studied before. We uncovered only one novel WD member candidate: GDR2 1992469104239732096.

4. Reliability of the GDR2 solution

The GDR2 provides high-quality astrometric and photometric measurements for an unprecedented number of sources. However, it still contains some solutions that are ill-behaved and need to be accounted for or removed from the analysis. Problems with the astrometry and photometry can arise for sources that are located in regions with high source densities, for instance in the Galactic plane and star clusters. Binary systems can also be problematic because GDR2 sources are treated as single stars in the astrometric solution, whereas binaries do not receive any special treatment (Gaia Collaboration 2018b; Lindgren et al. 2018). We therefore examined the quality of the GDR2 solutions for the recovered WD member candidates.

Gentile Fusillo et al. (2019) have conducted some cleaning of their WD sample, identifying many potentially spurious sources. However, in order to obtain a reliable list of WD member candidates, we further cleaned the WD sample based on the recommended astrometric and photometric flags. Informed by Gaia Collaboration (2018b), Lindgren et al. (2018) and Lindgren (2018; GAIA-C3-TN-LU-LL-124-01³), we retained the sources that satisfied the following three conditions: (a) duplicated_source = False; (b) astrometric_excess_noise < 1 mas or astrometric_excess_noise_sig < 2; and (c) ruwe < 1.4.

Specifically, the flag duplicated_source=True implies observational problems, crossmatching problems, processing problems, or stellar multiplicity, potentially leading to problems in the astrometric solution. The astrometric_excess_noise (ϵ_i) is the excess astrometric noise of the source postulated to explain the scatter of residuals in the astrometric solution. When it is high and significant, it can mean that the astrometric solution has failed for that source. Another possibility is that the observed source is a binary system, where the additional scatter can arise from the movement of the emission centroid due to the motion of the binary components. Finally, the cuts based on ruwe, which stands for renormalized unit weight error, ensured the removal of ill-behaved astrometric solutions.

None of the selected WD candidates exhibited increased astrometric noise or ruwe values; however, three of them (GDR2 4519349757791348480, GDR2 5338685962923467136, and GDR2 511159317926025600) were possible duplicated sources. These objects were then removed from the candidate list.

In order to identify the cases where the photometry is unreliable, we applied the following two quality indicators, as given in Gaia Collaboration (2018a): (a) $\text{phot_bp_rp_excess_factor} > 1.0 + 0.015(G_{BP} - G_{RP})^2$ and (b) $\text{phot_bp_rp_excess_factor} < 1.3 + 0.06(G_{BP} - G_{RP})^2$. The WDs that did not satisfy the above criteria were retained as member candidates, but we did not estimate their characteristics as the photometry cannot be considered reliable.

5. Parameter estimates for the recovered WD member candidates

In order to establish precise WD parameters, spectroscopic studies are usually needed. In addition to atmospheric parameters such as effective temperature, surface gravity, and chemical composition, spectroscopic data provide an additional check for cluster membership by comparing the WD spectroscopic-based luminosity with the luminosity derived from photometry when the cluster distance and extinction is adopted. Furthermore, spectroscopy is required to ascertain the WD atmospheric composition (unless ultraviolet photometry is available) and binarity status. Unfortunately, most of the new WD member candidates lack the needed spectroscopic data. However, we can assume that most of the recovered WDs are of the DA type, which is overwhelmingly the most dominant WD type found in OCs due to their typical ages, while only a handful of DB cluster WDs are known in the literature (e.g., Kalirai et al. 2005; Salaris & Bedin 2019; Marigo et al. 2020). Under this assumption, the GDR2 photometry enables us to compute the WD absolute magnitudes and colors, adopting the cluster distance and reddening. From these, the photometric-based estimates of WD parameters, such as mass M_{WD} and cooling age t_{cool} , can be derived.

While the Montreal WD cooling tracks were used for the photometric selection of viable OC WDs and can, in principle, be used to compute M_{WD} and t_{cool} estimates, they suffer from several shortcomings that can affect these estimates. Notably, they do not include the effects of residual nuclear burning, which can have a significant impact on the derived t_{cool} (Iben & Tutukov 1984; Camisassa et al. 2015; Althaus et al. 2010). Additionally, the Montreal WD cooling tracks assume unrealistic WD core compositions and do not include the impact of the energy release resulting from phase separation on crystallization, which also affects the derived t_{cool} . Then, to compute M_{WD} and t_{cool} , we used a combination of models, employing the tool from Cheng (2020). For the WDs with masses of $0.45 M_{\odot} \lesssim M_{WD} \lesssim 1.0 M_{\odot}$, we used the model from Renedo et al. (2010) with a metallicity of $Z = 0.01$, which is suitable for the solar neighborhood. For the high-mass WDs ($M_{WD} \gtrsim 1.0 M_{\odot}$), we adopted the model from Camisassa et al. (2019), in which such WDs are expected to be harboring O-Ne cores. In order to account for the errors in absolute magnitude and color, we performed a 10^4 -element Monte Carlo simulation for each WD, interpolating the M_{WD} and t_{cool} from the cooling tracks each time. For the simulations, we drew absolute magnitude and color samples from normal distributions (assumed to be independent), which are centered around the measured values and 1σ errors. We defined our 1σ absolute magnitude and color errors by adding in quadrature the error from the distance modulus (in the case of absolute magnitude), reddening, and instrumental errors. Resulting

³ http://www.rssd.esa.int/doc_fetch.php?id=3757412

Table 2. Novel or newly characterized WD-OC pairs recovered in this analysis.

GDR2 source ID	Associated cluster	P_{WD}	$\log t_{\text{cl}}$ (yr)	[Fe/H]	[M/H]	M_{WD} (M_{\odot})	t_{cool} (Gyr)
5856401252012633344	ASCC 73	0.867	8.190			$0.64^{+0.12}_{-0.11}$	$0.097^{+0.037}_{-0.03}$
5825203021908148480	ASCC 79	0.961	6.950			$0.37^{+0.13}_{-0.08}$	$0.007^{+0.004}_{-0.004}$
5826384584601681152	ASCC 79	0.916	6.950			$0.33^{+0.09}_{-0.06}$	$0.008^{+0.002}_{-0.005}$
5825187834899772160	ASCC 79	0.594	6.950			$0.29^{+0.07}_{-0.03}$	$0.01^{+0.002}_{-0.003}$
4092407537313874048	ASCC 97	0.465	7.900		0.129 ± 0.166	$0.24^{+0.06}_{-0.04}$	$0.035^{+0.023}_{-0.01}$
5508976051738818176	Alessi 3	0.995	8.870		-0.275 ± 0.065	$0.81^{+0.09}_{-0.09}$	$0.638^{+0.128}_{-0.109}$
4853382867764646912	Alessi 13	0.998	8.720		0.06 ± 0.15	$0.57^{+0.08}_{-0.08}$	$0.568^{+0.076}_{-0.07}$
4283928577215973120	IC 4756	0.986	8.987	-0.02 ± 0.01		$0.34^{+0.14}_{-0.07}$	$0.011^{+0.005}_{-0.006}$
6653447981289591808	Mamajek 4	0.990	8.824	0.09 ± 0.08		$0.85^{+0.11}_{-0.12}$	$0.282^{+0.073}_{-0.061}$
5289447182180342016	NGC 2516 ^(a)	0.999	8.475	0.08 ± 0.01		$0.71^{+0.21}_{-0.17}$	$0.149^{+0.069}_{-0.052}$
5294015515555860608	NGC 2516 ^(a)	0.998	8.475	0.08 ± 0.01		$0.98^{+0.11}_{-0.11}$	$0.077^{+0.027}_{-0.025}$
5597682038533250304	NGC 2527	0.996	8.910	-0.1 ± 0.04		–	–
5340220262646771712	NGC 3532	0.989	8.650	-0.07 ± 0.10		$0.5^{+0.12}_{-0.12}$	$0.3^{+0.061}_{-0.063}$
4476643725433841920	NGC 6633	0.532	8.900	-0.098 ± 0.037		$0.58^{+0.17}_{-0.16}$	$0.157^{+0.061}_{-0.055}$
2166915179559503232	NGC 6991	0.998	9.100	0.0 ± 0.03		$0.56^{+0.14}_{-0.12}$	$0.023^{+0.013}_{-0.012}$
418392888026931328	Ruprecht 147	0.996	9.330	0.16 ± 0.08		$0.49^{+0.27}_{-0.19}$	$0.162^{+0.091}_{-0.078}$
4183926006112672768	Ruprecht 147	0.955	9.330	0.16 ± 0.08		$0.49^{+0.11}_{-0.12}$	$0.481^{+0.076}_{-0.066}$
506514907785623040	Stock 2	0.939	8.500	-0.06 ± 0.03		$0.37^{+0.11}_{-0.08}$	$0.306^{+0.046}_{-0.045}$
508276703371724928	Stock 2	0.980	8.500	-0.06 ± 0.03		$0.39^{+0.48}_{-0.19}$	$0.169^{+0.159}_{-0.117}$
507054806657042944	Stock 2	0.999	8.500	-0.06 ± 0.03		$0.83^{+0.07}_{-0.08}$	$0.069^{+0.023}_{-0.018}$
507105143670906624	Stock 2	0.976	8.500	-0.06 ± 0.03		$0.63^{+0.07}_{-0.06}$	$0.234^{+0.043}_{-0.031}$
507119265523387136	Stock 2	0.995	8.500	-0.06 ± 0.03		–	–
507555904779576064	Stock 2	0.977	8.500	-0.06 ± 0.03		$0.35^{+0.05}_{-0.05}$	$0.118^{+0.018}_{-0.016}$
506862078583709056	Stock 2	0.999	8.500	-0.06 ± 0.03		$0.86^{+0.07}_{-0.08}$	$0.041^{+0.017}_{-0.013}$
458778927573447168	Stock 2	0.997	8.500	-0.06 ± 0.03		$0.48^{+0.09}_{-0.09}$	$0.069^{+0.021}_{-0.018}$
507362012775415552	Stock 2	0.990	8.500	-0.06 ± 0.03		$0.5^{+0.07}_{-0.07}$	$0.153^{+0.027}_{-0.029}$
507414067782288896	Stock 2	0.984	8.500	-0.06 ± 0.03		$0.29^{+0.02}_{-0.02}$	$0.028^{+0.004}_{-0.005}$
458066409683198336	Stock 2	0.994	8.500	-0.06 ± 0.03		$0.41^{+0.07}_{-0.05}$	$0.098^{+0.022}_{-0.014}$
463937282075547648	Stock 2	0.994	8.500	-0.06 ± 0.03		$0.36^{+0.05}_{-0.04}$	$0.065^{+0.012}_{-0.01}$
507128332197081344	Stock 2	0.861	8.500	-0.06 ± 0.03		$0.36^{+0.06}_{-0.05}$	$0.278^{+0.036}_{-0.03}$
507277870080186624	Stock 2	0.899	8.500	-0.06 ± 0.03		–	–
506864793008901632	Stock 2	0.698	8.500	-0.06 ± 0.03		$0.3^{+0.12}_{-0.08}$	$0.284^{+0.052}_{-0.054}$
507221863701989248	Stock 2	0.887	8.500	-0.06 ± 0.03		–	–
1992469104239732096	Stock 12	0.999	8.450			$0.35^{+0.44}_{-0.15}$	$0.127^{+0.176}_{-0.096}$

Notes. P_{WD} is the probability of the object being a WD, adopted from [Gentile Fusillo et al. \(2019\)](#), $\log t_{\text{cl}}$ is the cluster age, and $[\text{Fe}/\text{H}]/[\text{M}/\text{H}]$ is the cluster metallicity. Assuming that all recovered WDs are of the DA type, M_{WD} and t_{cool} are WD mass and WD cooling age estimates, respectively. ^(a)Recovered in [Holt et al. \(2019\)](#) but not characterized. Missing values of M_{WD} and t_{cool} for some objects are due to GDR2 photometry problems for these objects.

References. OC metallicities: [Bagdonas et al. \(2018\)](#), [Baratella et al. \(2020\)](#), [Carrera et al. \(2019\)](#), [Conrad et al. \(2014\)](#), [Fritzewski et al. \(2019\)](#), [Netopil et al. \(2016\)](#), [Netopil \(2017\)](#), [Reddy & Lambert \(2019\)](#), [Zhang et al. \(2019\)](#).

M_{WD} and t_{cool} estimates and their errors for the novel or newly characterized WDs are listed in Table 2, where the listed values correspond to the median values obtained from the simulations and the quoted errors are derived from the 68% confidence intervals.

It is apparent that we recovered mostly intermediate- and low-mass WD members. This is understandable when the properties of massive ($\gtrsim 0.9 M_{\odot}$) WDs and the magnitude limit of *Gaia* are considered. The highest-mass WDs are less luminous and cool more rapidly than their lower-mass counterparts. Thus, they remain bright enough for *Gaia* only in the

closest and youngest OCs. Additionally, high-mass WDs can be ejected from their parent OC due to the potential velocity kicks imparted on them during their formation by asymmetric mass-loss or dynamical interactions with other OC stars ([Fellhauer et al. 2003](#); [Tremblay et al. 2012](#)). Last, the number of young OCs potentially hosting sufficiently bright massive WDs in the solar neighborhood is low. Therefore, also taking the degradation of the astrometry and photometry quality of *Gaia* when approaching its magnitude limit into consideration, only very few massive WDs are recovered by our approach, as expected.

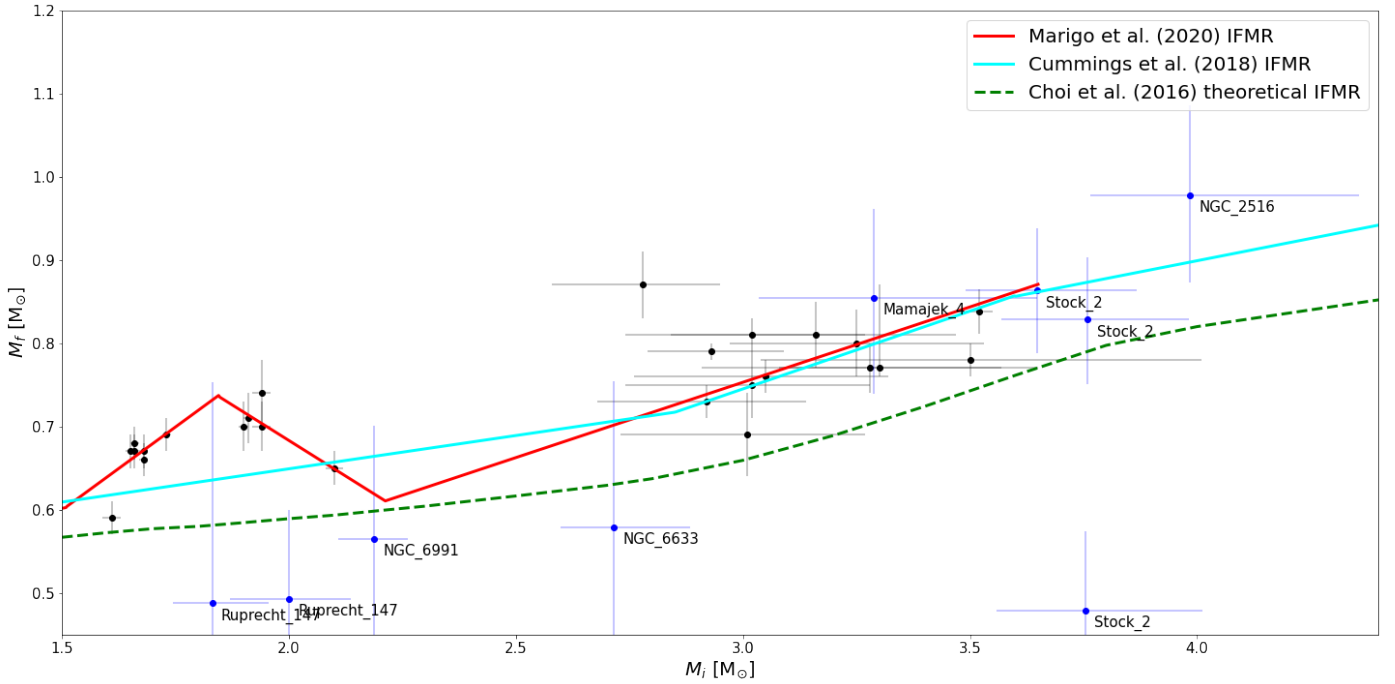


Fig. 6. Semi-empirical IFMRs in the range of M_i from 1.5 to $4.4 M_{\odot}$. The data points include the newly recovered and characterized WD OC members (in blue, with parent OC labeled, Table 4) and the previously published OC WDs from Table 3 and Marigo et al. (2020) (in black). The four-piece IFMR fit (red) is adopted from Marigo et al. (2020). The cyan line represents the IFMR fit adopted from Cummings et al. (2018), and the dashed green line is the theoretical IFMR derived from Choi et al. (2016).

Table 3. Recovered WD-OC associations previously discussed in the literature.

GDR2 source id	Associated cluster	Refs.
66697547870378368	Melotte 22	Eggen & Greenstein (1965)
3029912407273360512	NGC 2422	Richer et al. (2019)
5289447182180342016	NGC 2516	Holt et al. (2019)
5294015515555860608	NGC 2516	Holt et al. (2019)
5290767695648992128	NGC 2516	Reimers & Koester (1982)
659494049367276544	NGC 2632	Salaris & Bedin (2019)
661841163095377024	NGC 2632	Salaris & Bedin (2019)
665139697978259200	NGC 2632	Salaris & Bedin (2019)
664325543977630464	NGC 2632	Salaris & Bedin (2019)
662798086105290112	NGC 2632	Salaris & Bedin (2019)
661297901272035456	NGC 2632	Salaris & Bedin (2019)
661353224747229184	NGC 2632	Salaris & Bedin (2019)
662998983199228032	NGC 2632	Salaris & Bedin (2019)
661270898815358720	NGC 2632	Salaris & Bedin (2019)
661010005319096192	NGC 2632	Salaris & Bedin (2019)
660178942032517760	NGC 2632	Salaris & Bedin (2019)
661311267210542080	NGC 2632	Salaris & Bedin (2019)
5338718261060841472	NGC 3532	Koester & Reimers (1993)
4477214475044842368	NGC 6633	Reimers & Koester (1994)
2170776080281869056	NGC 7092	Caiazzo et al. (2020)
4088108859141437056	Ruprecht 147	Marigo et al. (2020)
4087806832745520128	Ruprecht 147	Marigo et al. (2020)
4183919237232621056	Ruprecht 147	Marigo et al. (2020)
4184169822810795648	Ruprecht 147	Marigo et al. (2020)

6. IFMR

Using the previously obtained M_{WD} and t_{cool} values and supplementing them with the values obtained from the literature, we can investigate the IFMR. In the IFMR analysis, an accurate

determination of the OC age is critical. This is particularly true for young OCs with young WDs, where the derived masses of the WD progenitors are very sensitive to the evolutionary time, which is derived from the OC age and WD cooling age.

We are interested in objects that have undergone single-star evolution, so we restricted the analysis to objects with $M_{\text{WD}} > 0.45 M_{\odot}$. Below this mass boundary, all objects are thought to be the product of close binary evolution (Tremblay et al. 2016).

If the cluster age t_{cl} and the WD cooling age t_{cool} are known, the lifetime of the progenitor can be given by $t_{\text{prog}} = t_{\text{cl}} - t_{\text{cool}}$. To calculate the progenitor mass from t_{prog} , an approximate mass-luminosity relation is commonly used for back-of-the-envelope calculations:

$$L/L_{\odot} \sim (M/M_{\odot})^{\alpha}. \quad (5)$$

In order to obtain more credible results, we used PARSEC version 1.2S (Bressan et al. 2012) and COLIBRI S_35 (Pastorelli et al. 2019) isochrones⁴ to determine the initial mass of the progenitor. For each WD, we performed 100 Monte Carlo simulations, each time drawing a value from the normal distribution of t_{cl} , cluster metallicity, and t_{cool} distribution obtained in the previous section. All distributions were assumed to be independent. Since t_{cl} measurements generally lack uncertainties, the 1σ error for t_{cl} was assumed to be 10% of its measured value. The metallicity distribution was also centered on its measured value, with 1σ being its uncertainty as adopted from the literature. The initial progenitor masses M_i and their errors were obtained in the same way as M_{WD} and t_{cool} in the previous section. The resulting IFMR is plotted in Fig. 6.

It can be seen from Fig. 6 that the newly characterized WDs are consistent with the nonlinear IFMR from Marigo et al. (2020), with a kink located over $1.65 M_{\odot} \lesssim M_i \lesssim 2.1 M_{\odot}$, which

⁴ http://stev.oapd.inaf.it/cgi-bin/cmd_3.3

Table 4. Initial progenitor masses M_i for the newly characterized WDs in Fig. 6.

GDR2 source id	Associated cluster	M_i (M_\odot)
6653447981289591808	Mamajek 4	$3.3^{+0.4}_{-0.3}$
5294015515555860608	NGC 2516	$4.0^{+0.4}_{-0.2}$
4476643725433841920	NGC 6633	$2.7^{+0.2}_{-0.1}$
2166915179559503232	NGC 6991	$2.2^{+0.1}_{-0.1}$
4183928888026931328	Ruprecht 147	$1.8^{+0.1}_{-0.1}$
4183926006112672768	Ruprecht 147	$2.0^{+0.1}_{-0.1}$
507054806657042944	Stock 2	$3.8^{+0.3}_{-0.2}$
506862078583709056	Stock 2	$3.6^{+0.2}_{-0.2}$
458778927573447168	Stock 2	$3.8^{+0.3}_{-0.2}$

they interpreted as a signature of the lowest-mass stars in the Galaxy that become carbon stars during the thermally pulsing asymptotic giant branch phase. Of particular interest are the WDs hosted by NGC 6991 and NGC 6633, which fall into the IFMR dip that, until then, had not been sufficiently characterized. There are also other WDs that fall into this gap (members of IC 4756, Alessi 62, and NGC 2527), which were either below the mass cutoff or had problems in their GDR2 parameters. The three-piece IFMR fit from Cummings et al. (2018) and the theoretical IFMR adopted from Choi et al. (2016) are also shown in Fig. 6. It can be seen that the IFMR fits of Marigo et al. (2020) and Cummings et al. (2018) are almost identical from $M_i \gtrsim 2.9 M_\odot$.

Apart from the IFMR kink at $1.65 M_\odot \lesssim M_i \lesssim 2.1 M_\odot$, there is a visible offset between the theoretical and observed masses from approximately $M_i \gtrsim 3.0 M_\odot$, where the observed WD masses are $\sim 0.1 M_\odot$ more massive than predicted, as has been noted in Cummings et al. (2018). Cummings et al. (2019) have later attributed this offset mainly to the effects of convective-core overshoot and rotational mixing in the main-sequence progenitors, where the rotational effects are not taken into consideration in the theoretical IFMR models. The newly characterized OC WDs with $M_i \gtrsim 3.0 M_\odot$ also continue to follow this trend, being $\sim 0.1 M_\odot$ more massive than what the theoretical IFMRs (e.g., Choi et al. 2016) predict.

Other WDs below the IFMR fit are most likely binaries, or possibly foreground objects, that have been incorrectly assigned to the OC. Interestingly, Stock 2 seems to host a large number of WDs scattered in the IFMR; some of them follow the IFMR fit by Marigo et al. (2020), but others are clustered around $M_{\text{WD}} = 0.4 M_\odot$. Such WDs may be members of binary systems. Additional scatter can be attributed to the effects of strong and variable extinction, which has been noted for this cluster (Spagna et al. 2009).

White dwarfs are the final products of the evolution of stars with initial masses (assuming solar metallicity) less than $8\text{--}10 M_\odot$ (Langer 2012; Smartt 2009); however, in binary systems, the initial mass for one of the components can be as high as $15 M_\odot$ (Wellstein et al. 2001) or as low as $6 M_\odot$ (Podsiadlowski et al. 2004). Finding a high-mass WD in a young OC can help identify initial masses for stars that undergo electron-capture SNe. We managed to identify one potential high-mass WD in NGC 2516. However, its cooling time only suggests a $\sim 4 M_\odot$ progenitor. Due to the shortcomings of this analysis, as described above, we did not recover any other high-mass

WDs and are therefore unable to put any new constraints on the boundary between neutron stars and WD formation.

7. Summary and conclusions

We searched for new potential WDs that are possible OC members using the WD catalog by Gentile Fusillo et al. (2019) and the OC catalog by Cantat-Gaudin et al. (2018a), both based on GDR2 data. Such associations are very valuable as ascertaining the membership of a WD to an OC allows us to adopt the OC distance to the WD. This distance is more precise than the distance determined from the WD parallax by itself as it is based on a large number of stars and because the WD parallaxes in the GDR2 exhibit high uncertainties due to their faintness and blue colors. This enables a more precise determination of the WD parameters. Furthermore, the nature of OCs as a coeval group of stars with a common origin allows us to study a number of topics, such as IFMR and metallicity effects.

Our study confirmed the cluster membership of several literature WD cluster members and uncovered a number of new associations. On the other hand, there are a lot of established literature OC WDs that do not seem to satisfy the astrometric and photometric criteria for cluster membership in the GDR2. Removing them from IFMR studies may alleviate the scatter that is present in the data.

The derived WD and progenitor masses of the novel WDs are broadly in line with the IFMR fit of Marigo et al. (2020), although a large number of binaries falling below the fit are also likely present. Some of the recovered WDs from NGC 6991 and NGC 6633 fall into the IFMR dip, which has been poorly characterized and deserves further study. There are several WDs lying in this gap that had to be discarded from the analysis due to their low derived masses (possibly due to binarity with a low-mass companion) or problems with the GDR2 photometry or astrometric solution (such as WDs hosted by IC 4756, Alessi 62, and NGC 2527). It could be worthwhile to observe these objects spectroscopically or revisit them in the next *Gaia* data release.

This work showcases the possibilities that precise astrometry can bring to WD studies. Naturally, spectroscopic observations of the WD cluster member candidates are still needed to confirm their WD status and type, as well as to provide more precise parameters and an additional check for cluster membership.

Acknowledgements. This work has made use of data from the European Space Agency (ESA) mission *Gaia* (<https://www.cosmos.esa.int/gaia>), processed by the *Gaia* Data Processing and Analysis Consortium (DPAC, <https://www.cosmos.esa.int/web/gaia/dpac/consortium>). Funding for the DPAC has been provided by national institutions, in particular the institutions participating in the *Gaia* Multilateral Agreement. This research has made use of the WEBDA database, operated at the Department of Theoretical Physics and Astrophysics of the Masaryk University.

References

- Agertz, O., & Kravtsov, A. V. 2015, *ApJ*, 804, 18
Althaus, L. G., Córscico, A. H., Isern, J., & García-Berro, E. 2010, *A&A Rev.*, 18, 471
Angelo, M. S., Santos, J. F. C., Corradi, W. J. B., & Maia, F. F. S. 2019, *A&A*, 624, A8
Anthony-Twarog, B. J. 1982, *ApJ*, 255, 245
Bagdonas, V., Drazdauskas, A., Tautvaišienė, G., Smiljanic, R., & Chorniy, Y. 2018, *A&A*, 615, A165
Baratella, M., D’Orazi, V., Carraro, G., et al. 2020, *A&A*, 634, A34
Bossini, D., Vallenari, A., Bragaglia, A., et al. 2019, *A&A*, 623, A108
Bressan, A., Marigo, P., Girardi, L., et al. 2012, *MNRAS*, 427, 127
Caiazzo, I., Heyl, J., Richer, H., et al. 2020, *ApJ*, 901, L14

- Camisassa, M. E., Miller Bertolami, M. M., & Althaus, L. G. 2015, *Boletín de la Asociación Argentina de Astronomía La Plata Argentina*, 57, 117
- Camisassa, M. E., Althaus, L. G., Córscico, A. H., et al. 2019, *A&A*, 625, A87
- Cantat-Gaudin, T., Jordi, C., Vallenari, A., et al. 2018a, *A&A*, 618, A93
- Cantat-Gaudin, T., Vallenari, A., Sordo, R., et al. 2018b, *A&A*, 615, A49
- Carrera, R., Bragaglia, A., Cantat-Gaudin, T., et al. 2019, *A&A*, 623, A80
- Cheng, S. 2020, *WD_models*, https://github.com/SihaoCheng/WD_models
- Choi, J., Dotter, A., Conroy, C., et al. 2016, *ApJ*, 823, 102
- Claver, C. F., Liebert, J., Bergeron, P., & Koester, D. 2001, *ApJ*, 563, 987
- Conrad, C., Scholz, R. D., Kharchenko, N. V., et al. 2014, *A&A*, 562, A54
- Córscico, A. H., Althaus, L. G., Miller Bertolami, M. M., & Kepler, S. O. 2019, *A&A Rev.*, 27, 7
- Cummings, J. D. 2017, in *Planetary Nebulae: Multi-Wavelength Probes of Stellar and Galactic Evolution*, eds. X. Liu, L. Stanghellini, & A. Karakas, *IAU Symp.*, 323, 157
- Cummings, J. D., Kalirai, J. S., Tremblay, P. E., Ramirez-Ruiz, E., & Choi, J. 2018, *ApJ*, 866, 21
- Cummings, J. D., Kalirai, J. S., Choi, J., et al. 2019, *ApJ*, 871, L18
- Dias, W. S., Alessi, B. S., Moitinho, A., & Lépine, J. R. D. 2002, *A&A*, 389, 871
- Dobbie, P. D., Napiwotzki, R., Burleigh, M. R., et al. 2009, *MNRAS*, 395, 2248
- Dobbie, P. D., Day-Jones, A., Williams, K. A., et al. 2012, *MNRAS*, 423, 2815
- Donor, J., Frinchaboy, P. M., Cunha, K., et al. 2018, *AJ*, 156, 142
- Eggen, O. J., & Greenstein, J. L. 1965, *ApJ*, 141, 83
- Evans, D. W., Riello, M., De Angeli, F., et al. 2018, *A&A*, 616, A4
- Fellhauer, M., Lin, D. N. C., Bolte, M., Aarseth, S. J., & Williams, K. A. 2003, *ApJ*, 595, L53
- Fontaine, G., Brassard, P., & Bergeron, P. 2001, *PASP*, 113, 409
- Fritzewski, D. J., Barnes, S. A., James, D. J., et al. 2019, *A&A*, 622, A110
- Gaia Collaboration (Prusti, T., et al.) 2016, *A&A*, 595, A1
- Gaia Collaboration (van Leeuwen, F., et al.) 2017, *A&A*, 601, A19
- Gaia Collaboration (Brown, A. G. A., et al.) 2018a, *A&A*, 616, A1
- Gaia Collaboration (Babusiaux, C., et al.) 2018b, *A&A*, 616, A10
- Gentile Fusillo, N. P., Tremblay, P.-E., Gänsicke, B. T., et al. 2019, *MNRAS*, 482, 4570
- Greggio, L. 2010, *MNRAS*, 406, 22
- Holt, W., Tucker, G., Buckner, A. J., & Sandquist, E. L. 2019, *Res. Notes Am. Astron. Soc.*, 3, 49
- Iben, I. Jr, & Tutukov, A. V. 1984, *ApJ*, 282, 615
- Kalirai, J. S., Richer, H. B., Hansen, B. M. S., Reitzel, D., & Rich, R. M. 2005, *ApJ*, 618, L129
- Kharchenko, N. V., Piskunov, A. E., Röser, S., Schilbach, E., & Scholz, R. D. 2005, *A&A*, 440, 403
- Kharchenko, N. V., Piskunov, A. E., Schilbach, E., Röser, S., & Scholz, R. D. 2013, *A&A*, 558, A53
- Koester, D., & Reimers, D. 1981, *A&A*, 99, L8
- Koester, D., & Reimers, D. 1985, *A&A*, 153, 260
- Koester, D., & Reimers, D. 1993, *A&A*, 275, 479
- Koester, D., & Reimers, D. 1996, *A&A*, 313, 810
- Langer, N. 2012, *ARA&A*, 50, 107
- Liebert, J. 1980, *ARA&A*, 18, 363
- Lindgren, L., Hernández, J., Bombrun, A., et al. 2018, *A&A*, 616, A2
- Lodieu, N., Pérez-Garrido, A., Smart, R. L., & Silvotti, R. 2019, *A&A*, 628, A66
- Marigo, P., Cummings, J. D., Curtis, J. L., et al. 2020, *Nat. Astron.*, 4, 1102
- Netopil, M. 2017, *MNRAS*, 469, 3042
- Netopil, M., Paunzen, E., Heiter, U., & Soubiran, C. 2016, *A&A*, 585, A150
- Olivares, J., Bouy, H., Sarro, L. M., et al. 2019, *A&A*, 625, A115
- Pancino, E., Lardo, C., Altavilla, G., et al. 2017, *A&A*, 598, A5
- Pasquini, L., Pala, A. F., Ludwig, H. G., et al. 2019, *A&A*, 627, L8
- Pastorelli, G., Marigo, P., Girardi, L., et al. 2019, *MNRAS*, 485, 5666
- Podsiadlowski, P., Langer, N., Poelarends, A. J. T., et al. 2004, *ApJ*, 612, 1044
- Raddi, R., Catalán, S., Gänsicke, B. T., et al. 2016, *MNRAS*, 457, 1988
- Reddy, A. B. S., & Lambert, D. L. 2019, *MNRAS*, 485, 3623
- Reimers, D., & Koester, D. 1982, *A&A*, 116, 341
- Reimers, D., & Koester, D. 1988, *A&A*, 202, 77
- Reimers, D., & Koester, D. 1989, *A&A*, 218, 118
- Reimers, D., & Koester, D. 1994, *A&A*, 285, 451
- Renedo, I., Althaus, L. G., Miller Bertolami, M. M., et al. 2010, *ApJ*, 717, 183
- Richer, H. B., Fahlman, G. G., Rosvick, J., & Ibata, R. 1998, *ApJ*, 504, L91
- Richer, H. B., Kerr, R., Heyl, J., et al. 2019, *ApJ*, 880, 75
- Romanishin, W., & Angel, J. R. P. 1980, *ApJ*, 235, 992
- Röser, S., Schilbach, E., & Goldman, B. 2016, *A&A*, 595, A22
- Salaris, M., & Bedin, L. R. 2018, *MNRAS*, 480, 3170
- Salaris, M., & Bedin, L. R. 2019, *MNRAS*, 483, 3098
- Smartt, S. J. 2009, *ARA&A*, 47, 63
- Spagna, A., Cossu, F., Lattanzi, M. G., & Massone, G. 2009, *Mem. Soc. Astron. It.*, 80, 129
- Tinsley, B. M. 1974, *PASP*, 86, 554
- Tremblay, P. E., Schilbach, E., Röser, S., et al. 2012, *A&A*, 547, A99
- Tremblay, P. E., Cummings, J., Kalirai, J. S., et al. 2016, *MNRAS*, 461, 2100
- Vagnozzi, S. 2019, *Atoms*, 7,
- van den Heuvel, E. P. J. 1975, *ApJ*, 196, L121
- Weidemann, V. 1977, *A&A*, 59, 411
- Wellstein, S., Langer, N., & Braun, H. 2001, *A&A*, 369, 939
- Williams, K. 2002, PhD thesis
- Williams, K. A., & Bolte, M. 2007, *AJ*, 133, 1490
- Zhang, J., Zhao, J., Oswalt, T. D., et al. 2019, *ApJ*, 887, 84

Appendix A: Proper motion diagrams, parallax distributions, and CMDs of the OC-WD associations

from Sect. 3. They are either novel candidates or were gathered from the literature.

In this section, we provide the proper motion diagrams, parallax distributions, and CMDs for the rest of the cluster-WD pairs

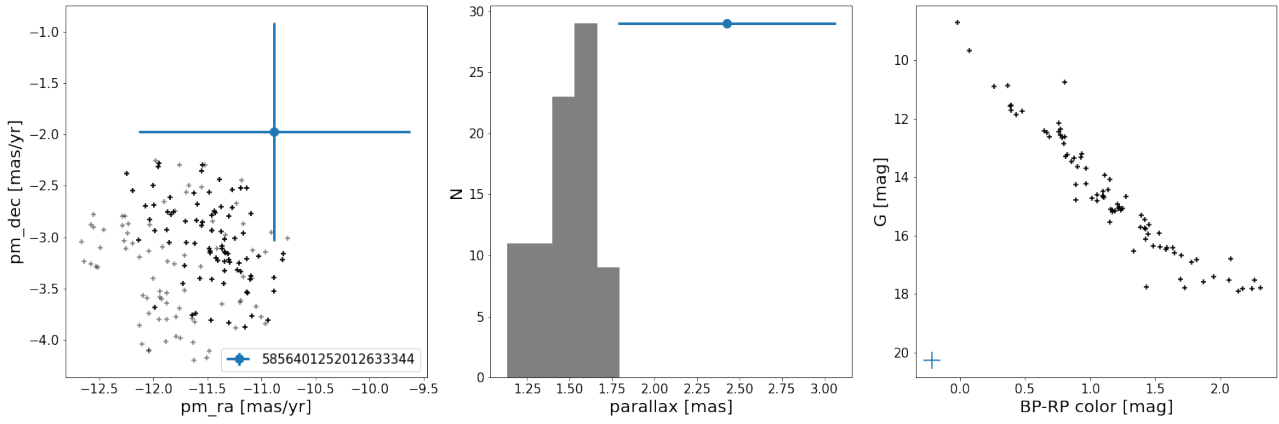


Fig. A.1. Same as in Fig. 5, but for ASCC 73.

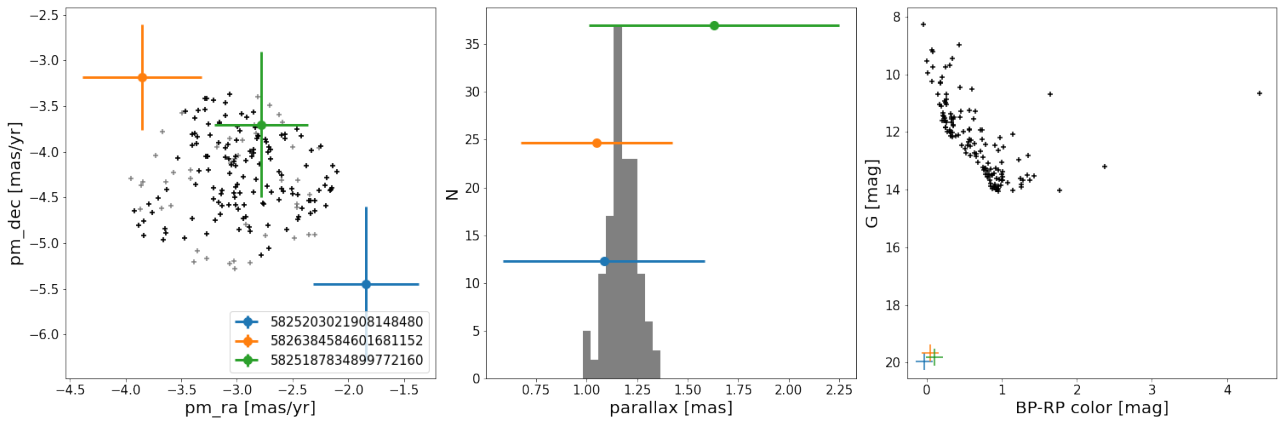


Fig. A.2. Same as in Fig. 5, but for ASCC 79.

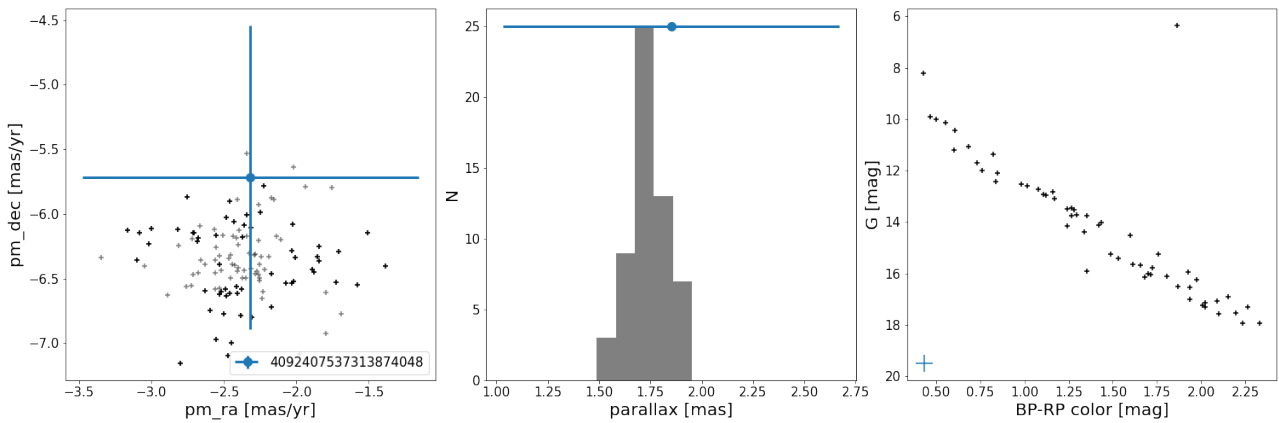


Fig. A.3. Same as in Fig. 5, but for ASCC 97.

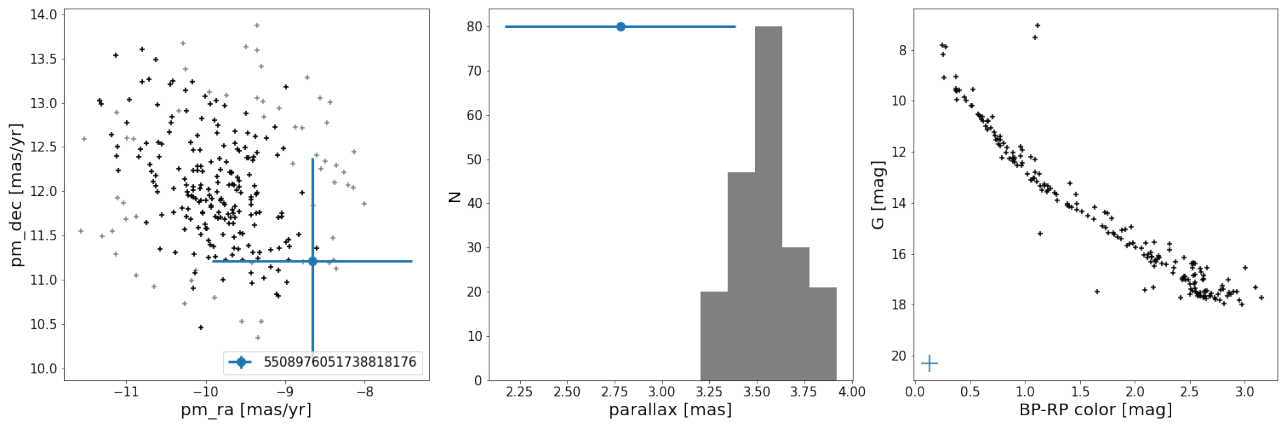


Fig. A.4. Same as in Fig. 5, but for Alessi 3.

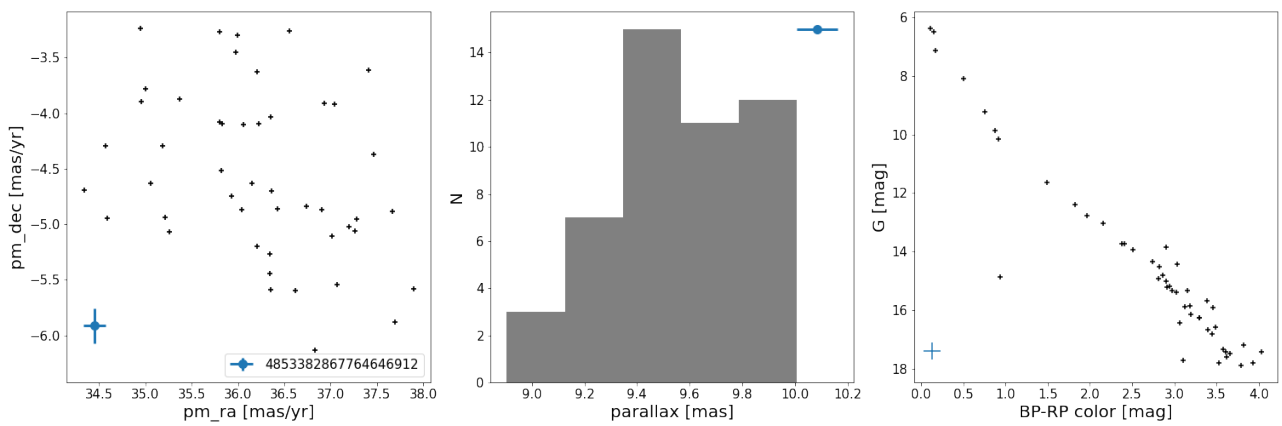


Fig. A.5. Same as in Fig. 5, but for Alessi 13.

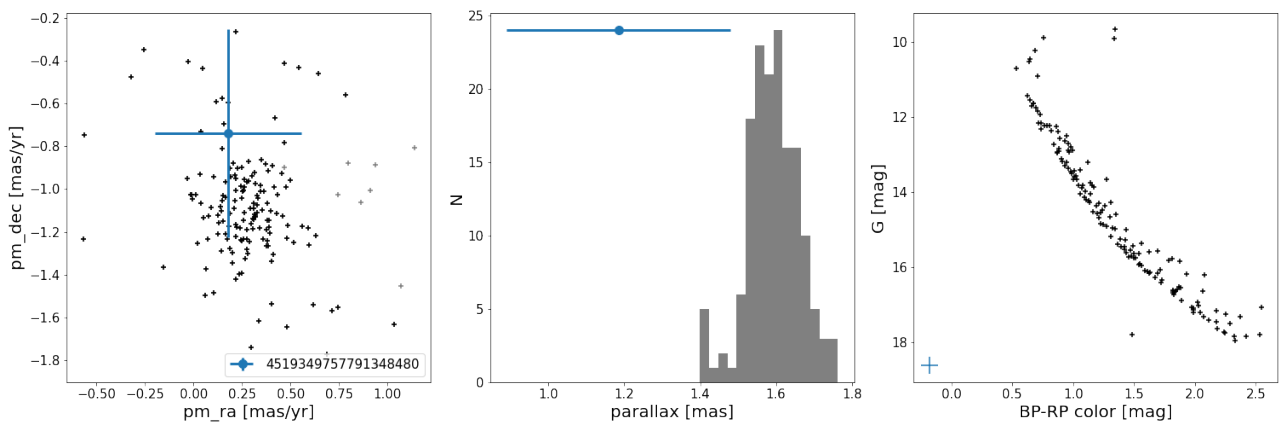


Fig. A.6. Same as in Fig. 5, but for Alessi 62.

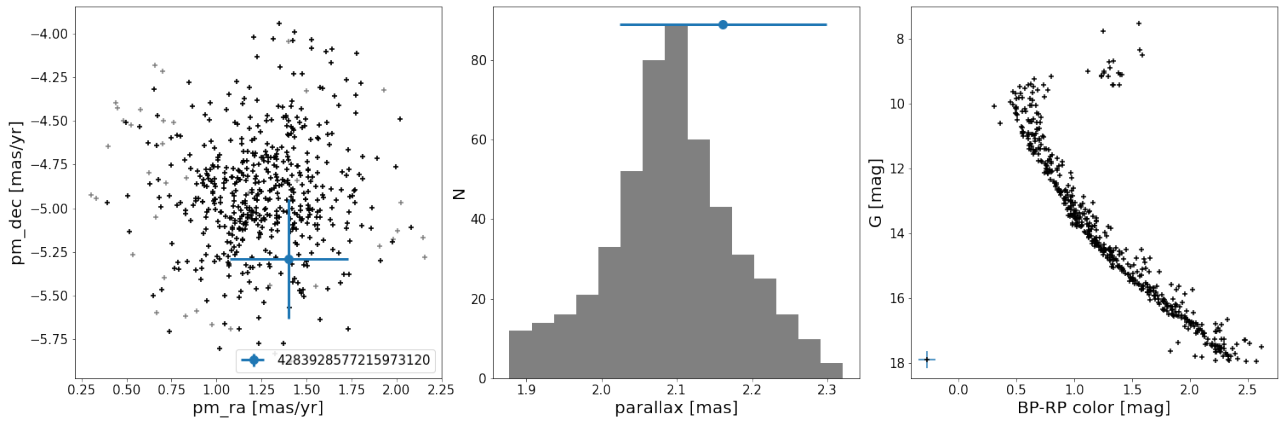


Fig. A.7. Same as in Fig. 5, but for IC 4756.

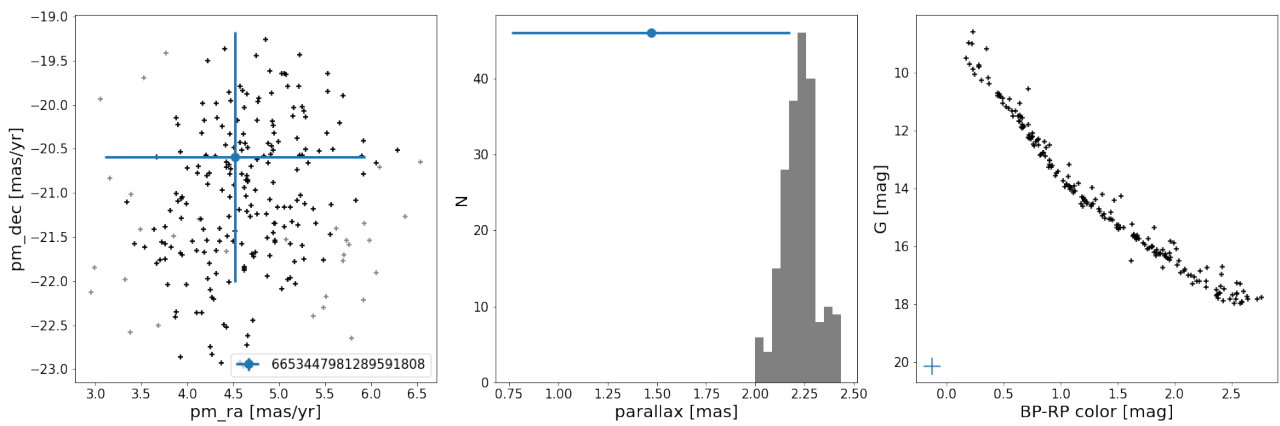


Fig. A.8. Same as in Fig. 5, but for Mamajek 4.

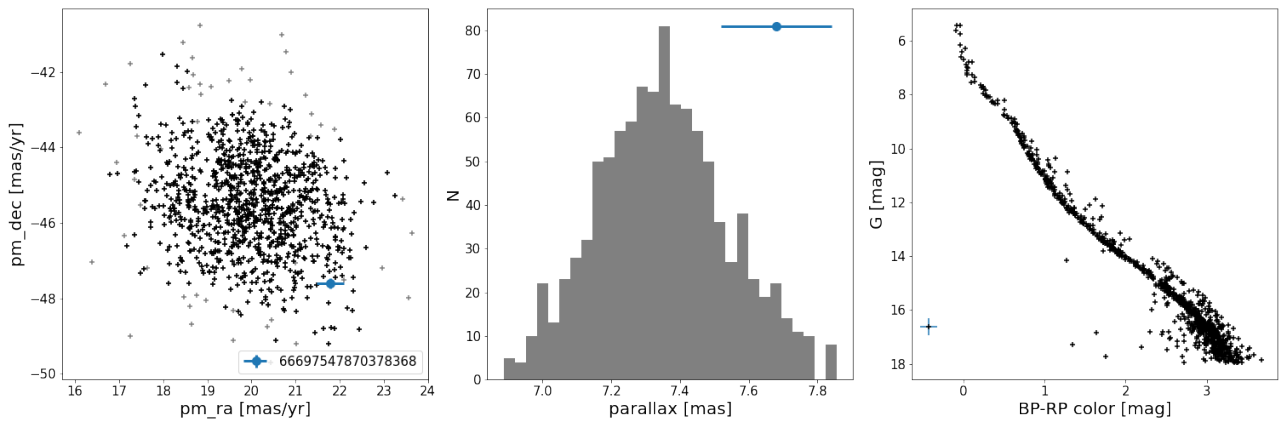


Fig. A.9. Same as in Fig. 5, but for Melotte 22.

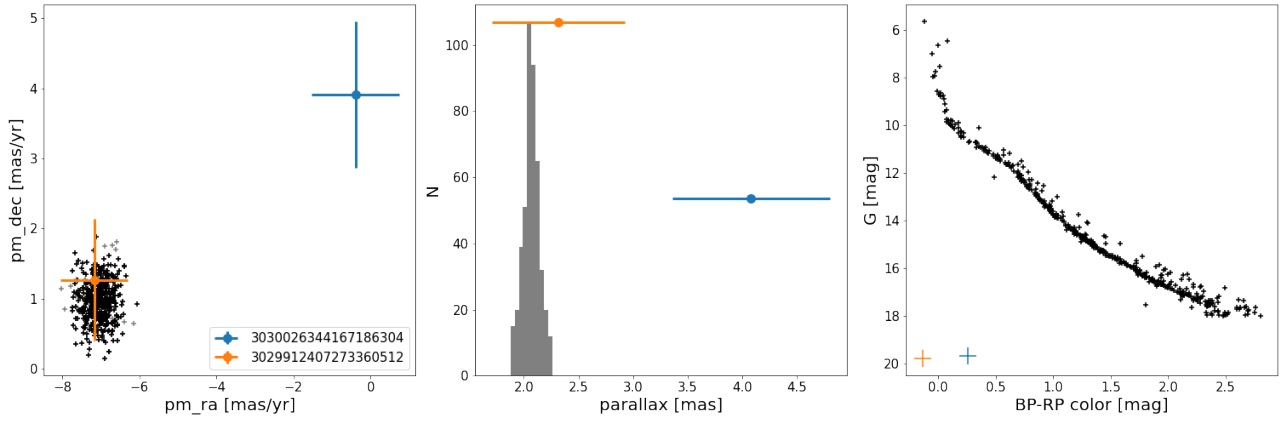


Fig. A.10. Same as in Fig. 5, but for NGC 2422.

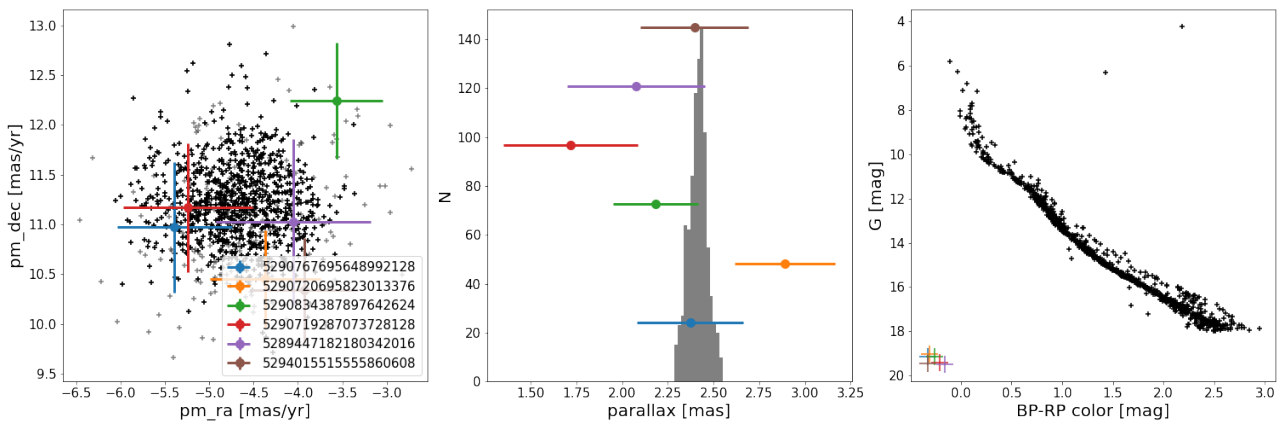


Fig. A.11. Same as in Fig. 5, but for NGC 2516.

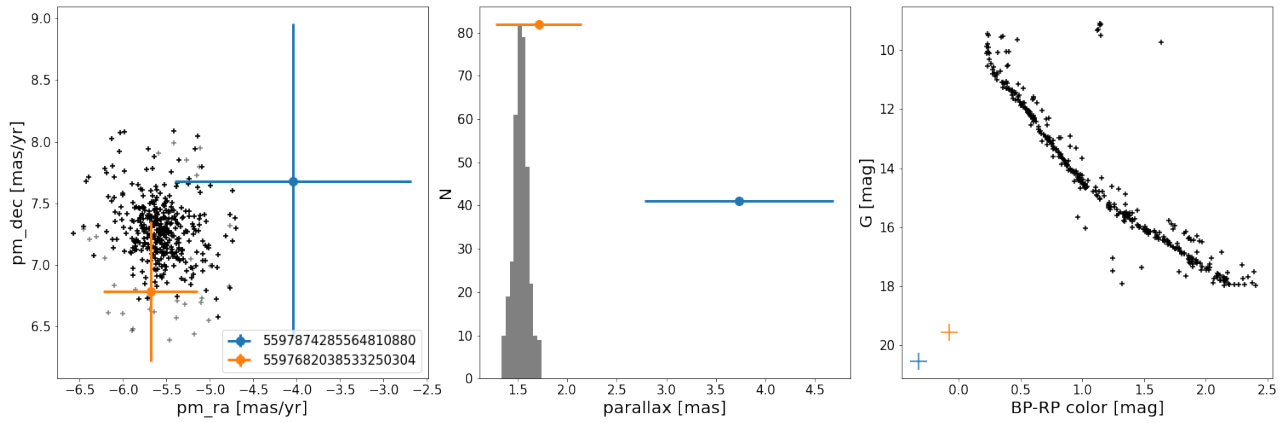


Fig. A.12. Same as in Fig. 5, but for NGC 2527.

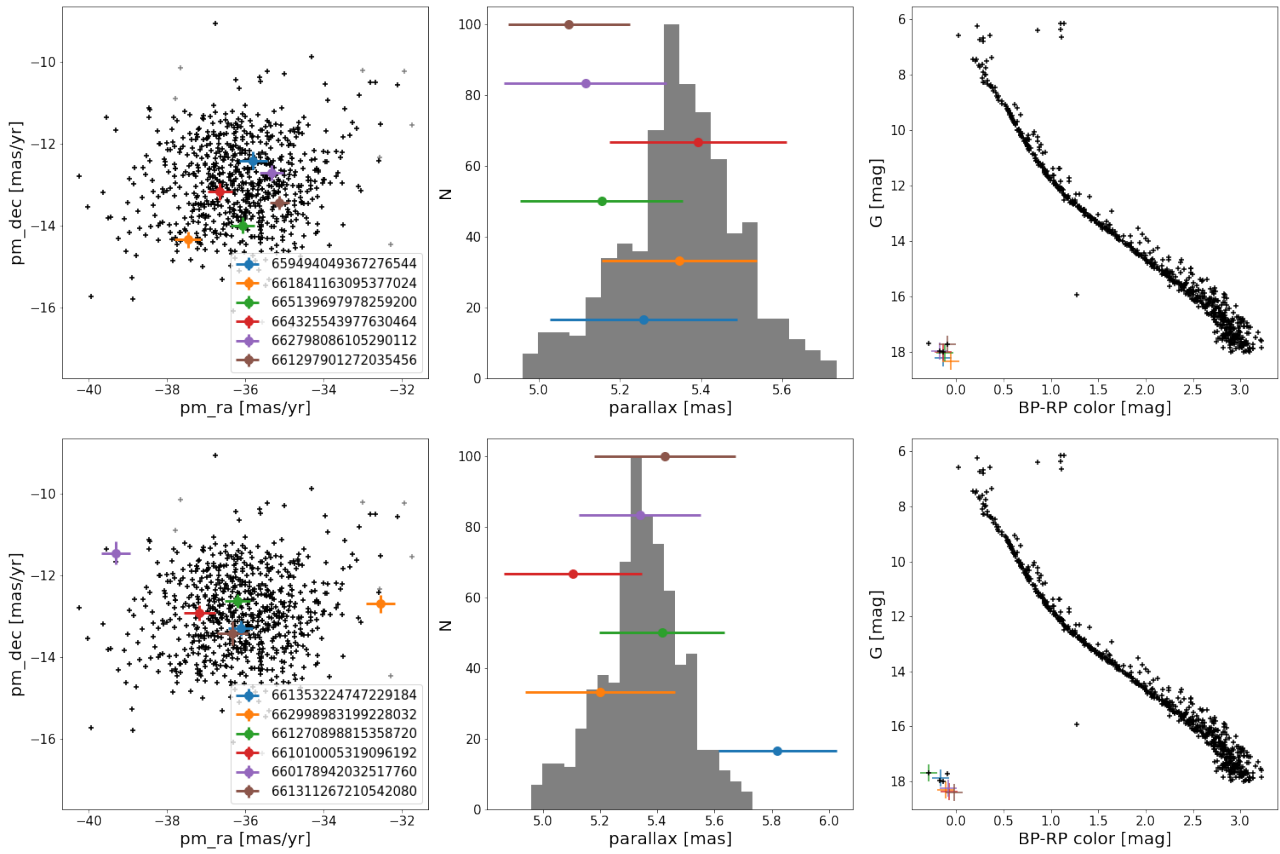


Fig. A.13. Same as in Fig. 5, but for NGC 2632.

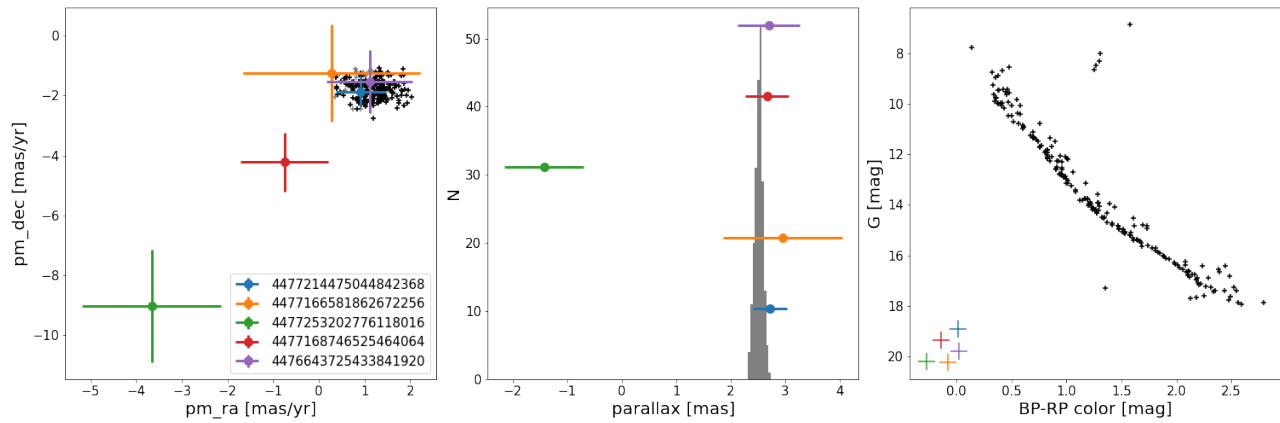


Fig. A.14. Same as in Fig. 5, but for NGC 6633.

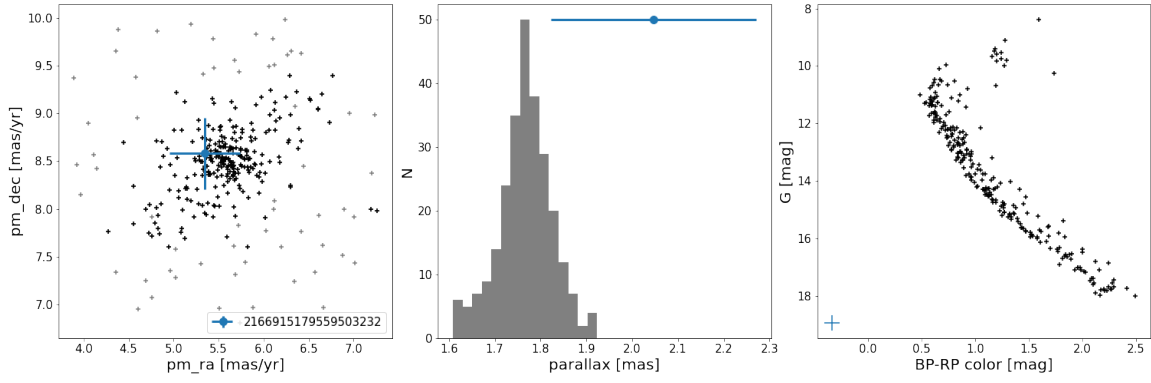


Fig. A.15. Same as in Fig. 5, but for NGC 6991.

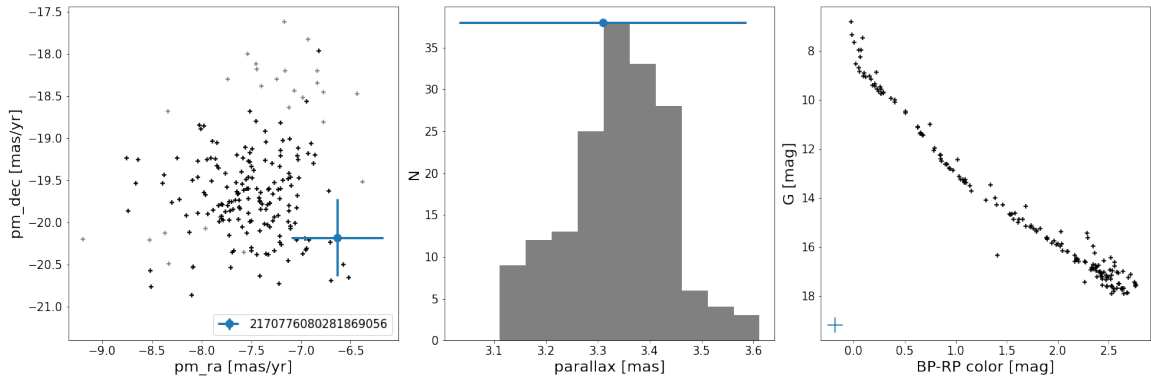


Fig. A.16. Same as in Fig. 5, but for NGC 7092.

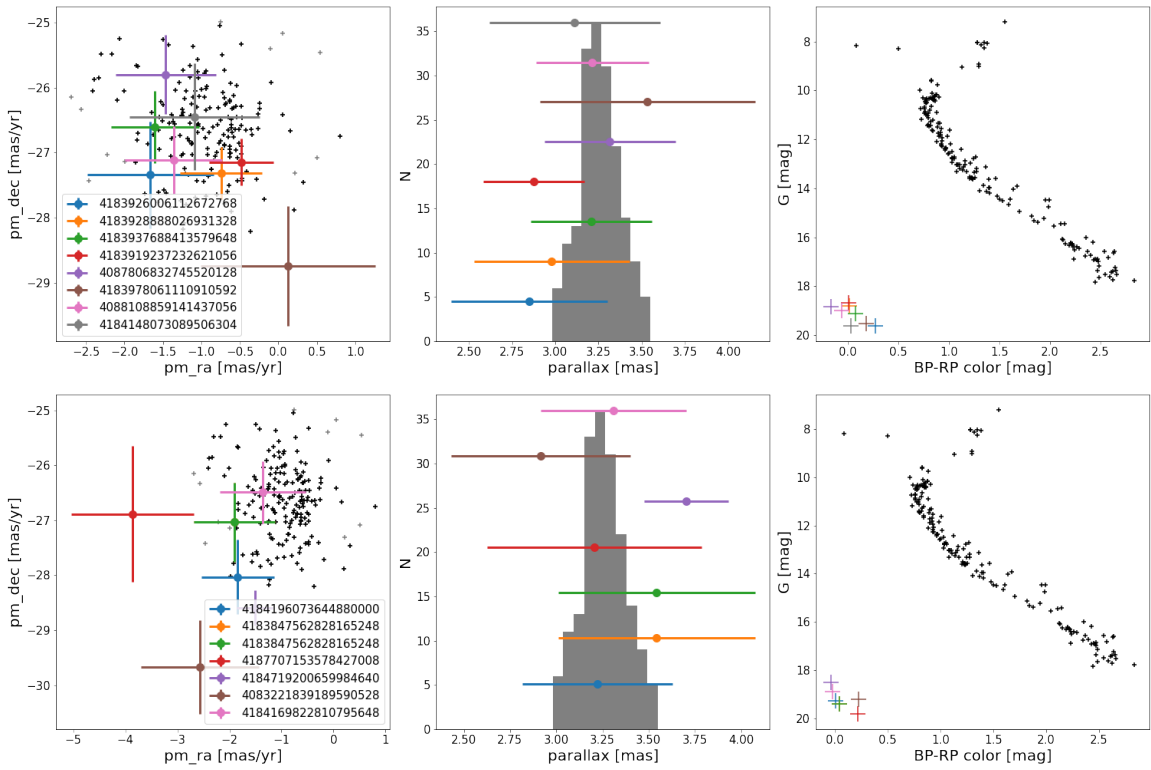


Fig. A.17. Same as in Fig. 5, but for Ruprecht 147.

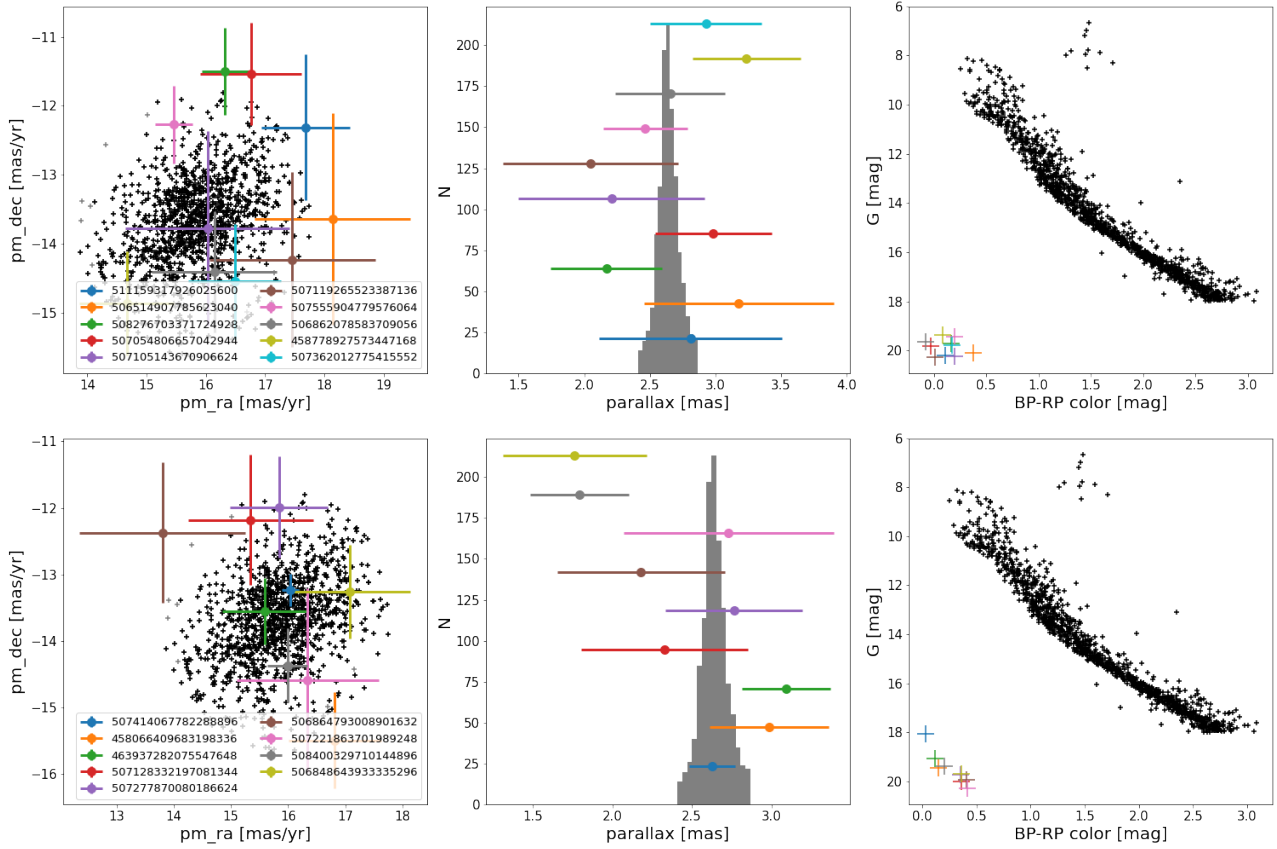


Fig. A.18. Same as in Fig. 5, but for Stock 2.

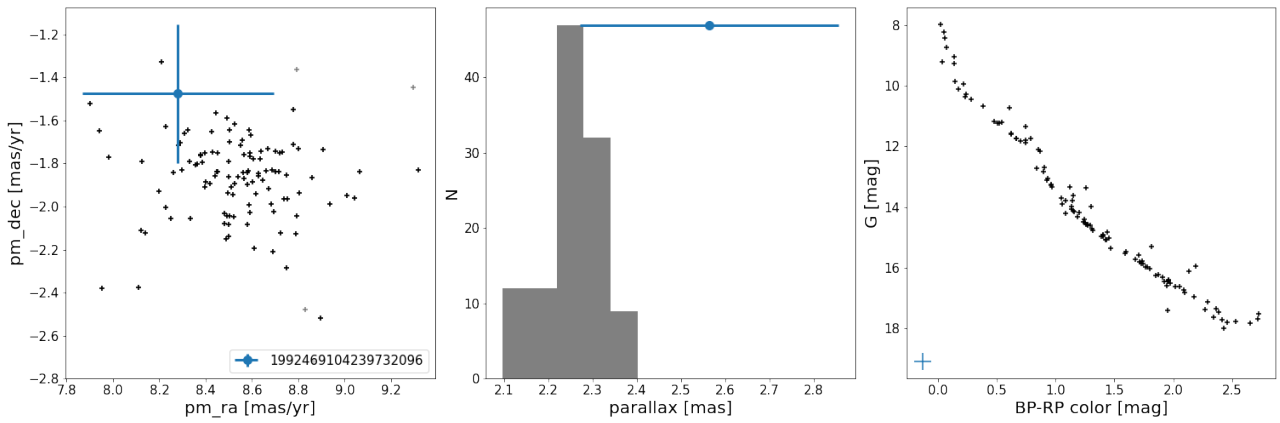


Fig. A.19. Same as in Fig. 5, but for Stock 12.

Appendix C

Unveiling stellar aurorae

Unveiling stellar aurorae: simulating auroral emission lines in hot stars induced by high-energy irradiation

Michal Kajan¹,[✉] Jiří Krtička¹ and Jiří Kubát²

¹Department of Theoretical Physics and Astrophysics, Faculty of Science, Masaryk University, Kotlářská 2, 602 00 Brno, Czech Republic

²Astronomical Institute, Academy of Sciences of the Czech Republic, Fričova 298, CZ-251 65 Ondřejov, Czech Republic

Accepted 2024 May 13. Received 2024 April 10; in original form 2024 January 3

ABSTRACT

Auroral emission lines result from the interaction between magnetic field and stellar wind, offering valuable insights into physical properties and processes occurring within magnetospheres of celestial bodies. While extensively studied in planetary and exoplanetary atmospheres, in ultracool dwarfs, and as radio emission from early-type stars, the presence of specific auroral emission lines in hot star spectra remains unexplored. In this study, we utilized TLUSTY code to simulate the auroral lines, while modelling the effect of the interaction between stellar wind and magnetosphere through X-ray irradiation. Utilizing high-resolution synthetic spectra generated from model atmospheres, we identified potential candidate lines indicative of auroral emission, which were absent in non-irradiated spectra. Emission lines in synthetic spectra were present primarily in the infrared domain. The most prominent line generated by irradiation was He II 69458 Å, which appeared in all our model atmospheres with effective temperatures ranging from 15 kK to 30 kK. We also calculated the minimum irradiation required to detect emission in this most prominent line. The presence of emission lines was interpreted by considering changes in the population of different excited states of given atoms. Besides the appearance of infrared emission lines, high-energy irradiation causes infrared excess. To complement our simulations, we also searched for auroral lines in Far Ultraviolet Spectroscopic Explorer (FUSE) observations, which are deposited in the Multimission Archive at Space Telescope catalogue. The comparison of observed spectra with synthetic spectra did not identify any possible candidate emission lines in FUSE spectra.

Key words: radiative transfer – software: simulations – stars: atmospheres – stars: early-type – stars: emission-line, Be – stars: magnetic fields.

1 INTRODUCTION

Significant populations of A and B-type main-sequence stars exhibit stable, large-scale magnetic fields that are detectable from spectropolarimetry. These magnetic fields typically possess a surface strength on the order of a few kilogauss (Morel et al. 2015; Shultz et al. 2018; Yakunin et al. 2020). The majority of these magnetic stars display a dominant dipole magnetic topology, although few exceptions exist. A model known as the Rigidly Rotating Magnetosphere, proposed by Townsend & Owocki (2005), describes many of the observed features associated with circumstellar magnetospheres of magnetic stars. According to this model, the matter accumulates in magnetospheric clouds corresponding to the minima of the effective potential along each field line.

The magnetosphere is filled with the stellar wind confined by the strong magnetic field. Various parameters can affect attributes and dynamics of the magnetosphere, including mass-loss, terminal velocity of the wind, and surface magnetic field strength as the most influential. For quantitative effects of the magnetic field, ud-Doula & Owocki (2002) and ud-Doula, Owocki & Townsend (2008) introduced a parameter for magnetic confinement η_* . If $\eta_* > 1$, the

wind is magnetically confined, which means that closed magnetic field lines exist in the magnetosphere.

The magnetic confinement parameter is associated with the Alfvén radius R_A , the radius where magnetic field energy density is equal to wind kinetic energy density. The position at which the centrifugal force, in a frame rigidly rotating with the star, balances the gravitational force, is denoted as the Kepler corotation radius, R_K . The comparison of these radii defines two distinct types of magnetospheres. In summary, the dynamical magnetosphere is defined as $R_A < R_K$ and the centrifugal magnetosphere is defined as $R_A > R_K$. Moreover, the centrifugal magnetosphere contains regions where the trapped material can corotate (see Romanova & Owocki 2016, for a review). Numerous observational effects exist as a piece of evidence for the magnetosphere in various spectral domains, specifically X-ray domain (Nazé et al. 2015), ultraviolet (UV, Marcolino et al. 2013), near-infrared (Oksala et al. 2015), radio (Leto et al. 2021), and H α (Owocki et al. 2020). Further details, including a visual schematic of the stellar magnetosphere, are provided by Shultz (2020).

Focusing on the most energetic part of the spectrum, a significant fraction of high-energy emissions in magnetic hot stars comes from magnetically confined wind shocks (MCWS). This phenomenon happens as the magnetically confined wind from different magnetic poles collides near the magnetic equator and creates wind shocks (ud-Doula & Owocki 2022). The brightness temperature of MCWS can be of the order of $\sim 10^7$ – 10^8 K (ud-Doula & Nazé 2016).

* E-mail: kajan@mail.muni.cz

Furthermore, in the radio part of the spectrum of a few magnetic stars, we can observe a curious effect created by Electron Cyclotron Maser Emission (ECME). This emission is non-common mainly because of its high polarization (Trigilio et al. 2004). The ECME is supposed to originate in the centrifugal magnetosphere, where fast electrons are trapped and accelerated towards the star while they emit radio emissions. Fast electrons are likely produced during reconnection events associated with matter leakage from the magnetospheres (Owocki et al. 2022).

The physical mechanism responsible for generating ECME closely resembles the auroral emissions observed on planets (Lamy et al. 2011; Badman et al. 2015) and on ultracool dwarfs (Nichols et al. 2012). The similarity extends to ultracool dwarfs and their exoplanets (Vidotto, Feeney & Groh 2019). Furthermore, Leto et al. (2021) derived a scaling relationship of the non-thermal radio luminosity from Jupiter, through ultracool dwarfs, to early-type stars, which shows that the mechanism is similar in all these celestial bodies. The resemblance of coherent radio emission to auroral emission led to its designation as Auroral Radio Emission (Leto et al. 2020). Stars on the main sequence exhibiting ECME radiation are alternatively designated as Main-Sequence Radio Pulse emitters (MRPs). Currently, from literature 17 stars are classified as MRPs (Das et al. 2022a, b).

The magnetospheric processes in hot stars resemble auroral activity in Earth and giant planets (Trigilio et al. 2011). Such magnetospheres are proverbial for their emission lines of molecules or neutral oxygen, which typically appear in UV region (Molyneux et al. 2014; Soret et al. 2016; Gustin et al. 2017). Magnetic chemically peculiar stars show emission lines in optical spectra (Castelli & Hubrig 2004; Sadakane & Nishimura 2017), but they are considered to occur due to Non-Local Thermal Equilibrium (NLTE) effects (Alexeeva, Ryabchikova & Mashonkina 2016; Mashonkina 2020). Krtićka et al. (2019) obtained dedicated phase-resolved with the Hubble Space Telescope (*HST*) spectroscopy of CU Vir and searched for auroral lines. However, the search turned out to be negative for unclear reasons. Therefore, the auroral emission lines have not yet been detected in magnetic hot stars.

There has never been a systematic search for these lines in hot stars. To remedy the situation, we present a systematic study of auroral lines formation in the spectra of hot stars resulting from impacting electrons.

The modelling of the effect of impacting electrons is partly motivated by the X-ray radiation during solar flares. Solar flares are known for their multithermal nature (Nagasawa et al. 2022). In our study, the effect of impacting electrons is modelled by X-ray irradiation of the stellar atmosphere with blackbody radiation.

The paper is organized as follows. In Section 2, we first search for auroral emission in Far Ultraviolet Spectroscopic Explorer (FUSE) data, which are described by Sahnou et al. (2000a, b) and Moos et al. (2000), taken from the Multimission Archive at Space Telescope (MAST) archive. Next in Section 3.1, we present a description of the input parameters in our model atmospheres utilized for irradiation. Then in Section 3.2, we mentioned physical changes in the irradiated model atmosphere and compare it with analytical relation. Subsequently, in Sections 4.1–4.3, we offer an overview of the emission lines which emerged from the irradiation in our models in UV, optical infrared (IR) regions, and also show a list of emission lines which appear irrespective of irradiation in the hottest model considered. Furthermore, in Section 4.4, we focus on the most prominent emission line observed in the highly irradiated spectra and establish the connection with population changes of ions in the irradiated models. Based on this context, we derived the minimum required irradiation

Table 1. List of magnetic stars found in FUSE catalogue.

ID	Sp. type (Simbad)	Reference
HD 23 478	B3IV	Bychkov et al. (2021)
HD 37 151	B8V	Bychkov et al. (2021)
HD 47 777	B3V	Bychkov et al. (2021)
HD 176 386	B9V	Bychkov et al. (2021)
HD 200 311	B9V	Bychkov et al. (2021)
HD 200 775	B2Ve (Herbig obj.)	Bychkov et al. (2021)

for the observation of the most prominent emission line and compared it with the kinetic energy of the wind taken from models and also with the energy emitted from magnetic stars in the radio region.

2 SEARCH FOR EMISSION LINES IN FUSE SPECTRA

The unsuccessful search for auroral lines in *HST* spectra of CU Vir by Krtićka et al. (2019) motivated us to look for their presence in other similar objects.

We selected the FUSE satellite, which has a relatively high-spectral resolution suitable for the search of narrow emission lines. To obtain the list of magnetic stars with available far-UV spectra, we cross-referenced a list of magnetic stars from literature (Petit et al. 2019; Bychkov, Bychkova & Madej 2021) with a list of stars observed by FUSE satellite available in MAST archive. However, only six stars met these criteria, presented in Table 1.

Subsequently, we downloaded spectral data of all magnetic stars supplemented with spectra of stars with similar spectral types for reference (listed in Appendix in Table A1). We compared the spectra of magnetic stars with three reference stars and with one non-irradiated spectrum with effective temperature which was closest to the temperature of a magnetic star. For comparison we scaled spectra to unity within a range 1118–1120 Å (Fig. 1, the remaining spectra are given in Appendix A, Figs A1–A5). Our focus was directed towards the identification of possible emission lines. To mitigate the impact of complex continuum variation, the spectra were subdivided into smaller segments for manual meticulous inspection.

However, due to high noise levels and smaller exposure time than referenced stars, it is notably challenging to classify anything as an emission feature. This challenge underpins our decision not to classify any feature as a potential emission.

3 DESCRIPTION OF IRRADIATED MODEL ATMOSPHERES

Lack of success in searching for auroral emission in the previous section motivated us to calculate the theoretical models explaining the absence of X-ray emission. We modelled the effect of fast electrons coming from magnetospheric reconnection by external X-ray irradiation. Although the exact state of the atmosphere differs for cases of the impact of electrons and X-ray irradiation, the subsequent processes of recombination and de-excitation do not depend on the mechanism of ionization and excitation.

3.1 Model atmospheres and synthetic spectra

We calculated stellar model atmospheres from scratch using the code TLUSTY¹ (Hubeny & Lanz 1995). The code calculates NLTE plane-

¹TLUSTY v. 200

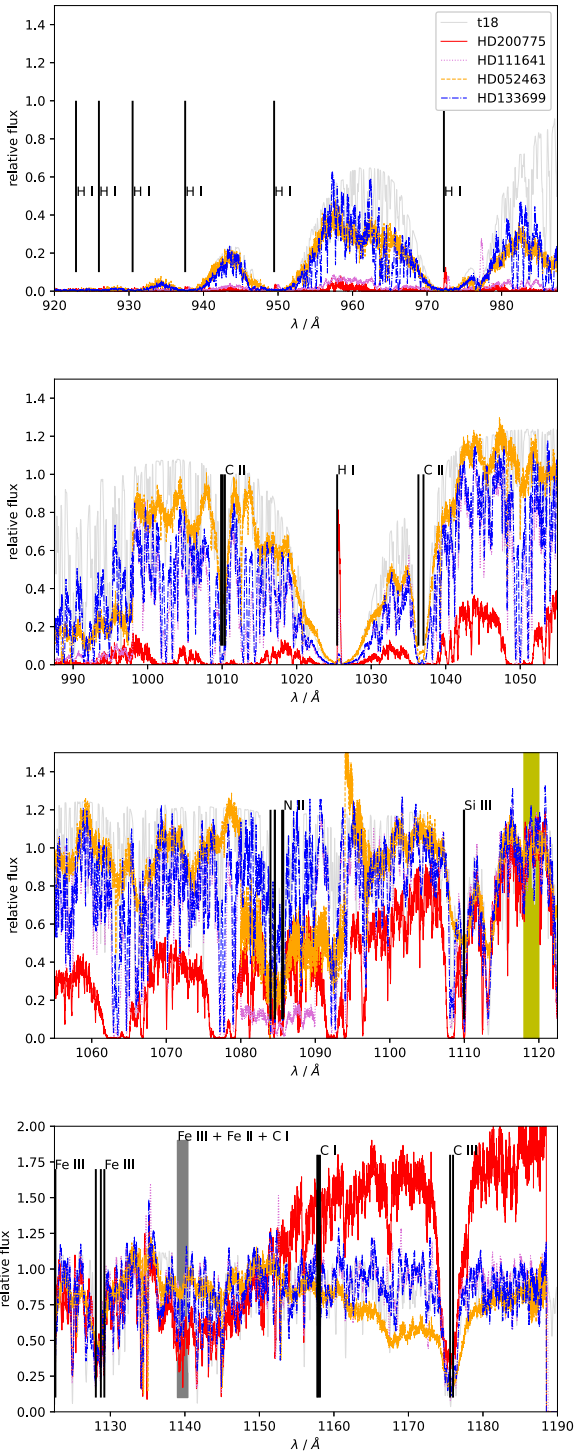


Figure 1. The normalized flux of the magnetic star HD 200775, alongside reference stars and the t18 model. The spectra of all observed stars have been rescaled to unity within the wavelength range of 1118–1120 Å (indicated by filled box), with respect to the t18 model. Prominent absorption lines have also been identified and annotated as thick vertical lines.

parallel model atmospheres in hydrostatic and radiative equilibrium. The models were calculated for different effective temperatures 15, 18, 21, and 30 kK and surface gravity $\log(g/1 \text{ cm s}^{-2}) = 4$ with different amount of external irradiation (Table 2). Metal abundances were set to solar values from Asplund et al. (2009). We calculated

Table 2. Parameters of the models with maximum adopted irradiation.

Model	T_{eff} (kK)	W	$\log(\frac{F_{\text{irrad}}}{F_{\text{bol}}})$
t15w12	15	10^{-12}	−3.771
t18w5_12	18	5×10^{-12}	−3.388
t21w12	21	10^{-12}	−4.355
t30w10	30	10^{-10}	−2.975

models with the following elements in NLTE: H, He, C, N, O, Ne, Mg, Al, Si, S, and Fe.

We employed irradiation in code TLUSTY using photons from the blackbody with the temperature set to $T_{\text{irrad}} = 10^7$ K, while we changed the dilution factor which affects the amount of flux impacting the stellar atmosphere. The dilution factor W of the irradiating flux is applied in the code in the equation $I_{\text{irrad}} = W \times B(T_{\text{irrad}})$. Here $B(T_{\text{irrad}})$ is the Planck function at the temperature T_{irrad} . The atmosphere is irradiated only between the minimum $\nu_{\text{min}} = 1 \times 10^{12}$ Hz and maximum $\nu_{\text{max}} = 5.5 \times 10^{16}$ Hz frequencies of the corresponding TLUSTY model. Therefore, the irradiating flux F_{irrad} is given by an integral of the Planck function between ν_{min} and ν_{max} .

From model atmospheres calculated by TLUSTY, we simulated synthetic spectra using the SYNSPEC² code (Hubeny & Lanz 1995). We have computed spectra for several irradiated and non-irradiated cases in the wavelength range of 900 Å to 10⁵ Å. We used two different line lists in SYNSPEC, one for wavelength under 7500 Å which is included from SYNSPEC web page³ and the second one above 7500 Å with primarily IR lines for the rest taken from the VALD data base (Piskunov et al. 1995). The turbulent velocity has been set to 2 km s^{−1}. We created the spectrum in SYNSPEC taking TLUSTY models as input with only including elements which were solved in NLTE in TLUSTY. This was done to prevent false emission from the heated upper atmosphere which was present when we first calculated the spectrum including elements which SYNSPEC calculated only in LTE. Subsequently, we applied the code ROTIN on calculated spectra to perform rotational and instrumental convolution. We assumed rotation of the star with $v_{\text{rot}} = 30 \text{ km s}^{-1}$.

3.2 Physical changes in the irradiated model atmospheres

We investigated changes induced by strong irradiation in stellar model atmospheres. For the case of the atmosphere of a grey accretion disc with external irradiation, Hubeny (1990, equation 3.23) introduced a penetration depth

$$\tau_{\text{pen}} = \frac{4}{3} W \left(\frac{T_{\text{irrad}}}{T_{\text{eff}}} \right)^4, \quad (1)$$

which separates regions of a dominant and weak influence of irradiation. In equation (1), we employed the corrected T_{irrad} , which corresponds to a blackbody that emits the same flux as used to irradiate model atmospheres. The effect of irradiation becomes negligible for optical depths higher than the penetration depth, while the atmosphere is strongly heated by irradiation above the penetration depth.

For our specific cases, the penetration depth from equation (1) does not exceed 0.02, even for the hottest model with the strongest irradiation. This is demonstrated in Fig. 2, where we compare the

²SYNSPEC v. 49

³<http://tlusty.oca.eu/Synspec49/synspec.html>

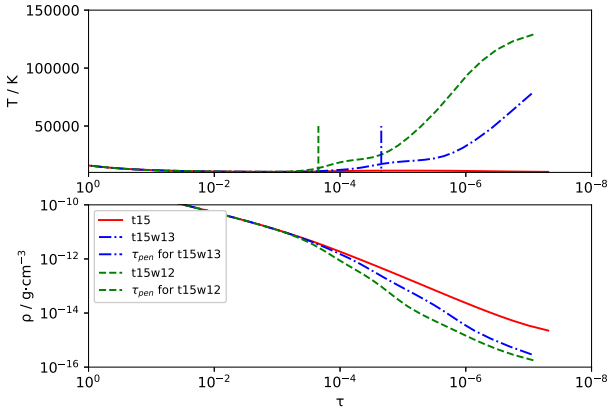


Figure 2. Variations of density and temperature as a function of the Rosseland mean optical depth in the models with and without irradiation. Plotted for the effective temperature 15 kK. The solid line denotes the model without irradiation, the dashed line denotes irradiation with a dilution factor set to 1×10^{-13} , and the dashed-dotted line denotes irradiation with dilution factor set to 1×10^{-12} . Upper panel: variations of temperature. Vertical dashed/dashed-dotted lines represent the calculated value of penetration depth from equation 1 for specified dilution and flux F_{irrad} from the irradiated body. Lower panel: variations of density.

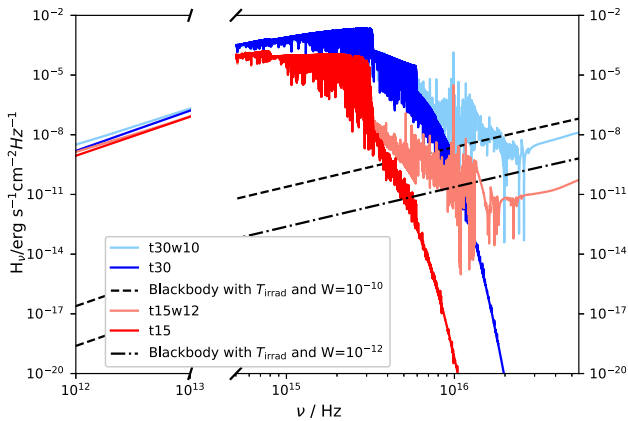


Figure 3. Emergent Eddington flux as a function of frequency for model atmospheres with and without irradiation. Dashed and dot-dashed lines correspond to the blackbody spectrum multiplied by a corresponding dilution factor.

variations of temperature in irradiated and non-irradiated model atmospheres, and we also marked the penetration depth for specific models. Only the outermost part of the atmosphere, where the Rosseland mean optical depth is significantly lower than one, experiences significant heating. The optical depth of the region where the irradiation starts to heat the atmosphere nicely agrees with penetration depth from equation 1. Additionally, as a result of hydrostatic equilibrium, the heating process results in a slight decrease in density within irradiated regions. Altered conditions have important implications for the modelling of stellar wind in irradiated stars due to adjustments of velocity and density at the base of the wind.

In Fig. 3, we show flux energy distribution for t15 and t30 models. From the plots, it follows that the changes caused by irradiation appear primarily at high frequencies.

4 SEARCH FOR EMISSION LINES IN SYNTHETIC SPECTRA

4.1 Change of the spectrum in UV

To search for emission lines in synthetic spectra, we calculated the difference in Eddington fluxes between the maximally irradiated and non-irradiated models from the SYNSPEC code. This difference was then divided by the theoretical non-irradiated continuum, $(H_{\lambda, \text{irrad}} - H_{\lambda, \text{non-irrad}})/H_{\lambda, \text{cont}}$, and plotted as a function of wavelength in Figs 4 and 5. To focus on significant emission lines, we adopted an arbitrary threshold of 5 per cent for the selection of emission lines from the relative spectra. When selecting this value we took into account challenges encountered in practical spectrum analysis related to factors such as wind, reddening, and so on. We also understand that the value of the threshold together with rotational convolution can increase or decrease the number of emission lines found, as we observed that higher rotational convolution stretches the emission.

Initially, our focus was directed towards the UV part of the spectrum. A comparison between emergent fluxes in the UV domain is shown in Fig. 4. We identified a few lines with emission features in the cores of absorption lines, nevertheless, their intensity is lower than the hypothetical continuum at a given wavelength. The most prominent of these emission features are shown in insets in Fig. 4. Several irradiated models exhibited lines with significantly stronger absorption features, particularly prominent were a doublet N V λ 1242, numerous blended Fe II and Fe III lines near λ 1084, a doublet Si IV λ 1402, a doublet C IV λ 1550, He II λ 1640, C III λ 2296, O II λ 2733, and He II λ 3203. However, in the case of Si IV λ 1402 for the irradiated t30 model, there was the inverse effect and the absorption feature was weaker. This suggests that irradiation has the potential to induce stronger absorption in a few elements. Even without consideration of X-ray irradiation, the identification of most of the emission or absorption features in UV stellar spectra poses a significant challenge, primarily attributable to the interplay of numerous factors. These include the determination of abundance, effective temperature and gravity, the presence of weak stellar wind, instrumental noise, and the influence of NLTE effects. Precise determination at a fine spectral scale is hindered by these factors. Moreover, the stronger or weaker absorption caused by irradiated spectra introduces another layer of complexity, making it even more susceptible to misinterpretation. To summarize this effort, we did not find any significant emission lines in the UV spectral region in our set of irradiated models. This explains the missing UV emission lines in CU Vir (Krtićka et al. 2019).

4.2 Lines in optical and NIR regions, and emission lines resulting from increased effective temperature

We found no significant emission line created by irradiation, stronger than 5 per cent, compared to non-irradiated models within the 2500–18000 Å wavelength range.

Still, in the t30 model, we identified a few emissions that appeared either as absorption lines or as a continuum without features in cooler models. These lines were found even in the model without irradiation, therefore, they are not caused by irradiation as per se but rather by the increase of effective temperature, indicating NLTE effects. Emission lines stronger by more than 5 per cent than continuum only in t30 model even without irradiation include C II λ 9903 Å, He I λ 10830 Å, Si II λ 13395 Å, Si III λ 13644 Å, H I λ 18750 Å, He I λ 21655 Å, He I λ 26252 Å. Additionally, in models under irradiation, the majority of these lines weakened with increasing irradiation.

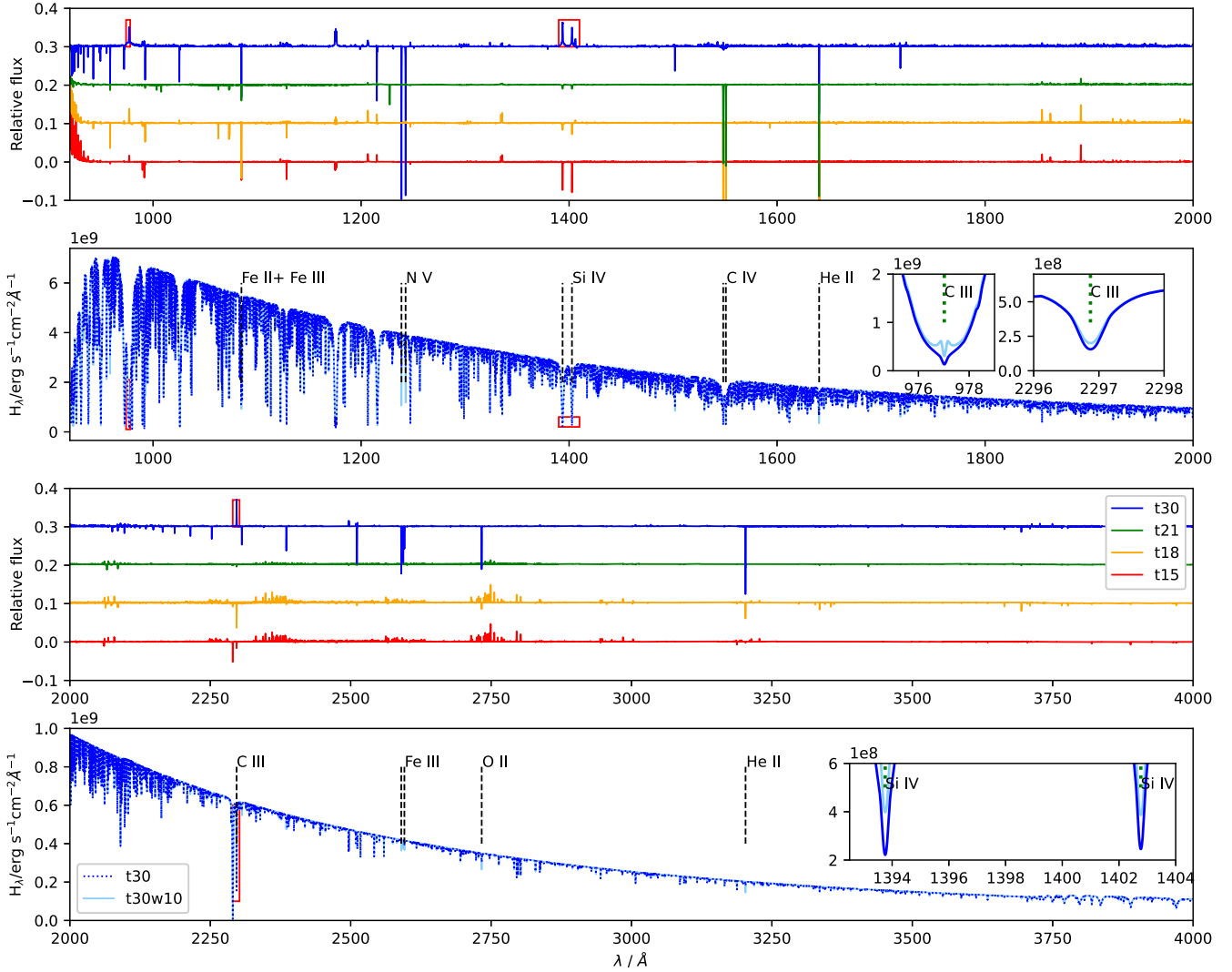


Figure 4. Comparison of irradiated and non-irradiated fluxes in the UV domain. The first and third panels give relative flux differences defined as the difference between irradiated model flux with adopted W given in Table 2 and non-irradiated flux divided by continuum. The plots for different effective temperatures are vertically shifted for better visibility. The second and fourth panels plot the Eddington fluxes of the t30 irradiated model (light solid line) and non-irradiated model (darker dashed line). The dashed vertical lines identify prominent lines. The insets show three zoomed-in parts of the Eddington flux in the regions where the relative flux shows at least a 5 per cent increase. They are also shown in the relative and also in absolute figures with red rectangles around them.

In the case of the $H\alpha$ $\lambda 6562$ Å line, the X-ray irradiation leads to a stronger absorption in the t18 and t30 models. For the t30 model, additional absorption of $He II$ $\lambda 6559$ Å becomes visible in the wing of $H\alpha$.

4.3 Emission lines in long-wavelength infrared

In the extended search to the IR part of the spectrum from 18 000 to 10^5 Å, we found many candidate emission lines. All potential candidate lines are listed in Table 3 sorted based on the number of models where the lines are present. Because models t18w5_12 and t30w10 are the most irradiated, we plotted them in Fig. 5, where we show relative Eddington flux plotted in the IR part of the spectrum. Except for the emission lines, we observed a relative increase in the continuum flux with a wavelength in both models. The corresponding IR excess is especially prominent in the case of the t30w10 model because the relative flux difference is higher than the adopted threshold of 5 per cent for wavelengths longer than $6 \mu\text{m}$.

4.4 The most prominent line

For a more detailed study, we focused on the most prominent candidate for the emission line. We selected the $He II$ 69458 Å emission line which was found in all irradiated models. This line corresponds to the transition between levels with principal quantum numbers 8 and 9. In comparison, we can also find strong emission at 97 104 Å in models t18 and t30, which represents the transition line of $He II$ between $n = 9$ and $n = 10$. Nevertheless, the transition line of $He II$ generated from $n = 7$ to $n = 8$ is at 47 620 Å was not found to generate emissions in any model.

We inspected changes in the population of $He II$ in $n = 9$ level and $He III$, and at the same time, we checked the Eddington flux around $He II$ 69458 Å line. This is shown for models t18, t21, and t30 in Figs 6–9. From the figures, it follows that the upper layers of irradiated atmospheres are not just heated but the population of these states is by ten orders of magnitude higher than in non-irradiated cases.

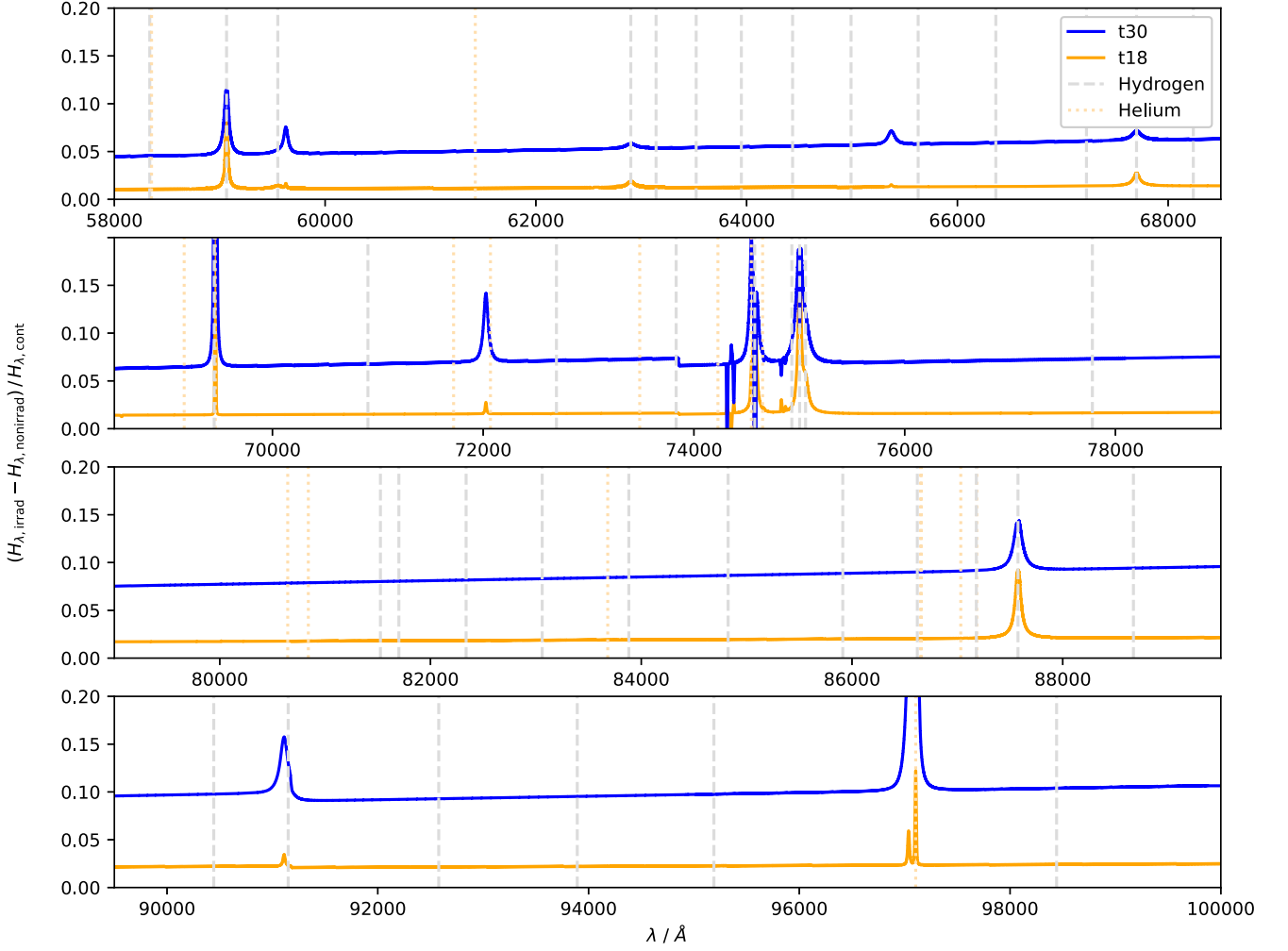


Figure 5. Relative flux differences defined as the difference between irradiated model flux with adopted W given in Table 2 and non-irradiated flux divided by continuum for t30 and t18 models. Selected hydrogen lines (dashed vertical lines) and helium lines (dotted vertical lines) are marked. The flux excess of the t30 model is more than 5 per cent of the theoretical continuum and increases with wavelength.

Table 3. Candidates emission lines from models.

Present in model/s	Candidate emission line wavelength in Å
t15, t18, t21, t30	69 458 (He II)
t15, t18, t30	75 003 (H I), 97 104 (He II)
t15, t30	40 493 (He II)
t18, t30	37 394 (H I), 46 524 (H I), 55 810 (He II),
–	59 064 (H I), 74 576 (H I),
–	74 585 (H I), 87 575 (H I)
t30 UV	976 (C III), 1393 (Si IV), 1402 (Si IV),
–	2296 (C III)
t30 IR	18 742, 28 251, 30 945,
(All He II)	40 510, 42 171, 60 960+ ^a

^aNote. Whole continuum for irradiated t30 model is higher than threshold for these wavelengths.

We also inspected b-factors of various levels of He II. In colder non-irradiated models b-factors tend to hover around unity even within regions characterized by lower Rosseland optical depth $\tau < 10^{-4}$. This trend also explains the adequateness of LTE models for colder stars. In contrast, for the hottest model in the non-irradiated case, the b-factors exhibit a more complex, but descending pattern for all ionization levels, and only in the case of $n = 20$ level, which

is the highest level considered in TLUSTY, the b-factor is near unity. However, in the case of irradiated models, the b-factors for He II are significantly higher reaching up to 10^6 for $n = 1$ within the low-optical depth region. As the excitation energy increases, the b-factors significantly decrease. Notably for $n > 5$, the b-factors consistently remain below ~ 2 . Levels with higher excitation energies tend to have more complex behaviour around $\tau \sim 10^{-4}$, marking the region where the temperature starts to increase in comparison with non-irradiated models. But as the opacity decreases, collective behaviour becomes evident, they are approaching unity similarly as if this region was in LTE.

We used the transition He II 69 458 Å to calculate the minimum required irradiation for which this line can be observed. We fitted minimum irradiation for which was emission shown versus the effective temperature of models. The fit is

$$\log(F_{\text{irrad}}/F_{\text{bol}}) = -2.406 - 0.1333 \times (T_{\text{eff}}/10^3 \text{ K}), \quad (2)$$

where F_{bol} is bolometric flux of model with given temperature and F_{irrad} is irradiated flux. For a given temperature, we can calculate the ratio of irradiated flux to bolometric flux required to observe the emission line. This relationship can be expressed as a linear fit of irradiation as a function of the effective temperature of the models,

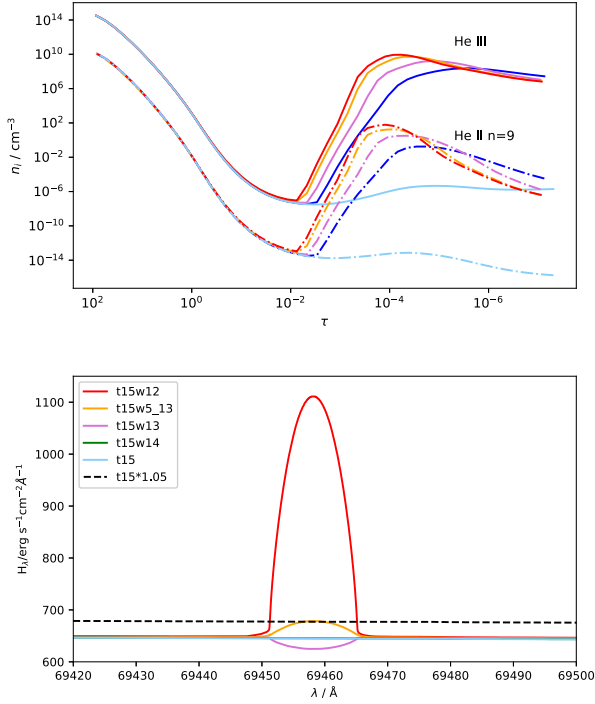


Figure 6. Model t15. Upper panel: population of He III (solid lines) and He II (dash-dotted lines) with a principal quantum number equal to nine for different values of irradiation as a function of Rosseland optical depth. Legend is same for both panels. The stronger irradiation causes higher ionization. The label w13 denotes $W = 10^{-13}$ and w5_13 denotes $W = 5 \times 10^{-13}$ etc. Bottom panel: Eddington flux around He II 69458 Å line for different values of irradiation. Dashed line marks adopted a threshold for classifying emissions as observable.

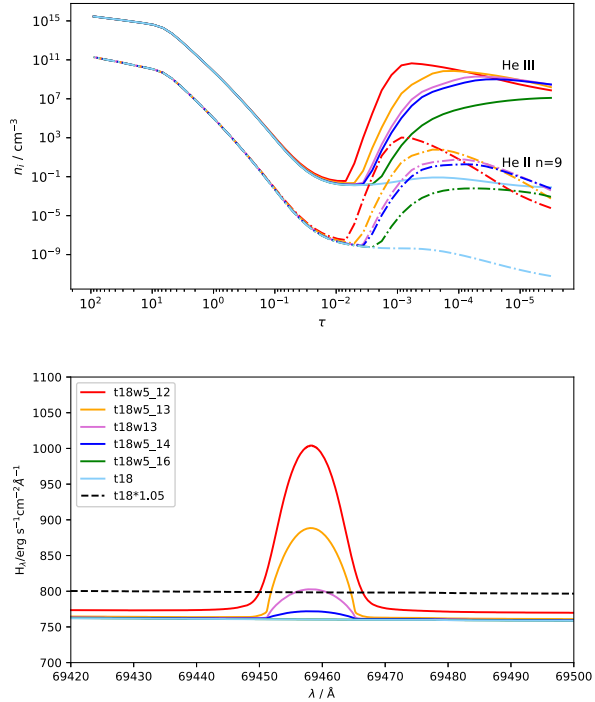


Figure 7. Same as Fig. 6 but for t18 model.

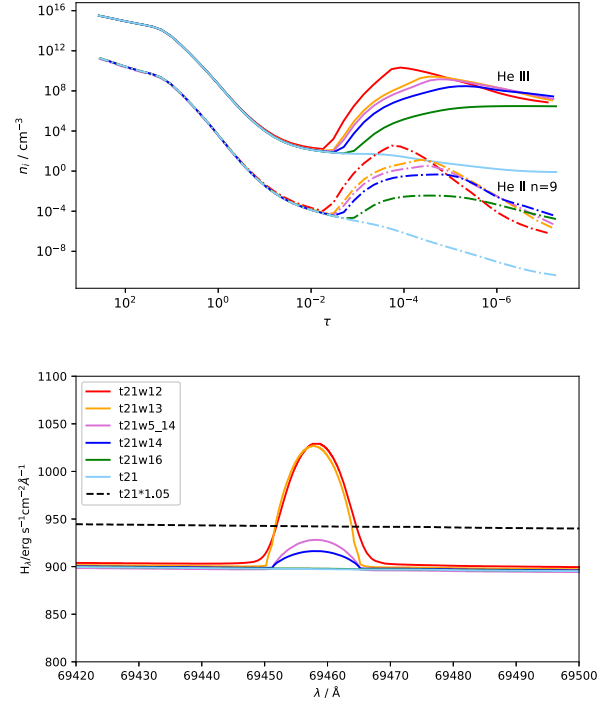


Figure 8. Same as Fig. 7 but for t21 model.

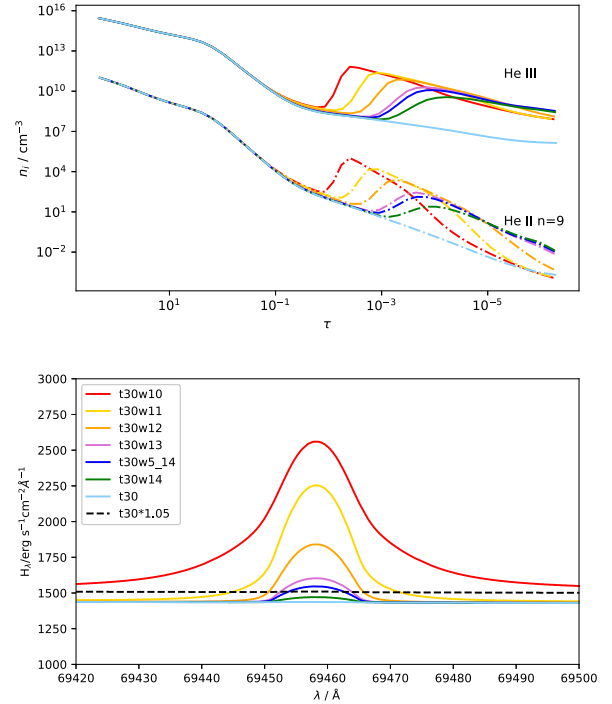


Figure 9. Same as Fig. 7 but for t30 model.

yielding the equation

$$\log(F_{\text{irrad}}/1 \text{ erg cm}^{-2} \text{ s}^{-1}) = 8.931 - 0.05479 \times (T_{\text{eff}}/10^3 \text{ K}). \quad (3)$$

We also plotted this fit in Fig. 10 for better representation. From this fit, we conclude that the required irradiation for generating an emission line is lower for a higher effective temperature of the star.

We also compared the minimum flux required to generate emission with stellar wind kinetic energy flux $\dot{M}v_{\infty}^2/(8\pi R^2)$ predicted for

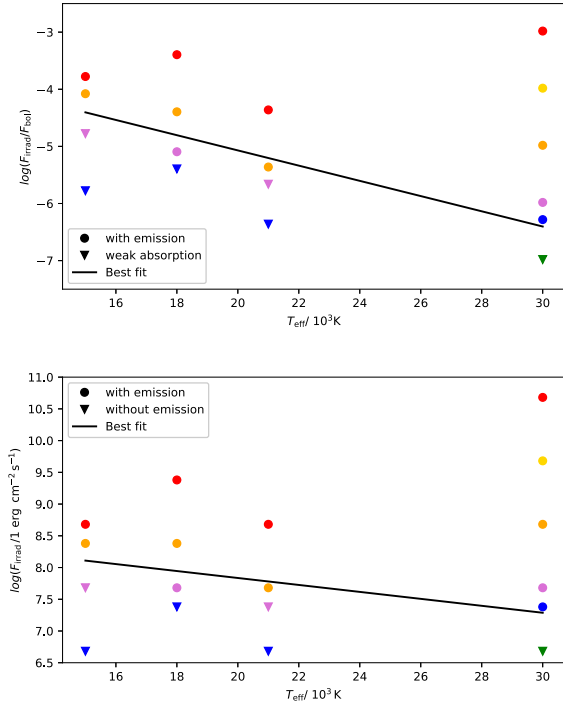


Figure 10. Grid of calculated models. We plot X-ray irradiation as a function of effective temperature. Models with emission lines present in the spectra are marked using circles with the same colour as in Fig. 6–9. Models where the emission is absent are marked using triangles. The solid line is the fit equations (2) and (3) of the minimum irradiation where the emission emission is present. The fit is based on t18, t21, and t30 models. Upper panel: ordinate is the logarithm of the ratio of irradiated flux to the flux of the model. Bottom panel: ordinate is the logarithm of the irradiated flux.

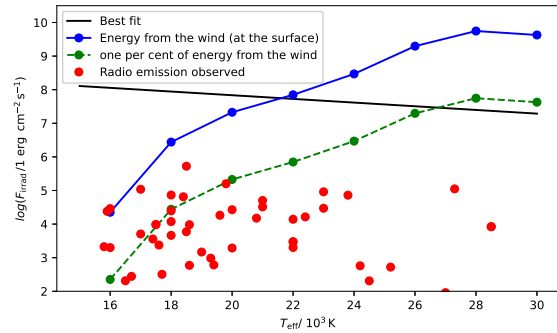


Figure 11. Comparison of the fit (solid black line) of the irradiation required to observe emission lines with energy generated in the wind (solid line with models marked with a circle, Krtićka 2014). Circles are integrated radio emissions from observations collected by Shultz et al. (2022). The dashed line represents 1 per cent of energy from the wind.

solar-metallicity main-sequence B stars (Krtićka 2014) and mean radio flux observed in magnetic early-type stars (Shultz et al. 2022) in Fig. 11. To calculate the radio flux, we derived the radius of the star from the luminosity and effective temperature given in Shultz et al. (2022).

Based on our models (Fig. 11), we concluded that the energy delivered from the wind is capable of inducing emission in stars with effective temperature exceeding 22 kK. However, if, for instance, only 1 per cent of the wind energy can be converted into irradiation

energy, then emission can be observed in stars with effective temperatures higher than 27 kK.

These findings may provide insight into understanding the challenges encountered in uncovering auroral lines, as demonstrated by Krtićka et al. (2019). In their study of CU Vir ($T_{\text{eff}} \approx 13$ kK), attempts to identify auroral lines in the UV region of CU Vir proved unsuccessful. Our models indicate that for this star, characterized by low effective temperature and weak observed X-ray emission (Robrade et al. 2018), the X-ray intensity alone is not sufficient to generate emission lines. Instead of emission lines, the irradiation in the UV part of the spectrum would manifest by stronger absorption features in a few specific lines. From this, it follows that hotter single or binary stars are more suitable candidates to search for emission lines, because the energy converted from mass-loss in hotter stars could be sufficient to generate observable auroral lines.

5 DISCUSSION

Our finding suggests that the emission lines due to intense X-ray irradiation may appear mainly in the IR domain. This is in agreement with results in literature (Hubeny & Mihalas 2014, equation 5.12), which state that within the IR regime, where the energy difference between two levels l and u divided by Boltzmann constant times the temperature is much less than one, or in physics notation $h\nu_{lu}/kT \ll 1$, emission in lines stemming from NLTE effects becomes notably more probable. From our model, the irradiation influences the formation of emission lines in the IR domain, in particular of hydrogen and helium.

Existing literature has reported the occurrence of X-ray emission in B-type stars with luminosities on the order of $\log(L_X/L_{\text{bol}}) = -7$ (Robrade et al. 2018). Notably, there are also stars with even stronger X-ray emission with $\log(L_X/L_{\text{bol}}) > -5$ (Berghoefler, Schmitt & Cassinelli 1996). Based on our work, these stars have the potential to exhibit infrared emission lines as effects of X-ray irradiation. However, we want to point out that our computational models revealed more subtle effects, the weaker and stronger absorption features in different lines in the UV portion of the spectrum, which can probably also be detectable.

A critical assumption underlying our work is that the effect of impacting electrons on the atmosphere can be adequately approximated with a weakened blackbody irradiation with a specific temperature. But for example in the Sun, the bremsstrahlung radiation is produced when the plasma particles, which are accelerated in the magnetic reconnection, inject the solar chromosphere. In this region two types of bremsstrahlung are produced: hard X-rays (above 20 keV) by relativistic particles and soft X-rays by strongly heated but thermal plasma (Dennis & Zarro 1993). However, during the solar flare and activity, the coronal plasma is strongly heated and is expected to emit thermal radiation. Similar consideration can be also relevant for stellar activity (ud-Doula, Townsend & Owocki 2006). However, in our model, we assumed that the particles released from the reconnection do not significantly penetrate the stellar atmosphere and their energy is reemitted as electromagnetic radiation. While this can be true in the solar case, relativistic electrons may have different penetration depths and different spectra, which is bremsstrahlung in nature. This is different from photons, whose penetration depth is given by opacity, and they are not repelled by electric charge. In the future, we plan to test the effect of modification of irradiation spectra and analyse relativistic impacting electrons. In any case, the energy transferred from impacting electrons and photons should be equal.

Irradiation in TLUSTY was also modelled by Vučković et al. (2016). Their irradiating flux had an effective temperature of 42 kK

and dilution factor was much higher than in our case (in the order of one hundredth). Therefore, our model has much more energetic but more diluted irradiation. Despite these differences, we both found that the physical changes in temperature, density, and pressure deep inside the star were negligible in comparison with non-irradiated models. Moreover, despite different irradiation parameters, the irradiation was changing the spectrum very subtly (Németh private communication).

A similar analysis of irradiated hydrogen NLTE model atmospheres of B stars was conducted in Kubát (2000), but with only hydrogen. Irradiation in both analyses affected the outer layers of models, but, in our case, the same irradiation caused the same increase in the temperature versus mass in the outer parts in all models independent of the effective temperature of the model. We attribute the differences to the fact that we use models including elements heavier than hydrogen. As opposed to the case of the pure hydrogen model, in models with heavy elements, most atoms are not fully ionized in t30 models, and, consequently, may still show emission lines. Additionally, hydrogen lines in proximity to $7.5 \mu\text{m}$ did not exhibit a monotonic correlation with increasing irradiation across all effective temperatures. Particularly, in the case of the irradiated t30 model, we observed a more complex relationship with irradiation.

Madej & Róžańska (2000) modelled a spectrum of a B3 V star irradiated by a thermal X-ray source with $T_{\text{irrad}} = 10^8 \text{ K}$. However, they focused on the UV and X-ray part of the spectra including only hydrogen, helium, and iron in LTE. Because of that the comparison of spectra cannot be done. Comparison of temperature versus optical depth showed a very similar pattern to our results, that is, heating of the outer parts of the atmosphere. In their case with higher irradiation $\log W \sim -16$ hydrogen behaved as in thermal equilibrium and caused the disappearance of the Lyman jump. However, they assumed a significantly higher irradiation flux than we included in our analysis, because we account just for a fraction q of irradiating blackbody given by the maximum frequency of the models. Our models did not converge for that high irradiation. For instance, the t18 model would require $\log W \sim -16 - 4 \log \left(\frac{T_{\text{rad}}}{T_{\text{irrad}}} \right) - \log q \sim -9$ to observe the disappearance of Lyman jump. After analysis of the flux immediately below 912 \AA , we identified that the flux increased in the irradiated versus non-irradiated model in all cases. For the cooler models, the increase was most visible and was approximately three times for the t15 model, two times in the t18 model, and roughly 20 per cent for the t21 model. For the t30 model, flux increased only in the order of per cent.

6 CONCLUSIONS

In this study, we searched for potential emission features in the FUSE spectra of magnetic stars, which contain spectral regions near the Lyman limit, and also analysed irradiated synthetic spectra. Our goal was to identify any potential auroral emission lines in spectra. In FUSE spectra we did not classify any emission features that could be attributed to the auroral emission of magnetic stars.

We conducted a comprehensive analysis and search for auroral lines in the synthetic spectra of OB stars. These auroral lines are a direct consequence of the ionization of the atmosphere resulting from the impacting electrons generated during magnetospheric reconnection events. To examine the impact of these electrons, we replaced electrons with a simplified X-ray irradiation model.

We found out that model atmospheres with X-ray irradiation show a significant increase in the temperature of the upper layers of the stellar atmospheres. This caused only a subtle effect in the UV region,

specifically weak emission or absorption components appearing in the centres of a few strong absorption lines.

The effects of high-energy irradiation are more pronounced in the long-wavelength region and lead to the appearance of several emission lines and infrared excess. In the IR part of the spectra, we compiled a list of potential emission lines. We selected the most prominent line He II 69458 \AA , which was observed in all our irradiated models and used it for the next analysis. Based on this prominent He II 69458 \AA line, we determined the minimum irradiation threshold necessary to observe the emission.

Subsequently, we calculated the best fit for the minimal required irradiation as a function of effective temperature, based on the basic assumption that the required irradiation solely depends on the effective temperature of the model. Fit shows that the required irradiation for observing the most prominent line decreases with increasing effective temperature, meaning that for hotter stars less irradiation is needed for the appearance of emission. Admittedly, hot stars can exhibit very strong radiatively driven winds, which can also serve as a source of emission in line and obstruct the detection of the auroral lines.

ACKNOWLEDGEMENTS

We would like to thank Dr Filip Hroch for the maintenance of the old MIRSAM server, which was used for the main part of the calculation of models, and for restoring the server after one of us had accidentally halted it. Next, we want to thank Dr Jan Benáček for the beneficial communication about Solar flares. We also thank Dr Péter Németh for discussing the influence of irradiation on stars and for sharing his experience with irradiation in code TLUSTY. We thank Dr Ján Budaj and Dr Martin Piecka for many stimulating conversations. Furthermore, we thank the anonymous referee for the valuable comments and suggestions, which have significantly improved the clarity and flow of the manuscript. And last but not least, we thank Dr Ivan Hubený for his time and his willingness to help with difficult questions about code TLUSTY.

DATA AVAILABILITY

TLUSTY and SYNSPEC are open-source software. The spectroscopic data underlying this work are free to download from the MAST archive and model atmospheres generated from TLUSTY will be shared on reasonable request to the corresponding author.

REFERENCES

- Alexeeva S. A., Ryabchikova T. A., Mashonkina L. I., 2016, *MNRAS*, 462, 1123
- Asplund M., Grevesse N., Sauval A. J., Scott P., 2009, *ARA&A*, 47, 481
- Badman S. V., Branduardi-Raymont G., Galand M., Hess S. L. G., Krupp N., Lamy L., Melin H., Tao C., 2015, *Space Sci. Rev.*, 187, 99
- Berghoefer T. W., Schmitt J. H. M. M., Cassinelli J. P., 1996, *A&AS*, 118, 481
- Bychkov V. D., Bychkova L. V., Madej J., 2021, *A&A*, 652, A31
- Castelli F., Hubrig S., 2004, *A&A*, 425, 263
- Das B. et al., 2022b, *ApJ*, 925, 125
- Das B., Chandra P., Shultz M. E., Leto P., Mikulášek Z., Petit V., Wade G. A., 2022a, *MNRAS*, 517, 5756
- Dennis B. R., Zarro D. M., 1993, *Sol. Phys.*, 146, 177
- Gustin J., Grodent D., Radioti A., Pryor W., Lamy L., Ajello J., 2017, *Icarus*, 284, 264
- Hubeny I., 1990, *ApJ*, 351, 632
- Hubeny I., Lanz T., 1995, *ApJ*, 439, 875

- Hubeny I., Mihalas D., 2014, *Theory of Stellar Atmospheres*. Princeton Univ. Press, Princeton, NJ p. 118
- Krtićka J. (2014) *Astronomy & Astrophysics*, A70 , 0004-6361
- Krtićka J. et al., 2019, *A&A*, 625, A34
- Kubát J., 2000, in Smith M. A., Henrichs H. F., Fabregat J., eds, ASP Conf. Ser. Vol. 214, IAU Colloq. 175: The Be Phenomenon in Early-Type Stars. Astron. Soc. Pac., San Francisco, p. 705
- Lamy L. et al., 2011, *J. Geophys. Res.*, 116, A04212
- Leto P. et al., 2020, *MNRAS*, 493, 4657
- Leto P. et al., 2021, *MNRAS*, 507, 1979
- Madej J., Rózańska A., 2000, *A&A*, 363, 1055
- Marcolino W. L. F., Bouret J. C., Sundqvist J. O., Walborn N. R., Fullerton A. W., Howarth I. D., Wade G. A., ud-Doula A., 2013, *MNRAS*, 431, 2253
- Mashonkina L., 2020, *MNRAS*, 493, 6095
- Molyneux P. M. et al., 2014, *Planet. Space Sci.*, 103, 291
- Moos H.W. et al., 2000, *ApJ*, 538, L1
- Morel T. (2015) *Proceedings of the International Astronomical Union*, 342 , 1743-9213
- Nagasawa S., Kawate T., Narukage N., Takahashi T., Caspi A., Woods T. N., 2022, *ApJ*, 933, 173
- Nazé Y., Sundqvist J. O., Fullerton A. W., ud-Doula A., Wade G. A., Rauw G., Walborn N. R., 2015, *MNRAS*, 452, 2641
- Nichols J. D., Burleigh M. R., Casewell S. L., Cowley S. W. H., Wynn G. A., Clarke J. T., West A. A., 2012, *ApJ*, 760, 59
- Oksala M. E., Grunhut J. H., Kraus M., Borges Fernandes M., Neiner C., Condori C. A. H., Campagnolo J. C. N., Souza T. B., 2015, *A&A*, 578, A112
- Owocicki S. P., Shultz M. E., ud-Doula A., Chandra P., Das B., Leto P., 2022, *MNRAS*, 513, 1449
- Owocicki S. P., Shultz M. E., ud-Doula A., Sundqvist J. O., Townsend R. H. D., Cranmer S. R., 2020, *MNRAS*, 499, 5366
- Petit V. et al., 2019, *MNRAS*, 489, 5669
- Piskunov N. E., Kupka F., Ryabchikova T. A., Weiss W. W., Jeffery C. S., 1995, *A&AS*, 112, 525
- Robrade J., Oskinova L. M., Schmitt J. H. M. M., Leto P., Trigilio C., 2018, *A&A*, 619, A33
- Romanova M. M., Owocicki S. P., 2016, in Beskin V. S., Balogh A., Falanga M., Lyutikov M., Mereghetti S., Piran T., Treumann R. A., eds, *Space Sciences Series of ISSI Vol. 54, The Strongest Magnetic Fields in the Universe*. Springer-Verlag, Berlin, p. 347
- Sadakane K., Nishimura M., 2017, *PASJ*, 69, 48
- Sahnou D.J. et al., 2000a, *Proc. SPIE*, 4013, 334
- Sahnou D.J. et al., 2000b, *Proc. SPIE*, 4139, 131
- Shultz M. E. et al., 2018, *MNRAS*, 475, 5144
- Shultz M. E. et al., 2022, *MNRAS*, 513, 1429
- Shultz M. E., 2020, in Wade G., Alecian E., Bohlender D., Sigut A. eds, *Proc. Polish Astron. Soc. Vol. 11, Stellar Magnetism: A Workshop in Honour of the Career and Contributions of John D. Landstreet*. p. 54
- Soret L., Gérard J.-C., Libert L., Shematovich V. I., Bisikalo D. V., Stiepen A., Bertaux J.-L., 2016, *Icarus*, 264, 398
- Townsend R. H. D., Owocicki S. P., 2005, *MNRAS*, 357, 251
- Trigilio C., Leto P., Umana G., Buemi C. S., Leone F., 2011, *ApJ*, 739, L10
- Trigilio C., Leto P., Umana G., Leone F., Buemi C. S., 2004, *A&A*, 418, 593
- ud-Doula A., Nazé Y., 2016, *Adv. Space Res.*, 58, 680
- ud-Doula A., Owocicki S. P., 2002, *ApJ*, 576, 413
- ud-Doula A., Owocicki S. P., Townsend R. H. D., 2008, *MNRAS*, 385, 97
- ud-Doula A., Owocicki S., 2022, *Handbook of X-ray and Gamma-ray Astrophysics*. Springer-Verlag, Berlin, p. 46
- ud-Doula A., Townsend R. H. D., Owocicki S. P., 2006, *ApJ*, 640, L191
- Vidotto A. A., Feeney N., Groh J. H., 2019, *MNRAS*, 488, 633
- Vučković M., Østensen R. H., Németh P., Bloemen S., Pápics P. I., 2016, *A&A*, 586, A146
- Yakunin I. A., Romanyuk I. I., Mikulášek Z., Janík J., Moiseeva A., Hümmelich S., 2020, *Azerbaijani Astron. J.*, 15, 93

APPENDIX A: FUSE SPECTROSCOPY OF MAGNETIC STARS

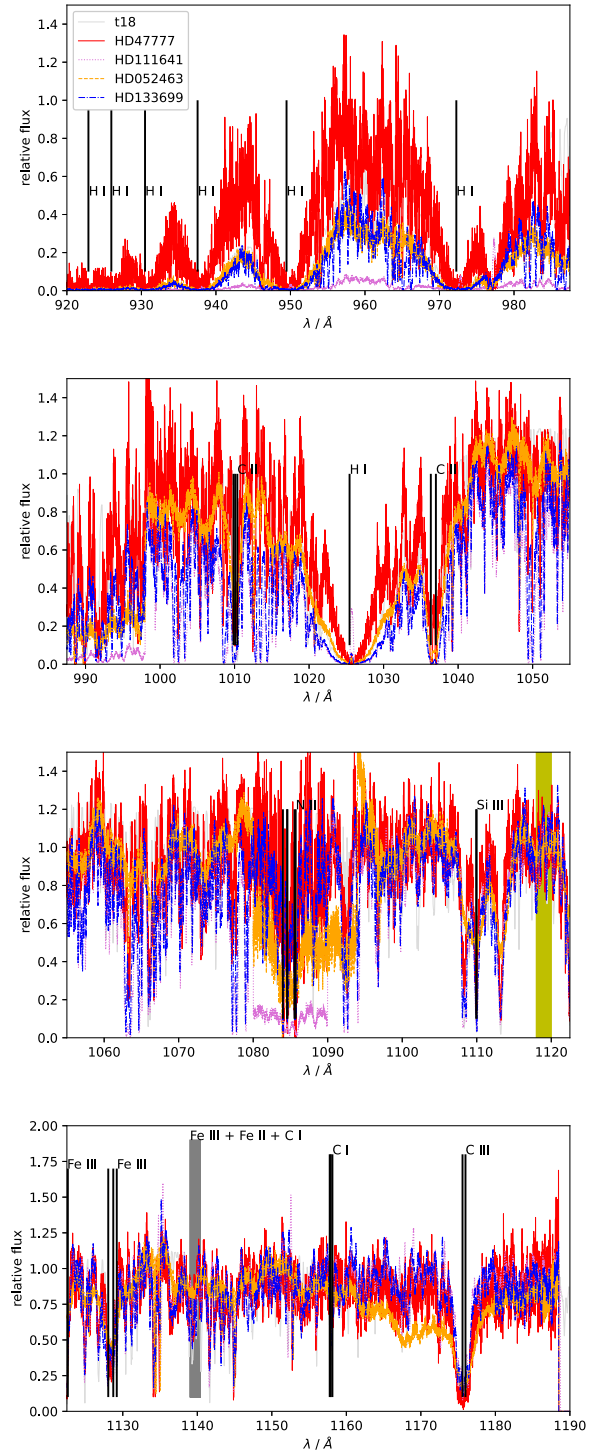


Figure A1. Same as Fig. 1, but for magnetic star HD 47777 and t18 model.

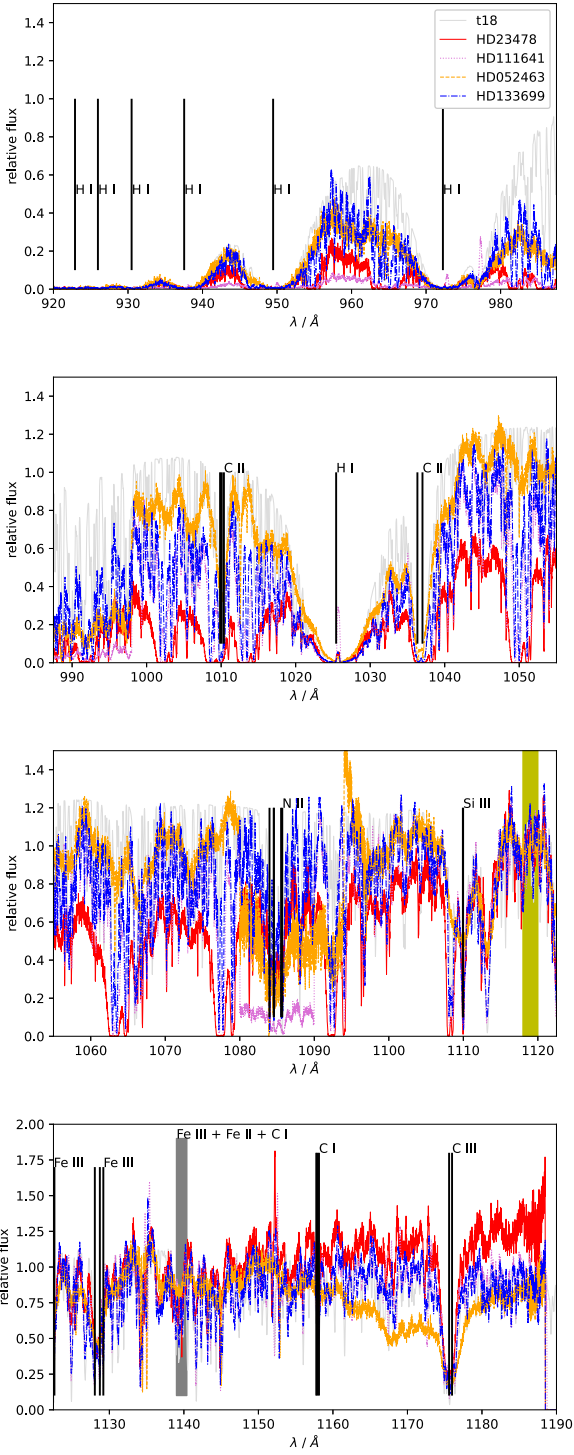


Figure A2. Same as Fig. 1, but for magnetic star HD 23478 and t18 model.

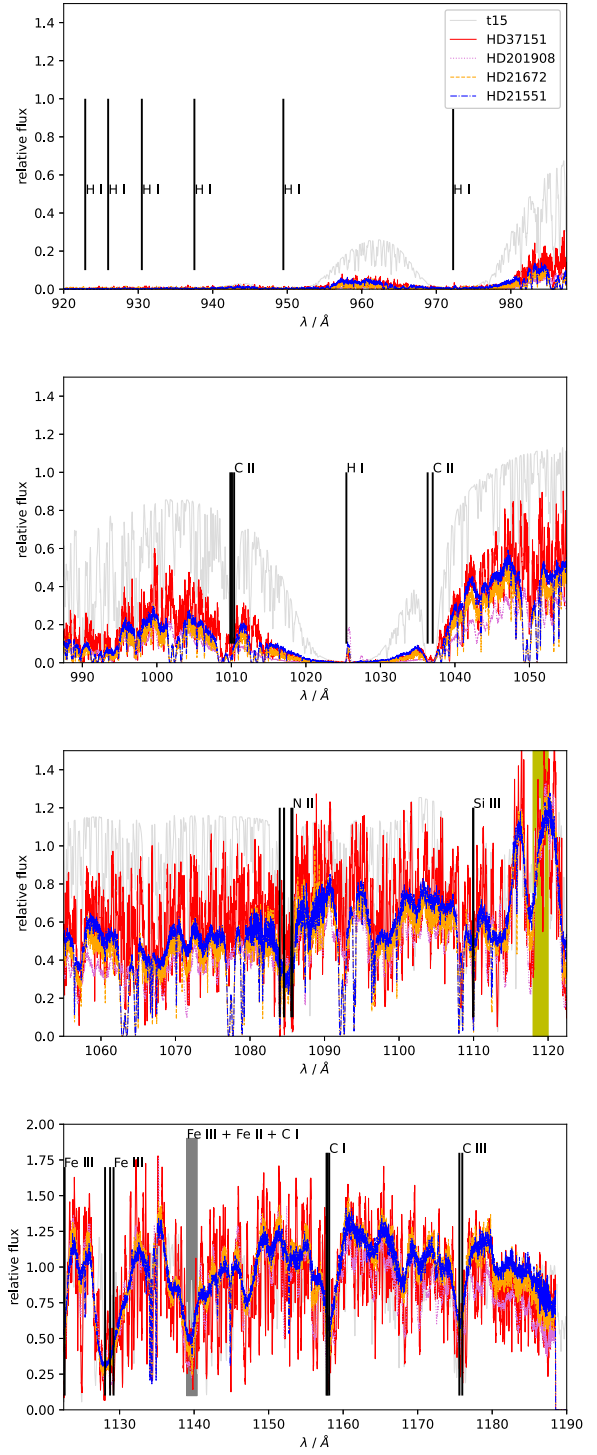


Figure A3. Same as Fig. 1, but for magnetic star HD 37151 and t15 model.

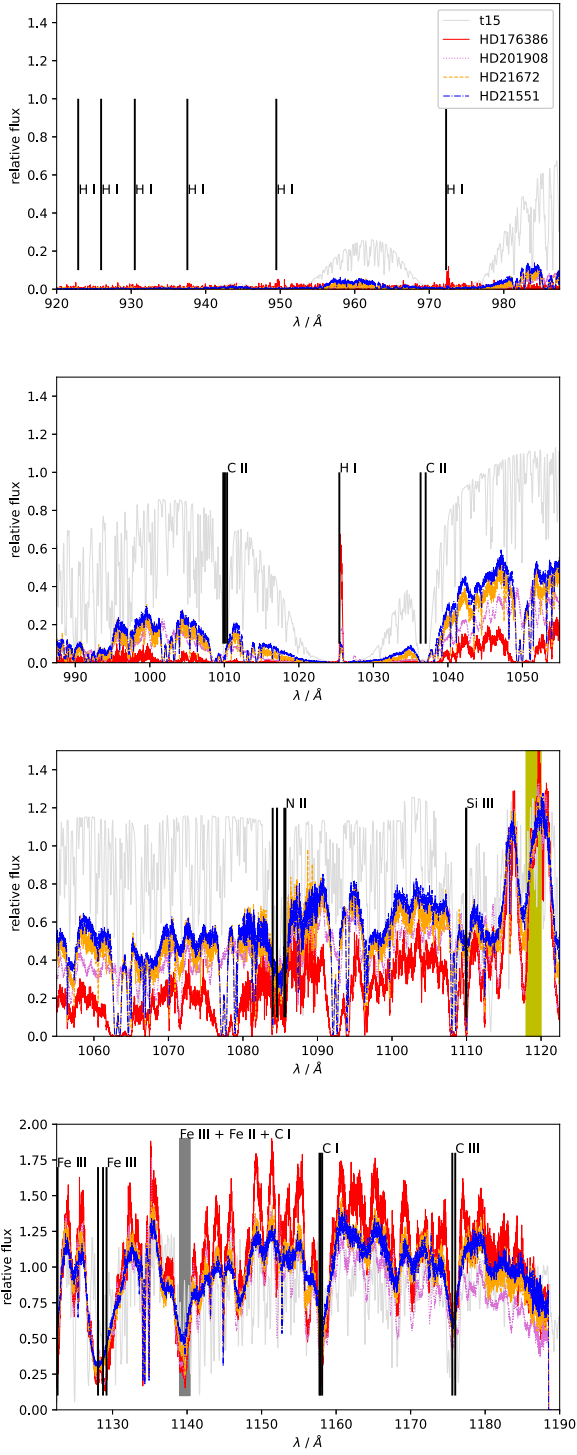


Figure A4. Same as Fig. 1, but for magnetic star HD 176386 and t15 model.

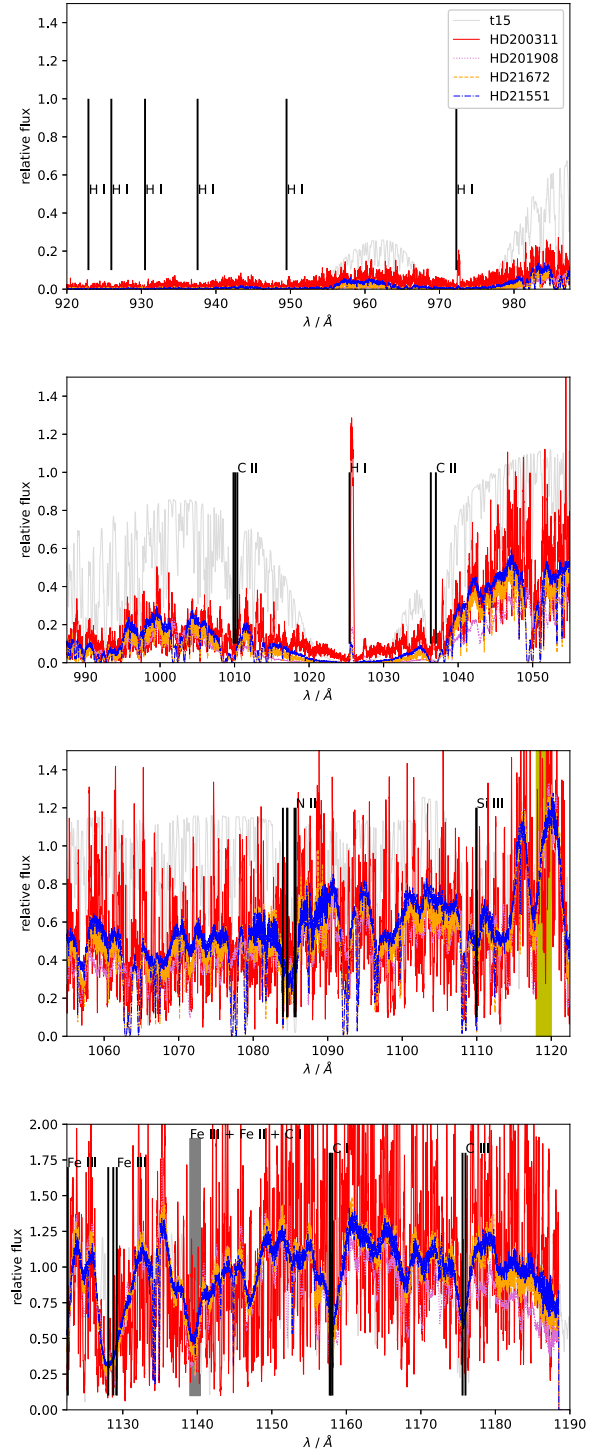


Figure A5. Same as Fig. 1, but for magnetic star HD 200311 and t15 model.

Table A1. Reference non-magnetic stars observed with FUSE.

ID	Sp. type (Simbad)	Used as reference for
HD 52463	B3V	HD 23478, HD 47777, HD 200775
HD 111641	B3V	HD 23478, HD 47777, HD 200775
HD 133699	B3V	HD 23478, HD 47777, HD 200775
HD 201908	B8V	HD 37151, HD 176386, HD 200311
HD 21551	B8V	HD 37151, HD 176386, HD 200311
HD 21672	B8V	HD 37151, HD 176386, HD 200311

This paper has been typeset from a \TeX/L\AA\TeX file prepared by the author.